Time-lapse seismic attenuation as a tool for monitoring hydrocarbons and CO_2 in geological materials

Thomas David Blanchard

Submitted in accordance with the requirements for the degree of Doctor of Philosophy

The University of Leeds

School of Earth and Environment

July 2011

Declaration

The candidate confirms that the work submitted is his own and that appropriate credit has been given where reference has been made to the work of others.

This copy has been supplied on the understanding that it is copyright material and that no quotation from the thesis may be published without proper acknowledgement.

The right of Thomas David Blanchard to be identified as Author of this work has been asserted by him in accordance with the Copyright, Designs and Patents Act 1988.

Acknowledgements

I would like to thank Roger Clark, Mirko van der Baan and Quentin Fisher for their supervision through my research. Their guidance, advice, questions and criticism has made this work much stronger than it would have been without them. A specific thank you to Roger for not only being my lead supervisor for the past 4 years, but an inspiring lecturer for the 4 before that.

I would also like to thank **NERC** for providing funding and **CASE** partners **BP** for providing a data-set to experiment with. In particular I would like to thank Ewan Laws for providing me with information and discussion regarding the Magnus field and Mel Dyce for discussions about 4D repeatability and processing. I would also like to thank the Lawrence Berkeley National Laboratory and the US department of Energy for providing data from a pilot CO_2 injection, and Tom Daley for providing the details concerning data acquisition and the geological properties of the injection site. I thank Tobias Muller for providing answers to questions about his 2004 paper and help in debugging my code of his 1D RPS model. I also thank Dr Philip Christie and Prof Jurgen Neuberg for acting as examiners.

I would also like to thank **Landmark Graphics Corporation** for providing **ProMAX** under the Landmark University Licence Program, and **CGGVeritas** for providing **Hampson-Russell** software, both of which were useful tools in data manipulation of extremely large data-sets. A special thanks to Cleve Moler for inventing **MATLAB**. Genius.

During my PhD I have had the pleasure of inhabiting several offices and buildings. My fellow office mates can be thanked in two separate groups. Firstly, thanks to the PhD "brain trust" (©Reine, 2009) for help with solving problems with code, providing a LaTeXthesis template and for useful discussions of all things geophysics. Secondly I would like to thanks the "entertainers" for providing me with light hearted moments that makes spending time in PhD office so memorable. I would like to thank Carl Reine for a mass of discussion and ideas and for providing me with several useful matlab codes along the way. I would also like to thank Lucky Moffat and Paddy Smith for having an unhealthy desire like myself to discuss all things Q.

Thanks to all of my friends in Leeds, but in particular my housemates Emma, Paddy, Seamus and Mark, for dealing with the best and the worst of me. I am extremely lucky to have Sophie, who over the last stages of my thesis has always been able to make the world better through her love and care. Finally I would like to thank my family, as without their encouragement and support in following my passions, I would not be here today.

Abstract

Both laboratory experiments and theoretical models have shown seismic attenuation to be sensitive to various petrophysical properties of rock and pore fluids, making attenuation a potentially useful time-lapse attribute to measure and interpret through rock physics models. Attenuation is rarely used as an interpretation tool due to the scarcity of reliable measurements and the wide choice of proposed mechanisms potentially responsible for the energy loss.

Current methodologies for estimating attenuation from seismic data (spectral ratio, centroid frequencies and instantaneous frequencies) have been applied to the specific geometries associated with prestack surface seismic data and vertical seismic profiles, and adapted where possible for direct comparison of waveforms from two vintages of data. Phenomena that inhibit reliable estimation of Q can be repeatable between vintages of data allowing the true change in attenuation to be found, even when apparent attenuation is several times larger then intrinsic attenuation. Time-lapse attenuation measurements are sensitive to other waveform changes. Two examples of this are; errors due to changes in dispersion being introduced through frequency dependent travel-times (up to 40% error on 1/Q) and frequency dependent reflectivity, the latter being particularly sensitive at low frequencies and where polarity of reflections change with angle; band-limited random noise and multiple energy both decrease the estimate of attenuation (by 39% for a signal to multiple ratio of 2:1) but leave the change in attenuation detectable, with band-limited random noise also increasing the uncertainty. Attenuation measurements are then made on two field data-sets; a time lapse VSP from a pilot CO_2 sequestration experiment where 1600 tonnes of CO_2 was injected into a thin (10m) aquifer; and a prestack surface seismic data-set from a mature hydrocarbon reservoir undergoing enhanced oil recovery through alternating water and gas injection.

For the VSP, attenuation changes are more detectable when directly comparing waveforms between vintages: however, the realistic synthetic (with a Q change of 100 to 20) indicated that the true magnitude of attenuation is unlikely to be recovered for such a small injection interval. In the real data, changes in attenuation ($\Delta(Q^{-1})$=0.024) and velocity (5% decrease) are qualitatively interpreted by use of a patchy saturation model as an increase in CO_2 saturation of between 10-30%.

Four methodologies are used to calculate attenuation from the surface seismic data-set and show coherent anomalies indicating the robustness of the measurement. The region adjacent to a water and gas injector shows an increase in Q^{-1} of ≈ 0.02. Changes in velocity ($\pm$5%) and amplitude (up to 150%) are also measured from the data and qualitatively agree with the attenuation measurements. A new quasi-linear inversion scheme is introduced to take these time-lapse attributes and solve for pressure and saturation changes using a patchy saturation model, giving 1-10% increases in gas saturation and up to 5MPa pressure changes around three water and gas injectors.

Contents

List of Figures

List of Tables

Conventions

Symbols

Q	Quality factor
$Q^{-1}_{\text{intrinsic}}$	Intrisnic attenuation
Q^{-1}_{app}	Apparent attenuation
Q^{-1}_{eff}	Effective attenuation
ω	Angular frequency
c	Velocity
α	Attenuation coefficient
f	Frequency
k_2	wavenumber of Biots slow wave
M	P-wave modulus
M^*	Complex P-wave modulus
K	Bulk modulus
K_{dry}	Dry bulk modulus
K_{sat}	Saturated bulk modulus
$K_{\text{fl}}/K_{\text{fn}}$	Fluid bulk modulus
K_0/K_{s}	Grain/Matrix bulk modulus
μ	Shear modulus
ρ	Density
ϕ	Porosity
κ	Permeability
ν/η	Viscosity
C	Clay content
t^*	t/Q, Time divided by Quality factor
S, A	Amplitude spectrum
R	Reflectivity
G	Geometrical spreading
τ	Vertical travel time
p	Horizontal slowness
$a(t)$	Analytic envelope
η^2	Frequency damping
θ^2	Inversion damping
f_{c}	Centroid frequency
σ, σ^2	Variance, Standard deviation
$P_{\text{p}}/P_{\text{c}}/P_{\text{d}}/P_{\text{e}}$	Pore/Confining/Differential/Effective Pressure
k_{S}	s-transform resolution factor

Abbreviations

VSP	Vertical Seismic Profile
PSQI	Prestack Q Inversion
AVO	Amplitude versus offset
CMP	Common mid point
QVO	Q versus offset
CF	Centroid frequency
IFM	Instantaneous frequency matching
TLIFM	Time-lapse instantaneous frequency matching
TWT	Two-way-time
NRMS	Normalised root mean square
N2S	Noise to Signal ratio
PRED	Predictability
RPS	Random patchy saturation

Chapter 1

Introduction

As a seismic wave propagates, energy from the coherent wave-front is lost due to various mechanisms, both an-elastic and elastic in nature. Many of these effects reduce the amount of high frequency energy faster than the low frequency energy thus decreasing the bandwidth of a wave as it propagates. This effect is called attenuation and is quantified by the quality factor, Q. Intrinsic attenuation is caused by an-elastic losses as a wave propagates and apparent attenuation is caused by elastic losses such as scattering. Therefore, when attenuation is measured from seismic data, it is composed of both the intrinsic and apparent attenuation.

Many mechanisms that cause the intrinsic loss of amplitude (or energy) have been theorised from the observations made under laboratory conditions (Johnston et al., 1979; Toksöz et al., 1979). These range from heat loss due to friction between grains in a rock to the interaction of multiple pore fluids within a rock (e.g squirt flow, Mavko & Jizba (1991)). The frequency dependence of attenuation therefore means that different mechanisms are excited more or less at different frequencies. It is thought that in the surface seismic bandwidth (10-400Hz) pore fluid mechanisms are the dominant cause of attenuation (Müller et al., 2010).

Attenuation is rarely measured from surface seismic data for two reasons. Firstly, the measured attenuation is composed of both an intrinsic and apparent component of attenuation (Spencer et al., 1982) and in some circumstances the apparent attenuation can be larger than the intrinsic component (or negative) (Van der Baan, 2002). This uncertainty makes interpretation of single vintage attenuation measurements difficult. Even when (or if) intrinsic attenuation can be measured accurately, the interpretation of attenuation is made more difficult by the abundant choice of mechanisms available (Mavko et al., 2003)

where each mechanism is dependent on properties of both the pore fluid(s) (density, viscosity, saturation) and the rock (bulk moduli, shear moduli, fracture size, fracture stiffness, porosity, permeability, density).

Frequent modelling and monitoring of production can help maximise the potential recovery from a hydrocarbon reservoir. By repeating seismic surveys it is possible to observe directly changes in the properties of seismic waves caused by production (Calvert, 2005). Attributes that are commonly measured are predominantly related to changes in the velocity and amplitude. It is a goal of a geophysicist to translate these observed changes into physical changes within the rock itself, ideally any changes in the pressure and saturation (as Landrø (2001) and MacBeth et al. (2006) show), and occasionally (in the special circumstance of a compacting reservoir such as Valhall, Barkved et al. (2005)) the porosity and permeability. Attenuation is not commonly measured as a time-lapse attribute and if measured correctly could provide additional insight into reservoir changes.

As mentioned above, attenuation estimates from seismic data are uncommon for two reasons.

- The unreliability of the measurement due to apparent attenuation
- The choice and complexity of the mechanisms that produce intrinsic attenuation.

However, by making time-lapse measurements these problems may be simplified somewhat. Firstly, if intrinsic attenuation changes are larger than the changes in apparent attenuation, then any change in the attenuation measured will be predominantly caused by intrinsic mechanisms. Secondly, in most reservoirs, many of the petrophysical properties that affect the magnitude of intrinsic attenuation measured should not change between vintages of data (mineral composition, porosity, rock density), leaving fewer unknowns to solve for and interpretation less ambiguous.

1.1 Aims and objectives of thesis

In this thesis I investigate the possibility of measuring and interpreting attenuation from both time-lapse surface seismic and vertical seismic profiles (VSP), which each have a specific geometry associated with them (Yilmaz, 2001). There are three main goals of this thesis that must be achieved if attenuation is to be a useful tool for monitoring hydrocarbon reservoirs and CO_2 sequestration. These are:

1. To understand what mechanisms are likely to be responsible for attenuation and how to interpret measured attenuation changes.

2. To understand the sensitivity and limitations associated with making a quantitative measurement of attenuation changes.

3. To identify the methodologies that are most robust in estimating attenuation, or more specifically time-lapse attenuation from surface seismic and VSP data.

Quantitative measurements of attenuation from surface seismic data have been made by several authors (Dasgupta & Clark, 1998; Matheney & Nowack, 1995; Quan & Harris, 1997), with most relying on the changes to a single attribute. Here I consider three methodologies that use changes in the log spectral ratio slope, centroid frequency and instantaneous frequency to measure changes in attenuation. With regards to these methodologies I aim to: adapt these methodologies, where needed, to meet specific acquisition geometries; develop the algorithms, when appropriate, to measure directly the changes in attenuation between vintages of data; and determine which of the methodologies is more robust in estimating time-lapse attenuation.

When attenuation changes occur, other changes to the seismic waveform will also occur. I aim to investigate and quantify where possible the sensitivity of time-lapse attenuation measurements to: incoherent noise; spectral contamination; amplitude and travel-time changes; and frequency dependent velocity changes.

Using two real time-lapse data-sets I investigate how repeatable attenuation measurements are between vintages of data. By comparing the magnitude of measured attenuation changes with those predicted from theoretical models I also aim to identify the likely mechanisms controlling the attenuation changes in the data-sets. Furthermore, I aim to develop a framework for measuring attenuation changes and relating them to changes in the petrophysical properties of the rock. Through the measurement of attenuation and other time-lapse attributes I aim to determine how much additional information attenuation estimates can provide in separating pressure and saturation in hydrocarbon reservoirs.

1.2 Layout of Thesis

I begin this thesis with an overview of the literature relevant to this topic. Beginning with the mathematical and physical definitions of attenuation I move on to discuss the

differences between intrinsic and apparent attenuation and the need for velocity dispersion to be present. I then look at a large number of proposed mechanisms that are thought to control the magnitude of attenuation. These relationships have been derived both theoretically and through observation of laboratory measurements. I pay special attention to mechanisms that are potentially responsible for large amounts of attenuation in the seismic bandwidth, and in particular to mechanisms that are applicable to multiphase fluids. I then look in more detail at some of these observations and relationships with particular interest in their sensitivity to various parameters such as frequency, pressure, porosity and saturation. I look at where attenuation measurements have been made previously for single vintage measurements of data (Dasgupta & Clark, 1998; Matheney & Nowack, 1995) and on the few occasions from time-lapse seismic data-sets (Williams, 2001). Finally I look at 4D seismic interpretation, with particular interest in existing methodologies that enable the separation of pressure and saturation.

In Chapter 3 I look in detail at the available methodologies for estimating attenuation changes from both surface seismic data and VSPs. I look in detail at 4 methodologies; the QVO (Dasgupta & Clark, 1998) methodology, the PSQI (Pre-stack Q inversion) methodology (Reine et al., 2011a), the centroid frequency methodology (Quan & Harris, 1997) and the instantaneous frequency matching methodology of Matheney & Nowack (1995). In this chapter I present the original methodologies and develop the methods for the specific geometries of surface seismic or VSP data. Through several assumptions, I also develop the methodologies so that attenuation can be calculated by direct comparison of the waveforms of different vintages of data.

In Chapter 4 I look at the sensitivity of time-lapse attenuation measurements. I give a synthetic example showing the repeatability of the apparent component of attenuation, yielding the true changes in intrinsic attenuation. The sensitivity of the methodologies outlined in Chapter 3 is investigated through the addition of bandpass filtered random noise. If attenuation changes occur it is also likely that other changes in the waveform will be present, such as amplitude and dispersion. Changes in dispersion are likely to impact attenuation measurements through frequency dependent travel times and reflection coefficients. The errors associated with these changes are investigated through numerical and synthetic examples and quantified where possible. The possible errors introduced through any assumptions made in the methodologies outlined in Chapter 3 are also examined.

I then move on to look at two real time-lapse studies, one from a pilot CO_2 sequestra-

tion experiment where a time-lapse VSP has been acquired and one from a hydrocarbon reservoir undergoing water and gas injection where two vintages of surface seismic data are available. Chapter 5 focuses on the time-lapse VSP acquired during the injection of CO_2 into a highly permeable, high porosity sandstone. I begin the chapter by creating a realistic synthetic data-set and test the feasibility of measuring attenuation from such a thin injection interval (5-10m). Synthetic data are analysed using three methodologies on both the full and down-going wave-field. Methodologies are parameterised carefully and attenuation is calculated from each vintage of data. A new approach is then introduced that enables the calculation of attenuation directly between traces of a VSP, even when the source spectra are not consistent between vintages. The chapter finishes with a qualitative interpretation of results as core data were not available to constrain attenuation relationships quantitatively.

Chapter 6 contains a case study of a mature hydrocarbon reservoir in the North Sea that is undergoing enhanced oil recovery through water and gas injection. Again a feasibility study is carried out by creating complex synthetic data that replicate the real data-set. I calculate attenuation changes through a range of the methodologies and the uncertainties associated with each of the methodologies are also estimated, providing insight into the stability of each method. Other more common 4D attributes (TWT, AVO) are also measured from the seismic data and compared with measured attenuation changes. A new inversion scheme is then introduced that uses a rock physics model to invert for changes in saturation and pressure from analysis of several time-lapse attributes.

Finally, in Chapter 7 I discuss the findings within this thesis, provide a summary of recommended future work and a summary of the main conclusions.

Chapter 2

Background

To understand how to measure and interpret attenuation changes it is necessary to understand what attenuation is, how it is defined and what mechanisms produce it. It is also important to understand how attenuation varies with changes in rock properties, especially properties that we would expect to change significantly over time in a hydrocarbon reservoir. I will look at a variety of attenuation relationships that have been observed in the laboratory; empirically fitted to measurements; and derived through physical theory.

To understand reservoir changes quantitatively, attenuation will need to be simultaneously interpreted with other, more commonly used, time-lapse attributes. I will look at what other attributes are commonly measured from seismic data and how to combine them with attenuation to interpret reservoir changes. The separation of pressure and saturation changes is a problem that a few have tried solving by direct inversion of conventional time-lapse attributes. I will look at these methods and also look at what additional information attenuation may be able to provide - quantitatively or qualitatively.

2.1 Attenuation theory

Attenuation is defined as the irreversible conversion of elastic wave energy into other forms (heat, fluid movement) as a wave propagates. I will refer to this attenuation as the intrinsic attenuation ($Q^{-1}_{\text{intrinsic}}$). Other frequency dependent amplitude changes can occur that can inhibit a successful measurement of the intrinsic attenuation, which I will term apparent attenuation, Q^{-1}_{app}. The effective (measured) attenuation (Q^{-1}_{eff}) can be describes as the sum of the inverse quality factors of the apparent and intrinsic attenuation (Spencer et al., 1982)

$$Q_{\text{eff}}^{-1} = Q_{\text{intrinsic}}^{-1} + Q_{\text{app}}^{-1}. \tag{2.1}$$

2.1.1 Intrinsic attenuation ($Q_{\text{intrinsic}}^{-1}$)

Intrinsic attenuation can be defined in several ways, but there are two definitions that are widely used. Attenuation is most intuitively described as the fraction loss of energy (ΔE) per cycle as a wave propagates

$$\frac{1}{Q} = \frac{1}{2\pi}\frac{\Delta E}{E} \tag{2.2}$$

where E is the peak strain energy (Aki & Richards, 2002). Aki & Richards (2002) show that for a material with a linear stress-strain relationship and under the assumption that $Q >> 1$, the amplitude of a plane seismic wave, $A(x)$, with initial amplitude A_0, at a distance x is given by the exponential decay

$$A(x) = A_0 e^{-\frac{\omega x}{2cQ}} \tag{2.3}$$

where ω is the angular frequency and c is the velocity. This can then be described by a simple exponential decay of the form

$$A(x) = A_0 e^{-\alpha x}, \tag{2.4}$$

where

$$Q(\omega) = \frac{\omega}{2\alpha(\omega)c(\omega)}. \tag{2.5}$$

Attenuation can also be described fundamentally as the ratio of the imaginary (M_{I}) to real (M_{R}) parts of the complex P-wave modulus (M) (Aki & Richards, 2002; Carcione et al., 1998; O'Connell & Budiansky, 1978; Ursin & Toverud, 2002).

$$\frac{1}{Q(\omega)} = \left|\frac{M_{\text{I}}(\omega)}{M_{\text{R}}(\omega)}\right| \tag{2.6}$$

By introducing a complex wave-number ($k* = k + i\alpha$) into the equation for a propagating wave it is possible to show that

$$Q(\omega) = \frac{|\omega|}{2\alpha(\omega)c_p(\omega)} - \frac{\alpha(\omega)c_p(\omega)}{2|\omega|} \tag{2.7}$$

(Ursin & Toverud, 2002). If we assume that attenuation is small then ($\alpha c_p(\omega) << 2|\omega|$) Equation 2.7 reduces to Equation 2.5:

$$Q(\omega) \approx \frac{\omega}{2\alpha(\omega)c(\omega)}.$$

O'Connell & Budiansky (1978) also showed that when a material can be assumed to be modelled by a network of springs and dashpots, equation 2.6 can then be expressed by

$$\frac{1}{Q} = \frac{1}{4\pi}\frac{\Delta\phi}{V_{\text{ave}}} \tag{2.8}$$

where V_{ave} is the average stored energy and $\Delta\phi$ is the energy dissipated per cycle. It is clear that there is a large resemblance between Equations 2.2 and 2.8.

Equation 2.5 is the generalised equation for the Quality factor (assuming low loss) where the Quality factor, attenuation coefficient and velocity are all permitted to be frequency dependent. The energy loss definition (Equation 2.2) is more intuitive when measuring attenuation from a seismic pulse and the complex modulus definition (Equation 2.6) is more useful when calculating the attenuation from theoretical rock physics models.

Although Q is in nature frequency dependent, it possible to have constant Q via either setting a linear relationship between α and ω (Kolsky, 1956; Wang, 2008), assuming a specific power law relationship between α and ω with $c_\infty = \infty$, or to assume that there are many mechanisms of different relaxation times superimposed upon one another (Liu et al., 1976). In this thesis I will assume that Q is constant over the frequency range of measurement, but will discuss the sensitivity of this assumption when analysing various attenuation mechanisms, laboratory measurements and theoretical models.

2.1.2 Apparent attenuation

In this thesis, apparent attenuation (Equation 2.1) will be defined as any other frequency dependent loss or gain of energy not caused by the attenuation mechanisms assumed responsible for the intrinsic attenuation. The causes of apparent attenuation can be classified in two groups:

- Interference and scattering (Q_{scatt})
- Other mechanisms (Q_{other})

Interference and scattering - Q^{-1}_{scatt}

Interference I define spectral contamination as any unwanted additional energy that alters the spectral estimate of the desired arrival from a single source. Examples of this are the interference cause by multiple energy, either long-path or short-path. Spencer et al. (1977) showed that for closely spaced reflections bounding an interval of velocity V and thickness z a minimum will be observed in the amplitude spectrum at frequency f_{t} where

$$f_{\text{t}} = \frac{V}{4z}. \tag{2.9}$$

Scattering The combined and repeated effect of reflection and transmission can cause frequency dependent effects. In the case of many short path multiples being produced during the transmission of a pulse through a 1D reflectivity series, O'Doherty & Anstey (1971) found that the simple relationship

$$T(\omega) = e^{-R(\omega)t} \tag{2.10}$$

(where T is the amplitude of the transmitted pulse, R is the power spectrum of the reflectivity series and t is the travel-time) can describe the effect that an elastic reflectivity series can have on the spectrum of an impulse source. If the reflectivity series behaves in a transitional manner (varying slowly) or cyclically (changing sign) the energy that is cut will be the low frequency or high frequency respectively.

It is possible to characterise the effect of 1D scattering through layered media by defining the properties of a reflectivity series through a spatial auto-correlation of itself (Van der Baan, 2001). Scattering attenuation can then be calculated as a function of various parameters for different distributions of reflectivity. Van der Baan (2002) showed that a constant scattering Q as a function of frequency can be generated if specific functions that mimic a fractal earth are used to represent the auto-correlation. The implications of this are that it is possible for both intrinsic and scattering attenuation to affect an impulse in the same way, making the separation of the two phenomena impossible. Scattering attenuation can be greater in magnitude than intrinsic attenuation (Van der Baan, 2002), and

apparently negative, leading to negative estimates of effective attenuation. It is possible to estimate the amount of scattering attenuation present from the statistical analysis of well-data. White et al. (1990) showed that an exponential auto-correlation function could be used to fit measured auto-correlations from well-data and calculated Q values due to scattering in the range of 120-750 in the 20Hz-150Hz bandwidth.

Obviously scattering can be far more complex than the 1D representations described above. It can occur on all length scales in a 3D geometry caused by inclusions, and diffraction, both in-plane and oblique to the direction of propagation expected from simple ray theory.

Other mechanisms Q^{-1}_{other}

There are many mechanisms that are responsible for the attenuation of seismic energy. These mechanisms will be described in detail in Section 2.2. However it is important to recognise at this point that we expect, in a time-lapse scenario, some mechanisms to dominate over others. Although many time-variant changes can occur in seismic reservoirs the majority of them are caused by either changes in fluid content or reservoir pressure. In certain circumstances it may be reasonable to assume changes in attenuation are caused primarily by a single mechanism. In this case, other mechanisms will add noise to the intrinsic attenuation desired.

2.1.3 Dispersion

Causality requires that if we know the attenuation for all frequencies then we also know the dispersion for all frequencies (Aki & Richards, 2002). The relationships between dispersion and attenuation vary according to the chosen relationship between the quality factor and the attenuation coefficient (Equation 2.5). It can be shown that for both the Kolsky model and for the nearly constant Q model of Liu et al. (1976) the following relationship can be used to describe dispersion (Ursin & Toverud, 2002).

$$\frac{c(\omega)}{c(\omega_{\text{ref}})} = 1 + \frac{1}{\pi Q}\ln(\frac{\omega}{\omega_{\text{ref}}}) \tag{2.11}$$

However, this is not true for all nearly constant Q laws; some have been developed in which Equation 2.11 does not accurately predict dispersion. Aki & Richards (2002) also showed that equation 2.11 can also be derived from laboratory observations of creep, so this will be the definition of dispersion used throughout this thesis unless stated differently

at the time.

2.2 Attenuation relationships

2.2.1 Overview

There are many relationships available to analyse the behaviour of attenuation when properties of the rock matrix or pore fluid are changed. Here I look at some of these relationships, from observations of laboratory measurements, empirical relationships and theoretical models. As I am primarily interested in attenuation changes with regards to changes in fluid content and pressure I will focus on observations and relationships that are able to give insight into the attenuation mechanisms that are sensitive to partial saturation.

2.2.2 Laboratory experiments

Values of attenuation have been measured as functions of frequency, gas saturation, effective pressure, porosity and clay content. Laboratory measurements can be split into two main categories, high frequency and low frequency and I will look at these observations separately.

High frequency measurements High frequency measurements are made using an ultrasonic source and lie in the frequency range beyond 5KHz. These have been made by several authors including Murphy et al. (1984), Prasad & Manghnani (1997), Toksöz et al. (1979),Cadoret et al. (1995) and Klimentos & McCann (1990). Many mechanisms have been suggested from these measurements and Johnston et al. (1979) made proposals from the measurements of Toksöz et al. (1979). They outline several possible mechanisms that explain the observed behaviour of experimental data ranging from mechanisms associated with matrix anelasticity, saturation fluid flow (viscosity) and partial saturation. A schematic of these proposed mechanisms is seen in Figure 2.1. Johnston et al. (1979) concluded that in saturated porous rocks, grain and crack friction (lubricated by fluid) plays a more important role than attenuation caused by fluid flow. However, measurements by Cadoret et al. (1995) and Cadoret et al. (1998) showed that attenuation was dominated by fluid flow, especially for partial saturation. Their findings also highlighted the point that fluids occupy pore space differently when water displaces gas (imbibition) or

when gas replaces water (drainage). During imbibition, they found (using a combination of x-ray imaging and ultrasonic measurements) that gas and water distribute themselves uniformly throughout the pore space, whilst during drainage, random distributions of gas clusters occur throughout the rock, particularly at high water saturation (Figure 2.2). The drainage experiments produced much larger values of p-wave attenuation, highlighting the importance of fluid distribution on the magnitude of attenuation. These are some of the more important observations made at ultrasonic frequencies because they can be represented by theoretical models, but this indicates that there may be significant differences in attenuation from water entering a light hydrocarbon reservoir, and gas being injected into an oil reservoir, purely due to the geometry taken up by the gas pockets.

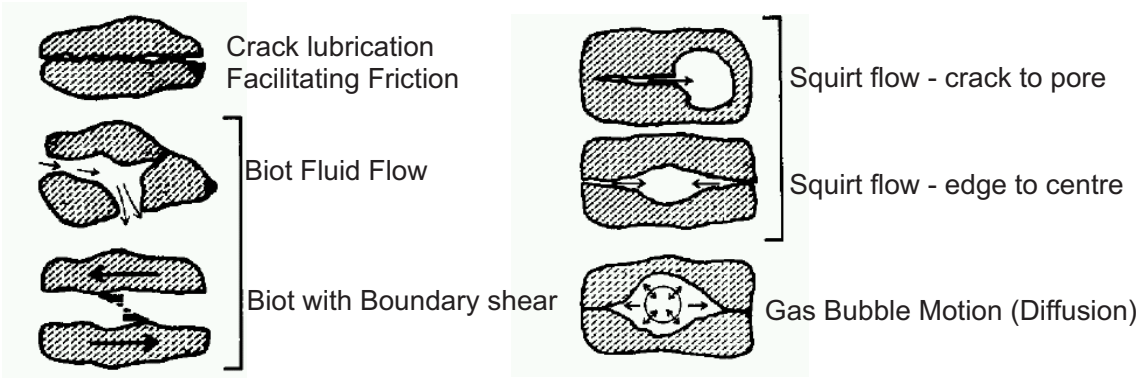

Figure 2.1: Schematic illustration of proposed mechanisms of Johnston et al. (1979).

Low frequency measurements More important in understanding the mechanisms occurring within the seismic bandwidth are the measurements undertaken at much lower frequencies achieved using methods such as as the resonant bar technique and forced deformation. Many workers have undertaken laboratory measurements of attenuation at frequencies in the 10Hz-kHz range (e.g. Batzle et al. (2006); Murphy (1982); Murphy et al. (1984); Winkler & Nur (1979)). Winkler & Nur (1979) carried out experiments using the resonant bar technique, looking at the effect of confining pressure, pore pressure, saturation and strain amplitude on attenuation. They highlighted the strain amplitude dependence of attenuation and therefore the need to keep strain amplitudes low for measurements to stay applicable to seismic waves. They also found that there is a peak in attenuation when gas saturation is around 65%. The observation of a peak in attenuation has also been seen at lower frequencies (500-900Hz) by Murphy (1982). The peak attenuation at these frequencies was at a higher water saturation than found in the work of Winkler & Nur (1979). The frequency dependence of the saturation at which the peak attenuation occurs

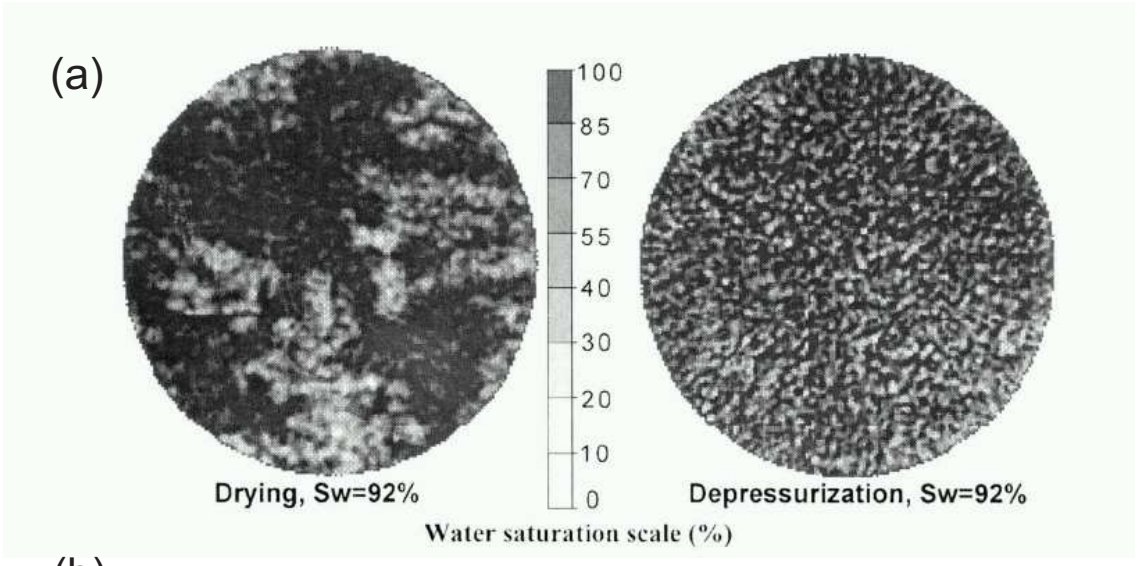

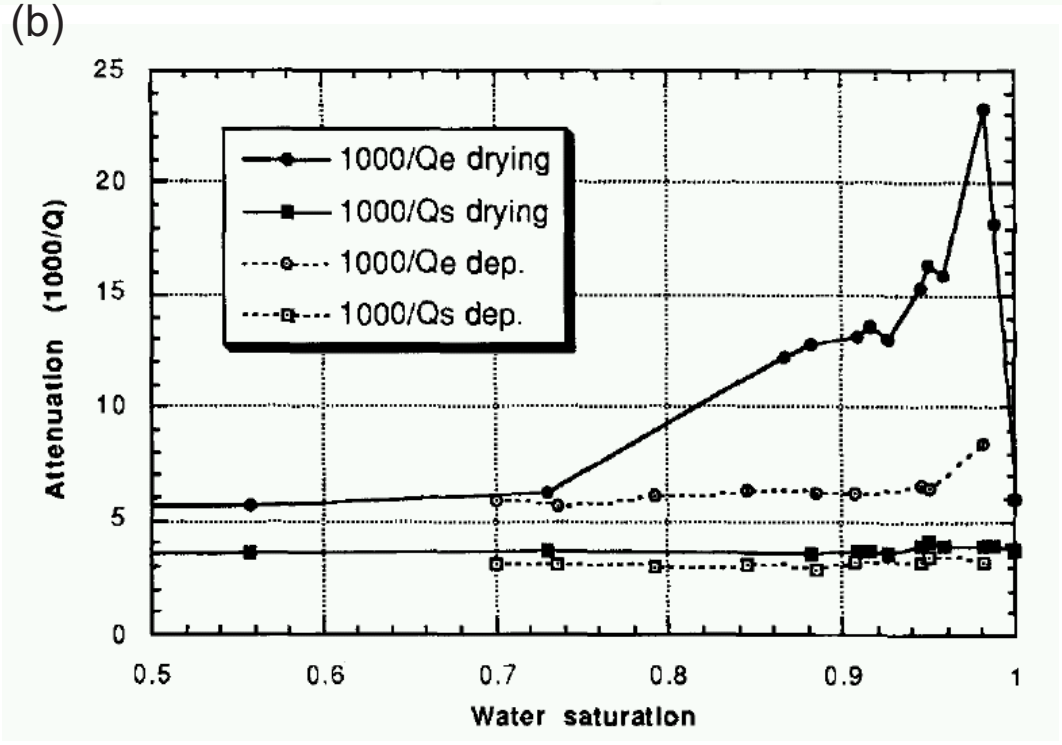

Figure 2.2: Results of Cadoret et al. (1998) showing (a) the distribution of gas saturation via drying (draining) and depressurization (imbibition) and (b) the attenuation measured at for each regime as a function of water saturation.

has been observed and a plot from Murphy (1982) can be seen in Figure 2.3. Yin et al. (1992) showed similar results to those of Cadoret et al. (1995) but for lower frequencies 500-900Hz, again observing that the saturation history (fluid distribution) had an influence on the magnitude of attenuation.

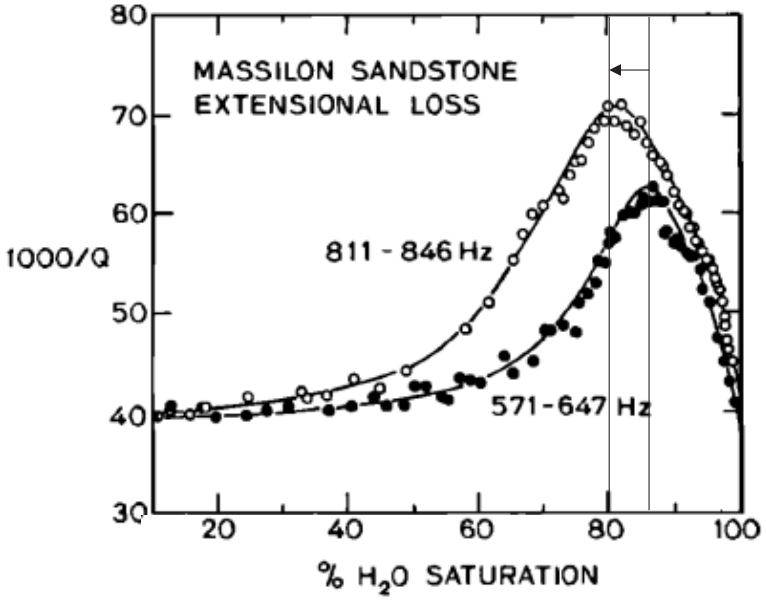

Figure 2.3: Frequency dependence of the P-wave attenuation peak, taken from Murphy (1982).

2.2.3 Theoretical relationships

The large number of mechanisms that are responsible for anisotropy and attenuation means that there are many theoretical models available that describe these effects. To date there is no single rock physics model that takes into account all of the mechanisms for attenuation, in anisotropic, heterogeneous, fractured and multiphase fluid-filled rocks. Here I look at a selection of theoretical models, paying special attention to those that describe mechanisms sensitive to fluid saturation and pressure changes in the seismic bandwidth. Of course, we are not limited to using models that explicitly deal with multiple fluids as it is possible to use single phase fluid models using effective fluid properties.

Fluid mixing laws

A methodology for estimating an effective fluid model is described by Mavko et al. (2003) and Avseth et al. (2005). The effective parameters that need to be calculated are the effective moduli, density and viscosity. Effective fluid moduli are commonly found by two different means of averaging, called the Voigt and Reuss bounds. The lower bound is the

Reuss average and is defined as:

$$\frac{1}{M_{\mathrm{r}}} = \sum_{\mathrm{i}=1}^{N} \frac{f_{\mathrm{i}}}{M_{\mathrm{i}}} \tag{2.12}$$

where M_{r} is the average property of the rock and f_{i} is the fraction of each fluid, i, with property M_{i}. This implies that it is impossible for a combination of fluids to have an effective modulus less than the harmonic average of those fluids. However, this effective modulus assumes that fluids are well mixed, and as previously observed from the laboratory and x-ray measurements of Cadoret et al. (1998), this is sometimes not the case. In the case of partial saturation it may be better to use the Voigt Upper bound, defined by

$$M_{\mathrm{v}} = \sum_{\mathrm{i}=1}^{N} f_{\mathrm{i}} M_{\mathrm{i}}. \tag{2.13}$$

This implies that no effective fluid can have moduli greater than the arithmetic mean of the constituents. Other upper and lower bounds are given by Hashin & Shtrikman (1963). The effective density and effective viscosity are usually calculated from the arithmetic mean of the constituents Mavko et al. (2003).

Fluid substitutions - Gassmann

The most commonly used theoretical approach for calculating the seismic properties of a rock filled with different fluids are the relationships of Gassmann (1951),

$$\frac{K_{\mathrm{sat}}}{K_0 - K_{\mathrm{sat}}} = \frac{K_{\mathrm{dry}}}{K_0 - K_{\mathrm{dry}}} + \frac{K_{\mathrm{fl}}}{\phi(K_0 - K_{\mathrm{fl}})} \tag{2.14}$$

$$\mu_{\mathrm{sat}} = \mu_{\mathrm{dry}} \tag{2.15}$$

where K_{dry},K_{sat},K_0 and K_{fl} are the bulk moduli of the dry frame, saturated rock, mineral and fluid respectively. In most cases this relationship is used to calculate the bulk modulus of a rock when it is fully saturated with a single fluid phase. For multiphase fluids, an effective bulk modulus can be calculated using the Reuss average. In Equation 2.14, the rock and fluid are assumed to have a single pressure (due to the low frequency requirements of the Gassmann derivation), however, it is more likely that each fluid will have a different pressure within the rock as the wave passes. It is therefore only correct to use this if we

assume that the fluids are well mixed at the smallest scale, hence use of the Reuss average is ideal (Avseth et al., 2005). There are, however, examples of using the Voigt average in the Gassmann relationships, when the fluid distribution can assumed to be patchy (Aki & Richards, 2002). The simplifications in the Gassmann relationships, particularly that of there being pressure equilibrium throughout the fluid and rock highlights the fact that we need a far more complicated model that considers pressure differences created as a wave passes through a rock. The starting point for this will be to look at the Biot laws.

Macroscopic flow (Global flow) - Biot

Although the equations of Gassman can be found in the low frequency limit of the Biot (1956) theoretical formula, I started with them because they are the most frequently used tool in applied seismology for the quantitative interpretation of fluid changes in a reservoir. The Biot laws encompass many different viscous and inertial reactions between a pore fluid and the matrix of the rock (Mavko et al., 2003) including the inertial drag of the fluid and rock matrix. Inertial drag is the effect of there being a lag between the acceleration of the matrix and the movement of the fluid. This effect is quite large at high frequencies, however, at lower frequencies the matrix and fluid movements are effectively locked in phase (Ahrens, T, 1995). This means that although this mechanism may provide some attenuation in the seismic bandwidth it is not likely to be the main cause as it is much smaller than observed attenuation. In fact, even at higher frequencies, Biot's equations underestimate the amount of attenuation present in laboratory measurements (Winkler, 1986). This is because the local flow (squirt flow) is not taken into account. The Biot relationships do not accommodate mechanisms associated with partial saturation so effective fluid moduli need to be estimated before using; this is not ideal as the interaction of two separate fluids and the associated mechanisms would not be taken into account.

Microscopic flow (Squirt flow) - Mavko-Jizba, BISQ

Microscopic attenuation mechanisms are mechanisms that exist on the pore scale. Squirt flow occurs because a seismic wave produces pressure differences within cracks and pores. If there are cracks connected to pores or cracks connected of different orientations, fluid flows between them and it is this flow that produces additional attenuation. The first work completed on this was a high frequency squirt relation by Mavko & Jizba (1991). However these relations could only be used at high frequencies (ultrasonic). Dvorkin et al. (1995)

extended the Mavko & Jizba (1991) model to all frequencies, and by including effective fluid moduli, squirt flow at partial saturation can be calculated. Squirt flow models require prior knowledge of the effective moduli of the dry rock, the effective modulus of the rock at high pressure (compliant cracks closed), bulk moduli of the fluid phases, rock density and porosity, and the viscosity of the pore fluid. The relationships contain a parameter that is proportional the characteristic squirt flow length, and determines the frequency scale of the dispersion. Sams et al. (1997) have shown that squirt flow can be used to describe the frequency dependent behaviour of attenuation by fitting observations at a range of frequencies to a squirt flow model using cracks with aspect ratios of $\approx 10^{-3}$.

Mesoscopic flow (fluid diffusion) - Patchy saturation models

Mesoscopic attenuation mechanisms are likely to be the dominant mechanisms in partially saturated rocks at the seismic bandwidth (Müller et al., 2010). Here I consider the White (1975) patchy saturation model model for partial saturation for a spherical patch geometry and then go on to consider some of the other options available with less stringent geometrical constraints.

White's patchy saturation model A patchy saturation model was developed by White (1975) to calculate the velocity and attenuation in a rock saturated with pockets of different fluids. A more rigorous solution was found by Dutta & Ode (1979), utilising Biot's equations of poroelasticity. A good overview and framework for the patchy saturation model is given in Mavko et al. (2003). They define a patch as a region of rock occupied by a single fluid phase where the length scale (L_c) of each patch is defined by the critical fluid diffusion parameter (D),

$$L_\mathrm{c} = \sqrt{D/f} \tag{2.16}$$

where

$$D = \kappa K_\mathrm{fl}/\nu \tag{2.17}$$

and K_fl is the fluid bulk modulus, ν is the fluid viscosity and κ is the permeability. When a seismic wave propagates, pressure equilibriates at length scales smaller than L_c but does not when neighbouring patches are at length scales larger than L_c. Fluid flow (diffusion) caused by these pressure differences is the mechanism for attenuation and dispersion. The

patches are defined by an inner sphere saturated with fluid 1 of radius a in the centre of a shell saturated with fluid 2 of radius b (Figure 2.4). It can therefore be seen that the saturation S_1 of fluid 1 is

$$S_1 = \frac{a^3}{b^3} \tag{2.18}$$

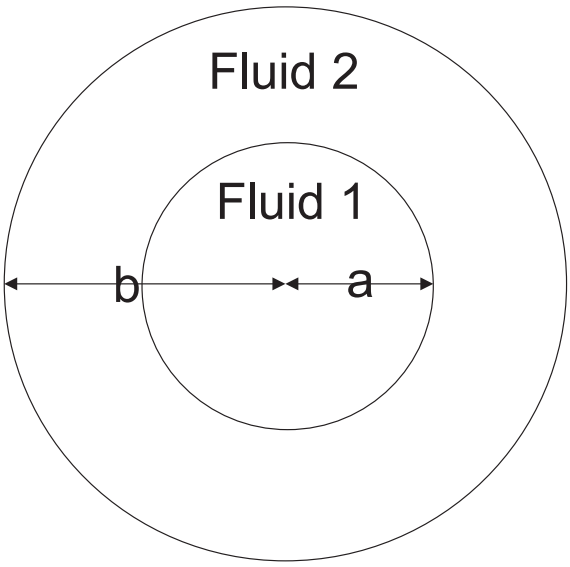

Figure 2.4: Schematic of White's (1975) spherical patchy saturation model.

The parameters needed for the model are the dry rock bulk modulus (K_{dry}), dry rock shear modulus (μ_{dry}), mineral bulk modulus (K_0), mineral density (ρ_0), porosity (ϕ), permeability (κ), fluid bulk moduli ($K_{\text{fl1}}, K_{\text{fl2}}$), fluid densities ($\rho_{\text{fl1}}$,$\rho_{\text{fl2}}$), fluid viscosity ($\nu_{\text{fl1}}, \nu_{\text{fl2}}$), fluid saturation ($S_{\text{fl1}}$), patch size ($b$) and frequency ($f$). Of all these parameters, the most difficult to constrain is the patch size. The attenuation peak is sensitive to the patch size and if the patch size is small compared with the fluid diffusion relaxation scale (L_{c}), pressure is equilibrated between fluids and no attenuation occurs. This then determines where the peak attenuation lies as a function of frequency. Rock physics models have been calibrated in the lab previously, however, patchy saturation models cannot be as patch sizes enforced in the lab are unlikely to match the patch sizes found in the field. A possible solution to this is to consider multiple patch sizes, or even random distributions of patch sizes.

Random patchy saturation (RPS) models Theory involving patchy saturated rocks has been taken further to try and reduce geometrical constraints imposed by the original

model of White (1975). Models have been developed for random distributions of saturation patches and these may be more realistic than patches of ideal geometry.

Here I look at a 1D random patchy saturation model of Gurevich & Lopatnikov (1995) (Equations 2.19 to 2.22) in which all of the material parameters are assumed to be stationary random functions of one co-ordinate direction z. The Bourret approximation (averaging method) described by Müller & Gurevich (2004) defines the complex P-wave modulus M^* in a random system as a function of the P-wave modulus for an effective homogeneous porous medium (M_0), the effective wavenumber of Biot's slow wave (k_2), an autocorrelation function ($\psi(\xi)$) of the fluctuating parameter ($\epsilon(z)$) and a dimensionless parameter s that is related to the degree of inhomogeneity of the medium where:

$$M^*(\omega) = M_0[1 - isk_2 \int_0^\infty \psi(\xi) e^{(ik_2\xi)} d\xi], \tag{2.19}$$

$$k_2 = \sqrt{(i\omega)} \frac{\langle \sqrt{(\frac{\eta}{\kappa} N)} \rangle}{\langle N \rangle}, \tag{2.20}$$

$$\psi(\xi) = \frac{\langle \epsilon(z)\epsilon(z-\xi) \rangle}{\langle \epsilon(z)^2 \rangle}, \tag{2.21}$$

$$\epsilon(z) = \alpha(z)J(z)/M(z) - \langle \alpha(z)J(z)/M(z) \rangle, \tag{2.22}$$

$$s = \left\langle \frac{1}{M} \right\rangle^{-1} \left(\left\langle \frac{\alpha^2}{L^2} N \right\rangle^2 - \left\langle \frac{\alpha}{L} \right\rangle^2 \left\langle \frac{1}{N} \right\rangle^{-1} \right), \tag{2.23}$$

$$\alpha(z) = 1 - K/K_\mathrm{s}, \tag{2.24}$$

$$J = 1/[(\alpha - \phi)/K_\mathrm{s} + \phi/K_\mathrm{f}], \tag{2.25}$$

$$M = K_\mathrm{sat} + 4\mu/3, \quad L = 4\mu/3, \quad N = JL/M. \tag{2.26}$$

The brackets $\langle\rangle$ represent an average of the property over the depth z.

Müller & Gurevich (2004) look at explicit forms of these relationships for specific random distributions, defined by the auto-correlation function in Equation 2.21. Müller & Gurevich (2004) defined explicitly the complex P-wave moduli for several distributions including a periodic function, static case (homogeneous saturation), power series and exponential correlation function.

I mentioned previously that White et al. (1990) found that an exponential correlation could be used to estimate the random distribution of well log information. Here I consider the case of an exponential correlation function $\psi(\xi) = e^{-2|\xi|/d}$ where d is the correlation length. This leads to the simplification of Equation 2.19 to

$$M(\omega) = M_{\mathrm{w}}[1 + \frac{s}{1 + \frac{2i}{k_2 d}}], \tag{2.27}$$

(Müller & Gurevich, 2004) where M_{w} is Wood's average P-wave moduli (Mavko et al., 2003) of the fluid saturated rocks.

2.2.4 Empirical relationships

Another approach to generate relationships between attenuation and various rock properties is to describe experimental results with simple empirical relationships. Klimentos & McCann (1990) derived empirical relationships between attenuation, porosity, and clay content with the resulting Equation (2.28) for a sandstone at 1MHz, and 40MPa.

$$\alpha = 0.0315\phi + 0.241C - 0.132 \tag{2.28}$$

Koesoemadinata & McMechan (2001) extended this work by performing various regressions on a catalogue of laboratory data (Table 2.1). The regressions were solved to find a set of coefficients to satisfy Equations 2.29 and 2.30. Added complexity comes from the fact that some of the coefficients are dependent upon a combination of parameters.

$$100/Q_{\mathrm{p}} = b_1 + b_2\phi + b_3 C + b_4 \ln(\kappa) + b_5(S_{\mathrm{w}}, f) - b_6(P_{\mathrm{e}}, S_{\mathrm{w}}, f) \tag{2.29}$$

$$V_{\mathrm{p}} = a_1 + a_2\phi + a_3 C + a_4 \ln(P_e) + a_5 S_{\mathrm{w}} + a_6 f \tag{2.30}$$

Constants b_1, b_2, b_3 and b_4 can be found easily: however, b_5 and b_6 are a series of fitted surfaces or volumes. They provide a useful estimation of attenuation and the variation with

pressure and saturation. At the same time as performing regression for Q_{p}, regressions for V_{p} and V_{s} were also undertaken.

Author	Q_{p}	Q_{s}	f	ϕ	C	P_{e}	S_{w}	κ
Clark et al. (1980)	X	X	X	X	X	X	X	X
Frisillo & Stewart (1980)	X		X	X	X	X	X	X
Murphy (1982)	X	X	X	X	X	X	X	X
Winkler & Nur (1979)	X	X	X	X	X	X	X	X
Klimentos & McCann (1990)	X	X	X	X	X	X	X	X
Best et al. (1994)	X	X	X	X	X	X	X	X
Best & McCann (1995)	X		X	X	X	X	X	
Tao et al. (1995)	X	X	X	X	X	X	X	X

Table 2.1: Database used by Koesoemadinata & McMechan (2001) to derive empirical relationships of attenuation.

There are some drawbacks with using these empirical models. The majority of the data that are used in the regression were acquired at ultrasonic frequencies. This means that the solution is under-determined for the lower frequencies and relies on extrapolation from higher frequencies. There may be a large assumption associated with this, as the attenuation mechanisms that are dominate at high frequencies may not exist at lower frequencies. The lowest frequency data used by Koesoemadinata & McMechan (2001) are at around 500Hz making the frequencies in the surface seismic bandwidth an extrapolation of the regression. As well as these assumptions, limitations arise in these empirical relationships as we are restricted to a water-gas mixture in a clean sandstone. Is is not clear how accurate these equations would be for an oil-water or water-CO_2 mixture in other lithology.

2.2.5 Q relationships

I have highlighted a selection of methodologies for modelling changes in attenuation, with specific interest in mechanisms controlled by partial saturation. Important relationships to characterise from these models are the frequency dependence, saturation dependence and pressure dependence of attenuation and the sensitivity of these to essential model parameters. To investigate briefly the behaviour of attenuation with these parameters I will use properties of a typical reservoir sandstone with a water/gas fluid mixture (Table 2.2).

Property	Symbol	Value
Bulk modulus (dry)	K_{dry}	7 GPa
Bulk modulus (grain)	K_0	35 GPa
Shear modulus (dry)	μ_{dry}	9 GPa
Density (grain)	ρ_0	2650 kg/m^3
Permeability	κ	2×10^{-12} m$^2 \approx$ 2D
Porosity	ϕ	0.08
Bulk modulus (water)	K_{w}	2.25 GPa
Bulk modulus (light gas)	K_{g}	0.1 GPa
Density (water)	ρ_{w}	999 kg/m^3
Density (light gas)	ρ_{g}	100 kg/m^3
Viscosity (water)	ν_{w}	5×10^{-4} Pa·s
Viscosity (light gas)	ν_{g}	3×10^{-5} Pa·s
Clay content	C	0.05

Table 2.2: Parameters used for comparison of rock models and empirical relationships, taken from Müller & Gurevich (2004).

Frequency

The general frequency dependence of attenuation and velocity is described by Mavko et al. (2003). Nearly all models have a high frequency limit (un-relaxed) in velocity and a low frequency limit (relaxed). There is therefore a range of frequencies for which the velocity changes between these limits; the frequency at which the velocity changes the most can be defined as the critical frequency (f_c) and hence is also associated with the peak attenuation. Depending on the mechanism this critical frequency occurs in different places. For the Biot model,

$$f_c \approx \frac{\phi\nu}{2\pi\rho_f\kappa}$$

and for the patchy saturation model of White (1975),

$$f_c = \frac{\kappa K_s}{\pi L^2 \nu},$$

where K_s is the Bulk modulus of the saturated rock and L is the lengthscale of the patch.

I compare the frequency dependence of Biot's global flow, White's spherical patchy saturation and Gurevich & Lopatnikov (1995) random patchy saturation models for a sandstone as described in Table 2.2. By calculating the dispersion curves and attenuation ($1/Q$) for a rock saturated with 80% water (with the co-saturant as light gas, Table 2.2) the magni-

tude and frequency dependence of attenuation can be shown. For the Biot model effective fluid properties (via the Ruess average) have been calculated and used as the pore fluid properties. We can see in Figure 2.5 that the magnitudes of attenuation associated with a typical sandstone are comparable for both patchy saturation models but very small for the Biot model, especially in the seismic band ($\approx 10^2$Hz). It can also be seen that the bandwidth over which attenuation and dispersion occurs is larger for the random patchy saturation model. This is a far more realistic model for measuring attenuation and comes closer to matching our need for a constant Q over our measurement bandwidth.

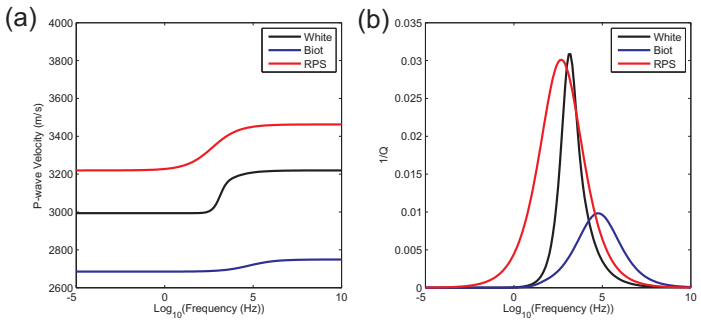

Figure 2.5: Frequency dependence of the P-wave velocity (a) and P-wave attenuation peak (b) for White's patchy saturation model, Biot fluid flow and the RPS model.

I now take a closer look at the RPS model, and the frequency dependence of the correlation length parameter (d). This is the parameter that controls the rate of the decay of the auto-correlation of the random media and effectively defines the centre length-scales at which the distribution of heterogeneity occurs.

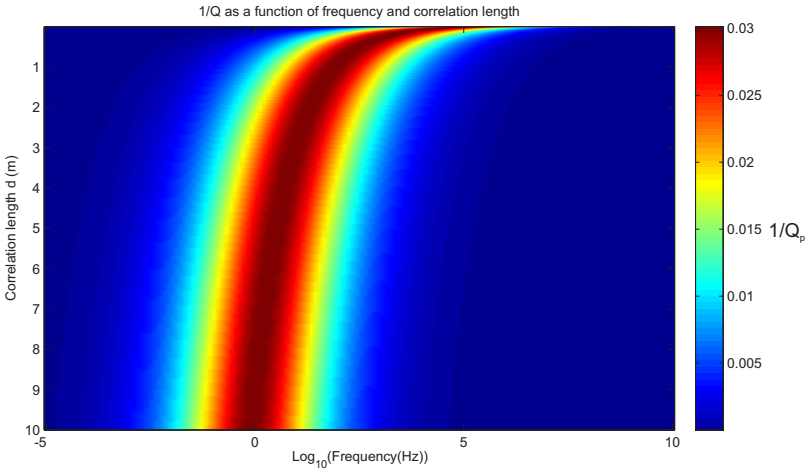

Figure 2.6: Q_p^{-1} dependence on frequency and correlation length of the RPS model.

Figure 2.6 shows the dependence of the characteristic frequency on the choice of the

correlation length (d). It shows that there is a large dependence at small correlation lengths but stabilises at larger correlation lengths. The frequency dependence of attenuation is not as severe for the random patchy saturation (indicated by the broader peak in Figure 2.5) due to the increased number of length scales of patches incorporated. In time-lapse studies, we would not expect frequency content to change significantly between vintages of data, however, if attenuation changes are to be modelled via a theoretical model a patch size or distribution must be carefully chosen.

Partial saturation

Partial saturation is one of the fundamental mechanisms for attenuation in the seismic bandwidth. We have already seen some of the characteristics of saturation dependence from laboratory measurements. Figure 2.3 showed that there is a sharp increase in attenuation with a few percent increase in gas saturation. The saturation at which the maximum attenuation occurs is also a function of frequency. Figure 2.7 shows attenuation and saturation as a function of the correlation length for the random patchy saturation model. It is clear that the choice of correlation length affects the magnitude of the maximum attenuation that is detected, however, the saturation at which the maximum attenuation occurs remains constant (80% water). This behavior is also seen in the empirical relationships of Koesoemadinata & McMechan (2001) (Figure 2.8). A similar attenuation curve can be extracted from Figure 2.7 at a correlation length of 1m and is plotted alongside the extrapolated empirical relationships in Figure 2.8.

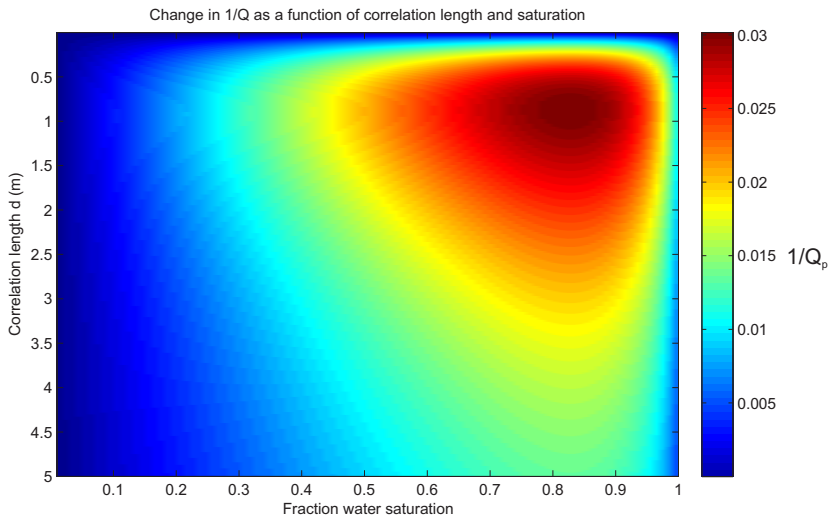

Figure 2.7: Q_{p}^{-1} dependence with saturation and correlation length (RPS model) calculated for 50Hz.

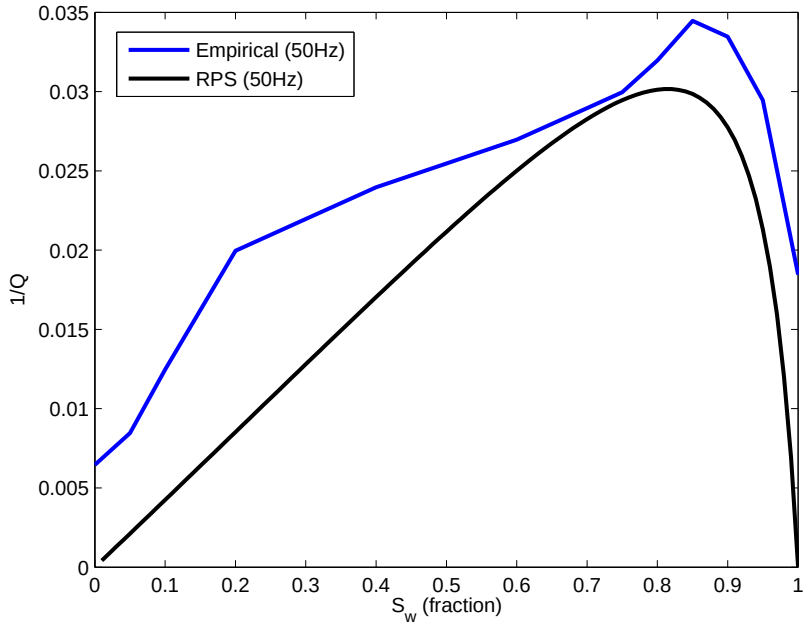

Figure 2.8: Q_{p}^{-1} plotted for both the extrapolated empirical relationships of Koesoemadinata & McMechan (2001) and the RPS model (d=1m). Note that the extrapolation may not be a valid assumption as attenuation mechanisms have been shown to be frequency dependent.

Pressure

The effects of pressure on attenuation can be quite complicated as there are various factors to consider. Differential pressure (P_{d}) and effective pressure (P_{e}) are the two pressures that can be used to describe the system of pressures occurring within a rock. The differential pressure is the difference between the confining pressure and the pore pressure and is described by equation 2.31 (Toksöz et al., 1979). The effective pressure is also used to describe the pressure system of rocks and includes a term to account for the capability of the pore space to deform. Effective pressure is described by equation 2.32 (Prasad & Manghnani, 1997) where n is the coefficient of internal deformation.

$$P_{\mathrm{d}} = P_{\mathrm{c}} - P_{\mathrm{p}} \tag{2.31}$$

$$P_{\mathrm{e}} = P_{\mathrm{c}} - nP_{\mathrm{p}} \tag{2.32}$$

Prasad & Manghnani (1997) presented laboratory data acquired in the bandwidth 0.8-1.3MHz that showed attenuation decreasing with increasing differential pressure (Figure 2.9). Their results also show that measurements of the effective stress and pressure dependent properties of the pore fluid are needed to explain these results fully.

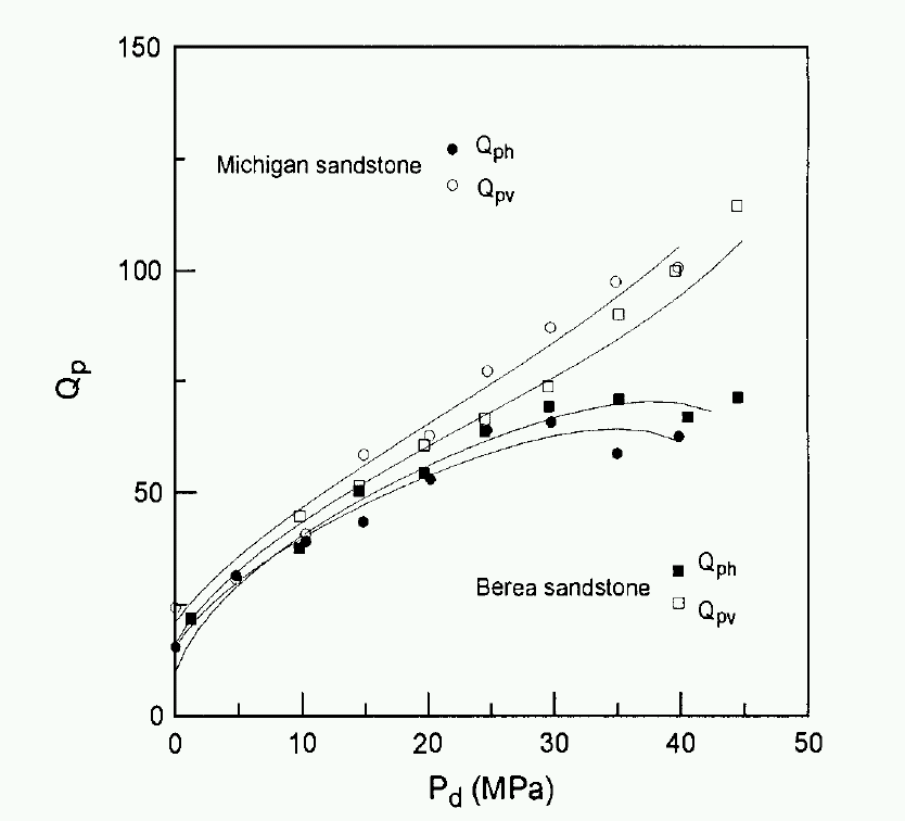

Figure 2.9: Q_p dependence with differential pressure (Prasad & Manghnani, 1997), v and h denote propogation in the vertical and horizontal direction respectively.

The work of Prasad & Manghnani (1997) was carried out on fully saturated rocks, therefore not taking into account attenuation mechanisms involving partial saturation. Using the RPS model we can plot attenuation as a function of pore pressure and correlation length (Figure 2.10). Fluid properties for oil, water and gas are calculated as a function of pressure via the empirical relationships outlined by Batzle & Wang (1992). It is clear here that attenuation decreases with pore pressure at higher pressures. This is due to the relative decrease in contrasts between the water and gas properties. It may be important to consider the effect of pressure with other mechanisms such as the closure of small cracks, but as mentioned above in the case of gas injection, one may expect fluid mechanisms to dominate over others.

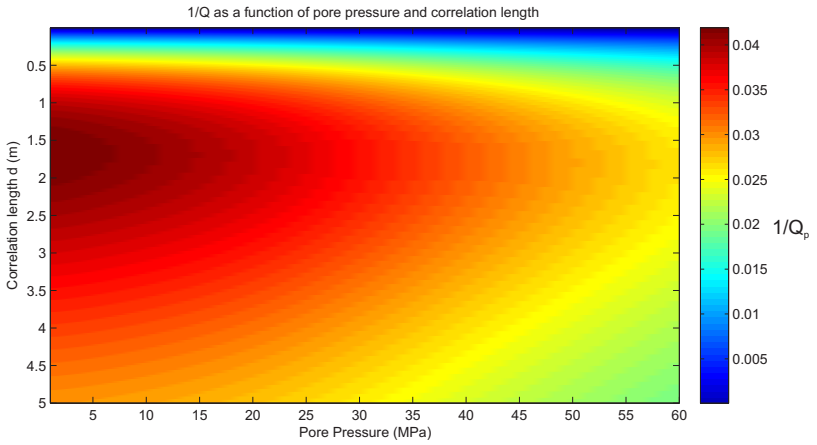

Figure 2.10: Q_p^{-1} dependence with pore pressure and correlation length (RPS model) at 50Hz.

When modelling reservoir properties, it may also be necessary to consider the effect of changing pressure on the properties of the rock matrix itself. This is normally achieved through the analysis of specific core samples in the laboratory. Properties of the rock matrix that are liable to change under effective stress are the porosity, permeability and elastic moduli (Mavko et al., 2003). These can be estimated via effective stress laws of Berryman (1992).

Porosity

The effect of porosity on attenuation has been shown through various laboratory experiments to be roughly linear (Johnston et al., 1979; Klimentos & McCann, 1990; Murphy, 1982). Koesoemadinata & McMechan (2001) and Klimentos & McCann (1990) both assumed a linear relationship when deriving empirical relationships for attenuation. We can also look at the behaviour as a function of porosity in the RPS model (Figure 2.11). At

20MP and a gas saturation of 20%, it can be seen that attenuation is non-linear as a function of porosity and has a peak at around 5% porosity.

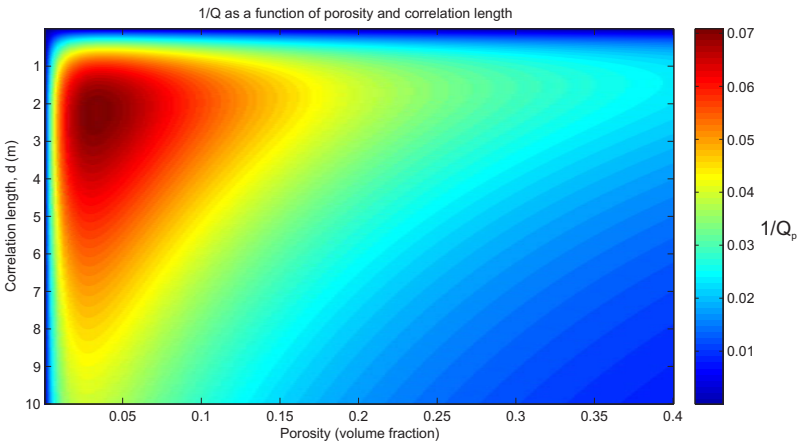

Figure 2.11: Q_p^{-1} dependence with porosity and correlation length (RPS model) at 50Hz.

It is only in special 4D cases that we would expect large changes in porosity of a rock over time, so the detailed analysis of this behaviour is not important at this stage.

2.2.6 Summary of attenuation relationships

No single mechanism or relationship can describe the behaviour of attenuation at all frequencies, for all lithology and for all saturations. It may even be the case that different mechanisms can lead to opposing effects as function of permeability, pressure etc. In order to interpret attenuation correctly it will be important to assume or determine correctly the underlying mechanisms responsible for the energy loss. The magnitudes of attenuation predicted in the seismic bandwidth are largest when the pore space is partially saturated with small amounts of gas (20%). The sensitivity of patchy saturation mechanisms to changes in pressure and saturation, combined with laboratory observations of patchy fluid distributions produced through gas injection suggests that attenuation may provide useful information from time-lapse data where gas injection is underway.

2.3 Q measurements from surface seismic and VSP data

There is a selection of literature with examples of attenuation being measured from surface seismic, cross-well seismic and VSP data. Methodologies for quantitatively estimating Q from surface seismic data have been developed using spectral ratios (Dasgupta & Clark, 1998), centroid frequencies (Quan & Harris, 1997; Rossi et al., 2007) and instantaneous

frequencies (Matheney & Nowack, 1995). Various methodologies for estimating attenuation from VSP data were tested by Tonn (1991) and more recently by Rickett (2006, 2007). The methodologies tested by Tonn (1991) include

- Amplitude decay method
- Analytical signal
- Wavelet modelling
- Phase Modelling
- Peak Frequency
- Rise-time method
- Pulse amplitude method
- Frequency matching technique
- Spectral modelling
- Spectral ratios

He concluded that no single method was superior to the others in all scenarios, but depending on the type of noise present some methods are more stable than others. The five best methods were methods based on the analytical signal, spectral ratios, spectral modelling, wavelet modelling and frequency matching. It is important to note that 4D noise behaves differently from single vintage noise and therefore the best method for estimating attenuation for a single vintage may not necessarily be the best at measuring changes in attenuation.

Single vintage measurements provide us with valuable information about the magnitude of attenuation that should be expected. This will be useful when comparing the attenuation predicted by empirical relationships and rock physics models.

Several methodologies for the estimation of attenuation from surface seismic data have been developed. Dasgupta & Clark (1998) and Reine et al. (2011a) are two methods that calculate attenuation from prestack surface seismic data using spectral ratios. Quan & Harris (1997) produced a methodology for performing attenuation tomography, looking specifically at the centroid (average) frequency. Matheney & Nowack (1995) outlined

an inversion strategy for calculating attenuation via a non-linear inversion that utilises instantaneous frequencies.

Methodologies used in this thesis are explained in more detail in the next chapter but we can gain some useful information from previous studies, in particular, the range of attenuation ($1/Q$) values that have been measured previously.

2.3.1 Comparison of absolute Q values measured from seismic data

Attenuation has been measured from surface seismic data by various authors, each producing slightly different ranges of Q, highlighting the diversity of single vintage measurements of effective attenuation. Dasgupta & Clark (1998) found $1/Q$ values that ranged from around 0.005-0.0278 ($36< Q <182$). Matheney & Nowack (1995) found $1/Q$ ranged between 0.00038-0.013 ($77< Q <2631$). Rossi et al. (2007) calculated $1/Q$ values ranging from 0.04-∞ ($0< Q <250$) and Reine et al. (2011b) calculated $1/Q$ values that ranged from -0.05 to 0.05 ($|Q| >20$). It is clear that there are some similarities between the attenuation values calculated from each of the methods at different locations. However, it is also clear that the absolute magnitude of attenuation varies between different methodologies and field locations. Sams et al. (1997) calculated attenuation measurements at a variety of frequencies, using VSP, cross-hole and laboratory (ultrasonic) measurements to highlight the frequency dependent nature of attenuation. These results were then fitted to a squirt flow model (Figure 2.12)

2.3.2 Previous time-lapse studies

Few previous time-lapse attenuation studies have been reported. One example is from Hedlin et al. (2001), where attenuation is measured from a VSP using spectral ratios and centroid frequency. The aim was to monitor the effect of a steam injection into a heavy oil reservoir (12° API). Changes in attenuation were found to be on the order of +0.003. Williams (2001) and Clark et al. (2001) measured changes in attenuation in a reservoir undergoing enhanced oil recovery from steam injection and found that magnitudes of $1/Q$ changed by up to ± 0.1, and were qualitatively interpreted as a combination of both saturation and pressure effects. Differences between the magnitude of changes in attenuation estimated in these experiments could be due to the frequency dependence of attenuation (comparing a surface seismic experiment with a VSP experiment) or different mechanisms controlling the attenuation change.

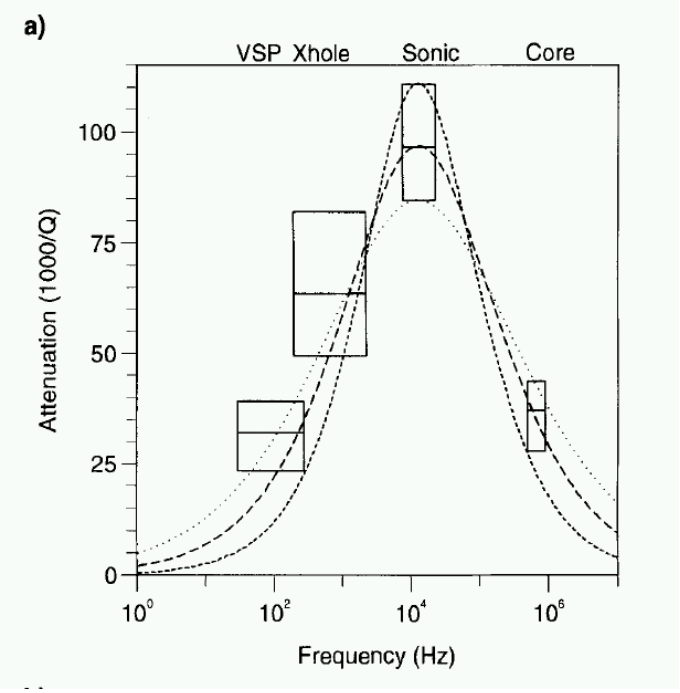

Figure 2.12: Measurements of attenuation made by Sams et al. (1997) using VSP, Cross-hole, sonic and laboratory data along with fitted curves (dotted lines) from a squirt flow model.

2.4 4D Seismic surveying

4D seismic analysis is heavily used in the industry today as a tool to monitor hydrocarbon recovery. It is also used as a tool to provide reservoir properties as inputs in reservoir modelling (Calvert, 2005). At present there is no technique that is commonly used to estimate time-lapse attenuation from repeated surveys. It is clear to see that attenuation could be a helpful addition to other techniques in determining changes in saturation, compaction and pressure. Attributes that are heavily used in 4D seismic monitoring include changes in:

- Travel time
- Amplitude (and AVO)
- Seismic impedance

It will therefore be important to compare any attenuation changes calculated with more standard attributes, especially when comparing noise thresholds and making conclusions about the usefulness of the attenuation measurements. To quantitatively interpret attenuation changes in terms of the true reservoir changes (saturation, pressure, porosity)

it will be necessary to include some of the more commonly measured attributes in the interpretation.

2.4.1 Repeatability

There are many problems present in 4D monitoring that can render attempts to gain useful changes in reservoir properties challenging. A list of such problems is given by Calvert (2005).

- Noise conditions
- Streamer positioning
- Temporal changes (ocean temperature, frozen ground)
- Source repeatability
- Near surface heterogeneity
- Non repeatable multiples

Any combination of these problems can cause differences in both amplitude and time. Differences in time and amplitude can be simple to quantify and this is achieved through analysis of various repeatability attributes. The repeatability of time-lapse seismic surveys is normally measured via 2 parameters; the NRMS (normalised root mean square) and Predictability (PRED) (Kragh & Christie, 2002). The NRMS is defined as

$$NRMS = \frac{200 \times RMS(a_\mathrm{t} - b_\mathrm{t})}{RMS(a_\mathrm{t}) + RMS(b_\mathrm{t})} \tag{2.33}$$

where,

$$RMS(x_\mathrm{t}) = \sqrt{\frac{\sum_{t_1}^{t_2}(x_\mathrm{t})^2}{N}}, \tag{2.34}$$

a_t and b_t are the traces from each vintage of data, and N is the number of samples in the time window from t_1 to t_2. NRMS values range from 0 to 200 with random noise producing a value of 141% and completely opposite traces producing a value of 200%. The predictability attribute can be defined by

$$PRED = \frac{\sum_{t_1}^{t_2} \Phi_{\mathrm{ab}}(\tau)\Phi_{\mathrm{ab}}(\tau)}{\sum_{t_1}^{t_2} \Phi(\tau)_{\mathrm{aa}}\Phi(\tau)_{\mathrm{bb}}} \tag{2.35}$$

where Φ_{ab} is the cross-correlation between traces a and b. Values range between 0 and 100% with 100% being the best repeatability.

2.4.2 Separating saturation and pressure changes

One of the key priorities for a time-lapse survey is to monitor the life of a field and ideally, quantitatively monitor changes in pressure and saturation within a reservoir. The literature has many examples of monitoring saturation and pressure changes independently (Landrøet al., 1999; Watts et al., 1996), however the combined inversion of saturation and pressure changes appears to be a more difficult problem to solve.

Landrø (2001) provides a methodology for discriminating between pressure and fluid saturation using changes in the AVO (amplitude versus offset) attributes between vintages of data. Empirical relationships were derived from laboratory experiments that related the change in P-wave velocity, S-wave velocity and density as functions of saturation and pressure for an oil-water mix. By combining these specific relationships for the Gullfaks field with the 2-term Shuey equation for AVO (Shuey, 1985), specific expressions for the change in saturation (ΔS,[volume fraction]) and pressure (ΔP, [MPa]) at the Gullfaks field were given:

$$\Delta S \approx 8(\Delta R_0 + \Delta G) \tag{2.36}$$

$$\Delta P \approx 23\Delta R_0 - 35\Delta G \tag{2.37}$$

where ΔR_0 is the change in the AVO intercept and ΔG is the change in the AVO gradient. This methodology provides a framework for the separation of pressure and saturation changes, however, a full laboratory rock physics study must be carried out to determine the behaviour of V_{p}, V_{s} and ρ with saturation and pressure.

MacBeth et al. (2006) also outlined a method for estimating pressure and saturation changes from time-lapse seismic data via inversion of several seismic attributes that respond differently to reservoir perturbations. Their method includes a careful calibration of the 4D seismic signature with production and pressure information.

It is clear in both of these methodologies that the more observations of changes in seismic attributes the better. Throughout this chapter I have highlighted the sensitivity of seismic attenuation to changes in pressure and saturation. Of particular interest is the high sensitivity of attenuation to very small increases in gas content from a fully oil or water saturated state.

2.5 Summary

- $1/Q$ can be defined in two ways, either through amplitude losses or complex moduli.
- Measured attenuation is composed of both an intrinsic and apparent component.
- Apparent attenuation can potentially be negative and larger in magnitude than intrinsic attenuation.
- Intrinsic attenuation is caused by a variety of mechanisms including grain boundary friction, global flow, squirt flow and fluid diffusion.
- Injection (gas increase) has been shown to produce heterogeneous patchy fluid distribution.
- Patchy saturation models predict the largest attenuation (and attenuation changes) observed in the seismic bandwidth.
- Methodologies are available that allow for the separation of pressure and saturation effects and the sensitivity of attenuation to small changes in saturation may provide additional information for this separation.

Chapter 3

Methodologies for quantitatively estimating time-lapse attenuation

In this chapter I will explain several existing methodologies for estimating attenuation quantitatively from single vintages of prestack surface seismic data and develop them to measure change in attenuation between vintages of data. I will also outline how these methodologies can be adapted to the geometry of vertical seismic profiles (VSP). All of the methodologies rely on a seismic attribute that is affected primarily by attenuation and modified during propagation (Tonn, 1991);

- The log spectral ratio slopes
- The instantaneous frequency
- The centroid frequency

Each of these properties of the seismic wave is affected in different ways by absorption. Log spectral ratio slopes can be analytically related to Q, and when Q is constant with frequency, the slope is proportional to $t^* = t/Q$. I introduce two related methodologies that utilise spectral ratio slopes. The QVO (Q vs. offset) methodology of Dasgupta & Clark (1998) and the PSQI methodology of Reine et al. (2011a) are explained, along with an extension that enables measurement of attenuation directly between vintages of data.

The centroid frequency can also be analytically related to Q, but only for frequency spectra that fit a few specific functions. Quan & Harris (1997) derived analytic relationships between Q and centroid frequency, for Gaussian, rectangular and triangular spectra. These have been primarily used as the input into Q tomography studies (Rossi et al., 2007). I

extend this methodology for measurements of attenuation from multiple prestack traces, following a similar work flow as the QVO methodology.

Unlike spectral ratio slopes and the centroid frequency, instantaneous frequency cannot be analytically related to Q, but its effect can be forward modelled or inverted for in a non-linear fashion. Matheney & Nowack (1995) describe a non-linear inversion scheme for estimating attenuation through the measurement of the instantaneous frequency.

I will begin this chapter by defining the difference between my use of the terms "Absolute" and "Direct" in relation to the measurement of a change in attenuation. I will then introduce a simple synthetic data-set that will be used to illustrate some of the steps within the methodologies, followed by descriptions of each of the methodologies for prestack seismic data, discussing the parameter choices and assumptions associated with each method. Finally, I will look at how the methodologies are adapted to the geometry of vertical seismic profiles.

3.1 Absolute vs. Direct

All the methodologies below can be performed in two ways; either by treating each vintage of data independently; or by directly calculating attenuation between vintages of data (Figure 3.1). I refer to these as the "Absolute" and "Direct" approaches, respectively. In the Absolute approaches, methodologies are described as used by their original authors. The Direct approaches will be presented as extensions to the original methodologies, stating any further assumptions or potential benefits from analysing the data this way. The sensitivity of some of these assumptions are addressed in the next chapter.

3.2 Synthetic data

Throughout this chapter I will show examples of some of the methodologies using a simple synthetic data-set. Synthetic data is created using a program called **SKB2** (Bouchon, 1981), a reflectivity code utilising the generalised reflection-transmission method of Kennett & Kerry (1979). Calculations are performed in the frequency-wavenumber domain and the earth response is calculated through integration of discrete wavenumbers of the reflected plane wave (Bouchon, 1981). An inverse Fourier transform is then used to convert data into the $t - x$ domain. In this synthetic example and throughout this thesis surface multiples are not included in the analysis, however, all interbred multiples are calculated.

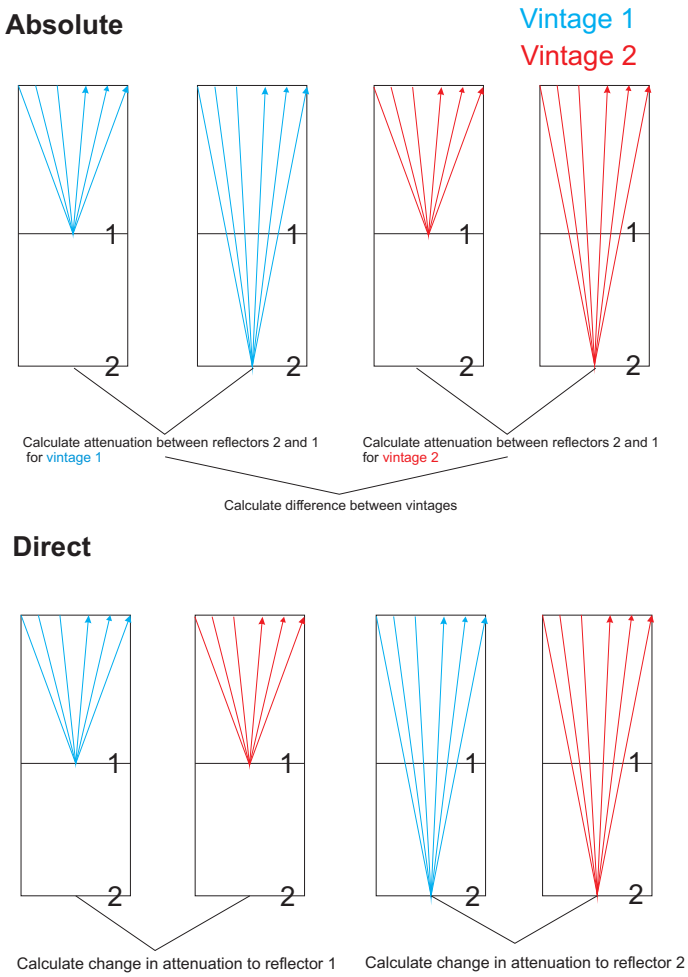

Figure 3.1: Schematic of the differences between the "Absolute" and "Direct" approaches for making measurements of changes in attenuation between vintages of seismic data.

Two common mid-point gathers (CMP's)(Figure 3.2) were created for a 3 layer model using a 50Hz zero phase ricker wavelet. The only difference between the models is the attenuation of the middle layer. One synthetic CMP has $Q = 80$ and the other has a $Q = 30$, mimicking the effect that an increase in gas saturation would have on Q. The difference between the gathers is also plotted in Figure 3.2, showing large differences between the synthetic data-sets, even for the top reflector. These differences are due to both the effect of the change in attenuation (amplitude and phase), timing (due to dispersion) and reflectivity changes (due to dispersion).

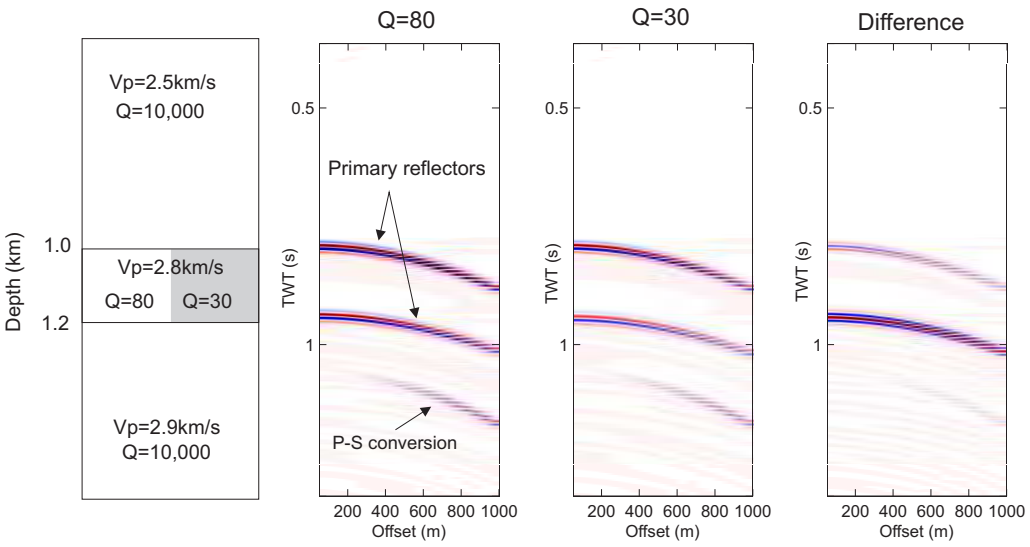

Figure 3.2: Figure showing model (left), synthetic data for Q=80 (centre left), Q=30 (centre right) and the subtraction of Q=80 data from Q=30 data (right). Synthetic data shown is the pressure component, created using a 50Hz Ricker wavelet plotted with normal SEG polarity.

Some of the methodologies require the reflected arrivals to be windowed and extracted from the data. Figure 3.3 shows the base reflector, extracted at the same time for each offset for both vintages of data, highlighting some of the timing differences caused by dispersion.

3.3 Q vs. offset - QVO

Spectral ratios have been used by many previous authors to estimate attenuation from seismic data (Raikes & White, 1984; Tonn, 1991). The QVO methodology, which utilises spectral ratios was first outlined by Dasgupta & Clark (1998) and calculates attenuation between two or more reflectors from prestack surface seismic data. Here I will outline how this is applied to the Absolute and Direct approach, highlighting any assumptions made and discuss the various parameter choices that exist within the methodology.

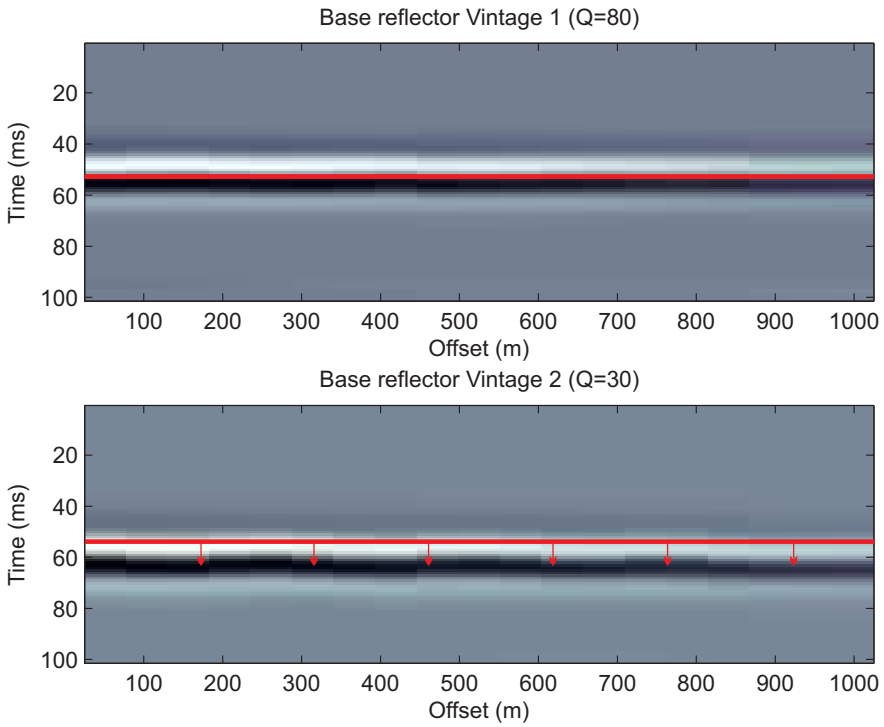

Figure 3.3: Figure showing windowed synthetic data for Q=80 (top) Q=30 (bottom) for the base reflector in the model. The red line acts as a reference point indicating the change in travel time caused by he difference in dispersion. Windows are centred on the calculated travel-time for each offset. Traces are plotted in SEG normal polarity.

3.3.1 Absolute QVO

The spectrum of a chosen reflector and offset (S_1) is divided by a reference spectrum (S_0)(preferably the source spectra) to give the log spectral ratio as a function of frequency (f)

$$S_1 = S_0 e^{\frac{-tf\pi}{Q}} RG \tag{3.1}$$

$$\ln(\frac{S_1}{S_0}) = \frac{-tf\pi}{Q} + \ln(RG) \tag{3.2}$$

where t is the two-way travel-time of the reflected arrival. R and G are terms containing information about the frequency independent reflectivity and geometrical spreading respectively. The log spectral ratio is therefore a straight line when plotted against frequency, with a gradient of $-\pi t/Q$ and an intercept of $\ln(RG)$. In the QVO methodology (Figure 3.4), a spectral ratio slope ($p = -t\pi/Q$) is calculated for each offset for a CMP of data, for each reflector of interest. Assuming small spread conditions (depth larger than offset), the travel time can be assumed to be proportional to the offset squared (Dasgupta & Clark, 1998). Spectral ratio slopes are then plotted against offset squared and the zero offset intercept predicted. Carter (2003) pointed out that if the prestack TWT is known then this second regression may be performed with time, making the small spread assumption unnecessary.

The interval $1/Q$ between two horizons (n and n $-$ 1) can be found using

$$Q_{\mathrm{n,n-1}} = \frac{t_{\mathrm{n}} - t_{\mathrm{n-1}}}{\frac{t_{\mathrm{n}}}{Q_{\mathrm{n}}} - \frac{t_{\mathrm{n-1}}}{Q_{\mathrm{n-1}}}}, \tag{3.3}$$

where t_{n} and $t_{\mathrm{n-1}}$ are the travel times to each reflector, and Q_{n} and $Q_{\mathrm{n-1}}$ are the effective attenuation measured for each reflector.

The work flow for the QVO methodology is summarised in the following steps;

1. Isolate two reflectors in a CMP.
2. Calculate spectral ratios between the reflected spectra and a reference spectrum (Figure 3.4).
3. Fit a spectral ratio slope for each reflector and offset (Figure 3.4).

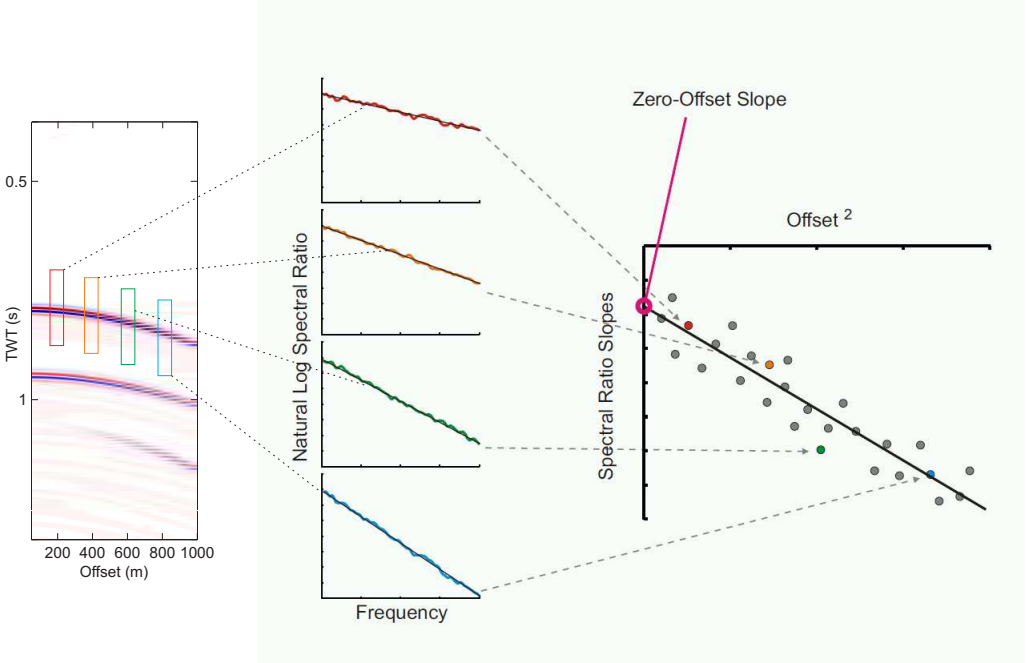

Figure 3.4: Schematic for calculating t/Q to a reflector of interest via the QVO methodology. Some figures taken and adapted from Reine (2009).

4. Find the intercept to the slope vs. offset squared (Figure 3.4).

5. Calculate the effective attenuation to each reflector.

6. Calculate interval attenuation between reflectors.

3.3.2 Direct

It is possible with several assumptions to infer a change in attenuation by directly comparing spectral ratio slopes of a reflector from one vintage to the next. If two amplitude spectra S and S' represent the reflections for two vintages of data from the same reflector, acquired using the same source and receiver locations then,

$$S(\omega) = S_0(\omega)e^{-\omega t/2Q}RG \tag{3.4}$$

$$S'(\omega) = S'_0(\omega)e^{-\omega t'/2Q'}R'G' \tag{3.5}$$

where the second vintage of data is denoted by $'$, source and reflector spectra are S_0 and S respectively and t is the two-way travel time. The direct log spectral ratio can now be found by dividing equation 3.4 by equation 3.5

$$\ln\left(\frac{S'(\omega)}{S(\omega)}\right) = \ln\left(\frac{S'_0(\omega)}{S_0(\omega)}\right) - \left(\pi f t'/Q' - \pi f t/Q\right) + \ln\left(\frac{R'}{R}\right) + \ln\left(\frac{G'}{G}\right). \tag{3.6}$$

It is most likely that if time-lapse changes in attenuation are present, small changes in velocity (and hence travel-time) and reflection coefficients may also be present. These changes would to some extent be frequency dependent. However if we can assume that a repeatable source is used (or data are globally matched to have the same spectra) to acquire both vintages of data, geometrical spreading is the same between vintages and the changes in reflection coefficient are frequency independent then we reduce equation 3.6 to

$$\ln\left(\frac{S'(f)}{S(f)}\right) = -\pi f\left(t'/Q' - t/Q\right) + \ln\left(\frac{R'}{R}\right). \tag{3.7}$$

This is now a straight line with an intercept relating to the change in reflectivity and a gradient (p) proportional to the change in t^* between vintages of data.

$$p = -\pi\left(t'/Q' - t/Q\right) = -\pi(\Delta t^*) \tag{3.8}$$

Using the synthetic data described previously, the direct log spectral ratios (Equation 3.7) are calculated for all offsets for the base reflector and shown in Figure 3.5.

The spectral ratio slopes (calculated between 10-180Hz) can then be plotted against offset squared (Figure 3.6). The second QVO regression against offset squared can then be performed and the zero offset change in t^* (Δt^*) found. If we now assume that there is no change in travel time between vintages of data ($t' = t$) we can re-write Equation 3.8 as

$$p = \pi t\left(1/Q_{\mathrm{v}2} - 1/Q_{\mathrm{v}1}\right) = \pi t(\Delta Q^{-1}). \tag{3.9}$$

The intercept from Figure 3.6 ($p = 0.010312 \pm 2.8 \times 10^{-14}$ s) can be divided by the zero-offset TWT of the reservoir interval to give a change in attenuation of $+0.023 \pm 6.25 \times 10^{-14}$ compared with the input change in attenuation of $1/30 - 1/80 = 0.0208$. Errors on the regressions themselves are very small therefore the differences are likely caused by coherent effects such as dispersion-related reflectivity and timing effects (these effects are investigated in the next chapter).

It is also plausible to calculate directly the change in attenuation for two reflectors of interest, and use Equation 3.3 to calculate the change in attenuation within a desired

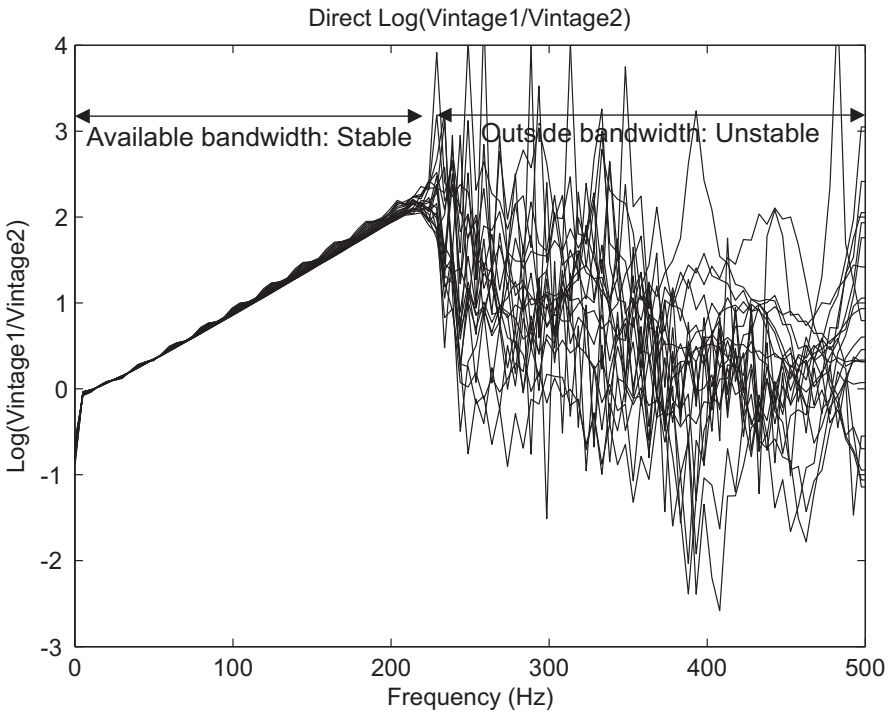

Figure 3.5: Direct spectral ratio slopes between vintages of seismic data, $\ln(S/S')$.

interval.

3.3.3 Parameter options

For the QVO methodology there are various parameters that we must define and options that we must choose.

Bandwidth It can be seen from Figure 3.5 that there is a stable spectral ratio slope in only a limited bandwidth. Spectral analysis should be carried out to decide on an optimal regression bandwidth.

Frequency estimation The size of the time window used in the FFT (Fast Fourier Transform) is an important parameter to choose correctly. A trade off exists between gaining better frequency resolution, and including unwanted arrivals by the lengthening of the FFT window. A taper must also be carefully chosen and Carter (2003) recommended using a taper with low side lobes such as a Hanning taper, as other tapers may limit the usable bandwidth. Reine (2009) showed that spectral estimates can be improved through the use of variable window transforms. This will be discussed in the PSQI methodology

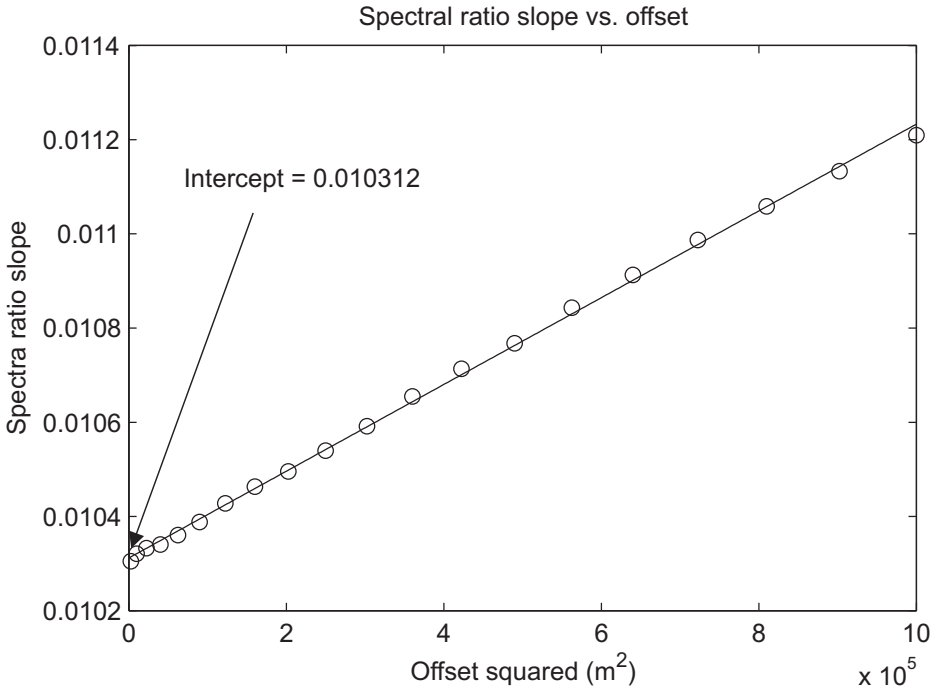

Figure 3.6: Direct spectral ratio slopes plotted against offset squared. The equation of the line of best fit is also shown. The intercept of this equation is equal to the zero-offset spectral ratio slope and is used to calculate the change in attenuation.

(Section 3.4).

Offset range It is important in the regression against offset squared to abide by the small spread approximation. Therefore the offset range should be limited, especially for shallow reflectors where some source/receiver directivity is also an issue (Hustedt & Clark, 1999).

Source spectrum It is generally recommended that source spectra are estimated from the data, especially if weighting is used in any of the regressions (if no weighting is used Carter (2003) showed that interval attenuation estimates are independent of source spectra). Ideally, the source spectrum should be different for each offset and reflector as source and receiver directivity is a frequency dependent phenomenon. Reine et al. (2011a) recommends using the τ-p domain to isolate pairs of arrivals of the same slowness, avoiding the need to estimate a source spectrum and allowing the direct calculation of attenuation between reflectors. This will be explained in more detail in the PSQI approach (Section 3.4).

Weighting It is possible to introduce weighting schemes into both of the regressions based on the coherency of the amplitude spectra at different frequencies and offsets (Gubbins, 2004; Reine, 2009).

3.4 PSQI - Prestack Q inversion

Testing and analysis of the QVO method continued through work by Carter (2003) and improvements to the methodology made by Reine et al. (2011a,b). Reine et al. (2011a) found that Q estimates could be significantly improved through better time resolution of the spectral content via the use of variable window transforms, such as an s-transform (Stockwell et al., 1996) rather than a fixed window FFT. He also highlighted two other improvements; by performing a simultaneous inversion in time and frequency rather than the two-stage regression in the QVO method; and that directivity and anisotropy can be overcome if events are isolated in the $\tau - p$ domain. Here I describe the PSQI method of Reine et al. (2011a), followed by the adapted direct version of the methodology.

3.4.1 Absolute PSQI

The PSQI methodology developed by Reine (2009) calculates the attenuation between two reflectors in a CMP gather. By isolating these events in the $\tau - p$ domain, pairs of events with the same slowness can be used to calculate the spectral ratios, avoiding problems that are caused by source directivity and anisotropy. However, this was a very recent development and is not used in this thesis. I will still outline this method, however, the methodology implemented here will use data in the $t - x$ domain. A schematic of the PSQI methodology is shown in Figure 3.7 and will be referred to throughout this section.

$\tau - p$ domain

A CMP of data is transformed into the $\tau - p$ domain via a 3D $\tau - p$ transform (Figure 3.7 (b)). Once in the τ-p domain, two reflectors are isolated at a constant horizontal slowness and used in the spectral ratio calculation where S_1 and S_2 are the amplitudes at a specific horizontal slowness (p) from reflectors 1 and 2 respectively.

$$\ln(\frac{S_2}{S_1}) = -\frac{\pi}{Q}\Delta t f + \ln(RG) \tag{3.10}$$

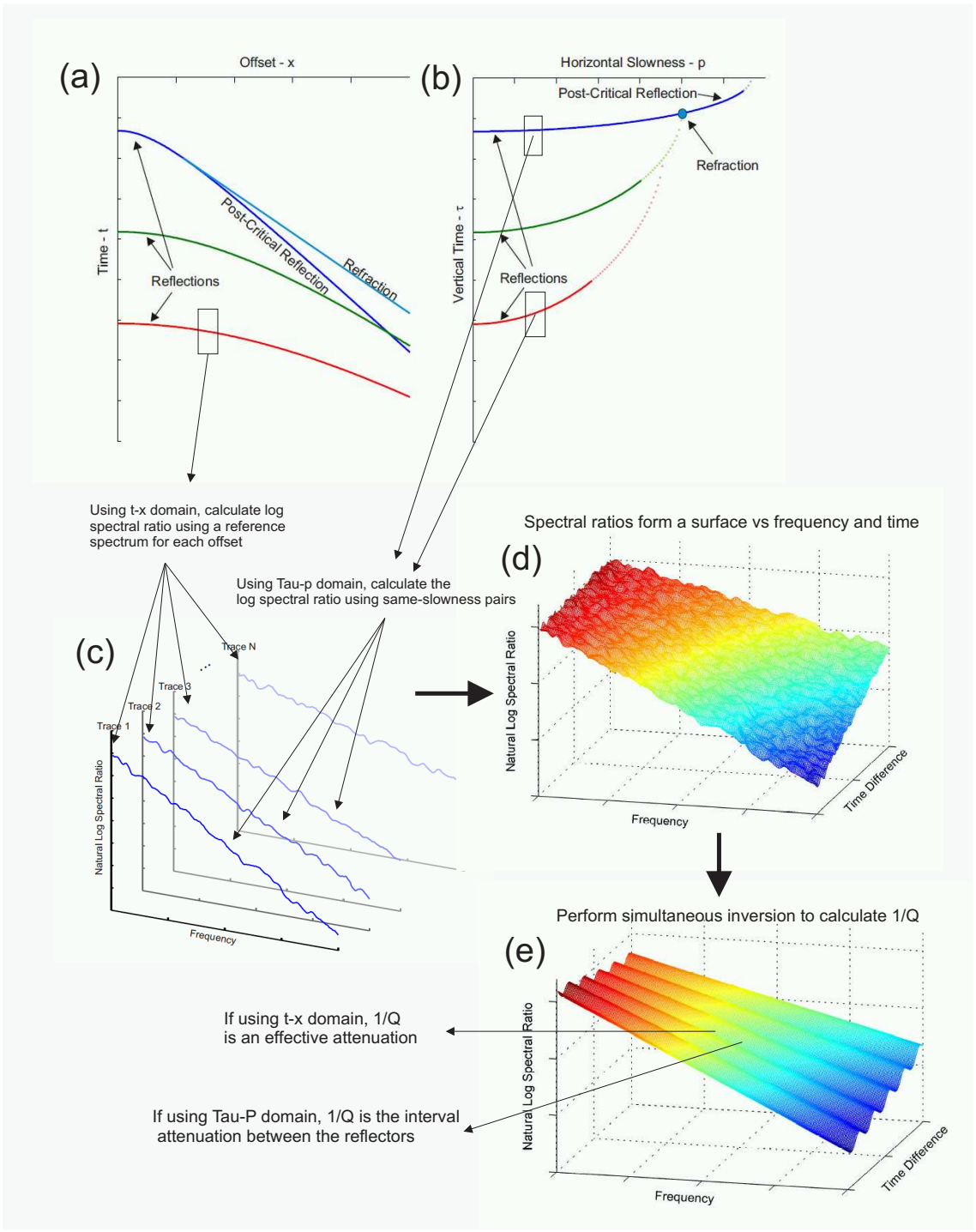

Figure 3.7: Schematic of the PSQI methodology. Data can either be analysed through the $t-x$ (a) or $tau-p$ domain (b). Spectral ratios (c) are calculated using a reference spectrum when the $t-x$ domain is used or by same slowness pairs of reflections in the $\tau-p$ domain. A spectral ratio surface (d) can then be plotted against frequency and time difference. If the $\tau-p$ domain is used, time-differences refer to the difference in travel times for each reflection. When the $t-x$ domain is used the full TWT to that reflector is used for the calculation. A surface can then be fitted to the data, where the slope is proportional to attenuation (1/Q). For $\tau-p$, this 1/Q is the attenuation in the interval between the two reflectors of interest and for $t-x$ this is an effective 1/Q where the interval attenuation can be calculated using Equation 3.3. Figures taken and adapted from Reine (2009).

Δt is the travel time difference between S_2 and S_1, and must be calculated separately using the vertical travel time (τ) and horizontal slowness (p).

The spectral ratios d can then be calculated for various Δt (n) and frequencies (m) (Figure 3.7 (c), (d)).

$$\ln(\frac{S_2(\Delta t_\mathrm{n}, f_\mathrm{m})}{S_1(\Delta t_\mathrm{n}, f_\mathrm{m})} = d(\Delta t_\mathrm{n}, f_\mathrm{m}) \tag{3.11}$$

A system of equations can then be set up to solve for a single value of attenuation.

$$d(\Delta t_\mathrm{n}, f_\mathrm{m}) = \Delta t_\mathrm{n} f_\mathrm{m} A + B_\mathrm{n} \tag{3.12}$$

where A represents the single slope that fits all of the data (Figure 3.7 (e)), and is proportional to the attenuation

$$A = -\frac{\pi}{Q} \tag{3.13}$$

and B_n is the intercept at $f = 0$ of the spectral ratio slope for each horizontal slowness. These equation can be set up as a linear regression of the form $\mathbf{d} = \mathbf{Gm}$ where $\mathbf{d}$ is a 1 by M×N vector containing the spectral ratios, $\mathbf{m}$ is a 1x(N+1) vector containing the A and the B_n intercepts, and $\mathbf{G}$ is the condition matrix (M and N are the number of frequencies and times used in the regression). This system of equations can be solved in a least squares fashion via

$$\mathbf{m} = (\mathbf{G}'\mathbf{W}\mathbf{G})^{-1}\mathbf{G}'\mathbf{W}\mathbf{d} \tag{3.14}$$

where $\mathbf{W}$ is an optional weighting matrix and $'$ denotes the transpose of a matrix.

T-X domain

The simultaneous regression can also be performed in the $t-x$ domain. However, two parts of the methodology defined above must change. Firstly, constant offset traces cannot be treated the same as constant slowness traces, therefore, a spectral ratio between common offsets in a gather should not be used. Instead, a single source reference wavelet should be used to calculate the spectral ratio for each reflector (Figure 3.7 (c)). The same regression

(Equations 3.12 and 3.14) can then be used (with the full travel time used as Δt) to calculate an effective attenuation to each reflector. Interval attenuation estimates can then be found using Equation 3.3.

3.4.2 Direct PSQI

The PSQI methodology can easily be adapted to make Direct time-lapse measurements. Consider two reflections from the same reflector from different vintages of data, S and S'. Assuming (as above) that data were acquired using the same source, and that there are no changes in travel-time and geometrical spreading, we may write.

$$\ln\left(\frac{S'(t,f)}{S(t,f)}\right) = -\pi f t\left(1/Q' - 1/Q\right) + \ln\left(\frac{R'}{R}\right) \tag{3.15}$$

For a single CMP of data we can calculate a spectral ratio and travel time at all offsets, for the same reflector in both vintages. This system of equations can be written as

$$\begin{pmatrix} d_{1,1} \\ d_{2,1} \\ \vdots \\ d_{\mathrm{N},1} \\ d_{1,2} \\ \vdots \\ d_{\mathrm{N},2} \\ \vdots \\ d_{1,\mathrm{M}} \\ \vdots \\ d_{\mathrm{N},\mathrm{M}} \end{pmatrix} = \begin{pmatrix} t_1 f_1 & 1 & 0 & \cdots & 0 \\ t_1 f_2 & 1 & 0 & \cdots & 0 \\ \vdots & \vdots & \vdots & \ddots & \vdots \\ t_1 f_{\mathrm{N}} & 1 & 0 & \cdots & 0 \\ t_2 f_1 & 0 & 1 & \cdots & 0 \\ \vdots & \vdots & \vdots & \ddots & \vdots \\ t_2 f_{\mathrm{N}} & 0 & 1 & \cdots & 0 \\ \vdots & \vdots & \vdots & \ddots & \vdots \\ t_{\mathrm{M}} f_1 & 0 & 0 & \cdots & 1 \\ \vdots & \vdots & \vdots & \ddots & \vdots \\ t_{\mathrm{M}} f_{\mathrm{N}} & 0 & 0 & \cdots & 1 \end{pmatrix} \begin{pmatrix} A \\ B_1 \\ B_2 \\ \vdots \\ B_{\mathrm{M}} \end{pmatrix} \tag{3.16}$$

$$\mathbf{d} = \mathbf{G}\mathbf{m} \tag{3.17}$$

and solved using a least square inversion (Equation 3.14).

In the Direct PSQI approach, there is no need to carry out a τ-p transform on the data, as spectral ratios are being taken using wavelets that have travelled along the same (or very similar) ray path. Figure 3.8 displays the direct spectral ratio surfaces for the synthetic data ($\mathbf{d}$, Equation 3.17) along with the fitted surfaces ($\mathbf{Gm}$, Equation 3.17).

In Figure 3.8 the time differences used in the inversion was the full TWT of the reflected arrivals yielding the change in 1/Q down to the reflector of interest. It is then possible to calculate interval changes (via Equation 3.3) between successive horizons. For the

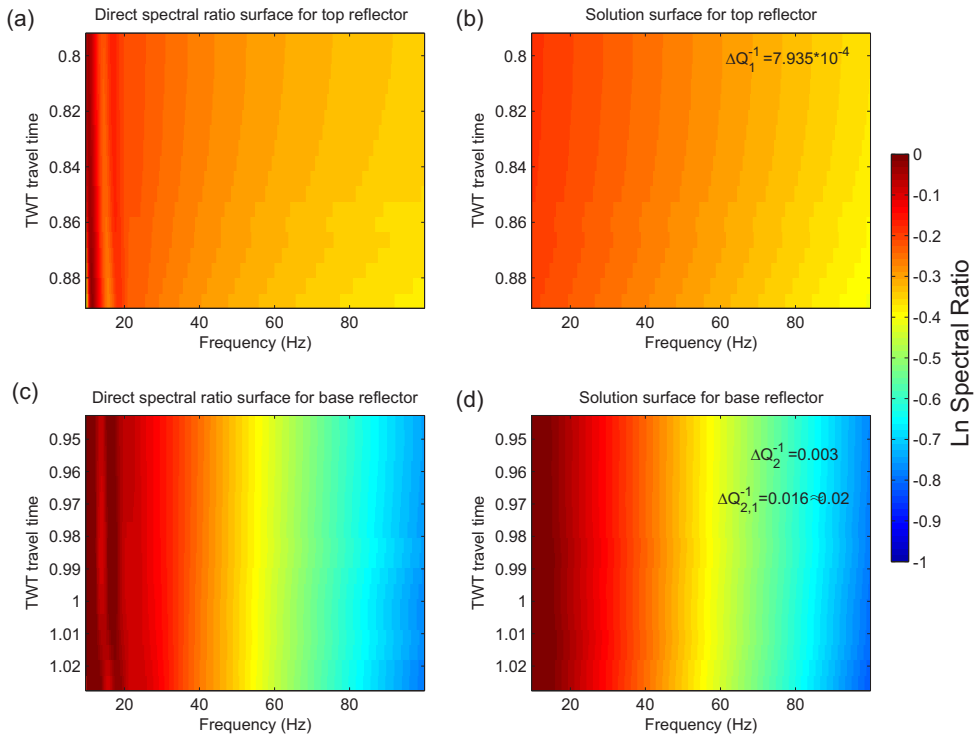

Figure 3.8: Direct Log spectral ratios plotted against time and frequency for the synthetic data. Figures (a) and (b) show the data and the fitted surface for top reflector and (c) and (d) show the data and fitted surface for the base reflector. The change in attenuation to each reflector is shown and the change in attenuation between the two reflectors can be calculated using Equation 3.3.

synthetic example the change in attenuation measured for the interval between the top and base reflectors is +0.016, similar, but not exactly the same as the input change in Q^{-1} of +0.02. Possible reasons for such discrepancies are investigated in the next chapter.

3.4.3 Parameter choices

The parameter choices for the PSQI methodology for both Direct and Absolute methodologies are different depending on whether the regression is being performed via the $\tau - p$ or $t - x$ domain. Once this choice has been made some of the following parameters will need to be chosen, depending on the properties of the data-set.

- The bandwidth to perform the regression.
- If weighting is to be included into the regression, and the nature of the weighting.
- If numerical damping should be included (Appendix A).
- S-transform resolution factor - the resolution factor determines the trade off between good time resolution and frequency resolution.
- The slowness or offset range depending if the $\tau - p$ or $t - x$ domain is used to isolate events.

3.5 Instantaneous frequency matching - IFM

The instantaneous frequency is defined as the rate of change of the instantaneous phase and can be written in terms of the Hilbert transform of a trace

$$f(t) = (\frac{1}{2\pi})\frac{y(t)\frac{dy^*(t)}{dt} - y^*(t)\frac{dy(t)}{dt}}{y^2(t) + y^{*2}(t)} \tag{3.18}$$

(Kanasewich, 1981), where $y(t)$ is the real part of the Hilbert transform and $y^*(t)$ is the imaginary part. Large amplitude spikes in instantaneous frequency are often generated in regions where the envelope ($a(t) = \sqrt{y^2(t) + y^{*2}(t)}$, denominator in equation 3.18) becomes close to zero. Small amounts of noise can therefore produce unrealistic frequency values. A damping parameter (ϵ^2) can be added to the denominator in equation 3.18 (See equation 3.19) to stabilise the calculation.

$$f(t) = (\frac{1}{2\pi})\frac{y(t)\frac{dy^*(t)}{dt} - y^*(t)\frac{dy(t)}{dt}}{a^2(t) + \epsilon^2} \tag{3.19}$$

Values of instantaneous frequency can also be weighted over a given window. The limits of the window are $t + T$ and $t - T$, and W is the squared envelope amplitude.

$$f(t) = \frac{\int_{t=t-T}^{t=t+T} f(t)W(t)dt}{\int_{t=t-T}^{t=t+T} W(t)dt}. \tag{3.20}$$

This ensures that instantaneous frequencies are weighted according to the amount of energy present at that time in the trace.

The instantaneous frequency matching (IFM) methodology is described by Matheney & Nowack (1995). By using a damped and weighted instantaneous frequency (Equation 3.20) it is possible to estimate the instantaneous frequency at any given point in a time series. In this section I describe the methodology of Matheney & Nowack (1995), and develop this methodology to make direct measurements between vintages. I then outline possible work flow and show its use on a simple synthetic data-set, exploring the effects of changing various parameters within the algorithm.

3.5.1 Absolute

Equation 3.20 will be used to calculate the instantaneous frequency. For the initial synthetic tests a damping value of $\epsilon = 1$ and weighting length of 20ms are used to stabilise the instantaneous frequency. I take the near offset arrival from the base reflector in both the Q=30 and Q=80 synthetic models and calculate the raw instantaneous frequency (Equation 3.18), the damped instantaneous frequency (Equation 3.19) and the damped and weighted instantaneous frequency (Equation 3.20) (Figure 3.9). In this example I have added a very small amount of random noise (0.15% of the maximum amplitude of the arrival) to help highlight the benefits of using a damped and weighted instantaneous frequency. The differences caused by the increased attenuation can be seen in the bottom panel of Figure 3.9, where the peak instantaneous frequency has been reduced by around 30Hz. It can also be seen that the "ramping" of the instantaneous frequency at the start of signal is less steep for the Q=30 model.

Instantaneous frequency matching attempts to satisfy the following functions, where $P_r^a(\omega)$ is the FFT of the attenuated wavelet, $P_r(\omega)$ is the FFT of the reference wavelet and $A(\omega)$

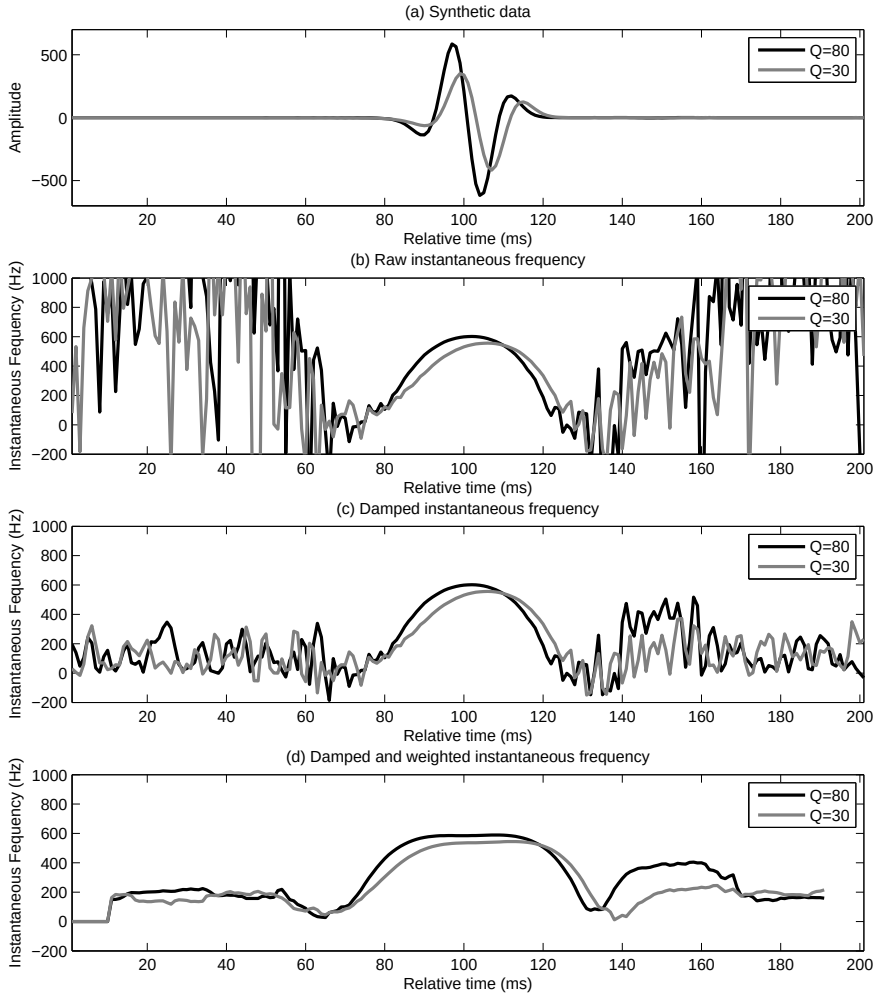

Figure 3.9: Figure showing from top to bottom; a) input data with 0.15% random noise, b) Raw instantaneous frequency of (a), c) Damped instantaneous frequency ($\epsilon = 1$) and d) Damped and weighted instantaneous frequency (window length = 20ms, weighted using instantaneous amplitude).

is the attenuation operator containing the value t/Q which is the total travel time divided by the effective attenuation of the medium:

$$P_r^a(\omega) = P_r(\omega)A(\omega) \tag{3.21}$$

$$A(\omega) = e^{-\frac{i\omega t}{Q\pi}\ln(\frac{\omega}{\omega_r})}e^{-\frac{\omega t}{2Q}} \tag{3.22}$$

(Matheney & Nowack, 1995), where ω_r is a reference angular frequency and dispersion and amplitude loss are related to the first and second exponential terms respectively.

These equations produce a non-linear problem of the form $\mathbf{d} = \mathbf{F}(\mathbf{m}) + \mathbf{e}$, where $\mathbf{d}$ is the observed instantaneous frequency, $\mathbf{F}(\mathbf{m})$ is the calculated instantaneous frequency which requires the model to calculate it and $\mathbf{e}$ is the error. This equation can be quasi-linearised by inverting for the residuals and finding a small improvement to the original model (Gubbins, 2004; Matheney & Nowack, 1995). This can be use to invert for a single instantaneous frequency or a number of instantaneous frequencies around the maximum envelope.

3.5.2 Direct

The IFM method can be extended to measure attenuation directly between vintages of seismic data. If we consider two wavelets from the same reflector from two different vintages, assuming the same source, then we can say that for vintage 1,

$$P(\omega) = P_s(\omega)A(\omega) \tag{3.23}$$

where $P(\omega)$ and $P_s(\omega)$ are the FFT's of a reflector of interest and the source, and for vintage 2:

$$P'(\omega) = P_s(\omega)A'(\omega). \tag{3.24}$$

where $'$ denotes the second vintage of data. We can then divide equation 3.24 by equation 3.23. By letting the source terms cancel we get

$$P' = P\frac{A'}{A}. \tag{3.25}$$

So P' can be modelled from the initial data P in a similar way as above, however, A (Equation 3.22) is now replaced by A'/A. Assuming that there is no change in travel time

$$\frac{A'(\omega)}{A(\omega)} = e^{-\frac{i\omega t}{\pi}(1/Q' - 1/Q)\ln(\frac{\omega}{\omega_r})} e^{-\frac{\omega t}{2}(1/Q' - 1/Q)} \tag{3.26}$$

An example of the direct inversion for the two traces shown in Figure 3.9 is give in Figure 3.10. Three iterations (the 1st, 2nd and 6th) are displayed showing the operator used (Equations 3.22 and 3.26), and the modelled trace, spectra and instantaneous frequency for each iteration. Differences in the instantaneous frequency are minimised, and in this synthetic example are indistinguishable between the 2 vintage of data after 6 iterations. The final change in t^* along the full ray path is found to be 0.00317s, and if all of the change in attenuation is assumed to be due to the interval between the top and base reflectors give a change in Q^{-1}=0.0232, which is of the same magnitude to input change of 0.02.

3.5.3 Parameter options

There is a large amount of parametrisation to choose from in the instantaneous frequency methodology.

- Damping (ϵ^2, Equation 3.19) when calculating the instantaneous frequency
- Weighting (T, Equation 3.20) for the calculation of instantaneous frequency
- Regression length for inversion (Number of instantaneous frequencies to be matched)
- Reference frequency for dispersion.
- Length of FFT window.

As the effect of each of the parameters is not as intuitive as in the case of other methodologies I now show the effect that various parameter choices have on the instantaneous frequency algorithm. Figure 3.11 highlights that Δt^* is not very sensitive to the choice of reference frequency, and that the solution converges after just three iterations, with the average Δt^* around 0.00317s with maximum and minimum values falling $\pm$0.00002s either side of this ($\pm$0.6%)

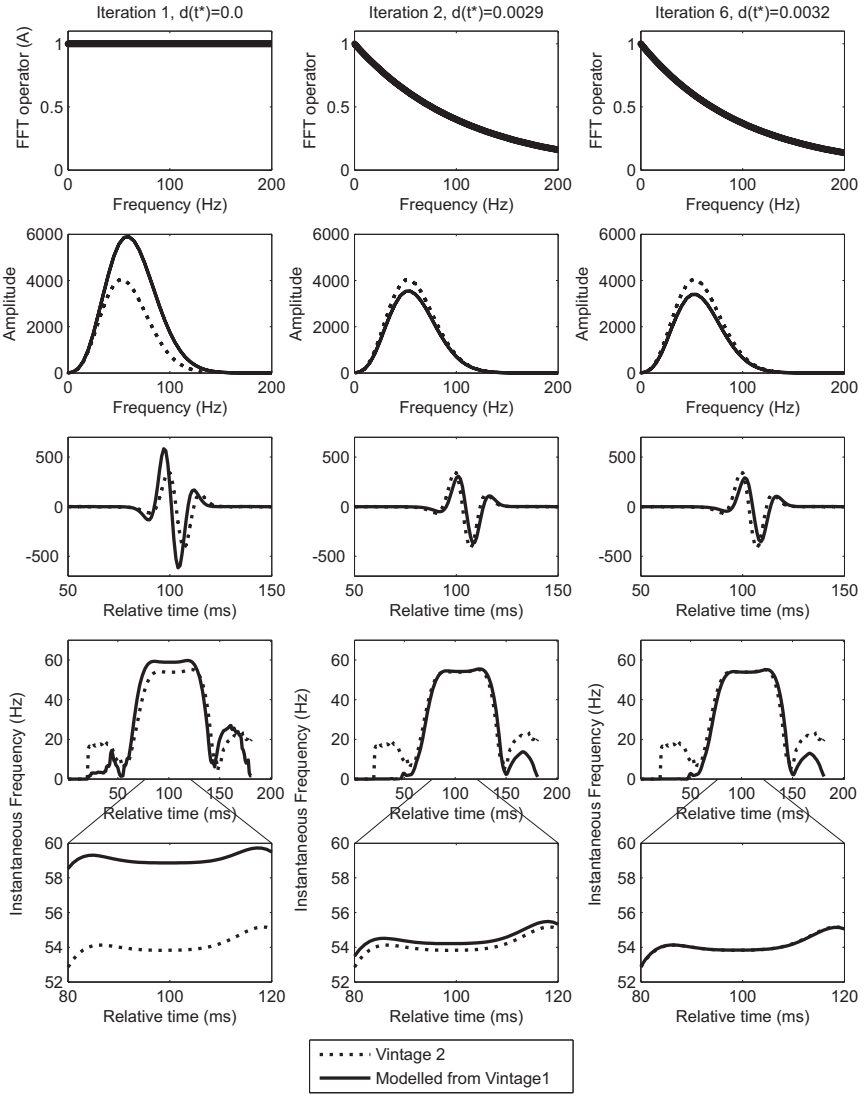

Figure 3.10: Figure showing 3 different iterations of the inversion. From top to bottom: Operator (Equation 3.26) used to multiply FFT of reference trace (vintage1); Spectra of product and vintage 2; Comparison of modelled trace and vintage 2; Instantaneous frequencies of modelled trace and vintage 2; region of instantaneous frequency that is inverted for. From left to right: 1st iteration; 2nd iteration; and 6th iteration. Note that the amplitude spectra still show differences, and these may be due to the constant frequency damping used, however, the instantaneous frequencies well matched.

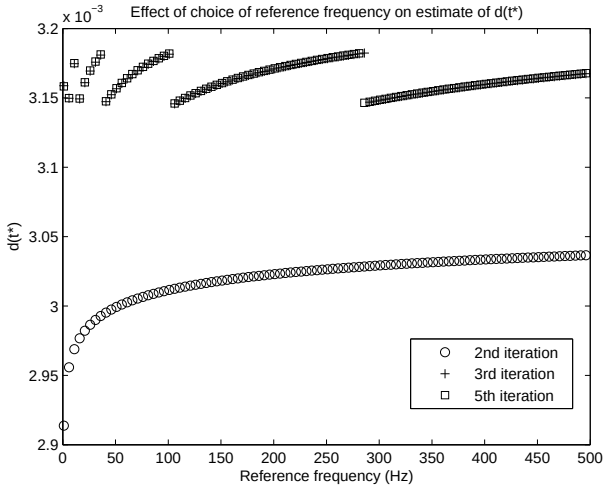

Figure 3.11: Comparison of convergence behaviour with changing the reference frequency.

The damping parameter has little effect on the final solution until the damping parameter becomes too large, at which point the inversion requires more iterations as it converges at a slower rate. At this point the instantaneous frequency has been over-damped as the damping value has become much larger than the maximum envelope of the signal (Figure 3.12).

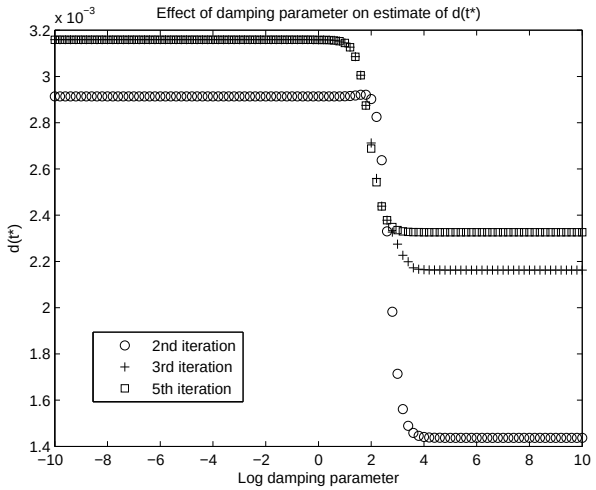

Figure 3.12: Comparison of convergence behaviour with changing the damping parameter ϵ (Equation 3.19).

There are significant improvements to be gained in the estimation of Δt^* with the increase in weighting length (Figure 3.13) whilst a decrease in accuracy as the number of samples used in the inversion exceeds the size of the wavelet (Figure 3.14). There will be an inherent relationship between these two parameters, for example, if lots of samples are to be included in the regression, a larger weighting length will be needed to stabilise the

waveform.

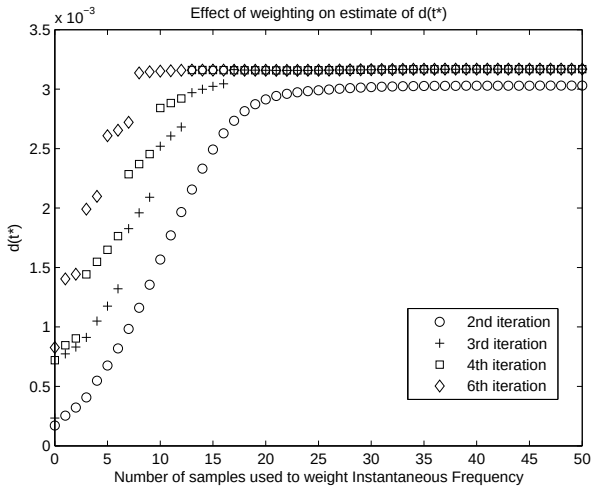

Figure 3.13: Comparison of convergence behaviour with changing the weighting length T of the data (Equation 3.20).

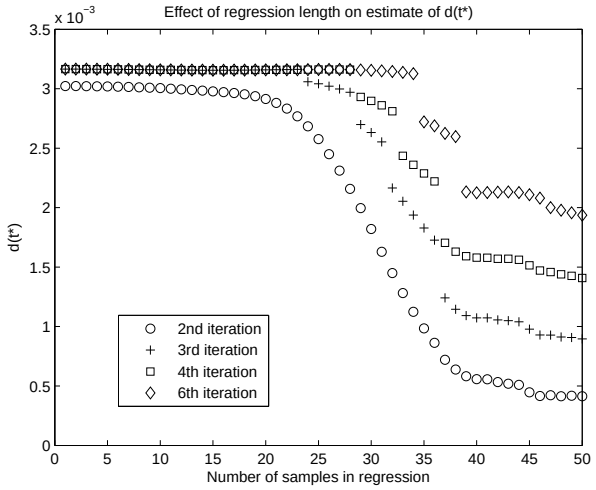

Figure 3.14: Comparison of convergence behaviour with changing regression length.

Finally, the length of the FFT must be long enough so that both the frequency and phase content of the data can be estimated adequately and then modified accurately. Figure 3.15 suggests that the longer the FFT window the more accurate the regression. However, this example is for a clean, isolated waveform. More complicated waveforms, noise, or waveforms that are interfering with each other may affect the choice of this FFT length.

Again, careful parametrisation of this methodology will be necessary on a data-set by data-set basis.

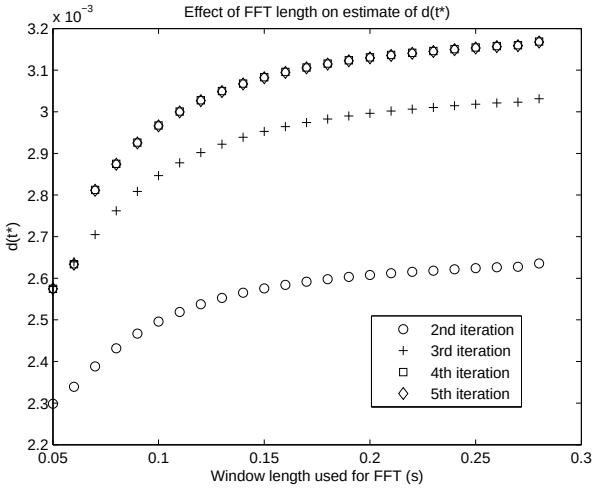

Figure 3.15: Comparison of convergence behaviour with FFT window length. Note: Length of FFT window is restricted to avoid including energy from other reflections.

3.6 Centroid frequency - CF

The centroid frequency method has been described in detail by Quan & Harris (1997) and also used in attenuation tomography methods by Rossi et al. (2007). The definitions of the centroid frequency (f_c) and the variance (σ_c^2) of a spectrum $S(f)$ are given by Quan & Harris (1997) as

$$f_c = \frac{\int_0^\infty fS(f)df}{\int_0^\infty S(f)df} \tag{3.27}$$

and

$$\sigma_c^2 = \frac{\int_0^\infty (f - f_c)^2 S(f)df}{\int_0^\infty S(f)df} \tag{3.28}$$

If the spectrum is initially $S(f)$, the attenuated spectrum ($S'(f)$) can be given by:

$$S'(f) = GRS(f)e^{-\pi ft/Q} \tag{3.29}$$

where G and R are factors associated with the frequency independent effects due to geometrical spreading and reflectivity respectively. Quan & Harris (1997) analytically derived the relationship between attenuation Q^{-1} and the statistical properties (f_c and σ^2) of the spectra. A Gaussian spectrum is defined by

$$S(f) = e^{\frac{-(f-f_0)^2}{2\sigma^2}} \tag{3.30}$$

where f_0 and σ_S^2 are the mean frequency and standard deviation of the spectrum, hence the relationship between attenuation and the centroid frequencies of the source (f_S) and receiver (f_R) spectra is given by:

$$\frac{1}{Q} = \frac{f_S - f_R}{\pi t \sigma_S^2} \tag{3.31}$$

where t is the travel time between the source and receiver.

Definitions were also given for a Boxcar spectrum of bandwidth B

$$\frac{1}{Q} = 12\frac{f_S - f_R}{\pi t B^2} \tag{3.32}$$

and a triangular spectrum of bandwidth B

$$\frac{1}{Q} = 18\frac{f_S - f_R}{\pi t B^2} \tag{3.33}$$

It is important to note that Quan & Harris (1997) found that the Gaussian spectrum is a reasonable approximation for most seismic source spectra. It is therefore possible to calculate effective $1/Q$ estimate for each offset and reflector in a CMP using reference spectra estimated from the data (near surface spectra).

3.6.1 Second regression

Equation 3.31 can be re-arranged to give,

$$\frac{t}{Q} = \frac{f_S - f_R}{\pi \sigma_S^2} \tag{3.34}$$

It is now possible to plot the the right hand side of Equation 3.34 against the TWT (t) for each prestack trace and perform a regression to find the slope. The slope of this will be equal to $1/Q$. This second regression is analogous to the second regression of the QVO methodology. It is also evident that the regression could be performed against offset squared as with the original QVO methodology. If measurements are made at different reflectors, then it is possible to calculate interval attenuation via Equation 3.3.

3.6.2 Direct

The direct methodology can be performed in the same way, apart from in this case, f_S and f_R are replaced by f_R and f'_R respectively (where $'$ denotes the second vintage) and σ_S^2 is replaced by the standard deviation of the first vintage of data. f_R and f'_R are the centroid frequencies for two events from the same reflector at the same offset for different vintages. This direct methodology again assumes that there is no change in source spectra or travel time between vintages of data.

Using the synthetic example, the direct changes in centroid frequency are calculated for both the top and base reflectors for all offsets. Figure 3.16 displays the spectra and centroid frequencies for the upper and lower reflections from a near offset trace and all measurements of Δt^* plotted against TWT. Using Equation 3.3 the change in Q^{-1} between the upper and lower reflections is found to be 0.0211, approximately equal to the expected change of 0.02.

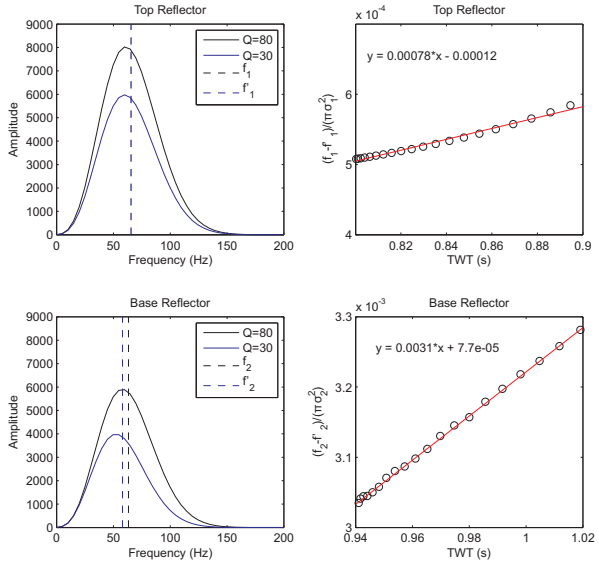

Figure 3.16: Example of the direct centroid frequency methodology, showing centroid frequency measurements for the top and base reflector for the near offset trace (left) and the regression against time for all offsets (right).

3.6.3 Parameters

The possible variables for the Centroid frequency methodology are:

- Frequency estimation (FFT, s-transform)

- Bandwidth to include for calculation.

Compared to other methodologies, there are fairly few parameters to be tested, however, the assumption of a Gaussian spectrum will be investigated in the next chapter.

3.7 VSP analysis

VSPs differ from surface seismic data as the geometry is different, allowing the measurement of attenuation of a transmitted wave. VSPs are in general acquired with a higher frequency source than that seen in surface seismic data, potentially allowing for a higher resolution sampling of the subsurface. It is possible to use any of the attributes described above to estimate attenuation from the VSP. The benefit of using VSP data to estimate attenuation are that transmitted waves can be analysed rather than reflected arrivals. This inherently makes the data less susceptible to noise from multiple energy.

Generally, VSP data are acquired using a string of geophones located down a borehole at a certain depth range (and small lateral offset) from the source location. After data are acquired at this string location, the string is moved to a different depth range, and a new source is used (at the same location) (Figure 3.17). To avoid biases due to source spectra differing from string to string, all the methodologies presented here are performed on a single string of data at a time.

Within the string, we can calculate the attenuation between all possible combinations of receiver pairs. A schematic of this is shown in Figure 3.18. When a measurement is made at two receivers at different depths, z_{n} and z_{m}, values obtained can either be plotted against the upper depth (z_{n}) and lower depth (z_{m}), or can be plotted against the midpoint between the receivers ($(z_{\mathrm{n}} + z_{\mathrm{m}})/2$) and the receiver spacing ($z_{\mathrm{m}} - z_{\mathrm{n}}$).

For two receivers at depths z_{n} and z_{m} the effective attenuation between them can be calculated using the spectral ratio method

$$\ln(\frac{S_{\mathrm{m}}}{S_{\mathrm{n}}}) = -\frac{\pi}{Q_{\mathrm{n,m}}} t_{\mathrm{m,n}} f + \ln(RG) \tag{3.35}$$

or the centroid frequency

$$\frac{1}{Q_{\mathrm{n,m}}} = \frac{f_{\mathrm{n}} - f_{\mathrm{m}}}{\pi t_{\mathrm{n,m}} \sigma_{\mathrm{n}}^2} \tag{3.36}$$

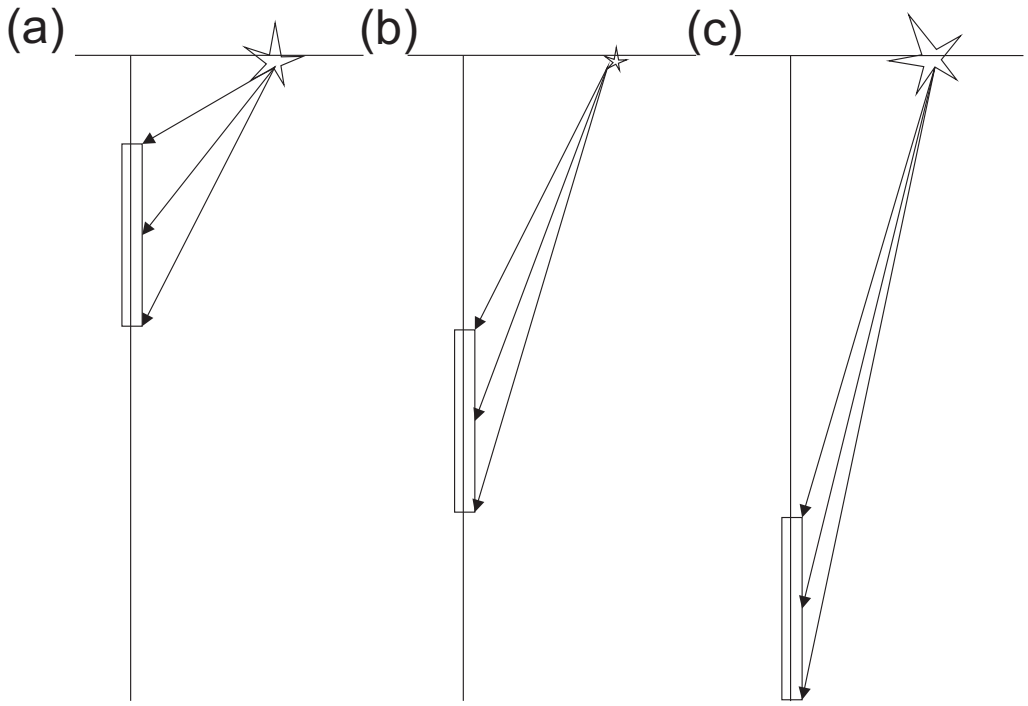

Figure 3.17: Schematic of the acquisition of a VSP, with the string of geophones progressively being moved down the borehole progressively from (a) to (c). The source spectrum may be liable to changes between acquisition at different depths.

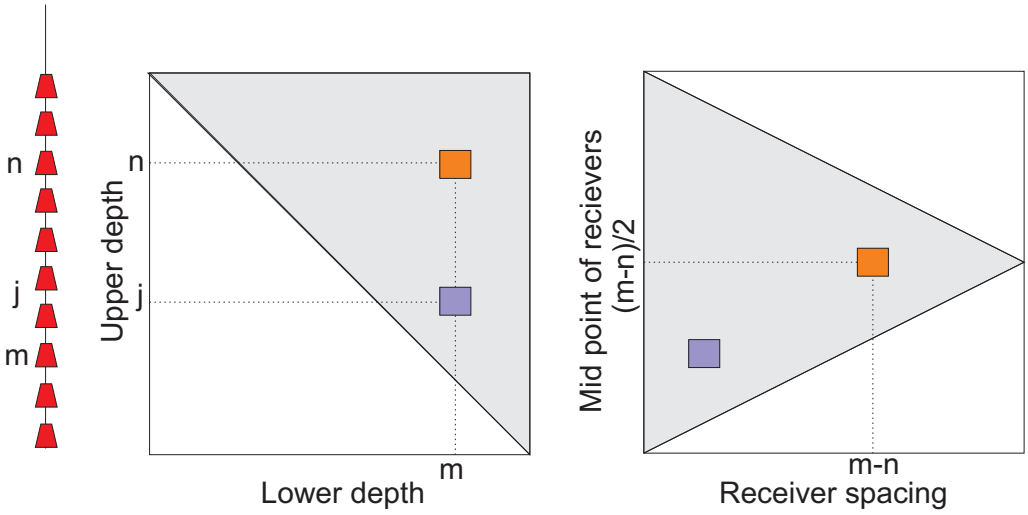

Figure 3.18: Schematic of the possible ways that VSP measurements of attenuation are displayed using 'tartan triangles'. Measurements can wither be plotted against the Upper and Lower receiver elevations or the midpoint and spacing of the receivers.

or by the instantaneous frequency by finding the operator

$$A(\omega) = e^{-\frac{i\omega t_{\mathrm{n,m}}}{Q_{\mathrm{n,m}}\pi}\ln(\frac{\omega}{\omega_r})} e^{-\frac{\omega t_{\mathrm{n,m}}}{2Q_{\mathrm{n,m}}}}, \tag{3.37}$$

by minimising the error in instantaneous frequencies between receivers. All of the parameter options remain the same and will be data-dependent. It can also be seen that the PSQI inversion scheme could be used to solve for a surface in time and frequency for all receivers from depths z_{n} to z_{m}.

3.8 Summary and discussion

I have described, following their original authors, 4 methodologies for estimating attenuation from prestack surface seismic data. I have where possible, extended these methodologies to enable the calculation of attenuation directly between vintages of seismic data. Although the direct methodologies require more assumptions in the calculation, if these assumptions are met then possible benefits include only needing to analyse a single reflector and avoiding artefacts associated with $\tau - p$ transforms.

Each of the methodologies have several parameters that need defining carefully before analysis takes place. This must be done on a data-set by data-set basis, as regression bandwidths, spectra shapes and source repeatability will vary. Incorrect parametrisation is likely to produce inaccurate results. The centroid frequency methodology requires the least parametrisation, however, the assumption that the spectra are Gaussian is likely not to be true in most cases.

Using the simple synthetic example, we have seen that the exact change in attenuation was not found by any of the methodologies tested. There may be numerous reasons for this but one of the most likely is the effect that changes in dispersion may have on the measurement. Changes in dispersion will cause different frequencies to travel at different velocities, hence some frequencies will be differently attenuated relative to a reference frequency. This frequency dependent velocity will also cause changes in the frequency dependent reflectivity of the data, imparting some bias on the measurement. I will attempt to quantify the magnitude of some of these effects in the next chapter.

Chapter 4

Numerical examples - sensitivity of time-lapse attenuation measurements

In this chapter, the sensitivity of time-lapse attenuation measurements is investigated using numerical examples and synthetic modelling. Various factors can affect the sensitivity of attenuation measurements and these can be incoherent (random) or coherent (systematic) in nature. I will attempt to quantify these effects either by deriving analytical relationships or by modelling the effect using synthetic data sets.

I will begin the Chapter by investigating the sensitivity of methodologies outlined in Chapter 3 to band-limited random noise. This will give an estimate of the effect that incoherent noise may have on measuring changes in attenuation. I then move on to investigate some of the coherent noise types that can bias our estimations of attenuation.

For the spectral ratio and centroid frequency methodologies, the way in which the frequency spectra are calculated can impact the measurement of attenuation. Reine (2009) showed that by using a time-frequency transform such as the s-transform, spectral contamination can be limited through better time-resolution of the spectral content. However, I go on to show that the s-transform, although being stable, can also have unwanted effects on the measurement of attenuation, particularly when higher frequencies are used.

Multiple energy entering analysis windows may affect measurements of the change in attenuation through interference, causing spectral notches (such as those found in thin bed tuning). The effects of interference are shown in a synthetic example where the top reservoir horizon is a tuned reflector.

If attenuation changes are present in the data it is necessary that there will be changes in velocity dispersion. Velocity dispersion can affect the estimates of attenuation, primarily in two ways. Firstly, with frequency dependent velocity comes frequency dependent travel-times therefore assuming a single travel-time for all frequencies is not valid. I quantify these errors by assuming a dispersion law and then comparing the expected change in attenuation with that produced with frequency dependent travel-times. Secondly, frequency dependent velocities will inevitably produce frequency dependent reflectivity. In the case of prestack surface seismic data, this yields frequency dependent reflectivity changes as a function of offset also. The effects of this are investigated using numerical examples of typical AVO curves, combined with analytical relationships of the spectral ratio method.

Finally, if time-lapse changes in attenuation are present, other frequency independent 4D changes in seismic properties could also be present. In the direct methodologies outlined in Chapter 3 I make the assumption that there are no changes in travel-time between vintages of data. I investigate the sensitivity of this assumption, for various changes in attenuation and frequency independent velocity. Time-lapse amplitude changes may also be expected to occur and although these changes would not be expected to affect the spectral ratio and centroid frequency methodologies, they may have some impact on the instantaneous frequency methodology. This is investigated by looking at a simple synthetic example and introducing frequency independent amplitude changes between vintages.

4.1 Incoherent noise - band pass filtered random noise

I have introduced several methodologies in Chapter 3 that measure attenuation via estimates of the log spectral ratio slopes, centroid frequency and instantaneous frequency. I now investigate the stability of these methodologies under different amounts of incoherent noise. I utilise the simple synthetic data-set created in Chapter 3, adding band-pass filtered random noise to the data at varying amplitudes. Band pass filtered noise is used as it will be more representative of the noise seen in the data due to scattered energy of the original spectrum. Noise at frequencies above the bandwidth of the source is not included as it would likely be filtered out before analysis.

The quantity of noise added (noise level) is measured as a percentage of the maximum amplitude of the near offset (50m) reflection from the 1st horizon. A 10-200Hz bandpass filter is used to filter the random noise which is then added to the traces of the data set

and three methodologies used to calculate the change in t^* with the expected change in t^* being 0.0032s. Comparisons will be made by looking at the ability of measuring the correct change in t^*, and the standard deviation of 10 realisation of the random noise at that noise level. By comparing these quantities, any coherent effects due to this noise will be able to be separated from incoherent effects. Coherent effects are identified by the measurement of t^* being incorrect with the standard deviation of 10 realisations being small, whilst incoherent effects are identified as they have a large standard deviation for 10 realisations of the noise.

I compare the PSQI, Centroid frequency and Instantaneous frequency methodologies. t^* values are calculated for 40 noise levels between 0 and 20% of the maximum amplitude. For each noise level, 10 realisations of the random noise are used to estimate the accuracy of the measurement. For all cases I compare the change in t* calculated via the absolute methodologies (treating each vintage separately) and via the direct methodologies, where only the base reflector is used in the analysis. The PSQI methodology is used with a bandwidth of 10-100Hz as this is a stable bandwidth for the regression. The Centroid frequency is calculated using all frequencies and the instantenous frequency is calculated using a weighting length (T) of 10 samples, a regression length of 10 samples and a damping value (ϵ^2) of 0.1.

The mean and standard deviation of the t^* values estimated from each methodology are calculated and plotted in Figure 4.1. In all methodologies the standard deviation of t^* estimates increases with percentage noise. It is clear that the spectral ratio methodology (PSQI) performs much better than the other methodologies, still predicting the correct polarity of attenuation past 10% noise. The Centroid frequency shows a drastic decrease in the ability to predict the correct change in attenuation even for extremely small magnitudes of attenuation, however, these effects can be classified as coherent in behaviour as the standard deviation of measurements does not increase significantly with noise level. The reduction in t* in the centroid frequency methodology may therefore be dominated by the increased spectral deviation. This effect can be confirmed by using a specific bandwidth to calculate the centroid frequency. By calculating the centroid frequency in the bandwidth used for the PSQI methodology (10-100Hz) (Figure 4.2) results now replicate the behaviour of the results from the PSQI methodology. This indicates that if noise levels are high in the data, a carefully chosen bandwidth of analysis for the centroid frequency may be nessessary.

Instantaneous frequency results show good prediction of the correct change in attenuation up to around 4% noise. The instantaneous frequency methodology shows similar behaviour to the centroid frequency methodology with predictions being damped down to zero rapidly past 4%. This effect may be caused by the damping parameter not being large enough at the higher noise levels. The sensitivity of the instantaneous frequency to the damping value is confirmed by allowing the damping value to equal the magnitude of the noise in the data (Figure 4.3). An improvement can be seen in the direct methodology (Figure 4.3), whilst the absolute methodology appears to show little improvement.

Of all methodologies the direct comparisons perform better at estimating the correct magnitude of attenuation and in most cases the absolute methodologies have a larger standard deviation of the 10 realisations. The bias seen in the absolute methodologies (a general underestimate of around -0.0005s) may be a result of coherent effects on the upper reflection. The increased deviation in the absolute methodologies is a consequence of calculating an interval attenuation, and hence addition of the deviation of both reflectors for both vintages.

4.2 Spectral estimation

Noise on spectral estimates via a fixed window Fourier transform occurs when unwanted energy from other arrivals falls into the analysis window. Reine (2009) showed that this effect can be reduced via the use of a variable-window time-frequency transform such as the s-transform (Stockwell et al., 1996). He concluded that this improvement arises for two reasons; firstly, shorter time windows are used to estimate the higher frequencies, meaning the primary (or wanted) arrival is better isolated from interfering events; secondly, there is an increased spectral averaging over the shorter time windows and rapid fluctuations in the spectrum are smoothed out. For both of these reasons the statistical error on the regression for attenuation is minimised.

Using the synthetic example in Chapter 3, I look at the direct spectral ratios of the near offset trace using a standard fixed window Fourier transform (Figure 4.4). This clearly highlights the limits of the stable bandwidth of the spectral ratio(0-200Hz). I can now compare this spectral ratio with those produced by the s-transform.

The s-transform is a variable window transform, meaning that the analysis window is not only a function of time, but of frequency as well. The s-transform window is defined as

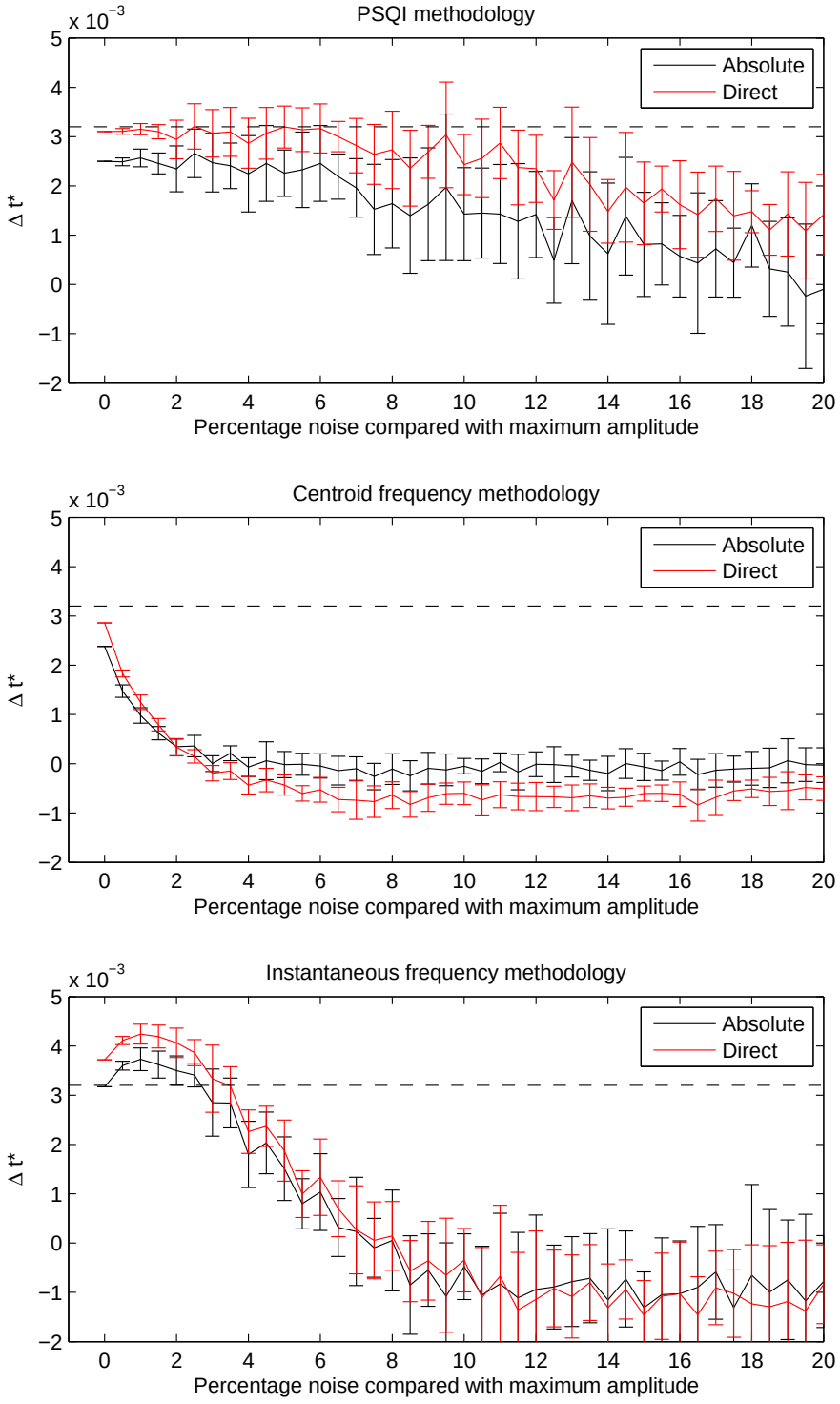

Figure 4.1: Comparison of the t^* [s] values estimated from the synthetic example introduced in Chapter 3. 10 realisations of band-passed noise were added to the CMP for each of the noise levels. Results for the PSQI methodology (top) Centroid frequency methodology (middle) and Instantaneous frequency methodology (bottom) are displayed for the absolute (black) and direct (red) approaches.

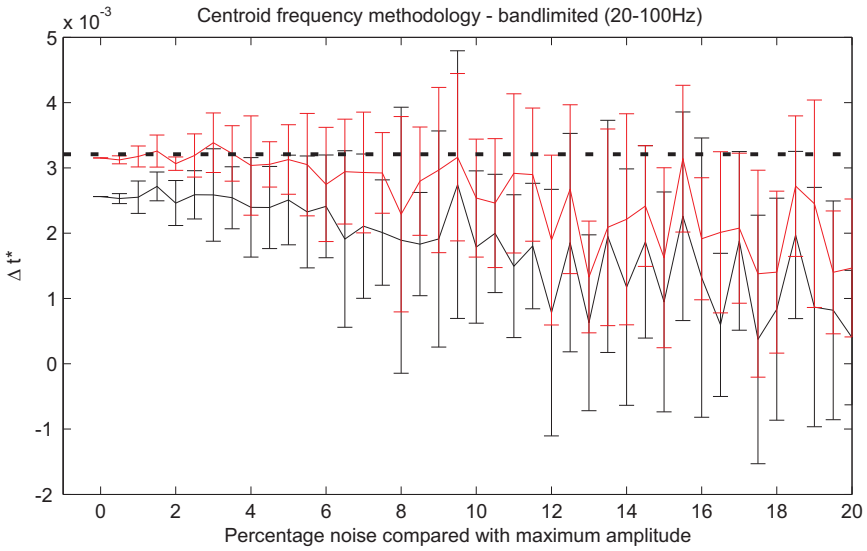

Figure 4.2: Comparison of the t^* [s] values estimated from the synthetic example introduced in Chapter 3 using a the Centroid frequency methodology with a defined frequency range.

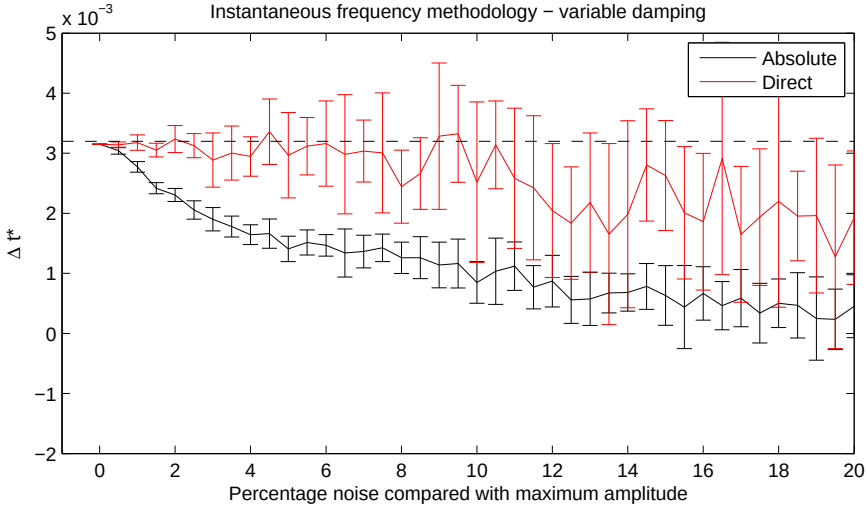

Figure 4.3: Comparison of the t^* [s] values estimated from the synthetic example introduced in Chapter 3 using the Instantaneous frequency methodology using a damping value proportional to the amount of noise introduced.

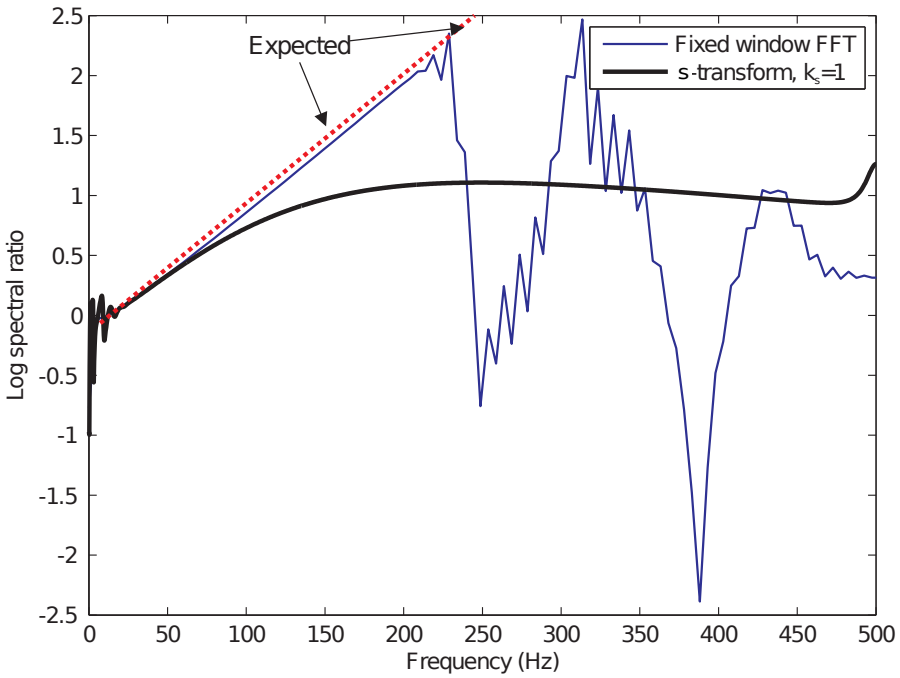

Figure 4.4: Comparison of spectral ratios ($\ln(S_{Q=80}/S_{Q=30})$) for a fixed window FFT and a s-transform with a resolution factor of $k_S = 1$. Data used is the first offset trace in Figure 3.3.

(Stockwell et al., 1996):

$$\omega_S(t,f) = \frac{|f|}{k_S\sqrt{2\pi}} e^{-\frac{t^2 f^2}{2k_S^2}} \tag{4.1}$$

where k_S is a resolution factor that determines the relative size of window. Once the variable window is calculated (Equation 4.1), the s-transform is calculated using:

$$S_S(t_0,f) = \frac{|f|}{k_S\sqrt{2\pi}} \int_{-\infty}^{\infty} s(t) e^{-\frac{-(t-t_0)^2 f^2}{2k_S^2}} e^{i2\pi f t} dt \tag{4.2}$$

which can be solved in the frequency domain as a multiplication of the Fourier transformed windows and the Fourier transformed trace. A small k_S produces relatively small windows, increasing the time-resolution, but decreasing the frequency resolution. A large k_S has the opposing effect of decreasing the time resolution, but better resolving the frequency content (less spectral averaging). Reine (2009) chose to use an arbitrary k_S=1 for good time resolution, but here I show that this is not always optimal and may even reduce the effectiveness of an attenuation measurement. Figure 4.4 compares the results of using a fixed window FFT with that of an s-transform with $k_S = 1$. It can be seen that the frequency averaging at higher frequencies impacts upon the steepness of the spectral ratio slope in the stable bandwidth of interest, whilst the fixed window FFT resolves the slope

far better at higher frequencies, particularly evident in Figure 4.4 from 100-200Hz.

Choice of resolution factor

I take the near offset trace from each vintage of the synthetic example (same traces as Figure 4.4) and show that the choice of resolution factor may be important when calculating attenuation. Figure 4.5 shows the effect of various values of k_S on the spectral ratios. The frequency resolution is increased for larger k_S whilst for small k_S energy is smoothed across the high frequencies having implications on the spectral ratio slopes. However, to have good frequency resolution (large k_S) requires compromising time resolution, and this effect can be seen by the appearance of noise at lower frequencies (increased contamination from the wrapping of larger windows). The effect on the estimate of attenuation can then be seen in Figure 4.6. Here I have calculated the attenuation for numerous bandwidths for 4 values of k_S. For large resolution factors the measured spectral ratio slope is far more stable for a greater combination of measurement bandwidths, whilst for small resolution factors, the measured slope changes almost linearly as the centre of the bandwidth increases. If the full bandwidth available is used this would in effect reduce the magnitude of attenuation observed. The results of Reine (2009) indicated that the increased time resolution increased the accuracy of measurement by avoiding unwanted energy in the frequency spectrum from other near-by arrivals. I have shown that there is a trade off between time-resolution and frequency resolution, as increasing the time-resolution too much can cause underestimates of the changes in attenuation from band-limited signals.

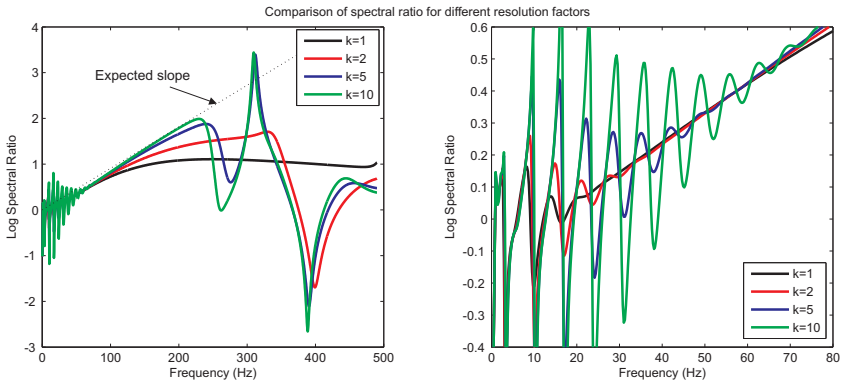

Figure 4.5: Direct spectral ratios for the near offset synthetic trace calculated using the s-transform and different resolution factors (Equation 4.1). The effect of the trade off between resolution in frequency and time can be seen by the lack of frequency resolution (smoothed spectra) at low k, and the contamination of lower frequencies at high k (due to worse time resolution).

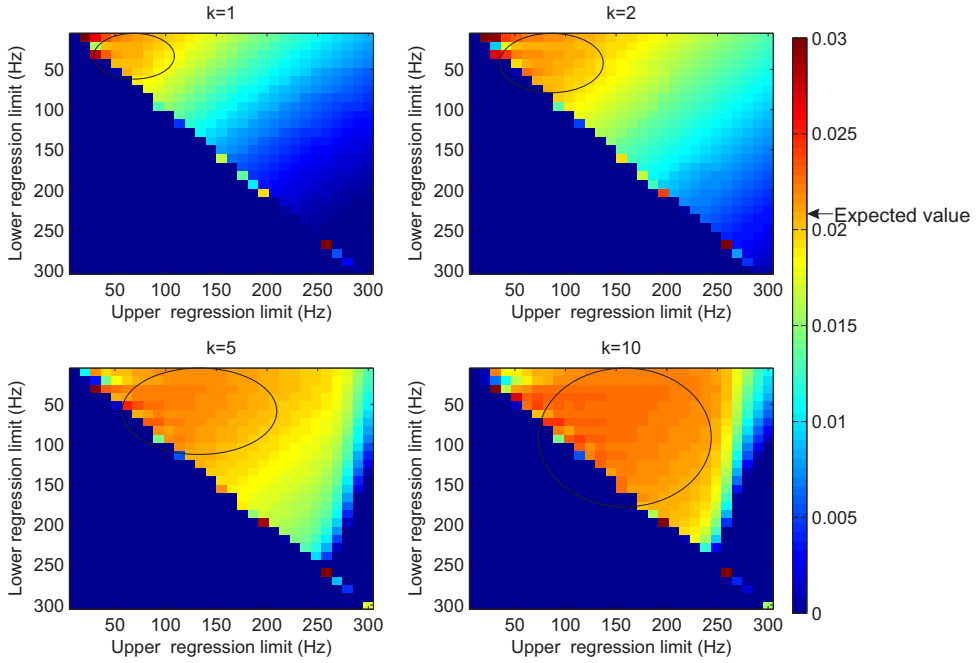

Figure 4.6: The effect of resolution on the value of $d\Delta 1/Q$ determined from many regression bandwidths, it is clear that the correct change in attenuation is calculated for a larger range of frequencies for larger values of k (Highlighted by circles).

4.3 Multiples

I investigate the effect of multiple energy on the estimate of changes in attenuation by taking an example of interference effects caused by thin bed multiples through a synthetic example of a tuned reflector.

4.3.1 Interference - Tuning example

Effects of thin bed multiples can inhibit the ability to measure attenuation quantitatively from single vintages of seismic data. Here I look at the effect of a tuned reflector on the estimation of attenuation. Using a simple synthetic example, it is possible to show the effect that a tuned reflector has on the estimation of attenuation from a single vintage will cancel between vintages of data. I write the effective attenuation (measured attenuation, Q_{eff}^{-1}) as the summation of the intrinsic attenuation (Q_{int}^{-1}) and the apparent attenuation dues to the tuned reflector (Q_{app}^{-1}).

$$Q_{\text{eff}}^{-1} = Q_{\text{int}}^{-1} + Q_{\text{app}}^{-1} \tag{4.3}$$

Synthetic traces for pre- and post-gas injection were created using the parameters in Table 4.1, where Q decreases between vintages of data (mimicking an increase in gas saturation). A single trace was calculated for each vintage at 175m offset.

Layer	Depth [m]	V_p [m/s]	V_s [m/s]	ρ [kg/m^3]	Q_p (Pre-injection)	Q_p (Post-injection)
1	500	3000	1400	2000	200	200
2	522	2800	1400	2000	200	200
3	700	3000	1400	2000	200	50
4	∞	3200	1400	2000	200	200

Table 4.1: Model parameters used for tuned synthetic example (Figure 4.7).

Figure 4.7 shows the log spectral ratio slope results from the synthetic data in which two oblique incidence synthetic traces were generated, for a reservoir with Q=200, dropping to Q=50 after injection (Figure 4.7b). In this case, for vintage 1, $Q^{-1}_{\text{meas}} = -0.0101$, $Q^{-1}_{\text{int}} = 0.0050$ so we infer that $Q^{-1}_{\text{app}} = -0.0151$, 3 times the magnitude of Q^{-1}_{int}. For the second vintage of data $Q^{-1}_{\text{meas}} = 0.0075$, $Q^{-1}_{\text{int}} = 0.0200$ and therefore $Q^{-1}_{\text{app}} = -0.0125$. The expected change in Q^{-1}_{int} is 0.0150, and the measured change in attenuation ($\Delta(Q^{-1}_{\text{meas}})$) is 0.0176, giving a change in apparent attenuation ($\Delta(Q^{-1}_{\text{app}})$) of 0.0016. In this case, changes in the intrinsic component dominate the changes in the apparent component, hence time-lapse attenuation changes can reliably reveal intrinsic attenuation changes. Changes in the apparent attenuation may also be caused by changes in the frequency dependent reflectivity and dispersion between vintages of data. The magnitude of some of these effects are investigated in the next section.

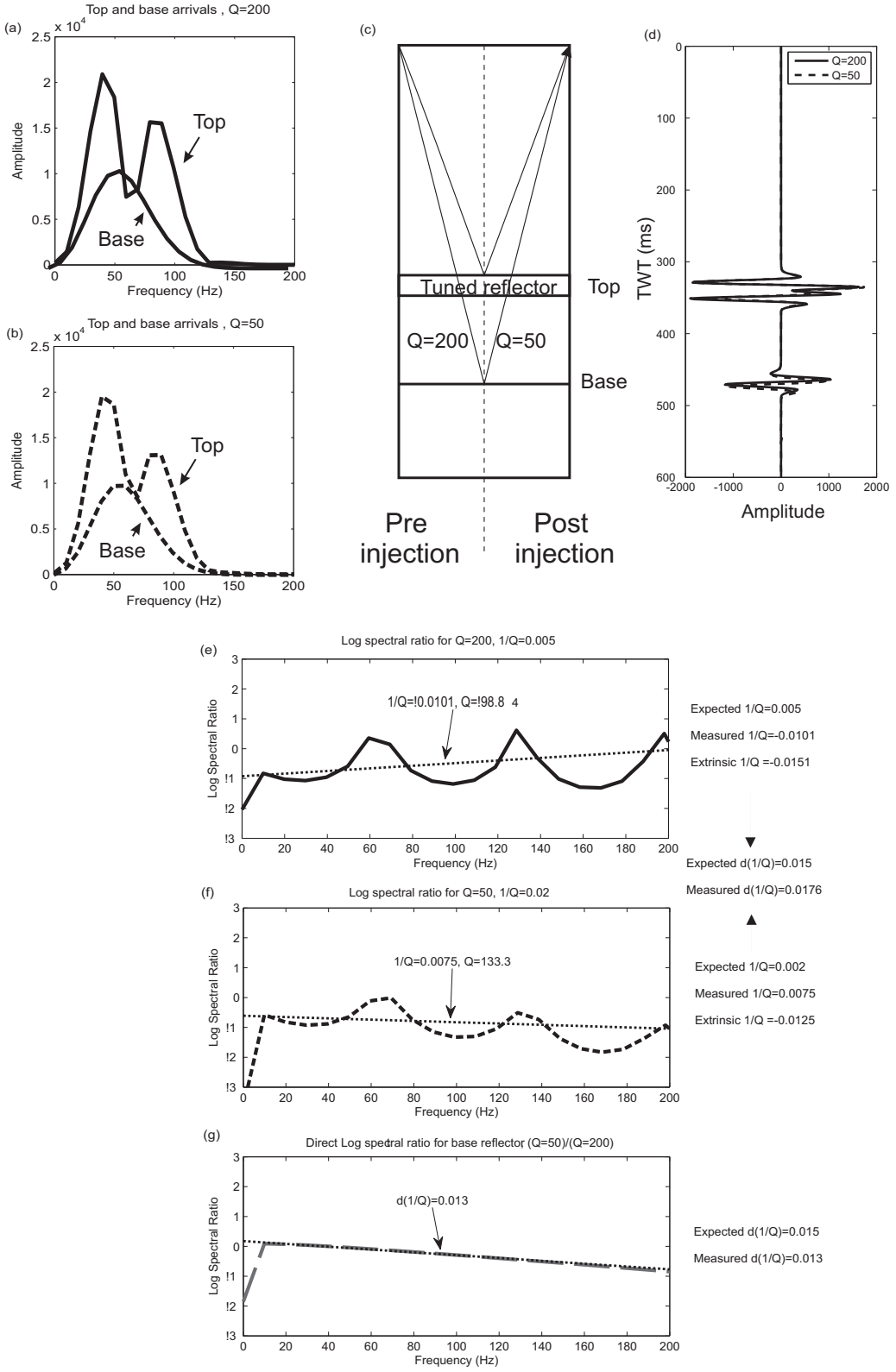

Figure 4.7: Simple synthetic of a tuned top reservoir event and the effect on attenuation estimates. Calculated spectra for a single offset of (a) pre-injection spectra (Q=200), (b) post-injection spectra (Q=50), (c) Schematic of synthetic model, (d) Synthetic traces used for analysis, (e) Log spectral ratio of Base/Top pre-injection, (f) Log spectral ratio of Base/Top post-injection, (g) Direct Log spectral ratio of base arrivals (Base(Q=50)/Base(Q=200)). Single vintage Q estimates are biased due to interference effects but the change in Q is recovered.

4.4 Dispersion

If attenuation changes occur then dispersion changes will also occur. Aki & Richards (2002) recommend that a good dispersion approximation for the majority of constant or nearly constant Q relationships is

$$c(f,Q) = \frac{v_{\mathrm{p}}(f)}{v_{\mathrm{p}}(f_{\mathrm{ref}})} = 1 + \frac{1}{\pi Q}\ln(\frac{f}{f_{\mathrm{ref}}}) \tag{4.4}$$

where $v_{\mathrm{p}}(f_{\mathrm{ref}})$ is the P-wave velocity at reference frequency f_{ref}, $v_{\mathrm{p}}(f)$ is the P-wave velocity at frequency f and Q is the quality factor related to the attenuation. There are two major effects that dispersion can have on the measurement of attenuation. Firstly, the travel-times are likely to change, causing certain frequencies travel for longer periods over the same distance, being attenuated more or less. Secondly, frequency dependent velocities then allow for the possibility of frequency dependent reflection coefficients. Figure 4.8 shows the behaviour of $\frac{v_{\mathrm{p}}(f)}{v_{\mathrm{p}}(f_{\mathrm{ref}})}$ as a function of frequency and $1/Q$, using a reference frequency of 1Hz. Although these changes appear to be fairly large (up to a 22% increase in velocity), when limited to surface seismic bandwidth (0-300Hz) and typical quality factors observed ($Q > 20$) the observed changes in velocity due to dispersion are limited to around 8%.

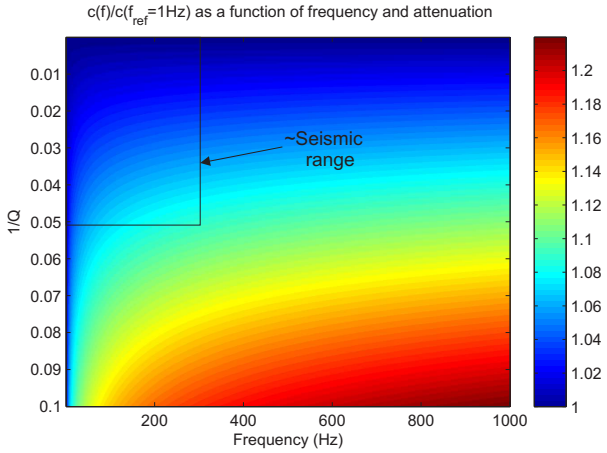

Figure 4.8: Ratio of $\frac{v_p(f)}{v_p(f_{\mathrm{ref}})}$ as a function of frequency and $1/Q$ for a reference frequency of 1Hz.

4.4.1 Frequency dependent travel time changes

I aim to quantify the error due to frequency dependent travel-time changes by looking at the spectral ratio slope produced by the direct comparison of arrivals from two vintages

of data that have passed through regions with two different Q values. We can see that the spectral ratio slope will therefore be

$$-\pi ft(\frac{1}{Q_2}-\frac{1}{Q_1}) \tag{4.5}$$

If frequency dependent velocities are introduced into this equation then the travel time will be frequency dependent and change between vintages of data

$$-\pi f(\frac{t_2(f)}{Q_2}-\frac{t_1(f)}{Q_1}) \tag{4.6}$$

By letting

$$\alpha_1(f) = t(f_{\text{ref}})/t_1(f) = v_1(f)/v(f_{\text{ref}})$$

and

$$\alpha_2(f) = t(f_{\text{ref}})/t_2(f) = v_2(f)/v(f_{\text{ref}})$$

it is possible to show that

$$-\pi f(\frac{t_2(f)}{Q_2}-\frac{t_1(f)}{Q_1}) = -\pi ft(f_{\text{ref}})(\frac{\alpha_2}{Q_2}-\frac{\alpha_1}{Q_1}) \tag{4.7}$$

By letting

$$t = t(f_{\text{ref}})$$

I compare the expected change in attenuation ($\frac{1}{Q_2}-\frac{1}{Q_1}$) with the attenuation that would be observed if frequency dependent velocity is present ($\frac{\alpha_2}{Q_2}-\frac{\alpha_1}{Q_1}$) and assuming $t = t(f_{\text{ref}})$ the error due to frequency dependent travel-times can be shown, independent of the absolute travel-time through the medium. True spectral ratio slopes (Equation 4.5) and the spectral ratio slope including the dispersion effects (Equations 4.7 and 4.4) are displayed in Figure 4.9 for a change in attenuation of $Q = 100$ to $Q = 10$ ($f_{\text{ref}} = 1$Hz).

By calculating the spectral ratio slopes for a combination of changes in attenuation it is therefore possible to calculate the error between the true spectral ratio slope (Equation 4.5) and the spectral ratio slope including dispersion effects (Equation 4.7). The measured change in attenuation is seen in Figure 4.10, comparing the true change, measured change with dispersion and the difference between the two. The error on the change in attenuation due to dispersion for any travel time, t, can be calculated by multiplying this error plot by the time travelled through the region of attenuation change.

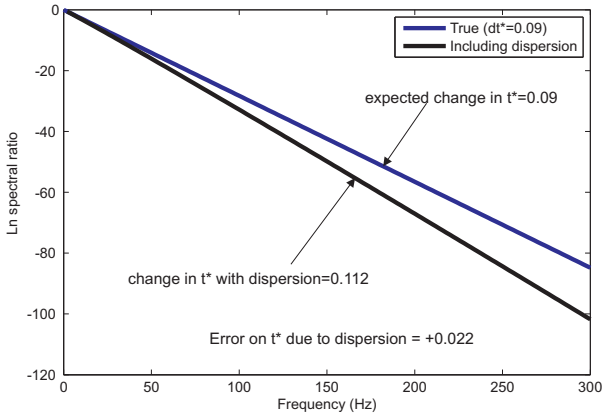

Figure 4.9: Example of the effect of dispersion on the log spectral ratios for a change in attenuation of Q_1=100 to Q_2=10 with a propogation time of 1s (Δt^* =0.09).

This error can also be shown as a percentage of the true change in attenuation (Figure 4.11). This plot provides a means to estimate the magnitude of the error on the $\Delta(1/Q)$ estimate for an input and output change in attenuation. It shows that the errors due to dispersion increase with increasing values of the absolute value of attenuation in each vintage. Large changes in attenuation at small Q^{-1} have a smaller percentage error than small changes in attenuation at larger values of Q^{-1}.

4.4.2 Frequency dependent reflection coefficients

The frequency dependence of velocity also produces frequency dependent reflectivity. I take a look at an example of the magnitude of reflectivity changes that one might expect for a typical AVO anomaly. Reflection coefficients can be derived from the full set of Zoeppritz equations (Aki & Richards, 2002; Zoeppritz, 1919), where the reflection coefficient is a function (Z) of the P-wave velocity (V_p), S-wave velocity (V_s), density (ρ) and incidence angle (θ) of two adjacent layers (1 (top) and 2 (bottom))

$$R(\theta) = Z(V_{\mathrm{p}1}, V_{\mathrm{p}2}, V_{\mathrm{s}1}, V_{\mathrm{s}2}, \rho_1, \rho_2, \theta) \tag{4.8}$$

I now attempt to determine what the effect of P-wave dispersion has upon the reflection coefficients. S-wave dispersion is ignored as it has been shown that it is likely to be a much smaller effect than P-wave dispersion (Chapman & Liu, 2006; Wilson et al., 2009). Using the dispersion equation defined above, Equation 4.8 can be written as a function of incidence angle, frequency (f) and Q

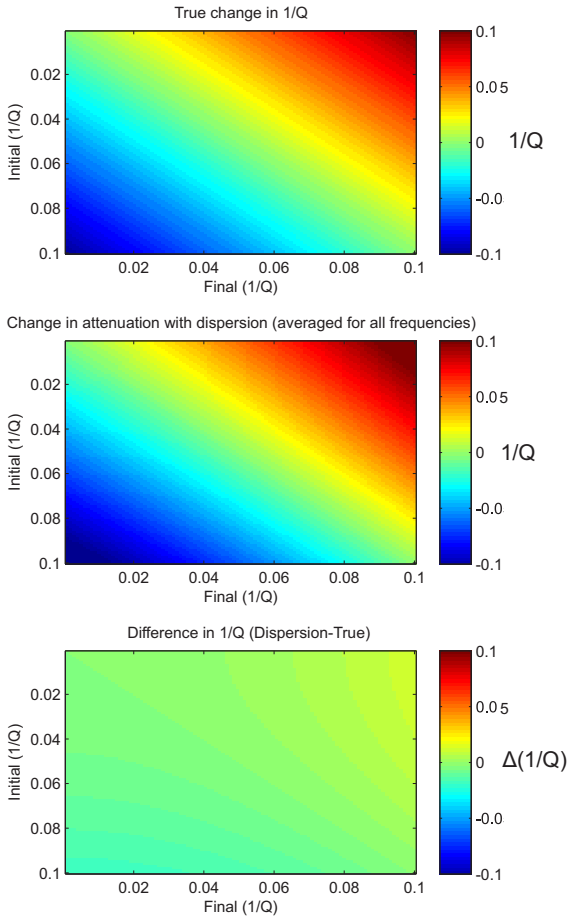

Figure 4.10: Figure showing the true change in attenuation (top), measured change after including dispersion (middle) and the difference between the two (bottom). It is difficult to see any major differences between the true change and the measured change.

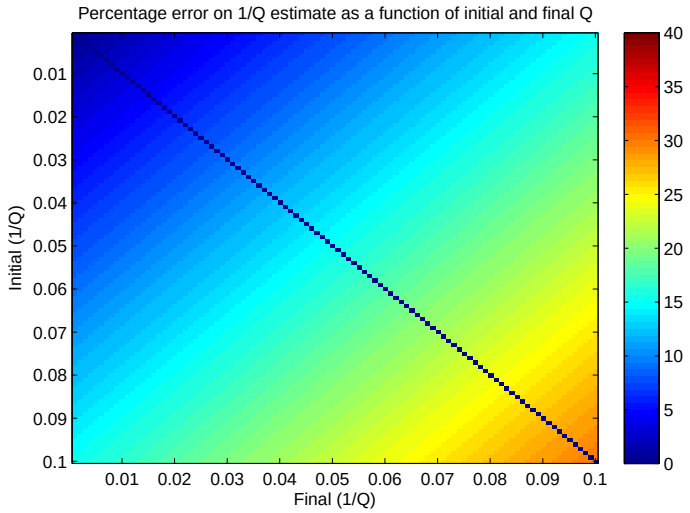

Figure 4.11: The difference shown in Figure 4.10 plotted on a different scale.

$$R(\theta) = Z(V_{\mathrm{p1}}(f, Q_1), V_{\mathrm{p2}}(f, Q_2), V_{\mathrm{s1}}, V_{\mathrm{s2}}, \rho_1, \rho_2, \theta) \tag{4.9}$$

where

$$V_{\mathrm{pn}}(f, Q_{\mathrm{n}}) = V_{\mathrm{pn}}(f_{\mathrm{ref}})c(f, Q_{\mathrm{n}}). \tag{4.10}$$

This now gives a relationship that can be used to calculate the effect that frequency dependent reflectivity can have on attenuation estimates. I will look at two AVO anomalies, one in which the reflectivity terms are of positive polarity up to 45 degrees and another where the AVO anomaly changes polarity at mid-angles. The model parameters used for the two examples are given in Table 4.2.

	Example 1	Example 2
V_{p1} [m/s]	3000	3000
V_{p2} [m/s]	3200	2950
V_{s1} [m/s]	2000	2000
V_{s2} [m/s]	2100	2100
ρ_1 [kg/m^3]	2000	2000
ρ_2 [kg/m^3]	2100	2100

Table 4.2: Parameters used in the two examples looking at the effect that frequency dependent reflectivity has on attenuation measurements.

In both examples, $Q = 100$ for the first vintage of data to replicate a fully water saturated sandstone. In the second vintage I have changed the Q in the bottom layer to 20, leaving the upper layer as $Q = 100$. The AVO curves at the reference frequency ($f_{\mathrm{ref}} = 1$Hz, no dispersion) for Example 1 and 2 are plotted in Figure 4.12.

Example 1 Figure 4.13 shows the reflection coefficients for both vintages of Example 1 for angles up to 45^o and frequencies up to 300Hz calculated using equations 4.4 and 4.9. There is a large contrast between the magnitude of the reflection coefficients between vintages. The contribution of reflectivity to the spectral ratio slopes has been shown to be

$$\ln(R_2/R_1) \tag{4.11}$$

where R_1 and R_2 are the absolute values of the reflection coefficients of the first and second vintages of data. Using Example 1, the log of the ratio of the absolute values of

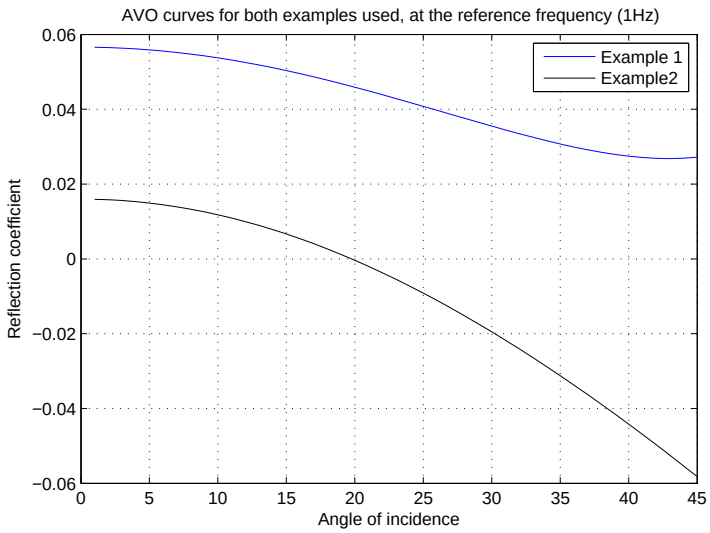

Figure 4.12: The AVO curves for the zero dispersion case (at the reference frequency=1Hz) for Example 1 (blue) and Example 2 (black). Example 2 is used as the reflection coefficients go from positive to negative at mid-angles.

the reflectivity is calculated (Figure 4.14). The ratios vary from 0 to 1.2, however, the error in t^* is proportional to the gradient of the spectral ratio as a function of frequency. The gradient with respect to frequency of Figure 4.14 is plotted in Figure 4.15. This indicates that the majority of the large spectral gradients occur at the lower frequencies whilst the majority of errors at frequencies above 25Hz are below 0.002 in magnitude.

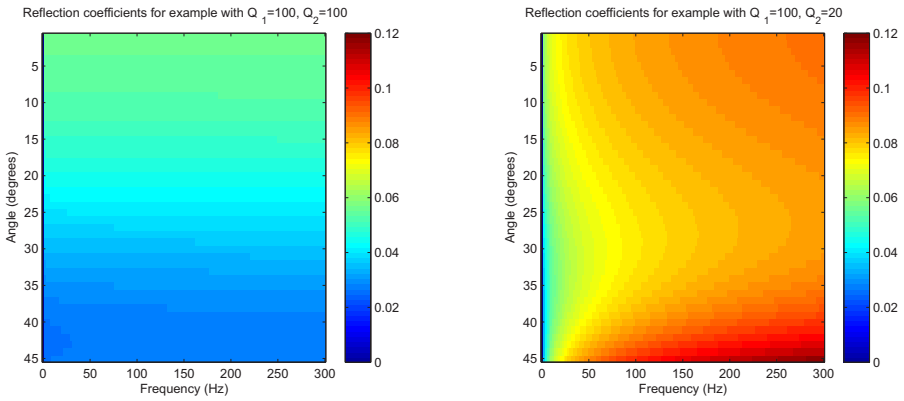

Figure 4.13: Example of the change in reflection coefficients by purely changing the attenuation in the bottom layer of a reflection.

Example 2 Example 2 was chosen as it provides an AVO curve that changes polarity at mid angles. The reflection coefficients for two vintages are seen in Figure 4.16. For the first vintage of data, the angle of zero crossing is not dependent on frequency, however in the second vintage of data it increases with increasing frequency. It is these differences in the zero crossing that are likely to produce large magnitudes from the ratios. The log ratio

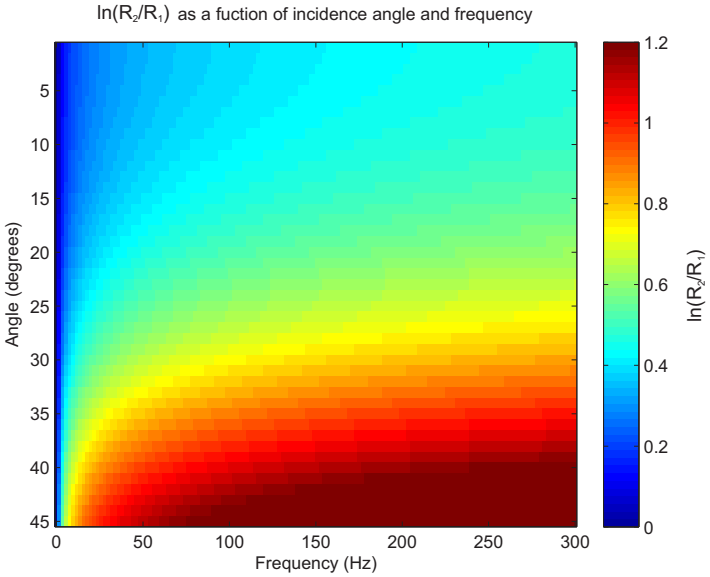

Figure 4.14: $\ln(R_2/R_1)$ for Example 1.

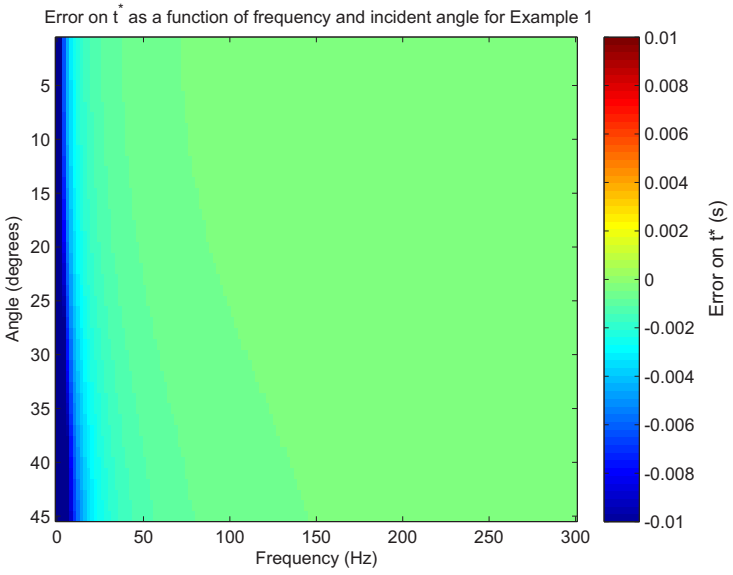

Figure 4.15: Error on t^* produced by frequency dependent reflectivity for AVO curve Example 1.

of the absolute values of the reflection coefficients are in the left hand plot of Figure 4.17, showing very large variation in the log ratio as a function angle and frequency. Again, as we are only interested in changes with frequency, the gradient is taken (Figure 4.17, right hand side) to produce the error in t^*. This is plotted on a different scale to Figure 4.15 because of the extreme values produced by the zero crossing of the AVO curve. The frequency dependence of the reflectivity has therefore produced large amplitude peaks and troughs in the spectral ratios. Effectively, the low dispersion zero crossing (Q=100) is responsible for the frequency independent noise spectral ratio notch, whilst the notch produced by the high dispersive case, is a frequency dependent effect.

These examples have shown that errors on spectral ratio slopes due to frequency dependent reflectivity may be large. The errors are larger around lower frequencies and enhanced where the AVO curves change polarity.

This implies that care must be taken when analysing horizons where one of the bounding layers may undergo changes in attenuation. In most scenarios this would imply that errors are more likely to occur when using a top reservoir reflection for analysis, where one would expect a change in attenuation to occur in the reservoir interval or above the reservoir.

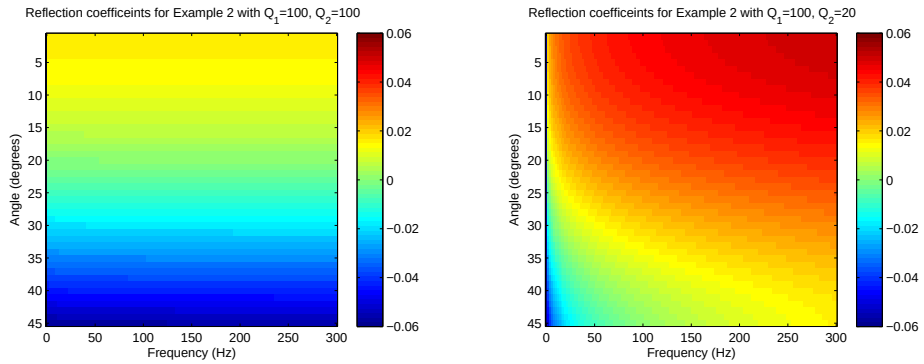

Figure 4.16: Reflection coefficients for the Q=100 and Q=20 models for Example 2.

The amount of bias produced by frequency dependent reflectivity is a function of the bandwidth of the spectral ratio regression. When the spectral ratio regression bandwidth used is at lower frequencies, it is likely that the bias due to the frequency dependent reflectivity will increase significantly. Analysis of well data may give a guideline of the magnitude of this error.

In both of the examples shown above, the frequency dependent reflectivity has generally caused a decrease in the low frequency energy relative to high frequency energy between vintages of data giving the appearance of a decrease in the attenuation between vintages

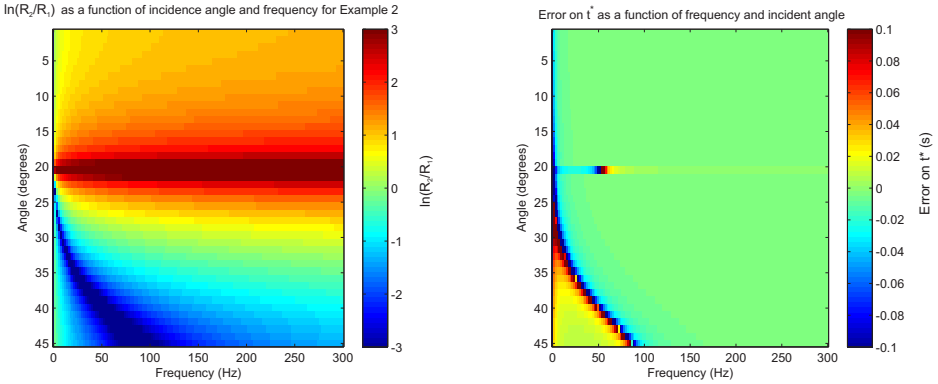

Figure 4.17: $\ln(R_2/R_1)$ (left) and error on t^* (right) for Example 2.

of data. If these examples were to be used by the direct methodology, an apparent increase in attenuation to the reflector would be observed. If the example reflections were used as the upper reflector to calculate an interval attenuation change, and apparent decrease in attenuation would be observed for that interval assuming no change in attenuation on either layer bounding the base reflector. However, this is not always the case as Figure 4.17 shows at large angles and low frequencies the opposite occurs due to the notch in the spectral ratio slopes.

The effect on the Centroid frequency may be inferred from these results. A decrease in the low frequency energy would produce a decrease in the the estimated change in attenuation between vintages of data.

4.5 4D Velocity changes

4.5.1 TWT changes

If each vintage of data is treated individually and processed via the Absolute methodologies described in the previous chapter, one would expect a velocity change to have no impact on our measurement of attenuation. However, if we generate our Q estimates via the Direct methodologies, it is assumed that there is no change in the travel-time for matching ray-paths between each vintage of data. Here I look at the sensitivity of the direct attenuation measurement to a change in TWT. The change in t^* between two vintages of data is given by:

$$\Delta(t^*) = \frac{t_2}{Q_2} - \frac{t_1}{Q_1} \tag{4.12}$$

If the data-sets are treated separately, both t_2/Q_2 and t_1/Q_1 are measured and t_1 and t_2 can be estimated independently (ignoring dispersion effects). The measured change in attenuation is then;

$$\frac{1}{Q_2} - \frac{1}{Q_1} \tag{4.13}$$

However, in the Direct methodologies, $\Delta(t^*)$ is measured directly and I assume that there is no change in travel time. If there is a change in travel time, this will lead to a bias in the attenuation measurement. By substituting $\alpha = t_2/t_1$ in to Equation 4.12 it can be shown that

$$\Delta(t^*) = t_1(\frac{\alpha}{Q_2} - \frac{1}{Q_1}) \tag{4.14}$$

therefore the measured change in attenuation for the direct methodologies is:

$$\frac{\alpha}{Q_2} - \frac{1}{Q_1} \tag{4.15}$$

If $t_1 = t_2$, $\alpha = 1$ and Equation 4.15 becomes Equation 4.13. The error in the direct measurement when there is a change in travel time ($\alpha \neq 1$) is given by the difference between Equations 4.15 and 4.13.

$$E_{twt} = \frac{\alpha - 1}{Q_2} \tag{4.16}$$

Assuming no change in the distance of the ray-path, $\alpha = t_2/t_1 = v_1/v_2$, and the error can be given as a function of the percentage change in velocity and the absolute value of attenuation of the second vintage of data.

$$E_{twt} = \frac{\%V_p}{100Q_2} \tag{4.17}$$

This equation is plotted in Figure 4.18 for positive increases in velocity.

4.5.2 Amplitude changes

Time-lapse amplitude changes should not affect measurements of attenuation made from the centroid frequency methodology or the spectral ratio methodology. However measurement via the instantaneous frequency may be vulnerable to changes in the frequency

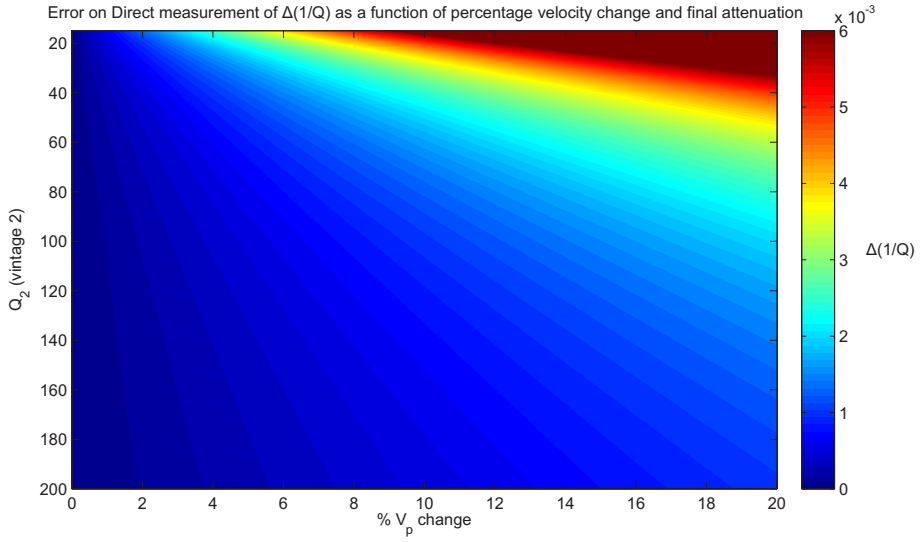

Figure 4.18: Error on the Direct measurement of $\Delta 1/Q$ as a function of the percentage velocity change and the final attenuation.

independent amplitude of a seismic wave. The damping value (ϵ^2) that is used as an addition to the analytic envelope (a) in the divisor in the equation

$$f(t) = (\frac{1}{2\pi})\frac{y(t)\frac{dy^*(t)}{dt} - y^*(t)\frac{dy(t)}{dt}}{a^2(t) + \epsilon^2} \tag{4.18}$$

will reduce the size of the instantaneous frequency. If the amplitudes are the same in each vintage of data the size of this damping parameter does not matter as it will have the same impact in both vintages. However, if amplitudes are reduced between vintages of data, ϵ^2 will have more of an impact on size of the instantaneous frequency recovered, reducing the magnitude of the instantaneous frequency calculated.

I test this sensitivity by calculating the change in t^* for a variety of damping parameters and amplitude changes. Amplitudes are changed by multiplying the second vintage of data by values between 0.8 and 1.2, representing change in reflector amplitude of $\pm 20\%$. Results can be sen in Figure 4.19 where an increase in amplitude between vintages results in the change in attenuation to be underestimated. Conversely, a decrease in amplitude between vintages causes an overestimate of attenuation changes. This highlights that the instantaneous frequency might be unstable and sensitive to changes in frequency independent amplitude unlike the other methodologies.

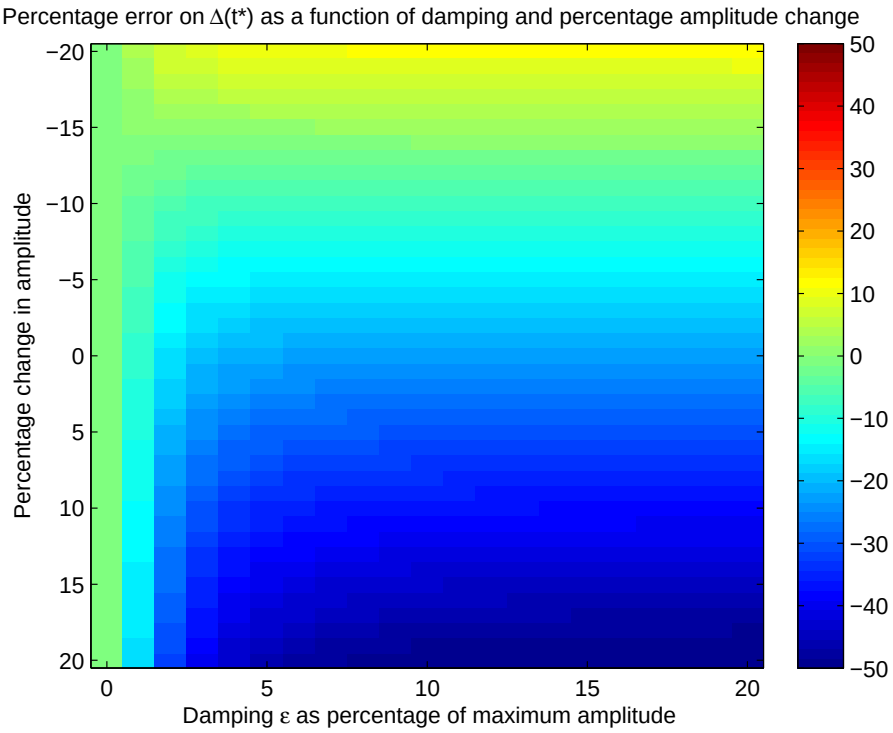

Figure 4.19: Percentage error on Q estimate due to the combined effect of damping and the change in amplitude.

4.6 Summary

In this chapter I have shown that changes in attenuation are sensitive to both coherent and incoherent noise. The effect of incoherent noise was investigated by adding band-pass filtered random noise to a synthetic prestack gather. The results of this analysis initially showed that the PSQI methodology is least sensitive to the amplitude of the noise added. However on close inspection of the Centroid frequency and instantaneous frequency methodologies improvements were made to the estimates by limiting the frequency range that the centroid frequencies are calculated from and using a damping value that is proportional to the noise level when calculating the instantaneous frequency. The results also suggested that the direct methodologies estimated the magnitude of attenuation more accurately than the absolute methodologies. This work showed that each of the methodologies should be parametrised carefully before analysis of any data-set is carried out.

I then showed a trade off between using a fixed window Fourier transform (where frequencies are well resolved) and a variable window transform (where time is well resolved). A fixed window allows for the best frequency resolution, resolving in particular the limits of

the usable bandwidth. However, fixed window transforms allow energy from other arrivals to have an impact on the spectral ratio slopes (poor time resolution). For the variable window transforms the opposite occurs, the frequency content of arrivals are better isolated in time, however, this occurs at the cost of frequency resolution. I have shown that this loss of frequency resolution can have a negative effect by leaking energy from a fixed bandwidth to outside the bandwidth, producing a damping of the attenuation estimate at higher frequencies (where more spectral leakage occurs).

The effect of multiples was investigated with quantitative analysis of the spectral ratio methodology. I investigated the impact on this using a synthetic example where a tuned reflector is present, causing a significant notch in the spectrum. Results from this example indicated that although the effect on single vintage measurement is large (causing a large apparent attenuation), these effects cancel between vintages of data allowing for a quantitative estimation of changes in attenuation.

When time-lapse changes in attenuation are present, one would also expect frequency dependent velocities to change (changes in dispersion). I have shown that dispersion can affect the estimate of attenuation via frequency dependent changes in amplitude and frequency dependent changes in the reflectivity. Frequency dependent travel-times were shown to have a minimal effect on the estimate of attenuation.

Where time-lapse changes in attenuation occur one would also expect time-lapse changes in velocity and amplitude to occur. In the direct methodologies a required assumption is that there is no change in travel-time so the sensitivity of this assumption was investigated and a plot yielding the expected errors as a function of velocity and the second vintage Q were given. When investigating the sensitivity of the instantaneous frequency matching methodology to changes in the size of the frequency independent amplitude I showed that the instantaneous frequency is sensitive to this particularly if large damping values are used when large amplitude changes occurring between vintages. The magnitude of this effect may be up to 50% for a 20% change in amplitude.

Chapter 5

Carbon Dioxide sequestration - VSP-Case Study

Geological sequestration of carbon dioxide is one of the proposed methods of storing carbon dioxide produced from hydrocarbon reservoirs and from the burning of fossil fuels from industrial plants. In the case of hydrocarbon reservoirs, the economic cost of CO_2 sequestration may be offset by the additional production of hydrocarbons (Lackner, 2003) through enhanced oil recovery. Where sequestration into hydrocarbon traps is not feasible, saline aquifers may also prove to be a useful trap for the sequestered CO_2. One example of CO_2 sequestration into a saline aquifer is in the Sleipner field (Arts et al., 2004), where over 4.26 million tonnes of CO_2 have been injected. In the case of Sleipner, a combination of time-lapse seismic, synthetic seismic modelling and reservoir flow simulation has been utilised to monitor the movement of injected CO_2 in the subsurface, which is essential in order to determine the extent of the fluid flow in the trap and to check the trap integrity. Any leaks to the surface would negate the costs involved in capturing and storing the CO_2. Where sequestration is made a legal requirement or involves a proposed CO_2 tax (such as Norway), verification of the amounts of CO_2 injected may also need be required, involving the need for more quantitative analysis of the seismic signals. Seismic observations of injected CO_2 have so far focused on both frequency independent amplitude changes and velocity changes (Arts et al., 2004; Daley et al., 2008; O'Brien et al., 2004; Torp & Gale, 2004). In this chapter I aim to look at the possibility of adding attenuation changes to this list of quantitative attributes.

The VSP data-set used here was acquired as part of The Frio Project - a pilot CO_2 sequestration experiment funded by U.S Department of Energy and the National Energy Technology Laboratory. The experiment was carried out by a consortium of research

institutions including the Bureau of Economic Geology, Lawrence Berkeley National Laboratory (LBNL), the US Geological Survey, Sandia Technologies (LLC) and Schlumberger. The Frio sand formation is located close to Houston (Texas) and several large CO_2 emitters (Figure 5.1). The aims of the project were to;

- Demonstrate that CO_2 can be injected into a saline aquifer without adverse health, safety, or environmental effects.
- Determine the subsurface distribution of injected CO_2.
- Demonstrate validity of conceptual models.
- Develop experience necessary for the success of large scale CO_2 injection.

Although not contributing directly to the aims above, I will use the VSP data to

- determine the feasibility of measuring attenuation changes in a small injection interval,
- assess the repeatability of attenuation measurements from VSP data-sets,
- compare the methodologies outlined in Chapter 3,
- identify the best methodology for estimating time-lapse attenuation,
- use changes in attenuation and velocity to infer changes in pressure and saturation.

5.1 Background

The Frio sand is a high porosity (ϕ=30-35%), high permeability (κ = 2Darcy) sandstone (Hovorka et al., 2006) and is around 22.8m thick, upward fining, with a typical dip of 16^o. It forms part of a set of uplifted beds with radially orientated faults caused by an underlying salt diapir. The injection interval is sealed by shales, sand and siltstone and temperature and pressure in the injection region are 55^oC and 15$\pm$0.3 MPa, respectively. 1600 tonnes of supercritical CO_2 were injected over a period of 10 days at depths between 1528.5 and 1534.7m with a density of 563kg/m^3 and P-wave velocity of 335m/s.

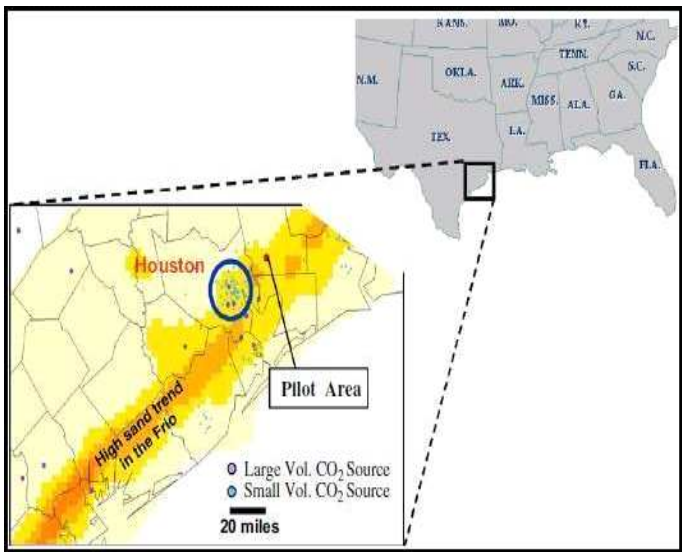

Figure 5.1: Map of region around Texas highlighting the extent of the Frio sand formation and its proximity to a number of high CO_2 producers.

5.1.1 Data Acquisition

Data were acquired at 8 source locations for both vintages of data (Figure 5.2). 3.5lbs explosive sources were used and were placed at 18m depth. Sensors used were 3 component geophones spaced 25ft (7.6m) apart. Four VSP shot locations (1-4, Figure 5.2) are primarily focused on monitoring the CO_2 injection as they have small offsets and four locations (5,6,8,9) focused on structural interpretation of the region, but all will be analysed in this chapter.

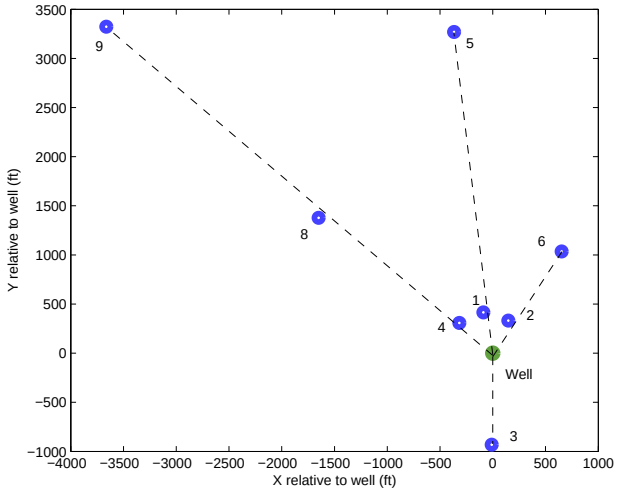

Figure 5.2: Shot locations relative to borehole location

Geophone strings of 40 receivers were used in acquisition, and moved up and down the

borehole to create a VSP. For some shots, multiple acquisitions were undertaken at the injection interval to gain better depth resolution (down to 4.8m). The receiver elevations can be seen plotted for each shot location for the pre- and post-injection surveys in Figures 5.3 and 5.4 respectively. Shot locations 1 and 3 have coverage from the shallow subsurface whilst other shot locations were only used to acquire data near the injection interval. The higher resolution data were also acquired for all shot locations in the injection interval. Figure 5.5 shows the vertical-component data recorded pre-injection at source location 1.

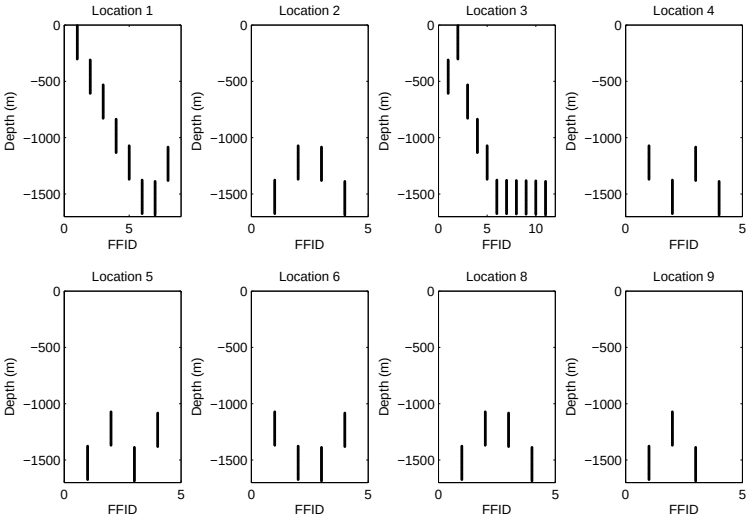

Figure 5.3: Receiver elevations for each shot and FFID (Field File identification number) for the pre-injection acquisition. Data are acquired with a fixed 7.6m geophone spacing. Multiple string elevations have been acquired in the injection region to increase resolution

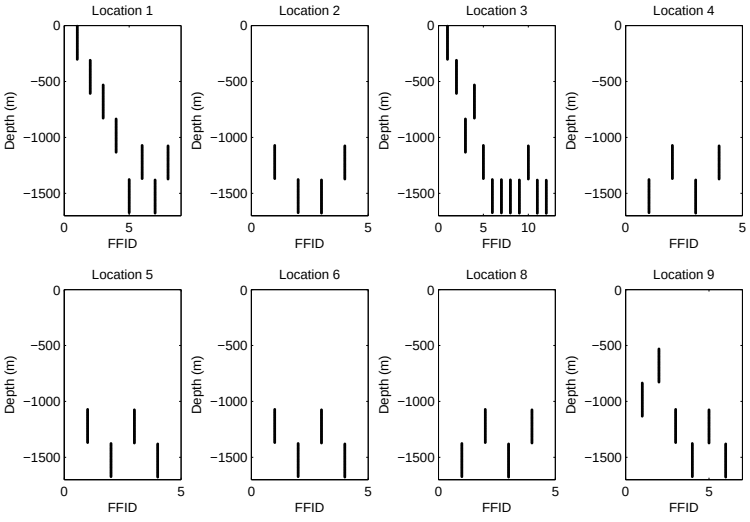

Figure 5.4: Receiver elevations for each shot and FFID (Field file identification number) for the post-injection acquisition. Data are acquired with a fixed 7.6m geophone spacing. Multiple string elevations have been acquired in the injection region to increase resolution

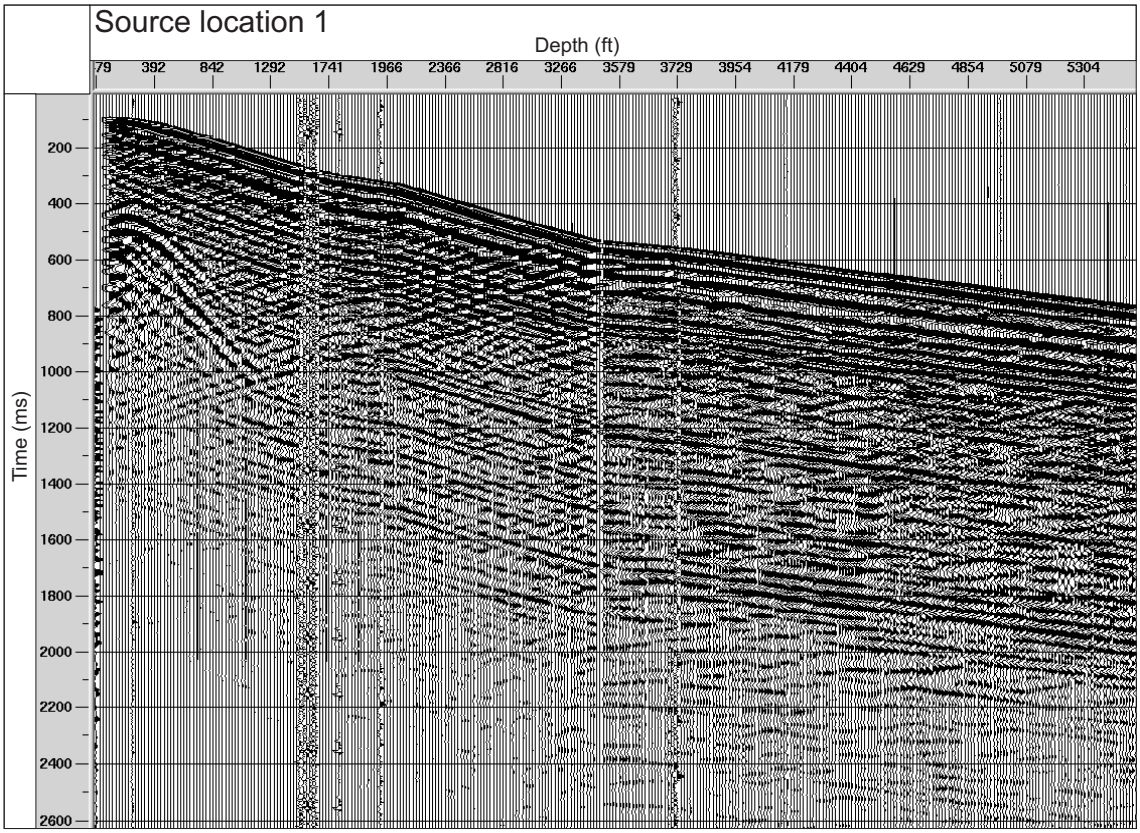

Figure 5.5: Vertical component recorded for all depths and FFIDs (Field file identification number) for the pre-injection data acquired from source location 1. Data is plotted in SEG normal polarity.

5.2 Synthetic test for feasibility

In order to test the feasibility of detecting changes in attenuation in a small injection interval, a synthetic VSP was created to try and resemble the real data-set. Firstly, the velocity model was calculated by picking the first arrival times of the VSP from source location 1 (Figure 5.2). Interval velocities are calculated via

$$V_{\mathrm{p}} = (\Delta Z/\Delta t)\cos(\theta) \tag{5.1}$$

where V_{p} is the P-wave velocity, ΔZ is the vertical distance between two receivers, Δt is the change in travel time between the two receivers, and θ is the angle subtended by the line from shotpoint to borehole and receiver to shotpoint (Stewart, 1984). The interval velocities are calculated between each adjacent pair of receivers and the velocity model for both the pre- and post-injection data-sets can be seen in Figure 5.6.

A blocky V_{p} model is then created from this by finding the larger changes in V_{p} from Figure 5.6. Using simple empirical relationships of Han & Nur (1986) and Gardner et al. (1974) a model for V_{s} (Equation 5.2) and ρ (Equation 6.1) can be calculated (Figure 5.7).

$$V_{\mathrm{s}}[\mathrm{km/s}] = 0.794V_{\mathrm{p}}[\mathrm{km/s}] - 0.787 \tag{5.2}$$

$$\rho[\mathrm{g/cc}] \approx 1.741V_{\mathrm{p}}^{0.25}[\mathrm{km/s}] \tag{5.3}$$

A minimum V_{s} of 0.4km/s was used in the model to avoid negative or zero V_{s} calculated from the empirical relationships. The model seen in Figure 5.7 represents the model used for the pre-injection case with a constant Q of 100 used as the background attenuation.

The post-injection model is the same as the pre-injection model apart the depth range 1533-1543m, similar in thickness and depth to the injection region in the real data-set. V_s and ρ remain constant between vintages of data, but P-wave velocity is changed from 2.6 km/s to 2.1 km/s. A 20% change in velocity was used in order to test methods against large changes in upgoing energy. A decrease in Q from 100 to 20 was used to represent an increase in attenuation in the interval due to the CO_2 injected. A more simplistic model would have been to include only a change in attenuation between vintages of data, however, the velocity changes observed by Daley et al. (2008) are very large and interference changes

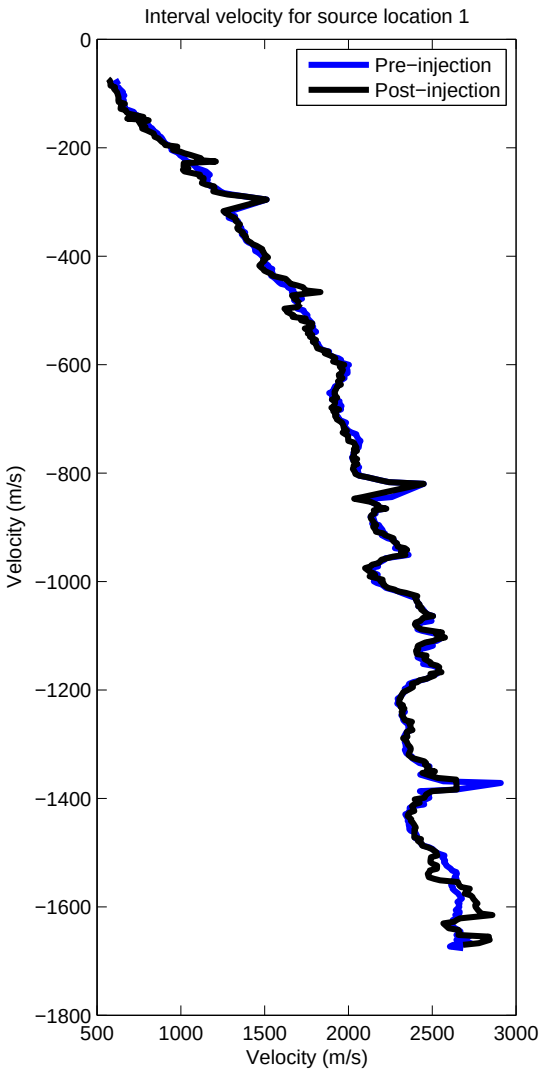

Figure 5.6: Interval velocity calculated as a function of depth using a straight line ray-path assumption for source location 1.

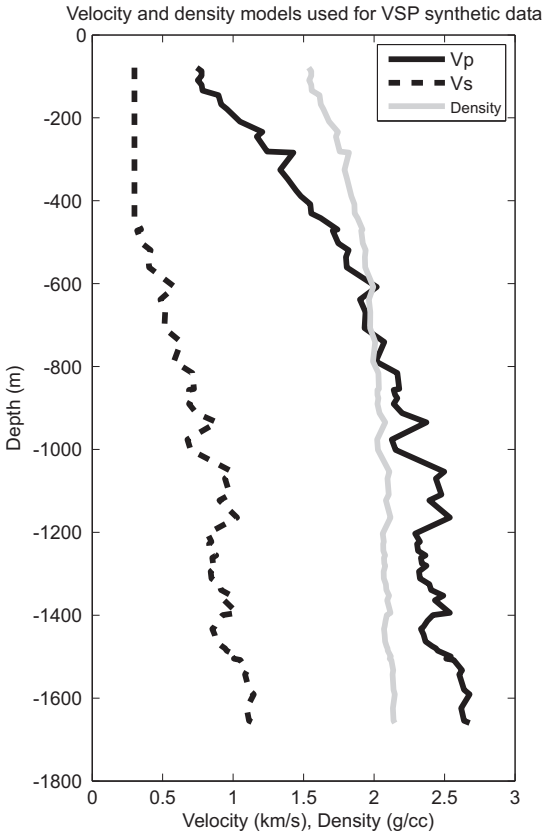

Figure 5.7: Model used to create synthetic data (82 layers). V_p is calculated from the travel time-information of the real data-set. Simple empirical relationships are used to complete the model, with a minimum V_s value.

caused by this change in reflectivity makes this synthetic example a more realistic test of the feasability for measuring intrinsic attenuation changes.

A source offset of 425m was used to match that of the acquisition of source location 1 from the real data-set and receivers were placed every 7.5m from 1200m to 1627.5m to match the geometry of the acquired data. Synthetic traces were created using a 1D reflectivity code (**skb**) at a sample rate of 0.5ms (again, the same as the real data-set) using a 200Hz Ricker wavelet. Surface multiples are not included but all interbed multiples are calculated.

With the synthetic data created, a simple comparison of the waveforms highlights the magnitude of the changes in the synthetic data. In Figure 5.8 the pre-injection and post injection data are plotted along with the difference (post-pre). The change in reflectivity can be seen mainly by the change in the up-going wave-field, and in particular, the strong reflection from the top of the injection interval. Including such drastic changes should also enable us to analyse the difficulties and benefits associated with separating the up-going and down-going wave-fields through the use of median filters. Other methodologies for testing wave-field separation are not considered here, but Reine (2009) recommended using median filters to avoid spectral leakage effects from $f - k$ domain operations.

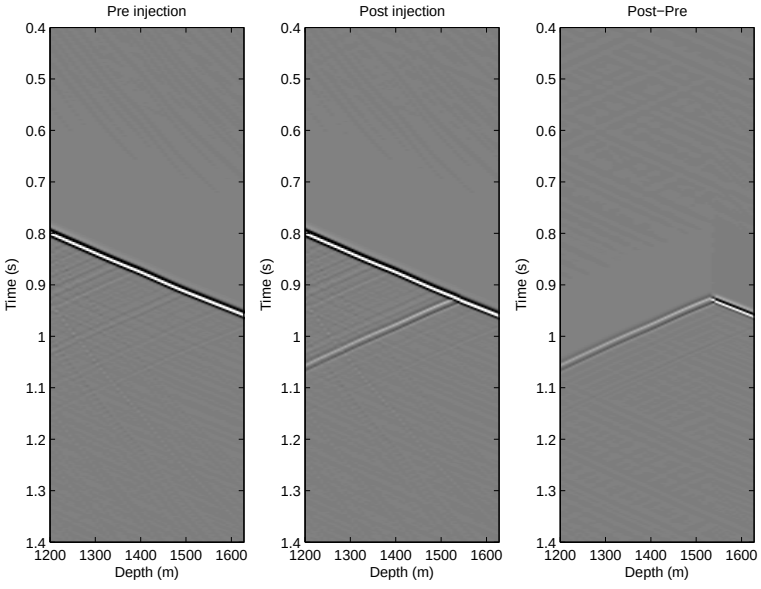

Figure 5.8: Synthetic data showing the pre-injection (left), post injection (centre) and subtraction of post minus pre-injection (right). All plotted on the same grayscale. Large changes are apparent in the up-going reflection from the reservoir and down-going reflection past the reservoir

5.2.1 Time picks

It is essential in all of the methodologies (and wave-field separation) to have available a user-defined time-pick of the first arrivals. Where this pick is located in the waveform may have an effect on the robustness of the Q estimates. For example, if a time-frequency transform is used to estimate the spectral content, results will be sensitive to the time at which the spectra are extracted. Similarly, if an attribute like instantaneous frequency is used then it may be more sensitive to noise later in the wavelet due to scattering and interference from short path multiples.

First breaks are difficult to pick from the synthetic data as a zero phase Ricker wavelet is being used. Instead, I will use a time-pick located at the peak envelope of the first arrival. The extraction of the first arrival could be achieved through the use of the synthetic model, however, the full work flow for real data will be used on the synthetic data-set too, in order to include picking errors in the analysis.

Once the maximum envelope has been picked for each trace, a window of data centred on this peak is taken and a cross-correlation performed. This not only gives a more robust estimate of the travel-time between receivers, but also ensures that we are analysing the same part of each wavelet on each trace.

5.2.2 Median filter

As seen in Figure 5.8, the up-going wave-field varies significantly between vintages of data and problems may arise by including this energy in the analysis of the down-going direct wave. It may therefore be beneficial to try and remove the up-going wave-field. To achieve this, the data are aligned on cross-correlation-corrected time picks. Once aligned, the trace to trace differences of the down-going wave-field are very small, whilst the up-going wave-field varies greatly. By applying an n-trace median filter, we can keep much of the down-going energy, whilst reducing the impact of the up-going energy. Median filters of 3, 5 and 10 traces are compared in Figure 5.9. Significant reduction in the up-going energy can be seen for all median filters, with greater reduction as the filter size increases. Median filtering may also have the effect of decreasing the sensitivity of the measurement itself with depth. For this reason, all three median filter lengths will be used to analyse the synthetic data as there may exist a trade off between the suppression of the up-going wave and the resolution of the attenuation measurement.

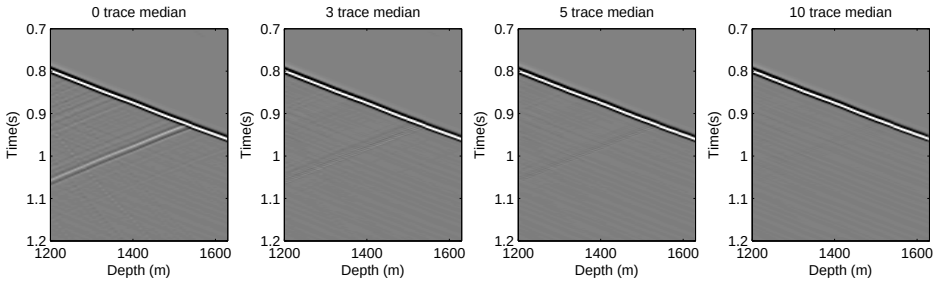

Figure 5.9: Comparison of median filters and ability to reduce up-going energy. (a) Raw data, (b) 3 trace median filtered down-going wave-field. (c) 5 trace median filter down-going wave-field. (d) 10 trace median filter down-going wave-field

As some of the methodologies are dependent upon the spectral content of the data, the effect of the median filters on the spectral content is shown in Figure 5.10 highlighting differences between the high frequency spectral content of the traces. The introduction of high frequency noise (above 200Hz) can be seen in all three median filtered data. On closer inspection of the down-going direct wave arrivals (Figure 5.11) the reduction in the coda energy can be seen clearly, however, there is no sign of increased high frequency noise. By zooming into the coda of the traces (Figure 5.12) the appearance of some small but sharp amplitude changes in the waveform become apparent. These effects may be responsible for the increased high frequency noise in the data. This behaviour along with the fact that resolution will be decreased means that wave-field separation may not increase our ability to detect attenuation changes. For this reason I will consider both median filtered and raw data when calculating attenuation.

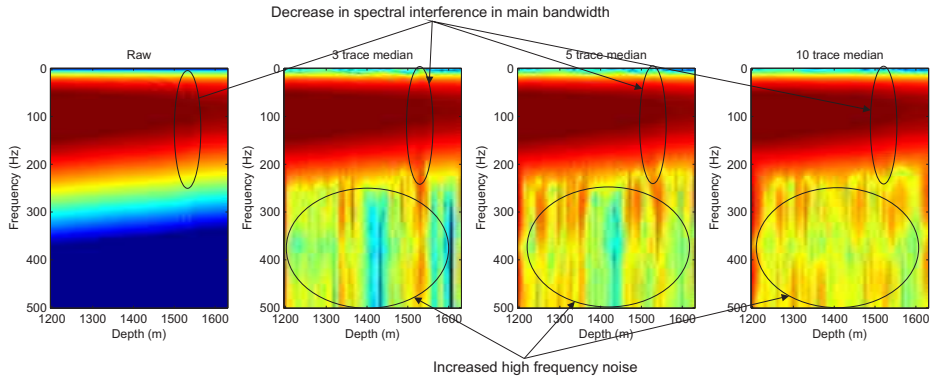

Figure 5.10: Normalised amplitude spectrum showing the effect of the median filter on the spectral content of the data from the post-injection case for the (a) raw data (b) 3 trace median filtered (c) 5 trace median filtered and (d) 10 trace median filtered. There is an increase in the noise at higher frequencies (>200Hz), however spectral noise in the main bandwidth of the data has been reduced, particularly around depths of 1500m.

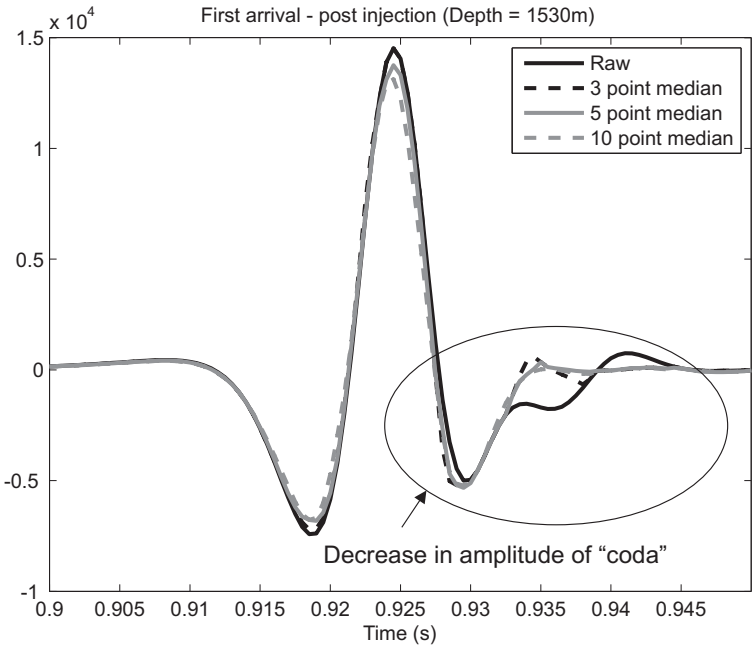

Figure 5.11: Comparison of a single trace (Depth =1530), with each median filter. Suppression of the larger amplitude contamination can be seen at around 0.93-0.94 seconds, however the increase in high frequency noise is not apparent.

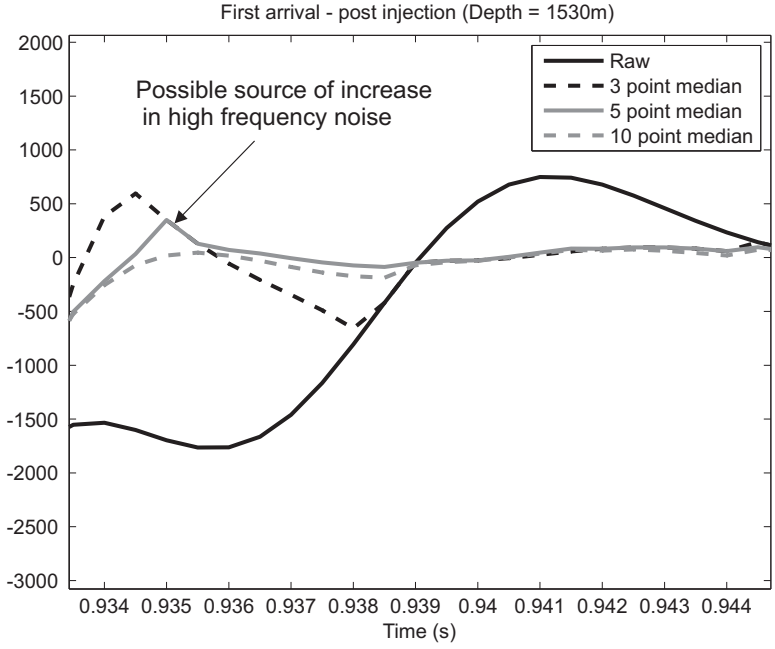

Figure 5.12: Zoom of Figure 5.11, highlighting the suppression of the larger amplitude, lower frequency energy, but the introduction of much more discontinuous features (around 0.935s). This more jagged wavelet causes the low amplitude, high frequency noise.

5.2.3 True change in attenuation

In each of the methodologies used, attenuation will be calculated between every possible pair of receivers (or depths) in each string to give a large suite of measurements, which are displayed in a way sometimes called a "tartan triangle". The true time-lapse change in attenuation between each of these receiver pairs can be calculated as we know the input change in velocity and change in $1/Q$. The expected change in $1/Q$ can be seen in Figure 5.13. This is what we aim to recover when measuring the change in attenuation between the pre- and post-injection synthetic data. Attenuation changes are calculated for all pairs of receivers as small separations provide good vertical resolution, whilst the larger receiver separations have been shown to contain less apparent attenuation and hence a more accurate measurement of Q (Adam et al., 2010). Adam et al. (2010) also showed that as the receiver separation decreases, the apparent attenuation increases linearly.

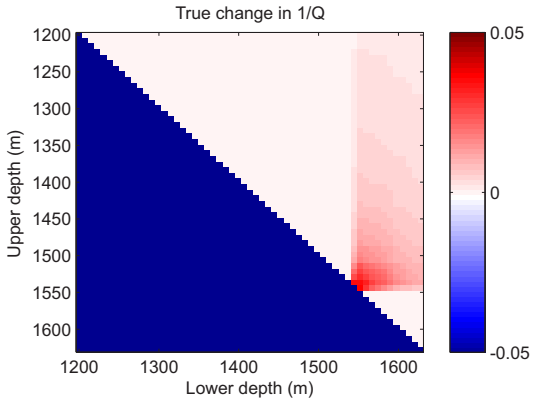

Figure 5.13: The true change in 1/Q for each receiver pair. A small change in attenuation is detectable for any pair of receivers, where one of those receivers either lies in or on the opposite side of the attenuation anomaly.

5.2.4 Inverting for a depth profile

Although we can calculate the change in attenuation between any combination of receivers to produce "tartan triangles" as seen above, a depth vs. $\Delta(t/Q)$ or depth vs. $\Delta(1/Q)$ is actually the desired output. The measured t^* between two receivers at depths d_i and d_j is the summed combination of the t^* values for all the receiver intervals between depths i and j. For the first vintage of data this can be described as

$$t^*_{d_\mathrm{i},d_\mathrm{j}} = \frac{t_{d_\mathrm{i},d_\mathrm{j}}}{Q_{d_\mathrm{i},d_\mathrm{j}}} = \sum_{\mathrm{n=i}}^{\mathrm{j-1}} \frac{t_{d_\mathrm{n},d_{\mathrm{n}+1}}}{Q_{d_\mathrm{n},d_{\mathrm{n}+1}}} \tag{5.4}$$

For the second vintage of data, assuming that acquisition was acquired at the same receiver depths, t^* (denoted by $'$ to represent the second vintage) is described by

$$t'^*_{d_\mathrm{i},d_\mathrm{j}} = \frac{t'_{d_\mathrm{i},d_\mathrm{j}}}{Q'_{d_\mathrm{i},d_\mathrm{j}}} = \sum_{\mathrm{n=i}}^{\mathrm{j-1}} \frac{t'_{d_\mathrm{n},d_\mathrm{n+1}}}{Q'_{d_\mathrm{n},d_\mathrm{n+1}}}. \tag{5.5}$$

Therefore the difference, or change in t^* between two geophones can be described by

$$\Delta t^*_{d_\mathrm{i},d_\mathrm{j}} = t'^*_{d_\mathrm{i},d_\mathrm{j}} - t^*_{d_\mathrm{i},d_\mathrm{j}} = \sum_{\mathrm{n=i}}^{\mathrm{j-1}} \frac{t'_{d_\mathrm{n},d_\mathrm{n+1}}}{Q'_{d_\mathrm{n},d_\mathrm{n+1}}} - \frac{t_{d_\mathrm{n},d_\mathrm{n+1}}}{Q_{d_\mathrm{n},d_\mathrm{n+1}}} = \sum_{\mathrm{n=i}}^{\mathrm{j-1}} \Delta t^*_{d_\mathrm{n},d_\mathrm{n+1}}. \tag{5.6}$$

A schematic of these t^* measurements can be seen in Figure 5.14. By considering all of the possible measurement pairs in the tartan triangles, a system of equations can be set up to solve for the changes between each geophone interval. Equation 5.7 shows the system of equations, displayed in matrix form.

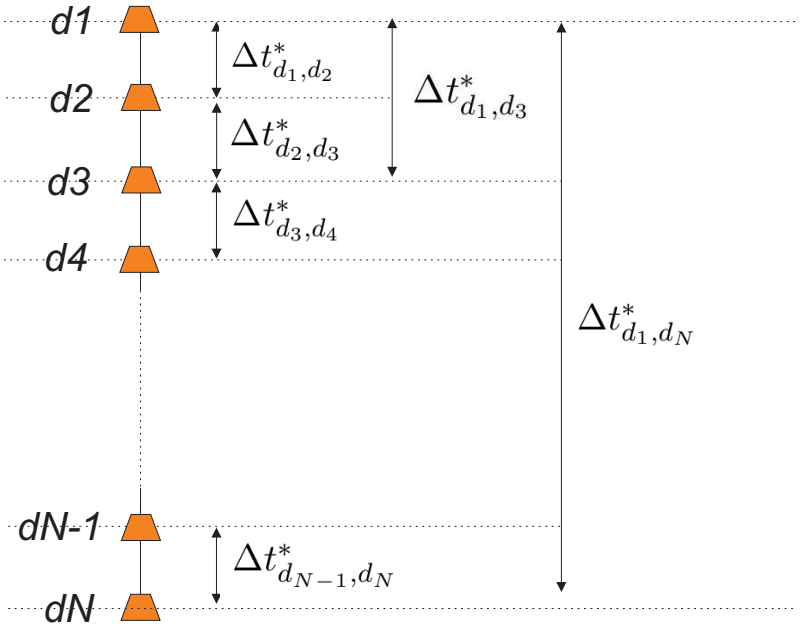

Figure 5.14: Sketch of a VSP with N receivers, showing some of the change in t* that are both used and solved for in the inversion for a single depth profile.

$$\begin{pmatrix} \Delta t^*_{d_1,d_2} \\ \Delta t^*_{d_1,d_3} \\ \vdots \\ \Delta t^*_{d_1,d_N} \\ \Delta t^*_{d_2,d_3} \\ \vdots \\ \Delta t^*_{d_2,d_N} \\ \vdots \\ \Delta t^*_{d_{N-1},d_N} \end{pmatrix} = \begin{pmatrix} 1 & 0 & 0 & \cdots & 0 & 0 \\ 1 & 1 & 0 & \cdots & 0 & 0 \\ \vdots & \vdots & \vdots & \ddots & \vdots & \vdots \\ 1 & 1 & 1 & \cdots & 1 & 1 \\ 0 & 1 & 0 & \cdots & 0 & 0 \\ \vdots & \vdots & \vdots & \ddots & \vdots & \vdots \\ 0 & 1 & 1 & \cdots & 1 & 1 \\ \vdots & \vdots & \vdots & \ddots & \vdots & \vdots \\ 0 & 0 & 0 & \cdots & 0 & 1 \end{pmatrix} \begin{pmatrix} \Delta t^*_{d_1,d_2} \\ \Delta t^*_{d_2,d_3} \\ \Delta t^*_{d_3,d_4} \\ \vdots \\ \Delta t^*_{d_{N-2},d_{N-1}} \\ \Delta t^*_{d_{N-1},d_N} \end{pmatrix} \tag{5.7}$$

The matrices above can also be described in vector notation as

$$\mathbf{d} = \mathbf{A}\mathbf{m} \tag{5.8}$$

where $\mathbf{d}$ contains all the observed changes in t^* for each combination of receivers, $\mathbf{m}$ contains the desired change in t^* between each pair of receivers and $\mathbf{A}$ is the condition matrix that relates the observed t^* values to the desired model $\mathbf{m}$. This can then be solved using a least squares regression to find the model parameters.

5.2.5 Spectral ratios

The spectral ratios can be used to calculate attenuation in two ways. Firstly, a simple trace by trace spectral ratio can be calculated for all combinations of depths, which I will call the "trace-by-trace" spectral ratio method. It is also possible to simultaneously invert all the spectral ratios for a given set of receivers (analogous to the PSQI methodology), which I will call the multiple trace analysis. From Figure 5.10 it is clear that a safe bandwidth to use, avoiding the effects of the increased noise due to the median filters would be 30 to 140Hz.

Measurements of the change in $1/Q$ are calculated for each of the median filtered data-sets and the raw data. Figures 5.15 and 5.16 show the results for the trace by trace and multitrace methodologies respectively. Each of the subplots in these Figures can be compared to the true change in attenuation seen in Figure 5.13. In Figure 5.15 the increased length of the median filter has a positive effect on recovering the true change in attenuation, however, there is introduction of noise at small spacings and large depths. The improvement in the multitrace method (Figure 5.16) is much clearer as large magnitude noise is decreased and the true increase in attenuation becomes more apparent.

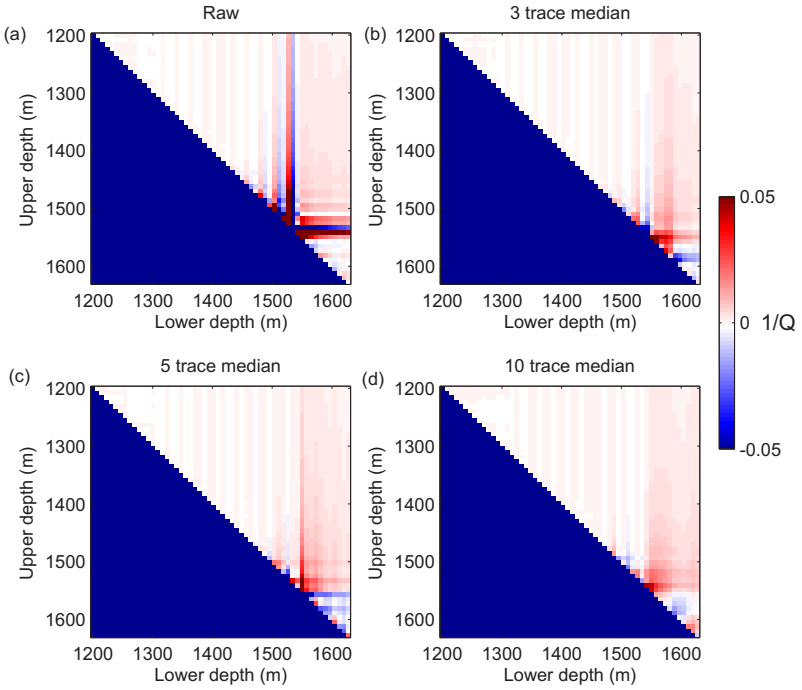

Figure 5.15: Simple trace to trace spectral ratio method was used to calculate the change in attenuation from the (a) raw (b) 3 point median filtered, (c) 5 point median filtered and (d) 10 point median filtered data.

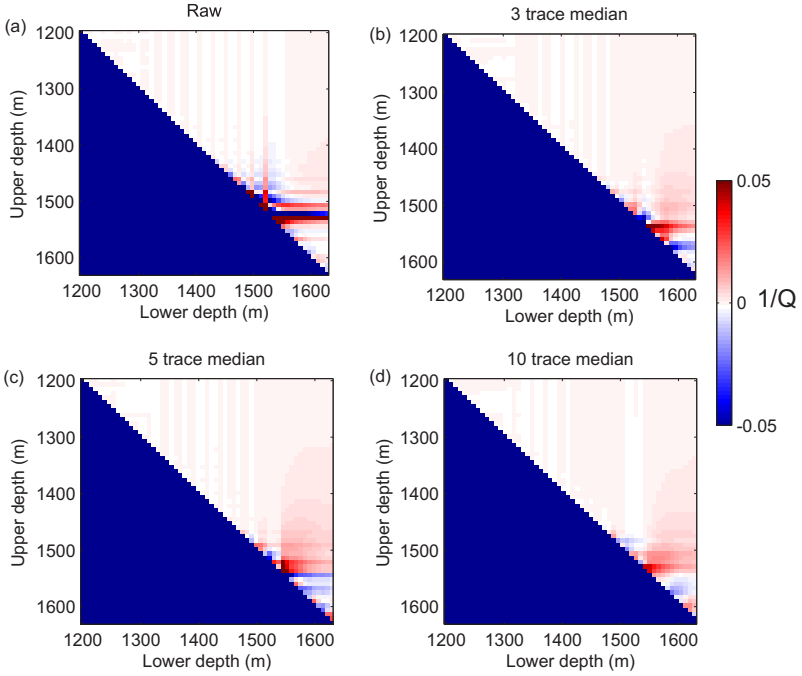

Figure 5.16: Multiple trace spectral ratio method was used to calculate the change in attenuation from the (a) raw (b) 3 point median filtered, (c) 5 point median filtered and (d) 10 point median filtered data.

5.2.6 Instantaneous frequency

Instantaneous frequency was used to calculate the trace-by-trace change in attenuation. The instantaneous frequency should be damped to reduce noise but as this is a data-set noise-free a damping of 2 was chosen (less than 1% of the amplitude of direct arrival). The instantaneous frequency should also be weighted and this was chosen to be 5 samples. The regression length was chosen to be 10 samples long, centred on the maximum envelope of the first arrival. Figure 5.17 shows the change in $1/Q$ for the raw and median filtered data. Here we see that the estimates from the raw data are very good, apart from an observed decrease in attenuation just above the injection interval. As the size of the median filter increases we see that this decrease in $1/Q$ is no longer present. However, we also see that decreases in attenuation have appeared at depths below the reservoir interval for small measurement spacings. Also visible is the decrease in sharpness of the results at small spacings, leading to the reduction of the resolution of measuring attenuation changes.

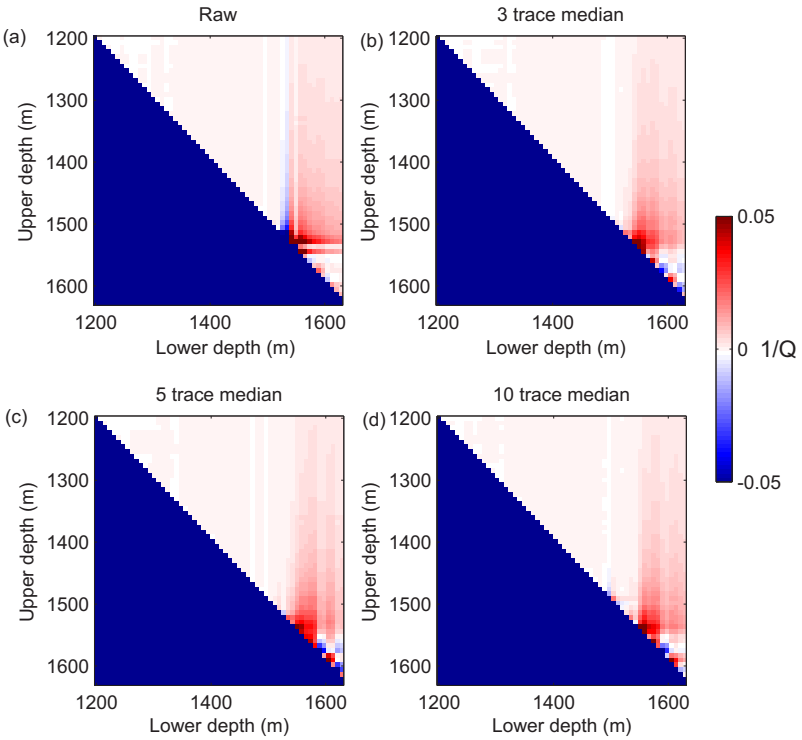

Figure 5.17: Trace by trace instantaneous frequency matching was used to calculate the change in attenuation from the (a) raw (b) 3 point median filtered, (c) 5 point median filtered and (d) 10 point median filtered data.

In comparison with the spectral ratio methodology, the raw data provides a good estimate of the change in attenuation, with arguably a decrease in the quality of the measurement with increasing median filter sizes. This may be because we are utilising an instantaneous

attribute and is therefore not affected as much by the up-going energy as it does not require a window of data to compute the spectral content.

5.2.7 Centroid frequency

The centroid frequency can be performed without the need to specify a bandwidth of choice, however when the results were first calculated using all frequency information up to the Nyquist frequency, the changes in attenuation appeared to be very noisy (Figure 5.18). As we have seen in Figures 5.10 to 5.12, there has been an increase in high frequency noise due to the median filters. This can be avoided by calculating the centroid frequency for a fixed bandwidth of interest (60-140Hz). Attenuation changes calculated using this fixed bandwidth can be seen in Figure 5.19. Figures 5.18 and 5.19 show that for the noise-free synthetic data, the best attenuation estimates are either made by using the raw data with a full bandwidth, or the median filtered data with a limited bandwidth.

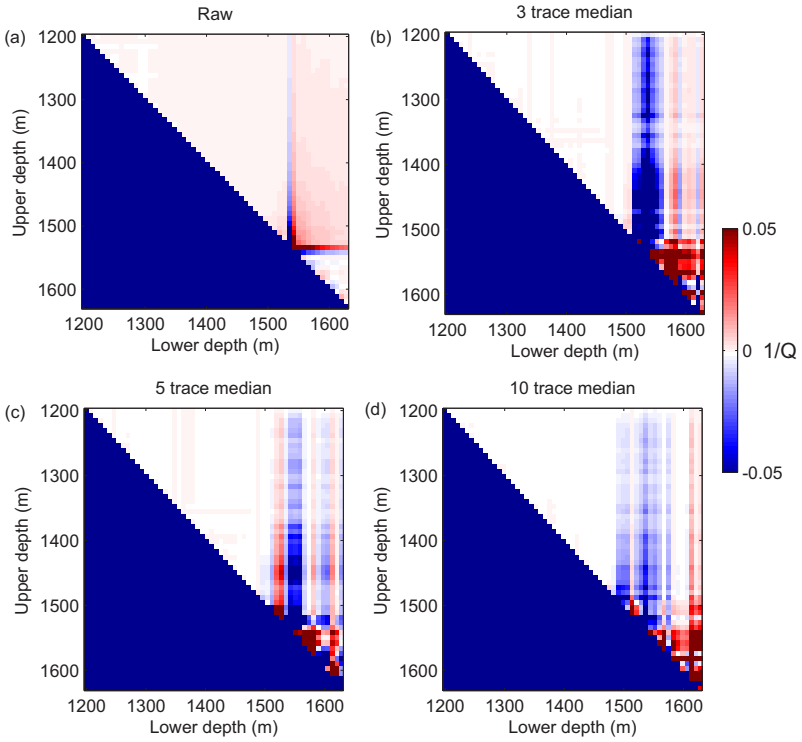

Figure 5.18: Trace by trace centroid frequency was used to calculate the change in attenuation from the (a) raw (b) 3 point median filtered, (c) 5 point median filtered and (d) 10 point median filtered data.

5.2.8 Comparison of methodologies

All of the methodologies appear to be able to resolve the changes in attenuation correctly from looking at the tartan triangles. I now go on to compare the results after inversion of

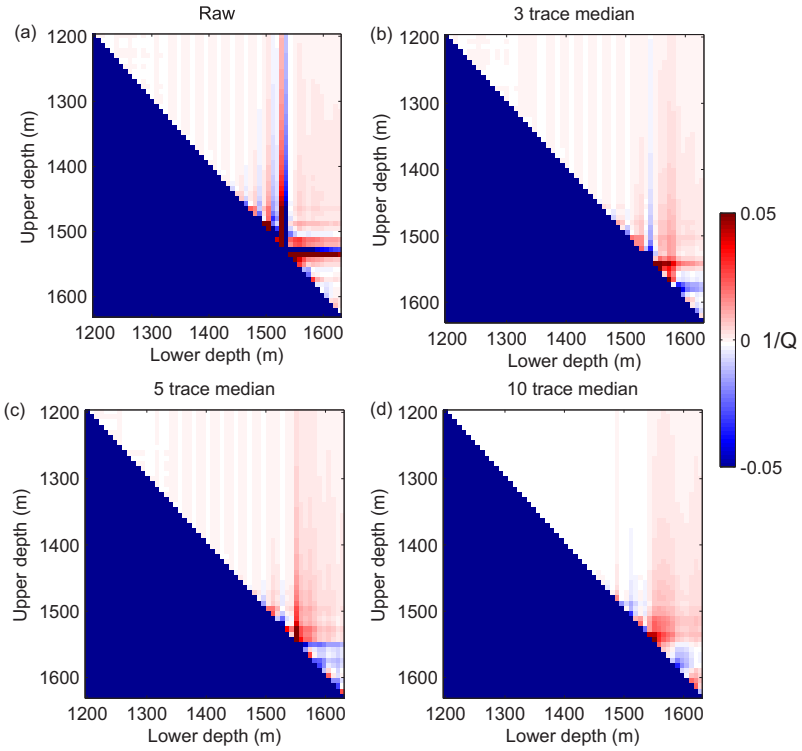

Figure 5.19: Trace by trace centroid frequency of a fixed bandwidth (60-140Hz) was used to calculate the change in attenuation from the (a) raw (b) 3 point median filtered, (c) 5 point median filtered and (d) 10 point median filtered data.

the tartan triangles for a depth vs. Δt^* profile. Damping tests were carried out to find an appropriate damping value to use. In general a damping value of $10^{1.6}$ was seen to have the best trade-off between minimising the data misfit but retaining a simple model. The resulting depth models are shown for the raw and 5 point median filtered data in Figures 5.20 and 5.21 respectively. It can be seen that none of the methodologies determines the correct magnitude of Δt^*, however, most predict the correct polarity of attenuation change in the region of interest. The median filtered data produce better results in all methodologies apart from the instantaneous frequency matching. The difference between the true and measured change in t^* can be seen for all methodologies, filter lengths and damping in Figure 5.22. It can be seen that there is a minimum in the misfit between damping values of 10^0 and 10^3 indicating the benefits from the correct choice of damping parameter. The lowest misfits for each of the methodologies have been gained via analysis of the median filtered data. For the trace by trace spectra ratio methodology, the 3 trace median filter performed best, for the instantaneous frequency matching methodology the 10 trace median filter performed the best and for the centroid frequency methodology the 3 trace median filter performed the best. It is clear that the errors on the models are never small with the error squared always being greater than 50% of the model squared

($1.1\text{x}10^{-7}$). I now go on to look at combining the estimates from each of the methodologies, in order to increase the detectability.

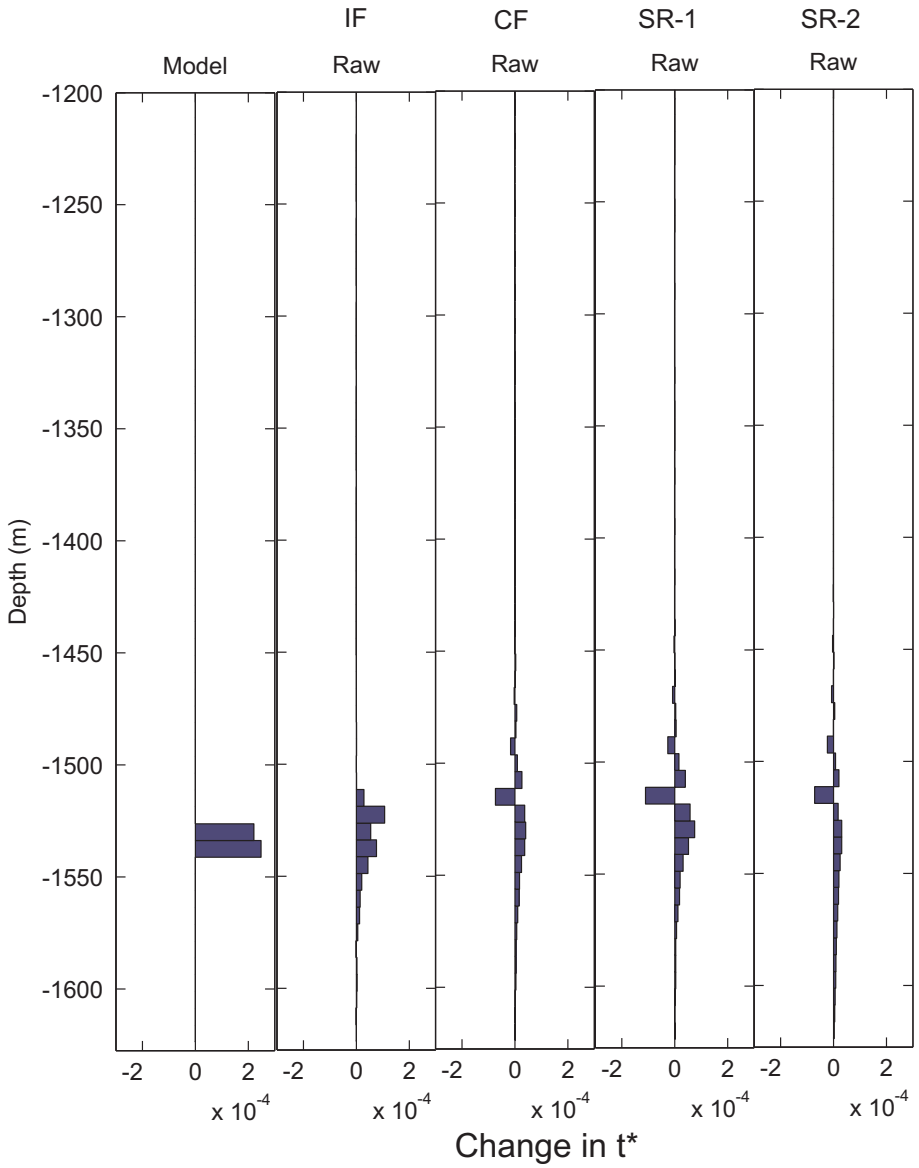

Figure 5.20: Models of Δt^* vs. depth for the raw data using each of the methodologies (IF=Instantaneous frequency, CF=Centroid frequency, SR-1=Trace by trace spectral ratio, SR-2=Multiple trace spectral ratio.

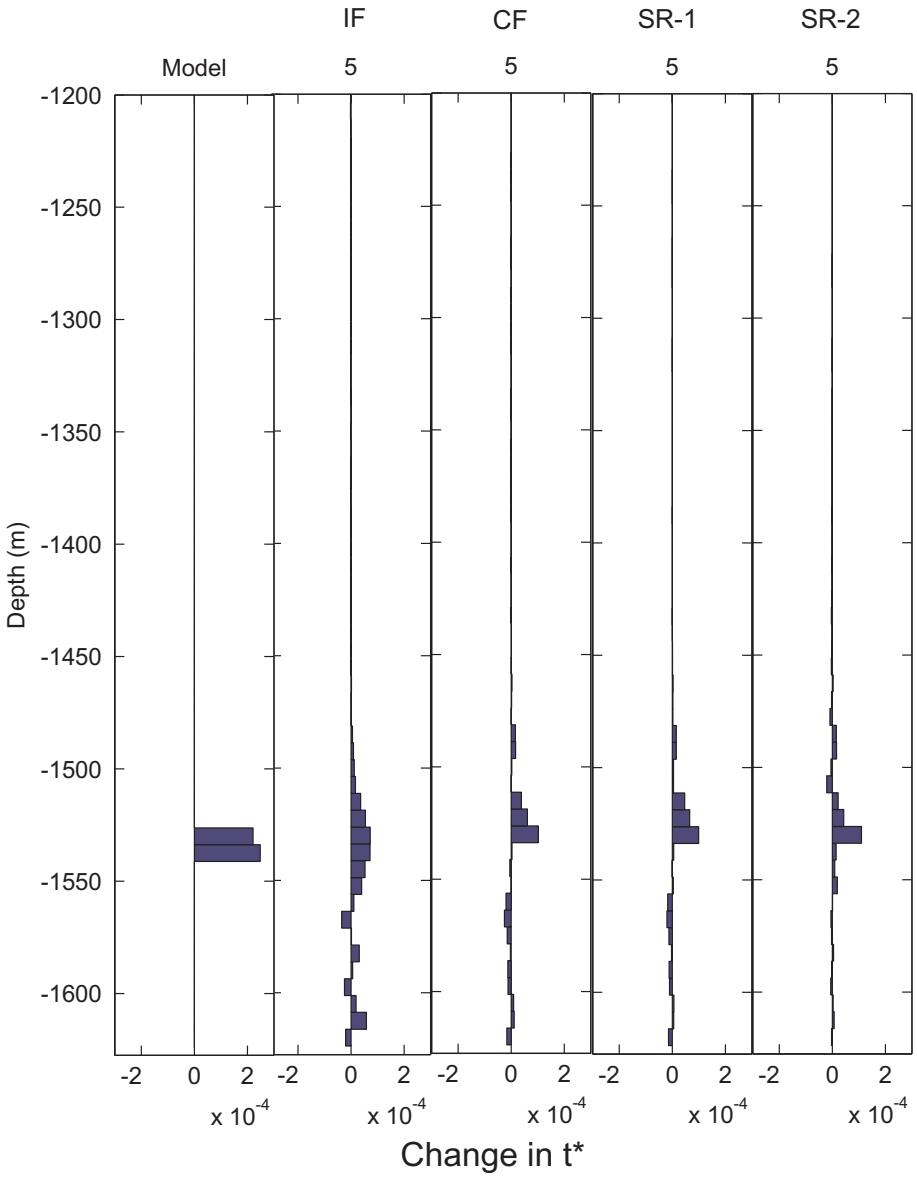

Figure 5.21: Models of Δt^* vs. Depth for the 5 point median filtered data using each of the methodologies (IF=Instantaneous frequency, CF=Centroid frequency, SR-1=Trace by trace spectral ratio, SR-2=Multiple trace spectral ratio.

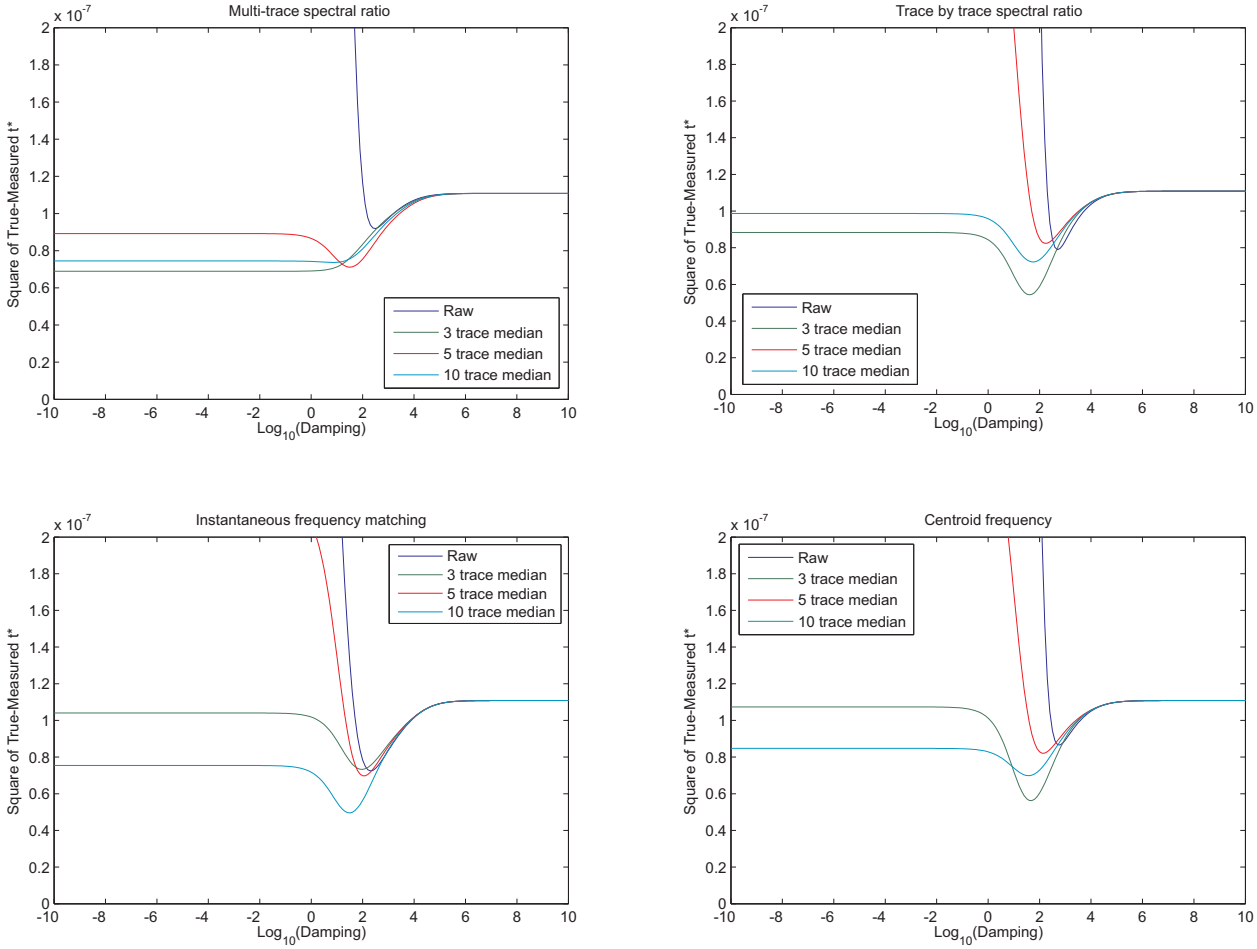

Figure 5.22: The error in the final model solution plotted against the damping value for each of the methodologies and median filter lengths.

5.2.9 Conclusions from synthetic study

- Instantaneous frequency has the best performance on noise free synthetic data with no median filtering.
- High frequency noise is introduced due to the use of a median filter for wave-field separation.
- The true magnitude of the signal is difficult to get back from the damped inversion scheme with such a small interval change in Q.
- Attenuation changes for such a small interval are detectable, however, quantitative interpretation may be difficult.

5.3 Real Data

The real data differ from the synthetic as the wavelet is different; the synthetic model was calculated using a zero phase Ricker wavelet (for numerical convenience) whilst the real data contains a minimum phase wavelet created from an explosive source. The differences in the wavelet means that we have different analysis points within the wavelet to perform the Q calculations. The source used was buried at depth and therefore a notch in the frequency spectrum can be observed due to the interference of the direct arrival and surface ghost.

Figure 5.23 shows an example of the direct waveform from the real data-set along with the picks made for that trace. For each trace, a time pick was made on the first break in energy (fb), the first peak in the wavelet (fp) and the first maximum of the trace envelope (fmax). Choice of time-pick is likely to be an important parameter when extracting frequency content from a time-frequency transform for the spectral ratio and centroid frequency methodologies, or choosing what part of the wavelet to perform the instantaneous frequency matching methodology.

As mentioned previously, the VSP data-set is made up of 8 different shot locations. To parametrise and test each of the methodologies I have chosen to use a single shot location. Shot location 1 was chosen for this purpose as it has full coverage from surface and is also one of the nearest (and most vertical) to the borehole where the receivers are located.

Results are calculated using the raw and the 5 point median filtered data-sets and I only show results from the 3 and 10 point median filtered data when more comparisons are

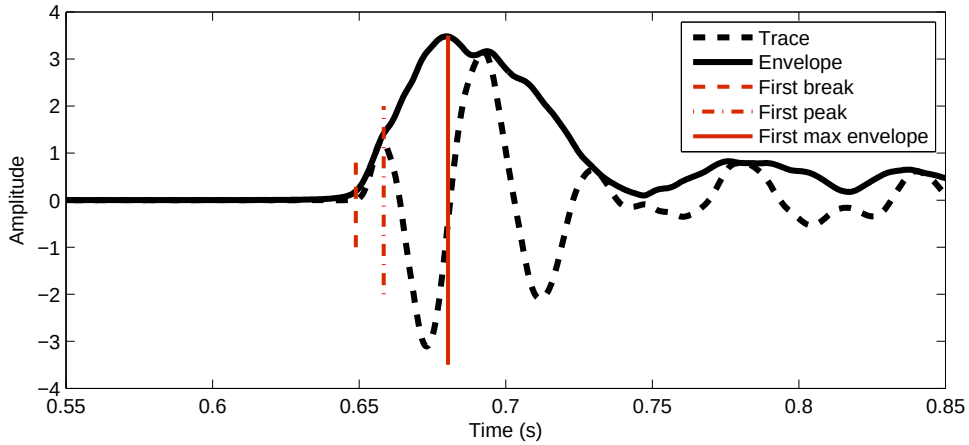

Figure 5.23: Example of a trace from the Frio VSP data-set (black dash) and the envelope of the signal (black solid), showing the three reference picks made on every trace. First break picks (fb, red dash), first peak pick (fp, red dot-dash) and first envelope maximum (fmax, red solid) were chosen as robust reference points within the wavelet.

needed. Figure 5.24 presents the raw, 3 point, 5 point and 10 point median filtered data, and highlights the residual up-going energy in the 3 point median filter, with little difference between the 5 and 10 point median filtered data.

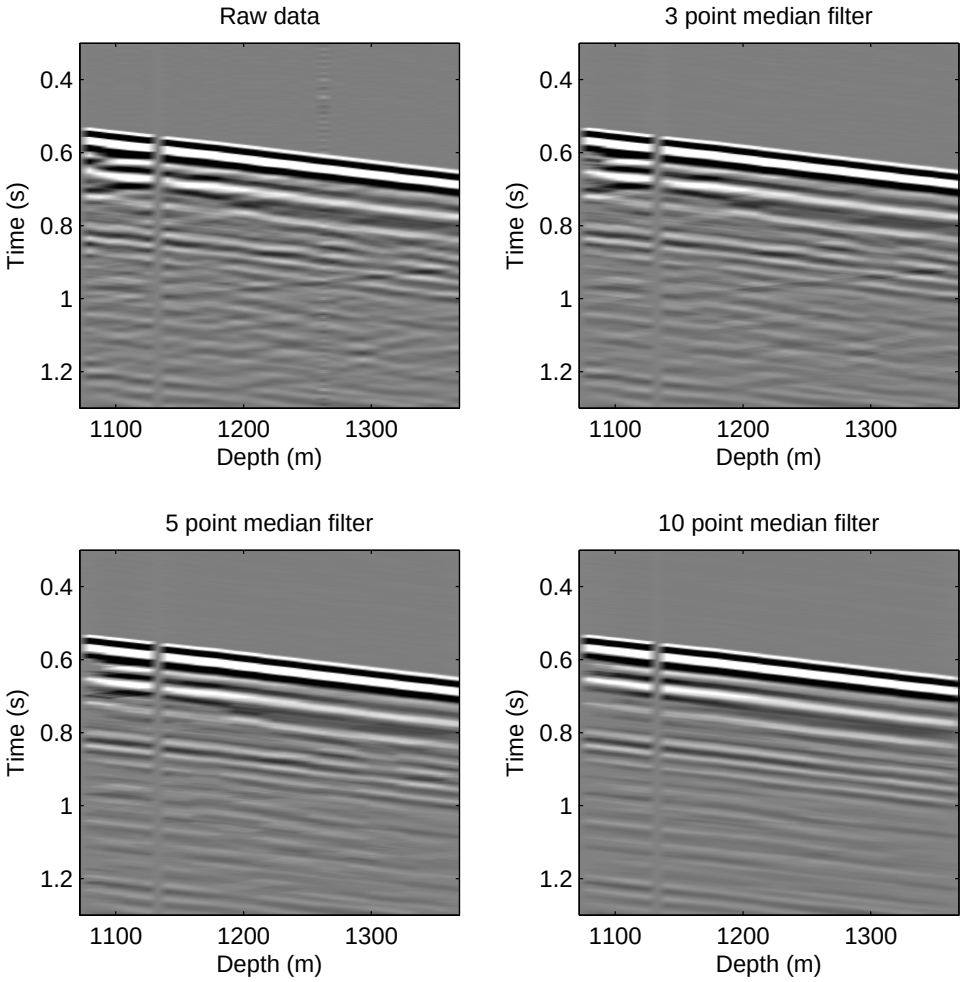

Figure 5.24: Wave-field after various median filters have been applied.

5.3.1 Spectral ratios

The most appropriate place to start with the spectral ratio comparison is to look at the spectra of the data, for all FFIDs (Field file identifications), for both the pre- and post-injection data-sets. Figures 5.25 and 5.26 display the frequency content for the pre and post injection acquisition, for all FFIDs within the data-set. Each FFID plot is normalised by the maximum amplitude and hence the decay of high frequency energy is observed, telling us that attenuation is present. Notches caused by interference of the direct and surface ghost arrival are evident at around 70Hz, but in general a large proportion of the energy is observed between 10 and 60Hz. The bandwidth of significant energy decreases from 10-250Hz at shallow depths, to 10-150Hz at lower depths.

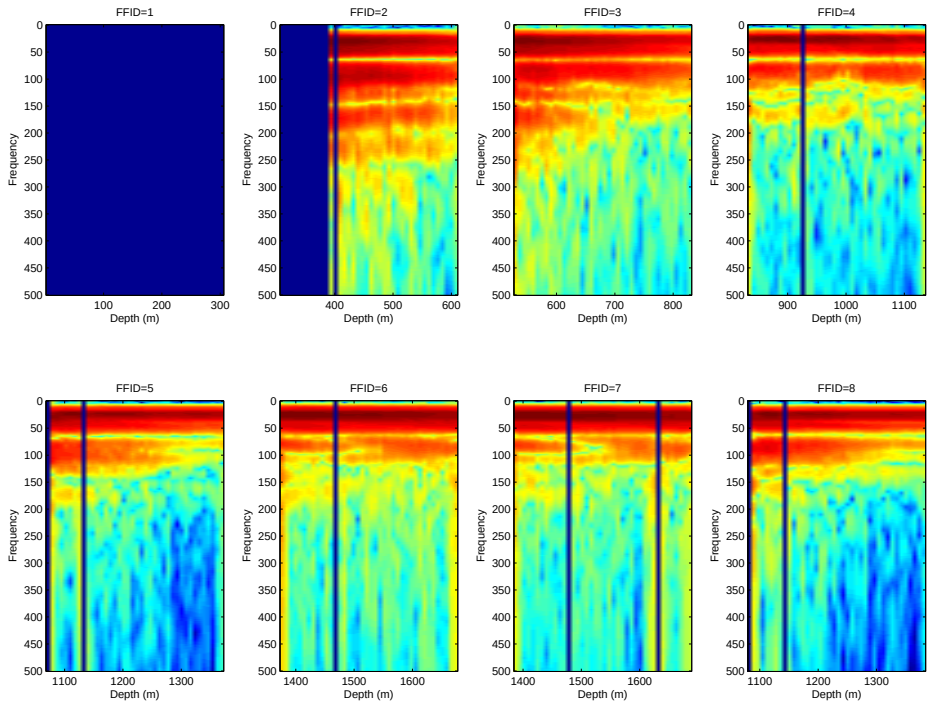

Figure 5.25: Spectral content of the pre-injection acquisition, source location 1. Traces killed in pre-processing are shown in dark blue.

As data was acquired with an explosive source, the frequency content of both vintages of data will differ. By plotting the direct spectral ratios between vintages of data (post/pre), we can highlight the relative differences in the source for a single depth range. The top left plot in Figure 5.27 shows the direct spectral ratios of all 48 trace pairs from FFID 6 and 5 (Depth range 1400-1680m) from the pre and post injection respectively. If there was a constant bias of the spectra between vintages of data, spectral ratios would plot on

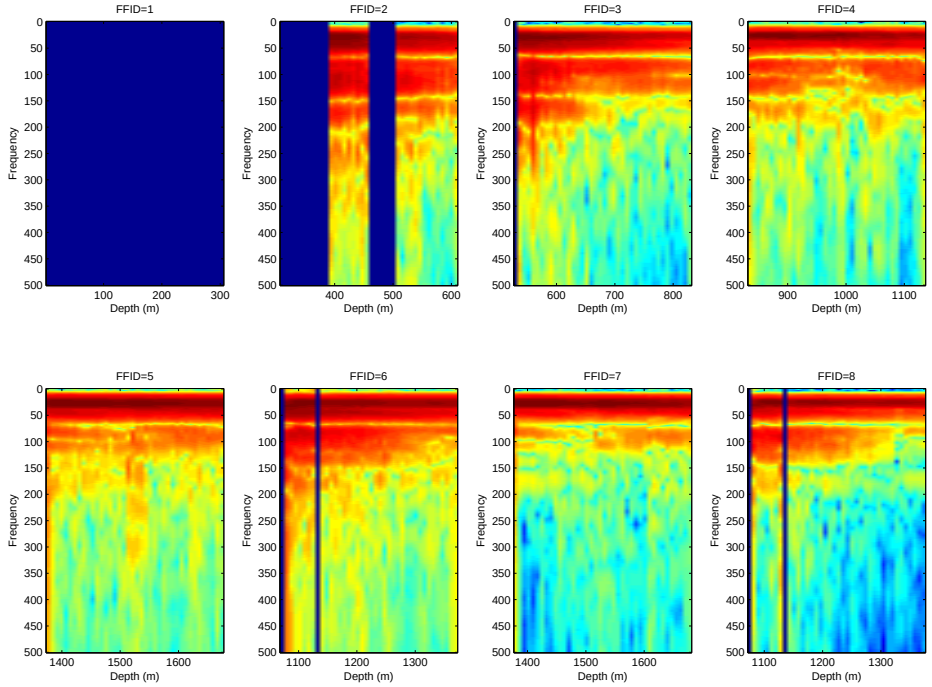

Figure 5.26: Spectral content of the post-injection acquisition, source location 1.

a single line. Where black lines show variation, the spectral ratios are dominated by noise. For the raw data, these direct spectral ratios suggest that there is repeatable energy up to around 200Hz, where the spectral ratios appear noisy. There is slightly more energy in the second data-set compared with the first, especially at higher frequencies, as the log spectral ratio is greater than 0. Figure 5.27 also shows the direct spectral ratios for the 3 point, 5 point and 10point median filters, highlighting the increase in high frequency noise introduced by the median filters, with the usable upper bandwidth now down from 200Hz to around 100Hz for the median filtered data. There is no significant difference between the 3, 5 and 10 point median filtered data. The implications of this reduced bandwidth may be important when considering whether to use median filtered or raw data in the analysis.

By looking at the spectral ratios between receiver pairs from a single vintage and single FFID, it is possible to perform a spectral ratio regression for Q for a multitude of regression bandwidths. Q values were calculated for various regression bandwidths for a large receiver gap (270m), a small receiver gap (67.5m) and a small receiver gap (7.5m) and are shown in Figure 5.28. In all of the log spectral ratios a linear region can be seen in the 5-150Hz band giving evidence that suggests attenuation is present and that it is roughly

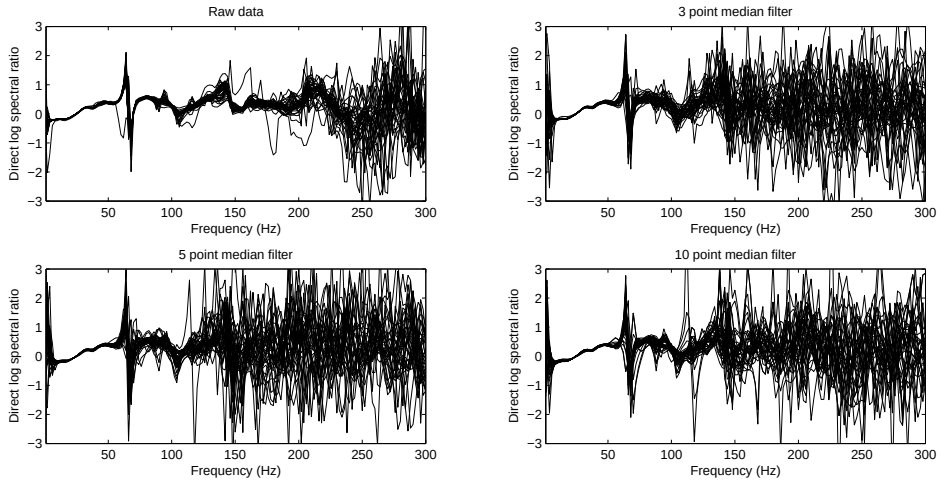

Figure 5.27: Direct spectral ratios of a whole FFID between vintages, demonstrating the spectral differences between vintages of data.

constant over the bandwidth. Within the 5-150Hz bandwidth, the effect of the spectral notch can also be seen, particularly in the smallest receiver separation. The spectral ratios are plotted alongside panels showing the attenuation for a variety of bandwidths. For the larger separations, a stable region of spectral ratios can be seen in the 10-150Hz bandwidth. Positive values of Q of 10-30 are observed for all bandwidths between 0 to 150Hz, suggesting the appropriate bandwidth. The large slope seen in the spectral ratios for the small spacing produces very small values of Q because of the associated small travel time.

A more quantitative analysis can be completed if the residual error of the regression is calculated and normalised by the number of observations used in the regression. A comparison of the residual error as a function of bandwidth for both the pre and post injection scenarios can be seen in Figure 5.29. A sharp increase in the residual error is observed when the upper bandwidth of the regression reaches around 250Hz. By comparison, this same analysis on the 5 trace median filtered data yields a decrease in the stable upper bandwidth to 150Hz (Figure 5.30). Again, this highlights the trade off between including noise due to up-going reflections and keeping a large bandwidth for Q estimation. From these plots I choose to use a bandwidth of 10 to 150Hz for the raw data and a bandwidth of 10-100Hz for the median filtered data.

Δt^* values are calculated for source location 1 using two methods of frequency estimation. Firstly a 500ms (1000 sample) FFT was used with a Hanning taper centred on the maximum envelope of the direct wave. Secondly, the s-transform was used (resolution

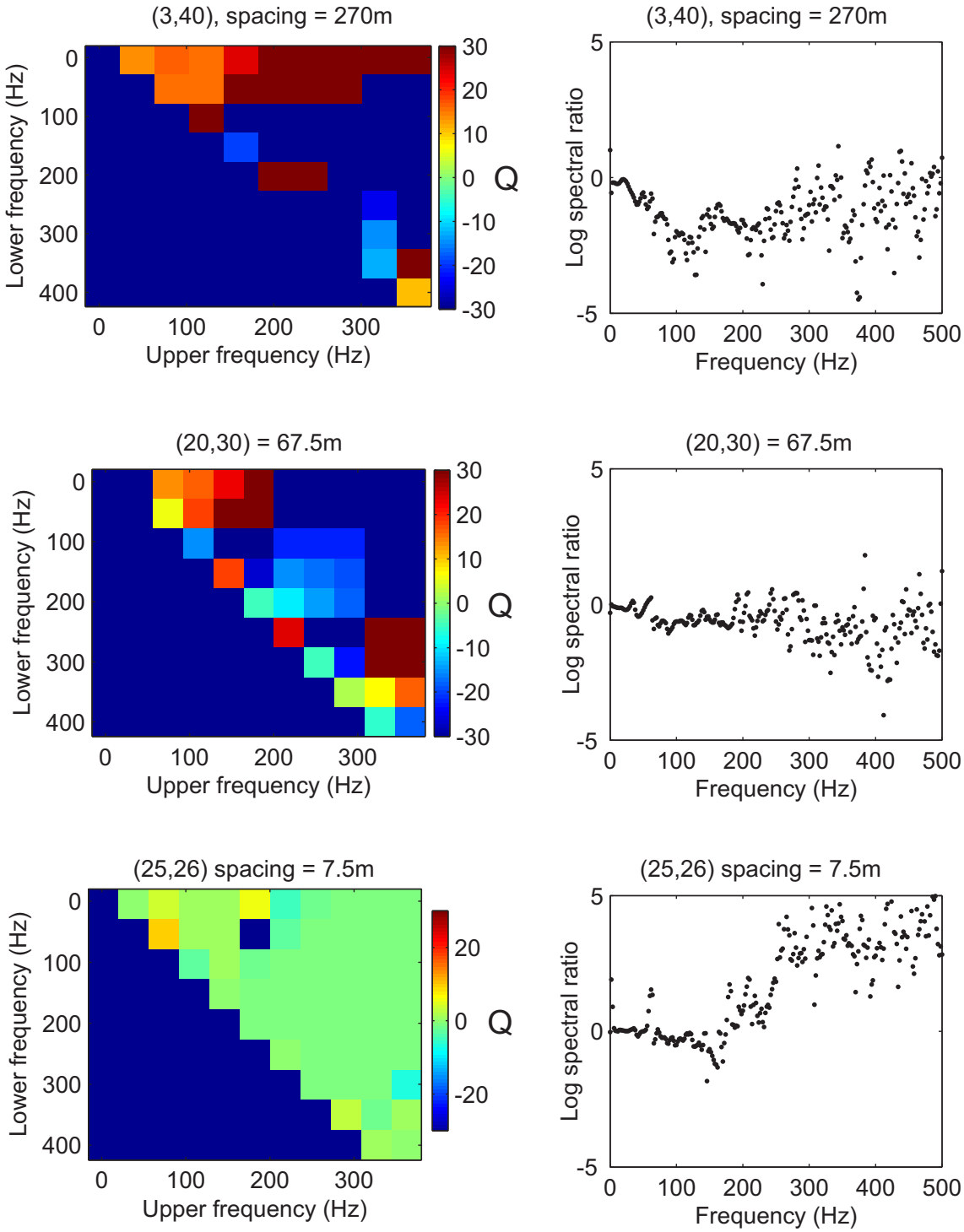

Figure 5.28: Comparisons of the Q values (left) and spectral ratios (right) for 3 different receiver separations. Geophones 3 and 40 (270m separation) were used for the top panel, 20 and 30 (67.5m separation) were used for the middle and 25 and 26 (7.5m separation) used for the bottom panel.

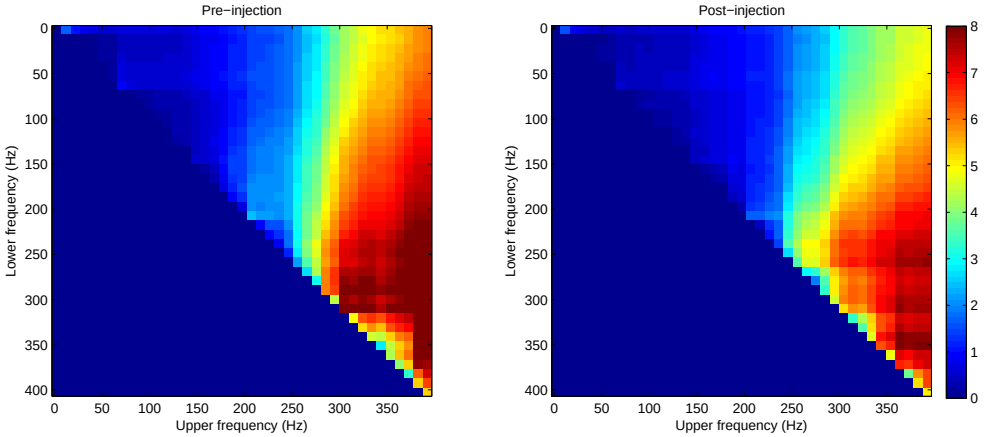

Figure 5.29: Average residual error squared on the regression for the log spectral ratio slopes for all combinations of receiver pairs for pre-injection (left) and post-injection data (right) using the raw data.

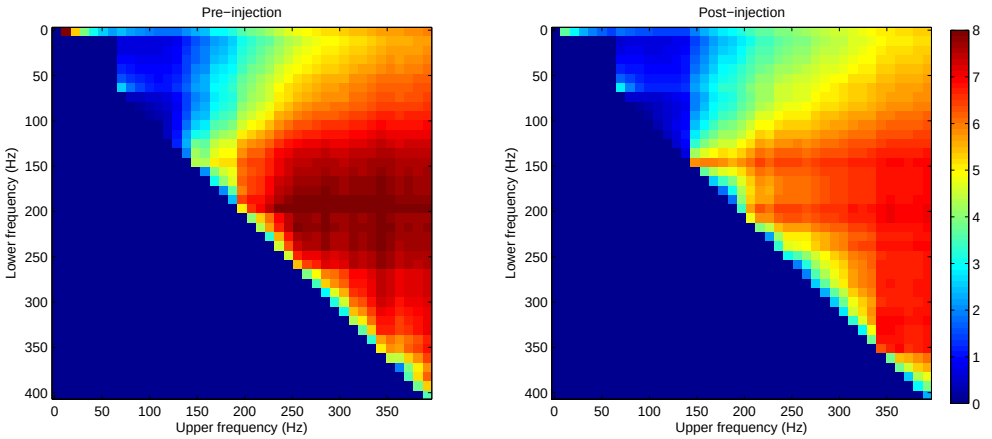

Figure 5.30: Average residual error squared on the regression for the log spectral ratio slopes for all combinations of receiver pairs for pre-injection (left) and post-injection data (right) using the 5 trace median filtered data.

factor, k_s=5) to calculate changes in t^*. Due to the dispersive nature of seismic waves, spectral content was extracted from the time-frequency transform in two ways. Firstly, the data are extracted for all frequencies at the maximum envelope time pick and secondly, in order to accommodate frequency dependent travel times, the maximum energy for each frequency within a 20ms window (40 samples) was also extracted (termed "snap" from now on). This gives three comparisons for the spectral estimation and calculation of the attenuation between vintages of data.

The Δt^* tartan triangles for all 3 spectral estimations (FFT, s-transform no-snap, s-transform snap) for the raw and 5 trace median filtered data are plotted in Figure 5.31. All plots broadly show similar results with an apparent increase in attenuation in the injection region (1530m depth). It is clear that there is a significant increase in noise for the un-snapped s-transform results, whilst the FFT and snapped s-transform produce much lower levels of noise. It can also be seen that the median filtered data also have a lower noise level than the raw data for all of the frequency estimates. By averaging the change in t^* at depth for all spacings (Figure 5.32) and also calculating the standard deviation of those measurements, any significant anomalies can be found where the average anomaly is greater than the deviation. An increase in attenuation can be seen in all of the methodologies in the injection region ($\approx$1520m).

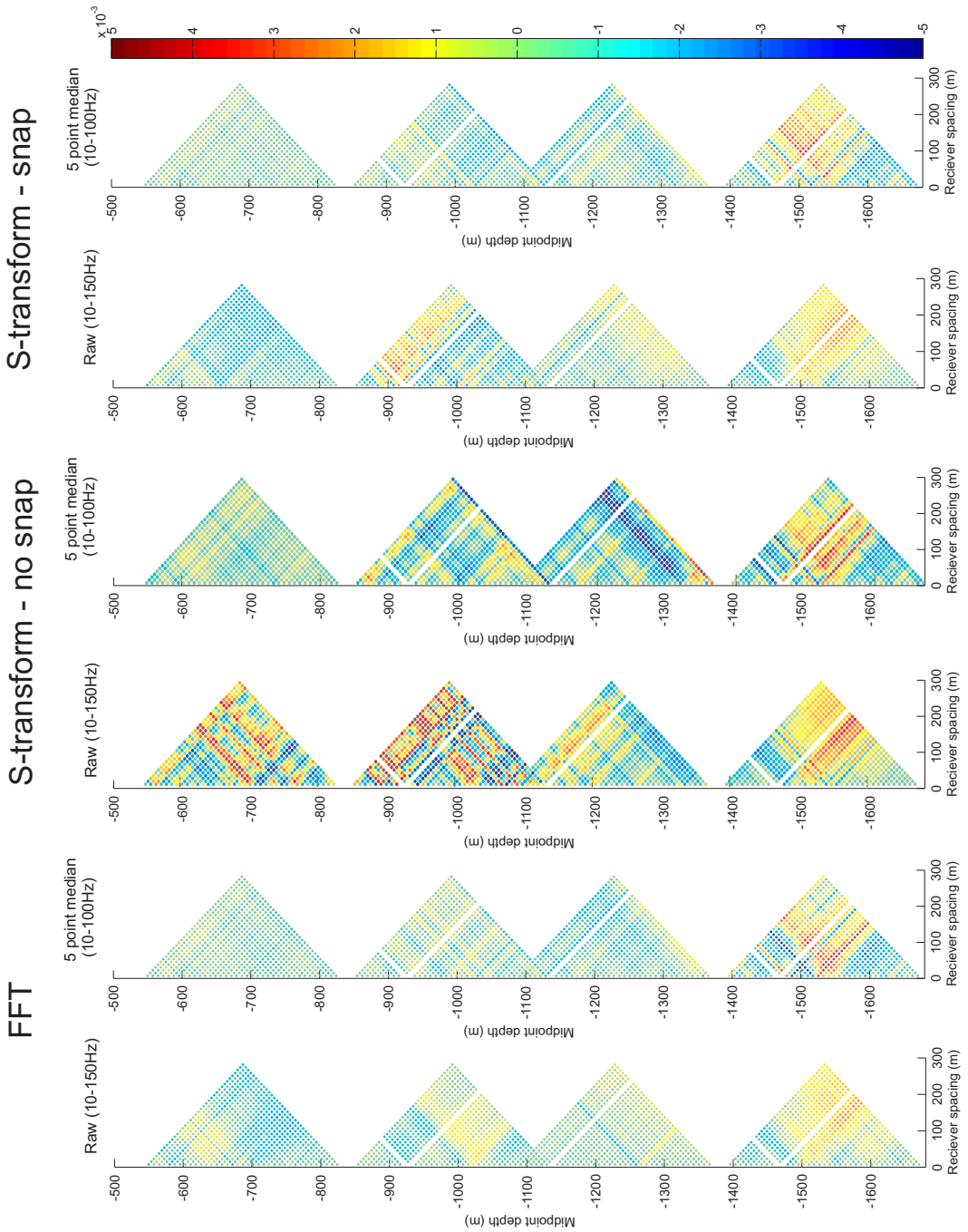

Figure 5.31: All of the spectral ratio results for t^*. Compare with sechmatic Figure 3.18.

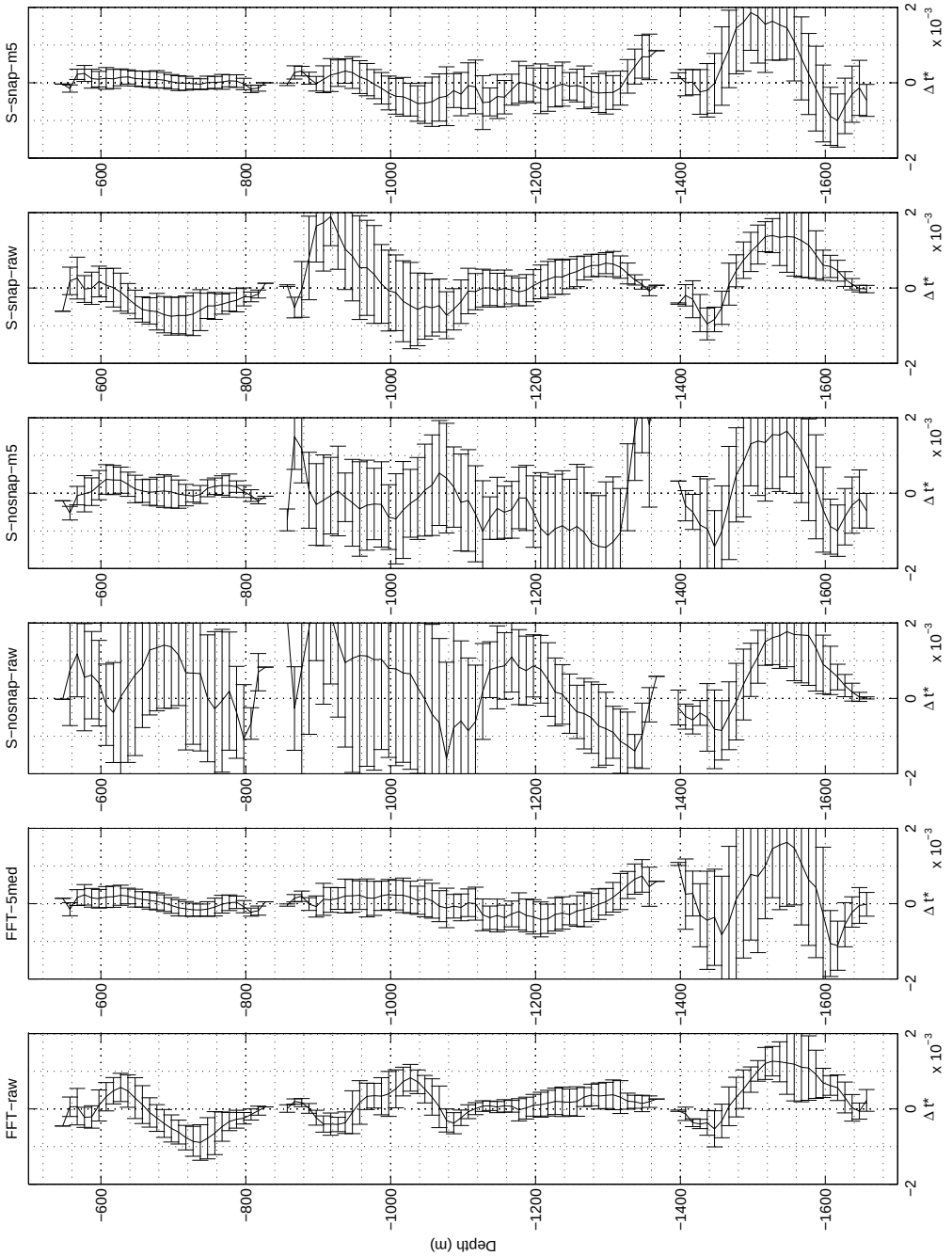

Figure 5.32: Average t^* results for all of the spectral ratio methodologies.

5.3.2 Instantaneous frequency

When using the instantaneous frequency several parameters need to be decided upon including the frequency damping, the weighting length and the regression length. I choose to use a window length of 301 samples to perform the instantaneous frequency matching as this window is large enough to contain the whole of the direct arrival. An extra measure to stabilise the inversion for real data can be to include model damping in the inversion. This does however provide another parameter that must be decided upon. In order to parametrise the inversion, I look at a pair of traces bounding the injection interval and calculate t^* for a range of parameters. The direct arrivals are windowed (301 samples, 150ms) centred on the maximum envelope pick as this should provide the most stable reference point.

I look at the the effect of the damping parameter (ϵ^2) and the weighting length on the calculation of the instantaneous frequency as for a single FFID for the pre-injection dataset (Figure 5.33). With no damping and smoothing it is difficult to see if there is any coherent change in instantaneous frequency as a function of depth apart from at the very start of the wavelet. As damping and weighting is increased the decrease of instantaneous frequency with depth becomes more apparent. This suggests that if we model the instantaneous frequencies around the peak envelope, a large weighting and damping value may be needed, but if the start of the waveform is to be modelled, it may be more appropriate to use a short weighting function. Use of a large weighting and damping function will favour frequencies measured at large amplitudes, and dominate over subtle changes at the start of the waveform.

I test all of the parameters on two good quality traces from an FFID that straddles the injection interval. Parameters tested include the frequency damping (ϵ^2, values of 0, 1, 2, 3, 5, 20, 30 and 50), weighting length (T in samples, 0 to 100), regression length (rl in samples, 0 to 100) and the inversion damping (θ^2, values of 1, 10^4, 10^6, 10^7 and 10^8). Results for the first vintage of data can be seen in Figure 5.34. This highlights the behaviour of the t/Q estimates with each model parameter. The t/Q estimates become stable as the ϵ^2, T and rl are all increased. This may be as expected as the signal has been smoothed, with instabilities caused by low amplitudes minimised. As θ^2 is increased, there is a reduction in the size of the model solution. The same parameter tests were performed for the post-injection data using two traces acquired using the same acquisition geometries as those used for the pre-injection case (Figure 5.35). In order to minimise the

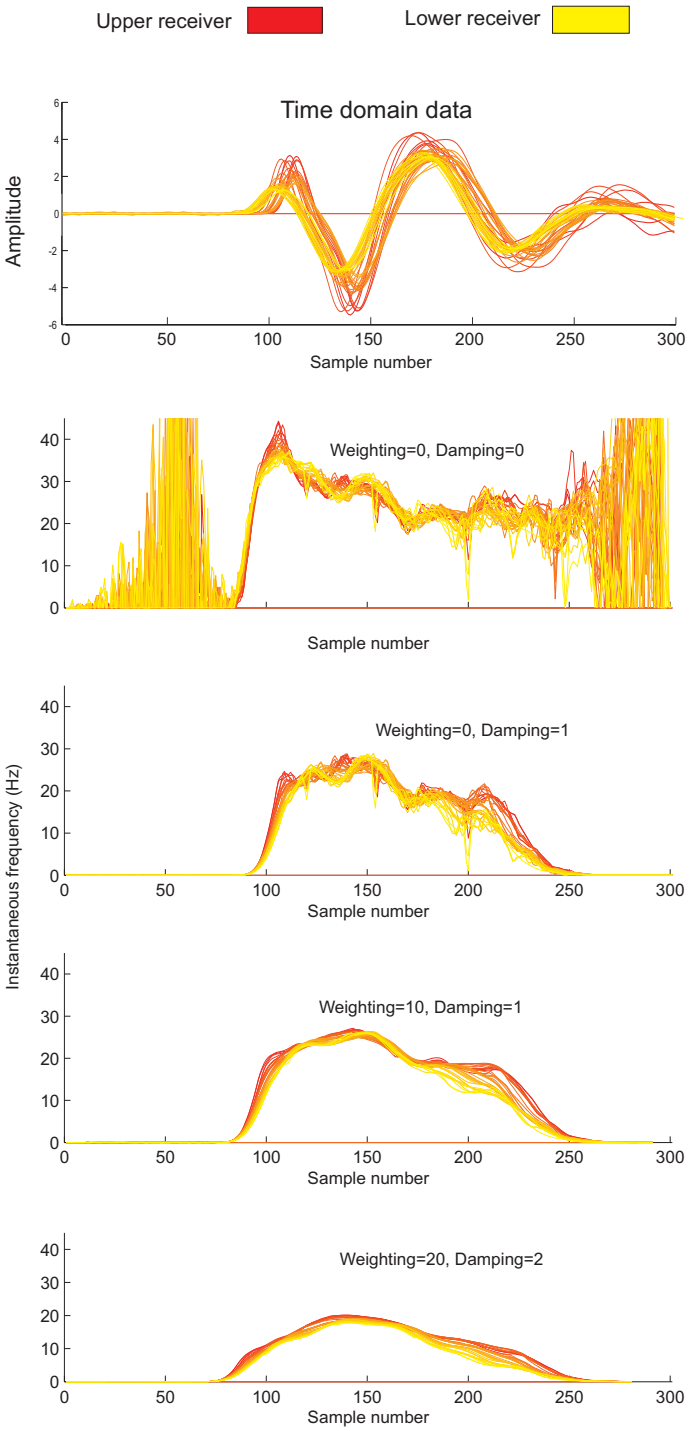

Figure 5.33: Example of the instantaneous frequency for a single FFID. As the colour represents the location of the trace in the FFID, with red being associated shallow receivers and yellow with deeper receivers, the instantaneous frequency should decrease as a function of depth (red to yellow).

impact of the frequency damping (by reducing the size of the instantaneous frequency) ϵ^2=5 was chosen. Including inversion damping will be important for ensuring that the model converges to a reasonable values of attenuation. The parameter tests show that the inversion for these two traces does not rely on damping to stabilise the result, however for noisy traces it may be necessary. The parameter tests do tell us when the inversion is over-damped and this can be seen for damping values of 10^7 and 10^8, particularly at high frequency damping. I choose to use an inversion damping of $\theta^2 = 10^6$, as this provides a reasonable amount of damping without considerably affecting the model complexity. I then choose to use a regression length of 60 samples and a weighting length of 60 samples.

As with the spectral ratio and centroid frequency methodologies the change in attenuation is calculated for shot location 1 for both the raw and the 5 point median filtered data (Figure 5.36). The raw and 5 point median filtered data are very similar showing a coherent increase in attenuation at a depth of around 1000m and a coherent decrease in attenuation in the injection region. The average Δt^* for each depth is also plotted in Figure 5.36. The standard deviation of the results highlights that the only significant attenuation change occurs at a depth of around 1000m. It would be expected that the instantaneous frequency methodology would produce results similar to those from the spectral ratio methodologies, however, the opposite polarity change in attenuation is seen in the reservoir interval. This will be discussed further after the analysis of the centroid frequency and other shot locations.

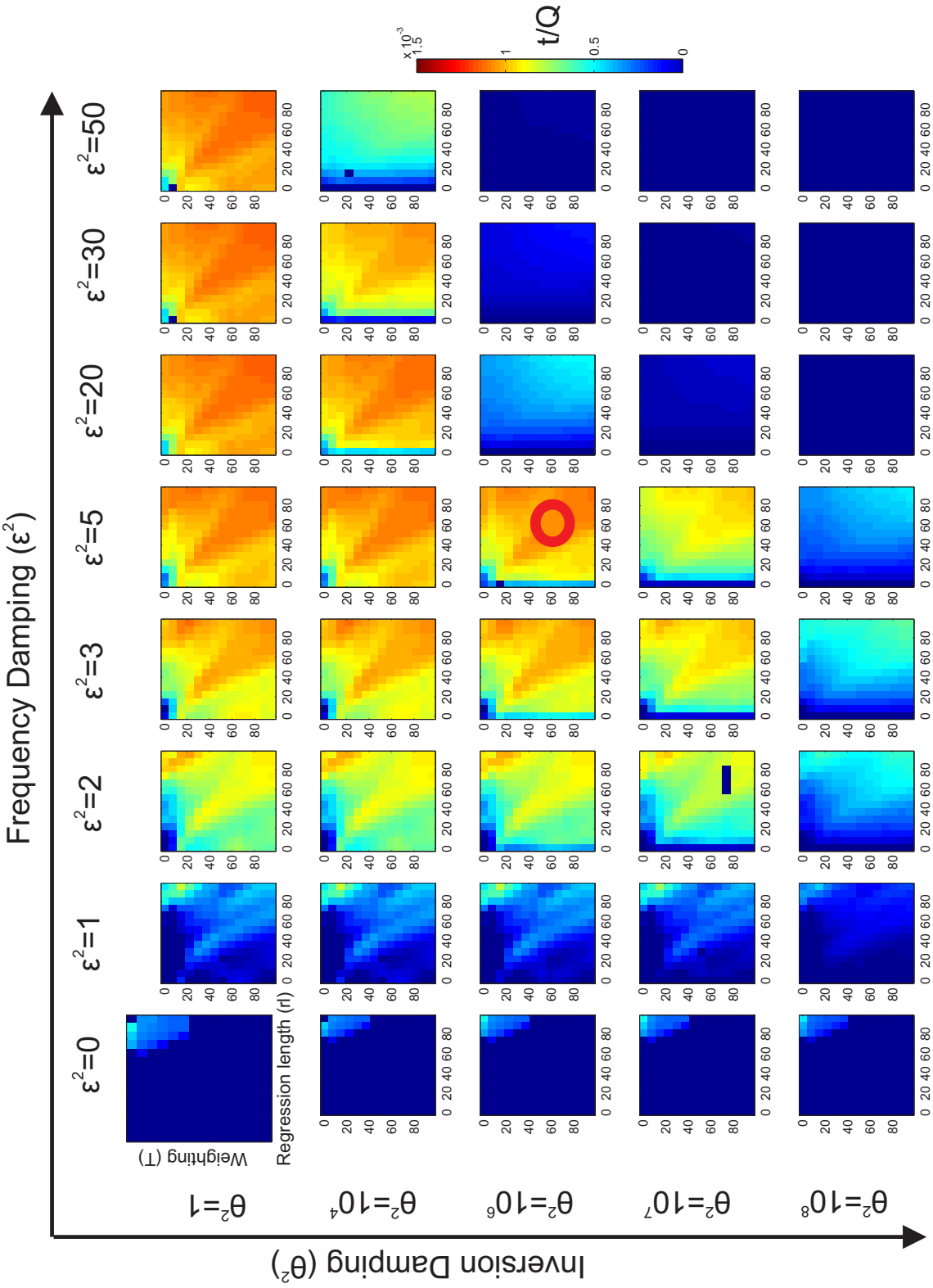

Figure 5.34: Parameters tests for a pair of traces from the pre-injection data-set. t/Q values are calculated for a range of frequency damping (ϵ^2), regression length (rl), frequency weighting (T) and inversion damping (θ^2). Red circle indicates parameters chosen for inversion. This was chosen as a reasonable amount of damping and frequency damping can be included without underestimating the amount of attenuation.

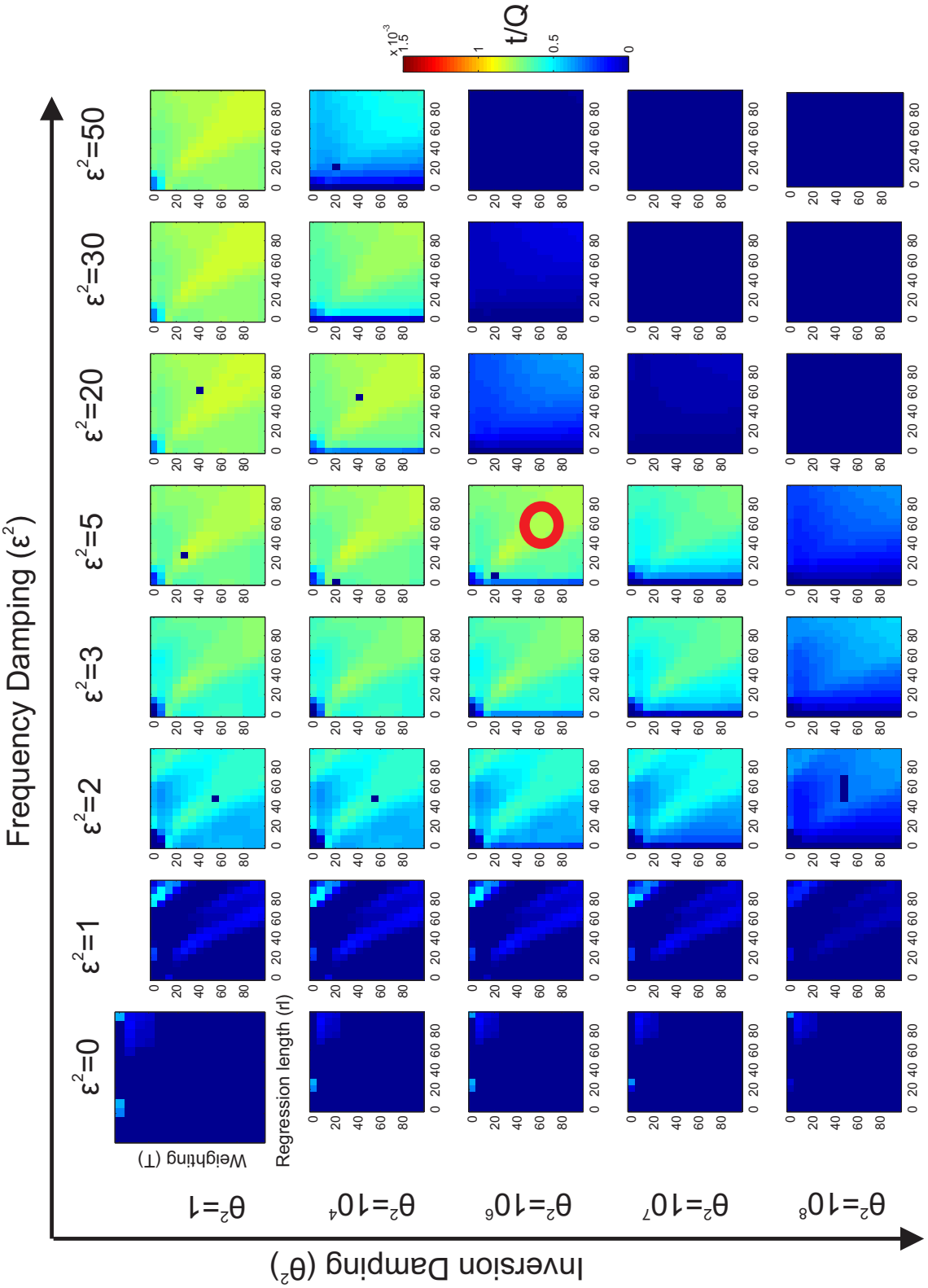

Figure 5.35: Parameters tests for a pair of traces from the post-injection data-set. t/Q values are calculated for a range of frequency damping (ϵ^2), regression length (rl), frequency weighting (T) and inversion damping (θ^2). Red circle indicates parameters chosen for inversion. This was chosen as a reasonable amount of damping and frequency damping can be included without underestimating the amount of attenuation.

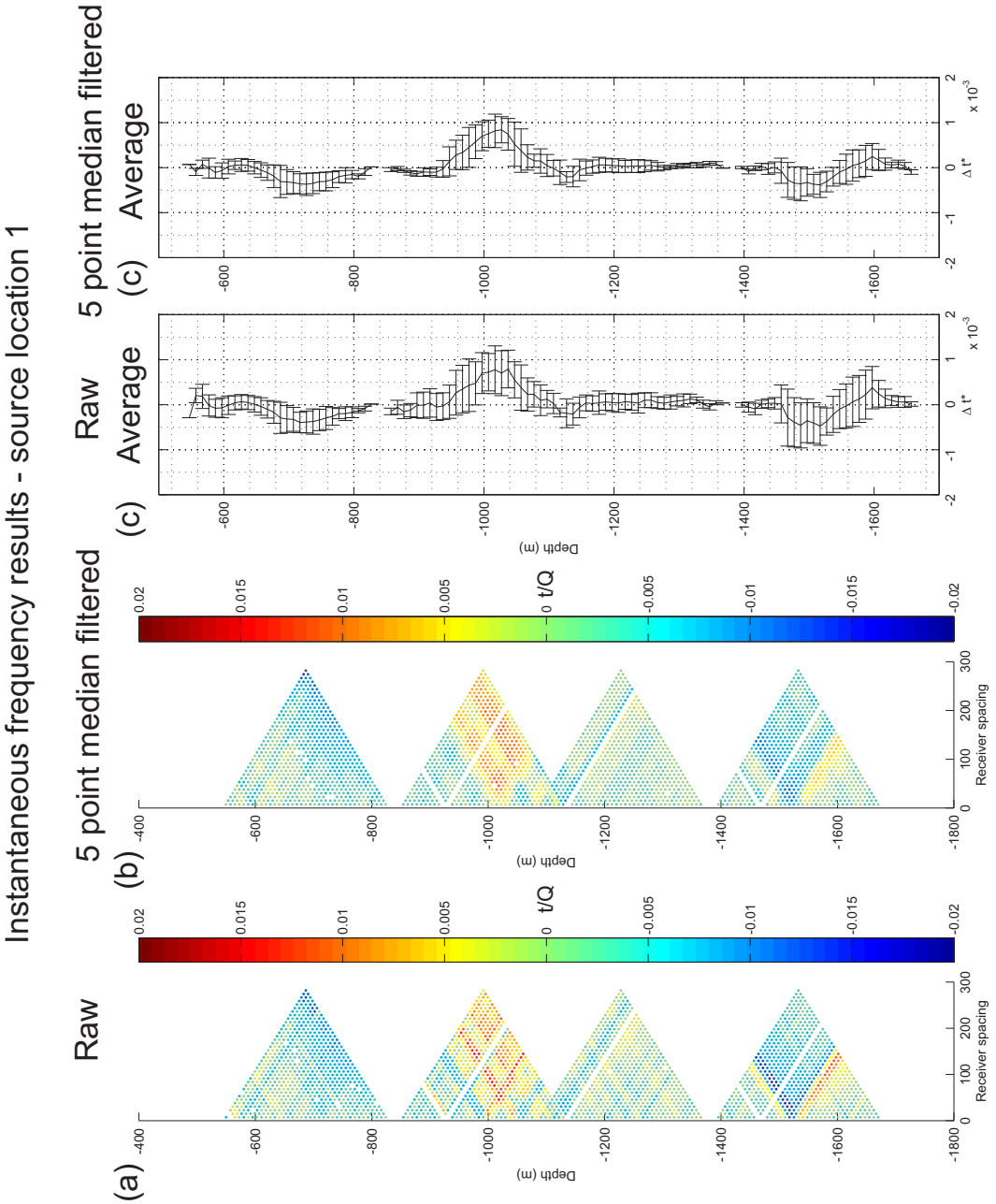

Figure 5.36: Change in attenuation calculated for source location 1. (a) and (b) show the tartan triangles of source location 1 for the raw and 5 trace median filtered data respectively and (c) and (d) show the average change in t^* for all receiver spacings for the raw and 5 point median filtered data.

5.3.3 Centroid frequency

It can be seen from Figure 5.37 that the trace spectrum cannot be assumed to be Gaussian, mainly due to the existence of the surface ghost notch at around 60-70Hz. It may therefore be necessary to estimate the centroid frequency for a specific range of frequencies. Figure 5.37 shows the Gaussian distributions that would be generated through estimation of the centroid frequency for different bandwidths. It can clearly be seen that either of the shorter bandwidths fit that range of frequencies better than the estimation for all frequencies.

I now go on to look at how well the spectrum fits a Gaussian function for a range of bandwidth measurements. In order to achieve this, the centroid frequency, standard deviation and energy in a specific bandwidth are estimated from the data. The measured Gaussian distribution is then compared with the true spectrum and the misfit calculated. An example of this result for a single trace can be seen in Figure 5.38 and shows two regions, where the Gaussian assumption may be reasonable. In order to check that this is consistent across the data, the average misfits for all traces for source location 1 for each vintage can be seen in Figure 5.39.

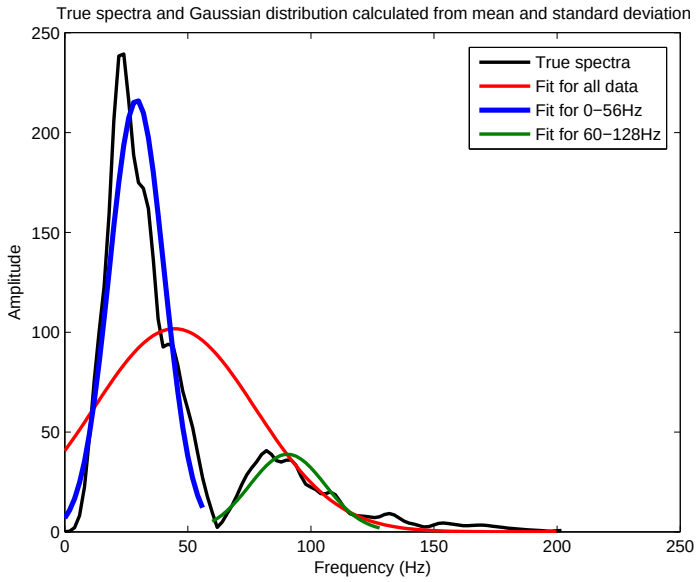

Figure 5.37: Spectrum of a single trace (black) plotted with the estimated Gaussian distributions for 3 different bandwidths of data.

From Figure 5.39 I choose to calculate the change in Δt^* for three different bandwidths; 2-56HZ, 60-128HZ and the full bandwidth. These are calculated for Source location 1 for both the raw and 5 trace median filtered data (Figure 5.40). The effect of the median filter on decreasing the impact of the up-going wave can be seen in the lower frequency

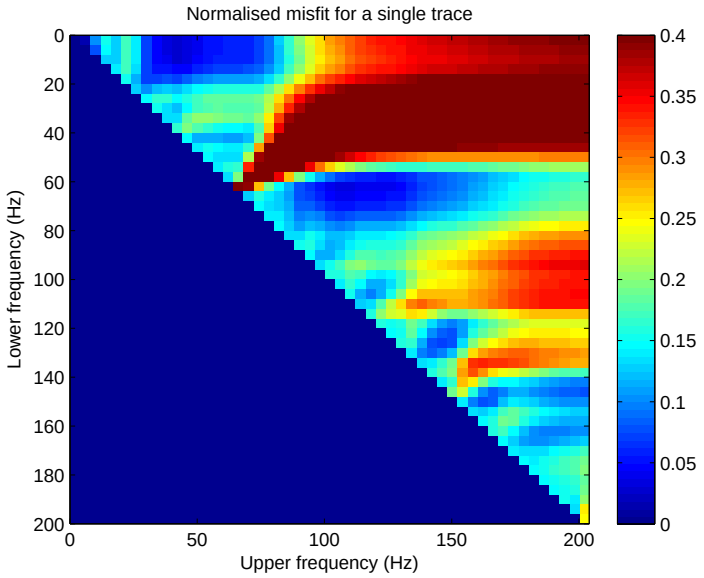

Figure 5.38: Misfit between measured Gaussian properties and real data spectrum for a single trace.

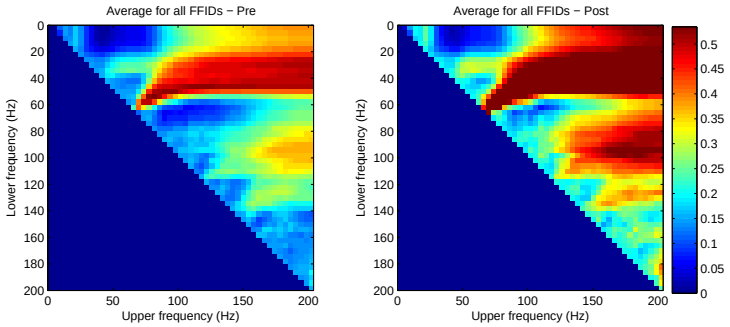

Figure 5.39: Misfit between measured Gaussian properties and real data for shot 1, for pre-injection (left) and post-injection (right).

range, as the noise has been reduced, particularly in the injection region. Conversely, for the high frequency and all frequency estimates the negative impact of the median filter can be seen as the coherency of the anomaly in the injection region has been reduced. This difference is particularly evident in the estimate using all frequencies. The varying magnitudes of the changes in attenuation, indicate that the absolute values of the change in t^* is dominated by the size of the standard deviation of the estimated spectrum. These results may also suggest the presence of frequency dependent attenuation changes, as there are no coherent anomalies in the low frequency range, but coherent anomalies in the higher frequency range.

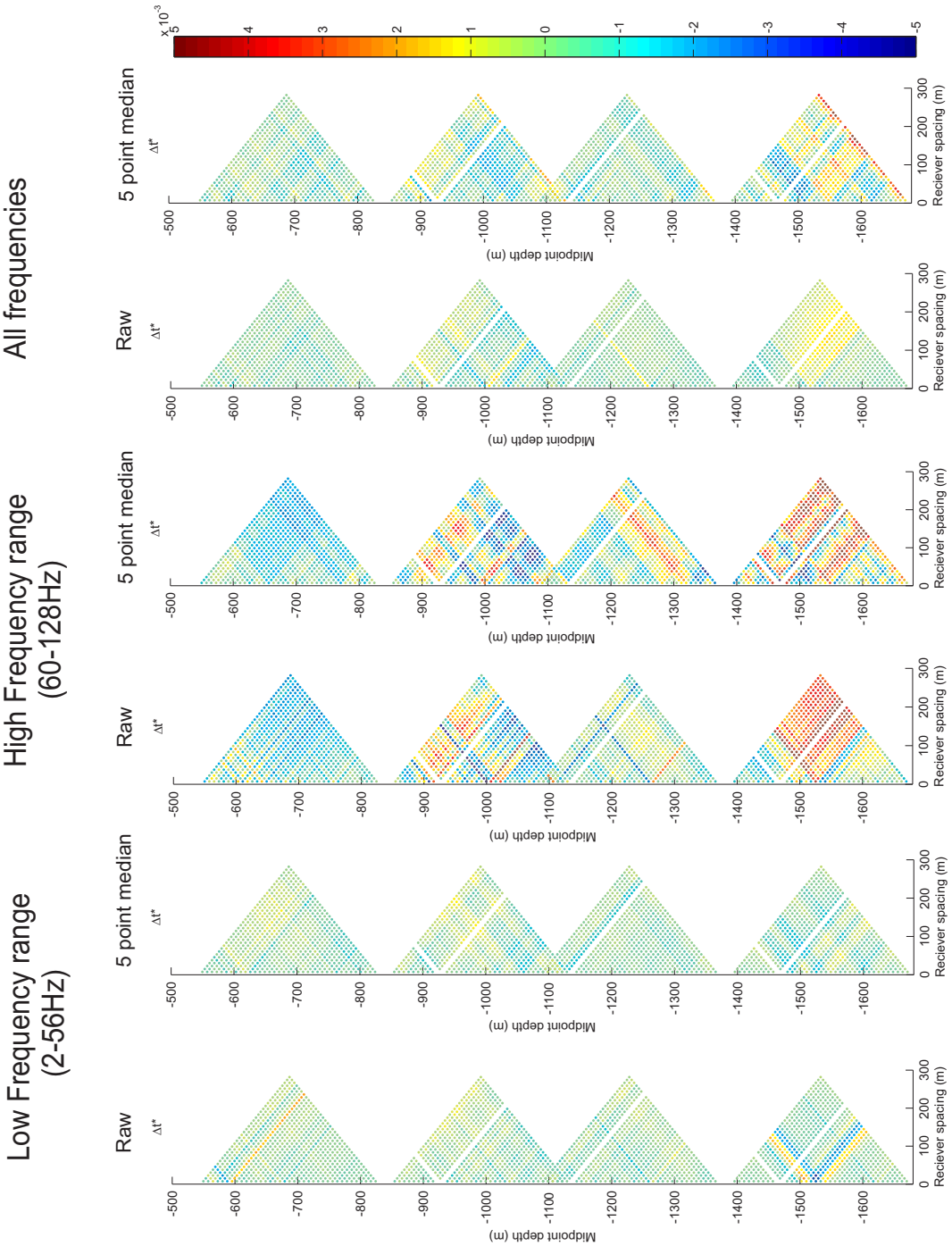

Figure 5.40: All of the centroid frequency results for t^*. Layout given by schematic in Figure 3.18.

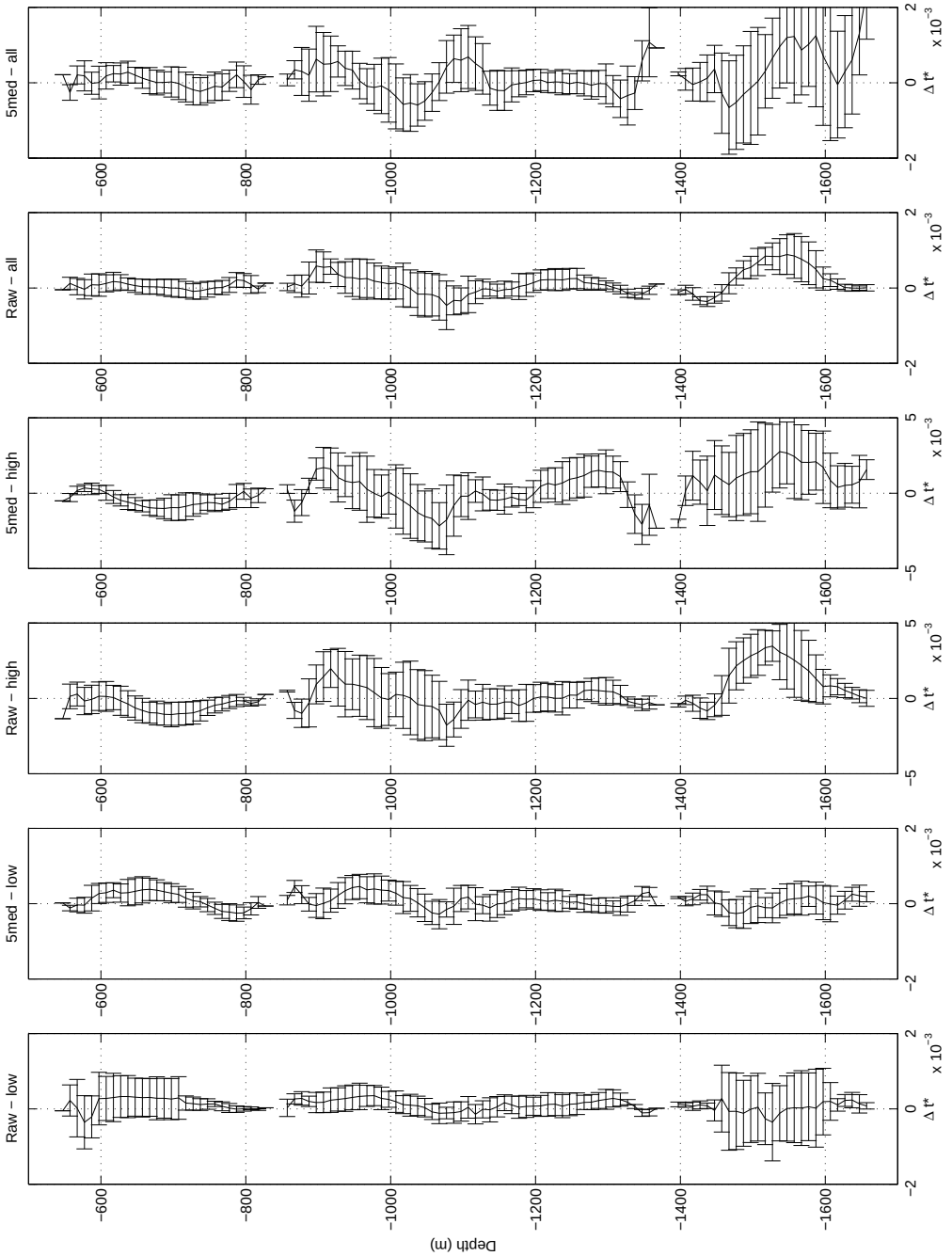

Figure 5.41: Average t^* results for the centroid frequency methodologies.

5.3.4 Final Q results

Absolute Q estimates

To begin with I take a look at the absolute measurements generated using the spectral ratio methodology for both the pre- and post-injection data-sets for source location 1 (Figure 5.42). Absolute values of attenuation range from -0.1 to 0.1, indicating the possibility of two things. Firstly, if the large positive values are due to the intrinsic attenuation, very small Q values are present in the subsurface (Q=10). Secondly, with such large magnitudes of negative attenuation being measured, there must be a very large component of apparent attenuation present within the data. However, the repeatability of the attenuation measurements between vintages is clearly visible indicating that the apparent attenuation, although large is repeated between vintages.

Change in Q

The change in t^* is calculated for all 8 source locations using the three methodologies. Spectral ratios are calculated in the bandwidth 10-100Hz using the 5 point median filtered data and the s-transform with the snap to the maximum energy (Figures 5.43 and 5.44). The centroid frequencies are calculated using the upper frequency range on the raw data (Figures 5.45 and 5.46). The instantaneous frequency matching is performed using the parameters used above on the 5 point median filtered data (Figures 5.47 and 5.48).

The spectral ratio "tartan triangles" in Figure 5.43 show little similarity with the results of source location 1 with the exception of source location 5. From looking at the source location map, this may be expected, as source location 1 and 5 are along the azimuth away from the well. This may suggest that the source of the increase in attenuation is predominantly located in this direction away from the well. The average change in t^* vs. depth are plotted in Figure 5.44 and indicate that there are significant anomalies at source location 1, 2, 5 and 8 suggesting an increase in t^* in the injection interval.

The centroid frequency "tartan triangles" (Figure 5.45) again show that there are few similarities between the source locations, but show similarities with the spectral ratio methodology, particularly for source location 1. Average values as a function of depth (Figure 5.46) show significant anomalies in the injection region for source location 1 and 2 with an increase in Δt^*.

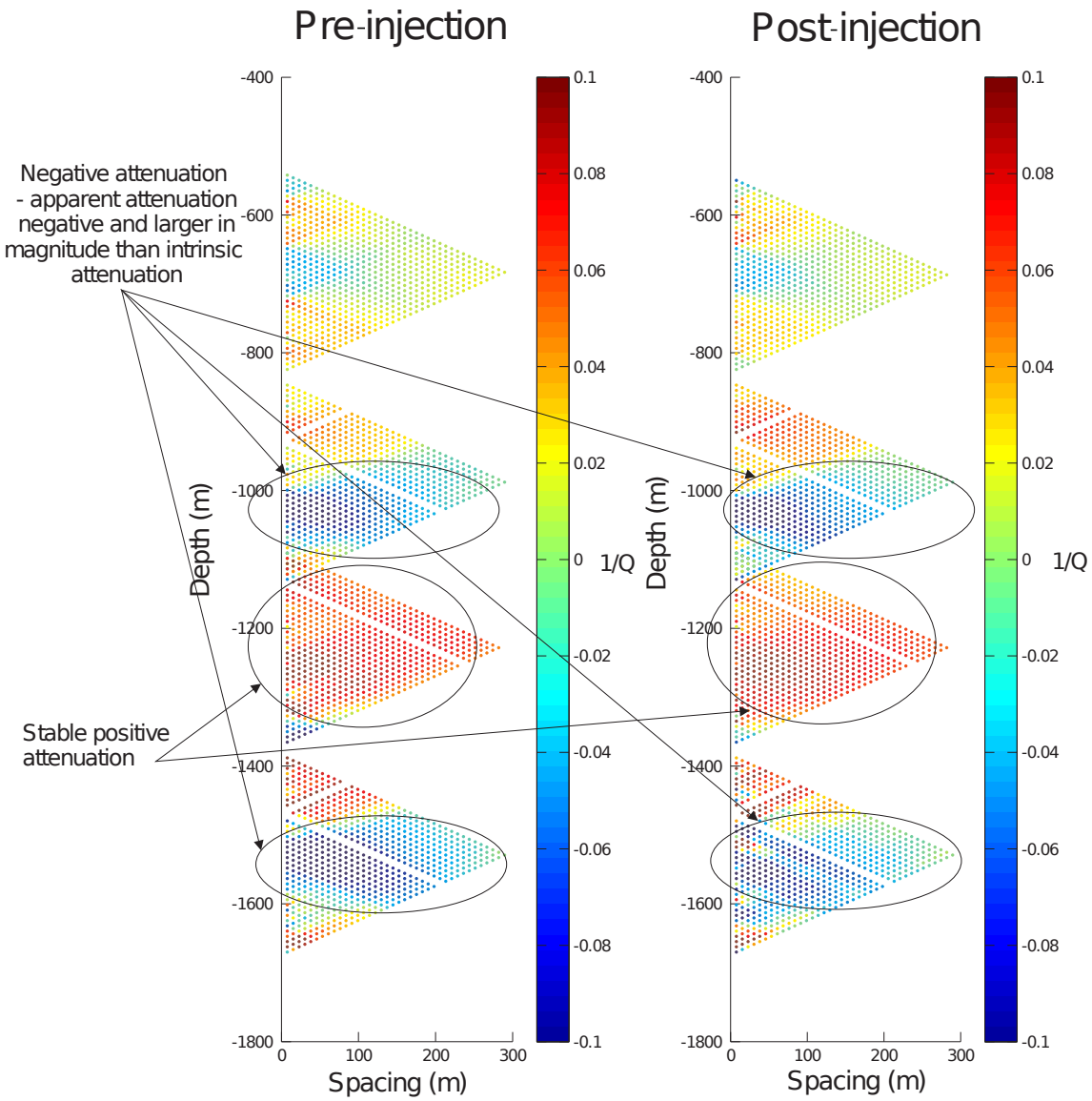

Figure 5.42: $1/Q$ calculated at source location 1 for the pre-injection (left) and the post-injection (right) data-set.

The "tartan triangles" produced from the instantaneous frequency matching (Figure 5.47) show more coherent anomalies across the source locations. A decrease in attenuation at the reservoir interval is evident in source locations 1, 2, 3, 5 and 8. This suggests that the opposite change in attenuation has been observed in comparison to the spectral ratio and centroid frequency methodology, and may suggest that the changes we are detecting in all of the methodologies are not changes in the intrinsic component of attenuation but changes in the apparent component of attenuation. However, I have shown in Chapter 4 that the instantaneous frequency methodology is sensitive to changes in the amplitude of the trace. An increase in amplitude between vintages of data would therefore produce anomalies such as these between vintages of data.

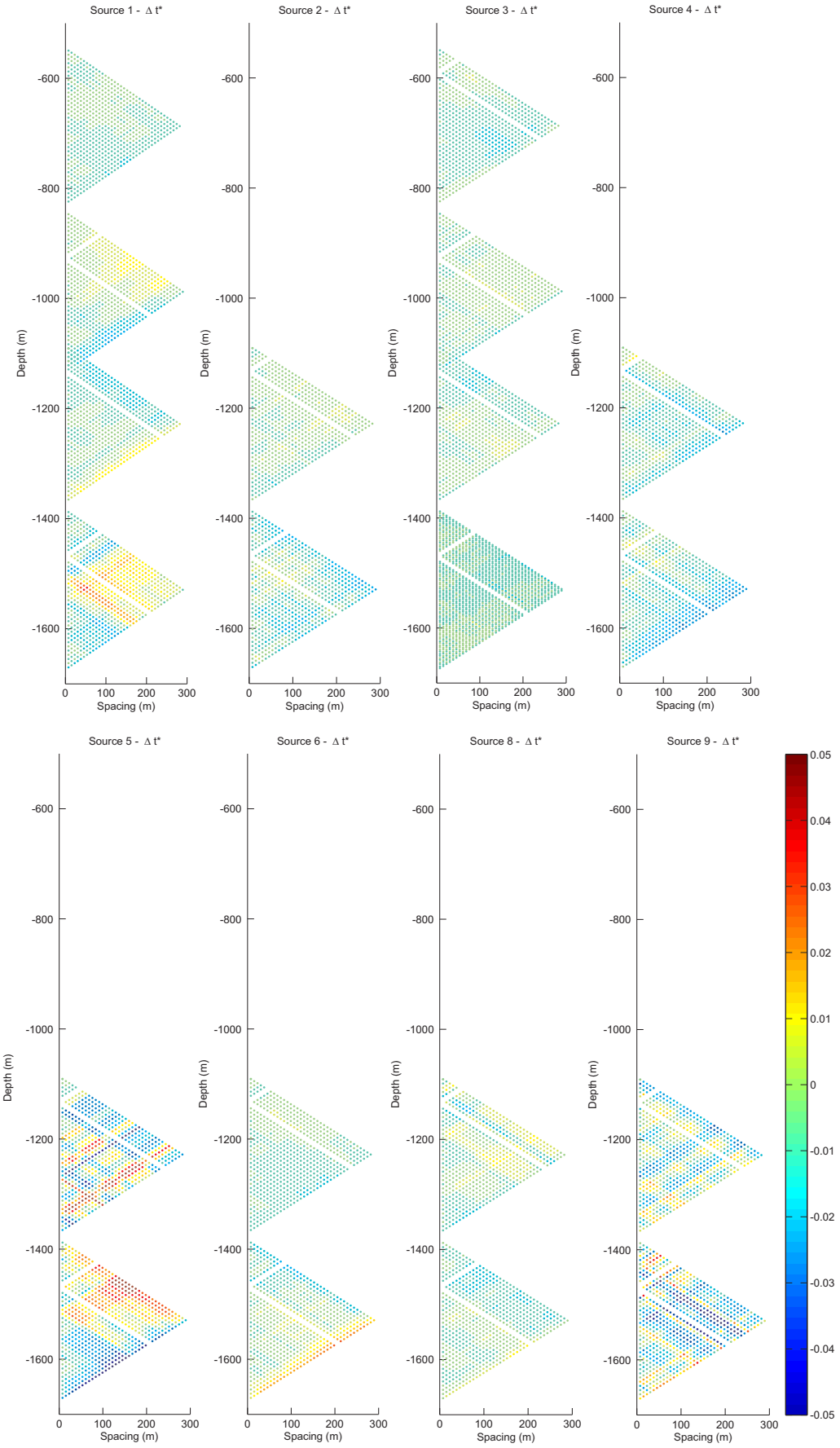

Figure 5.43: Δt^* results for spectral ratio methodology for all sources.

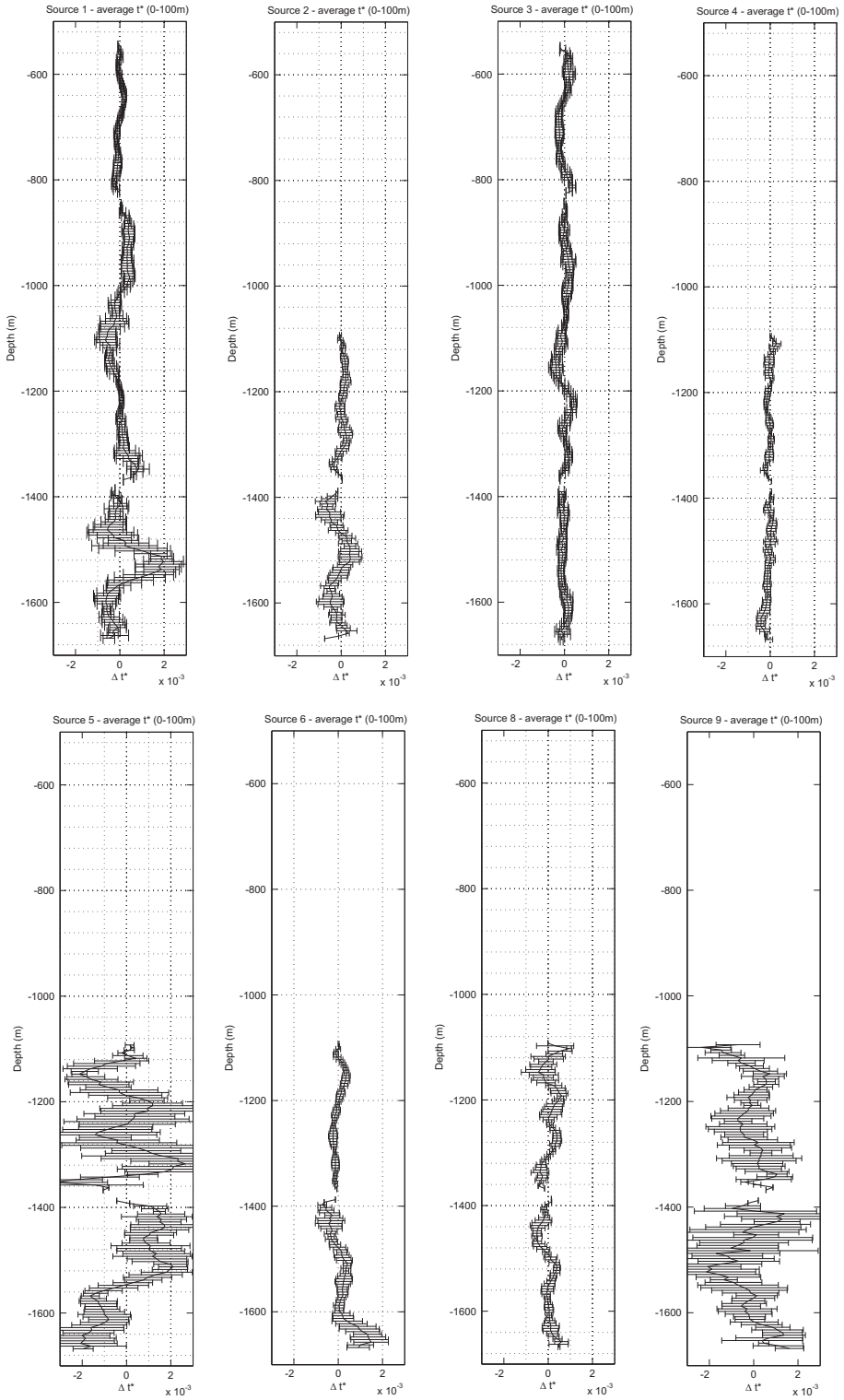

Figure 5.44: Average Δt^* results for spectral ratio methodology for all sources.

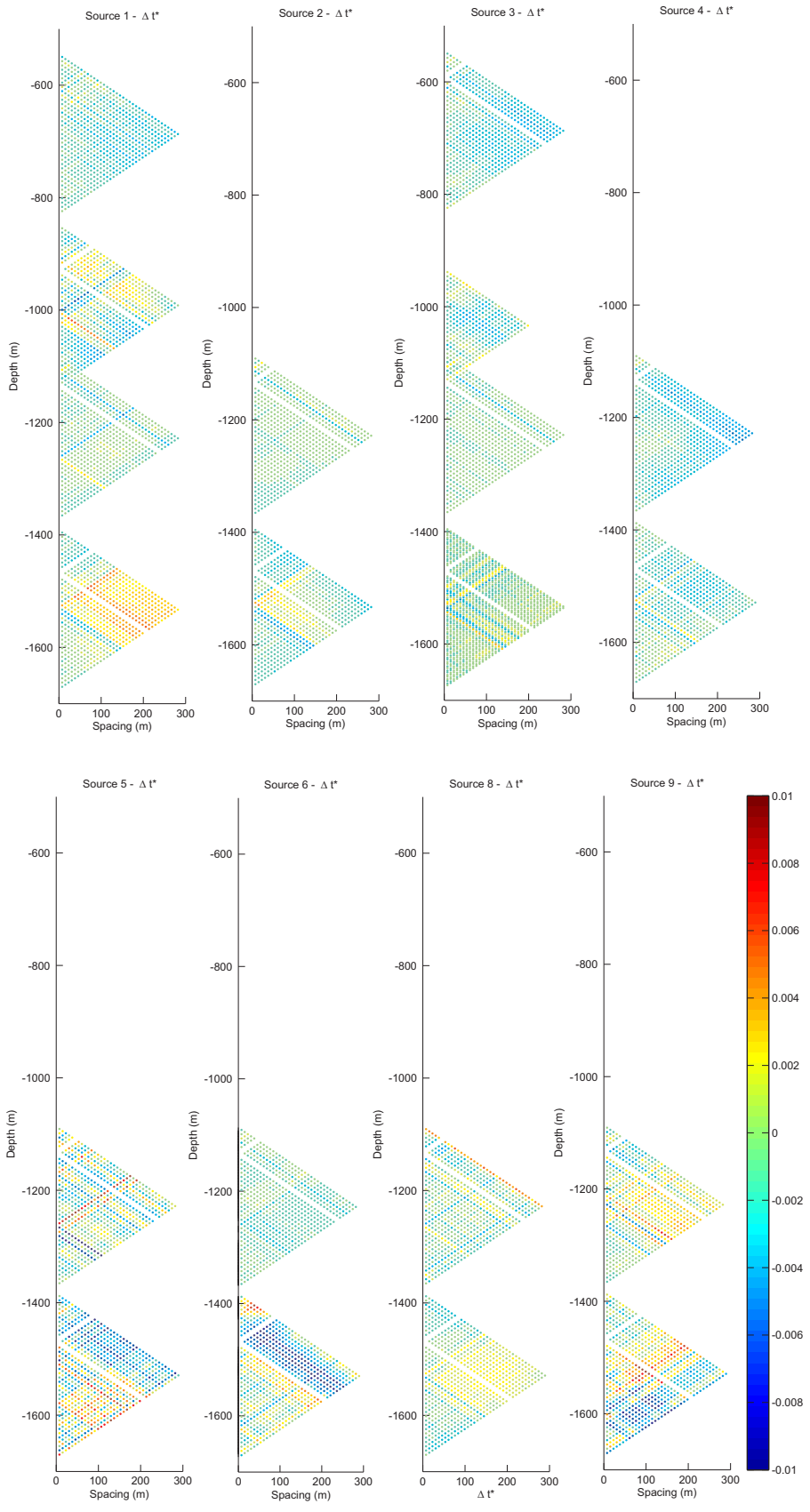

Figure 5.45: Δt^* results for Centroid frequency (high freq) methodology for all sources.

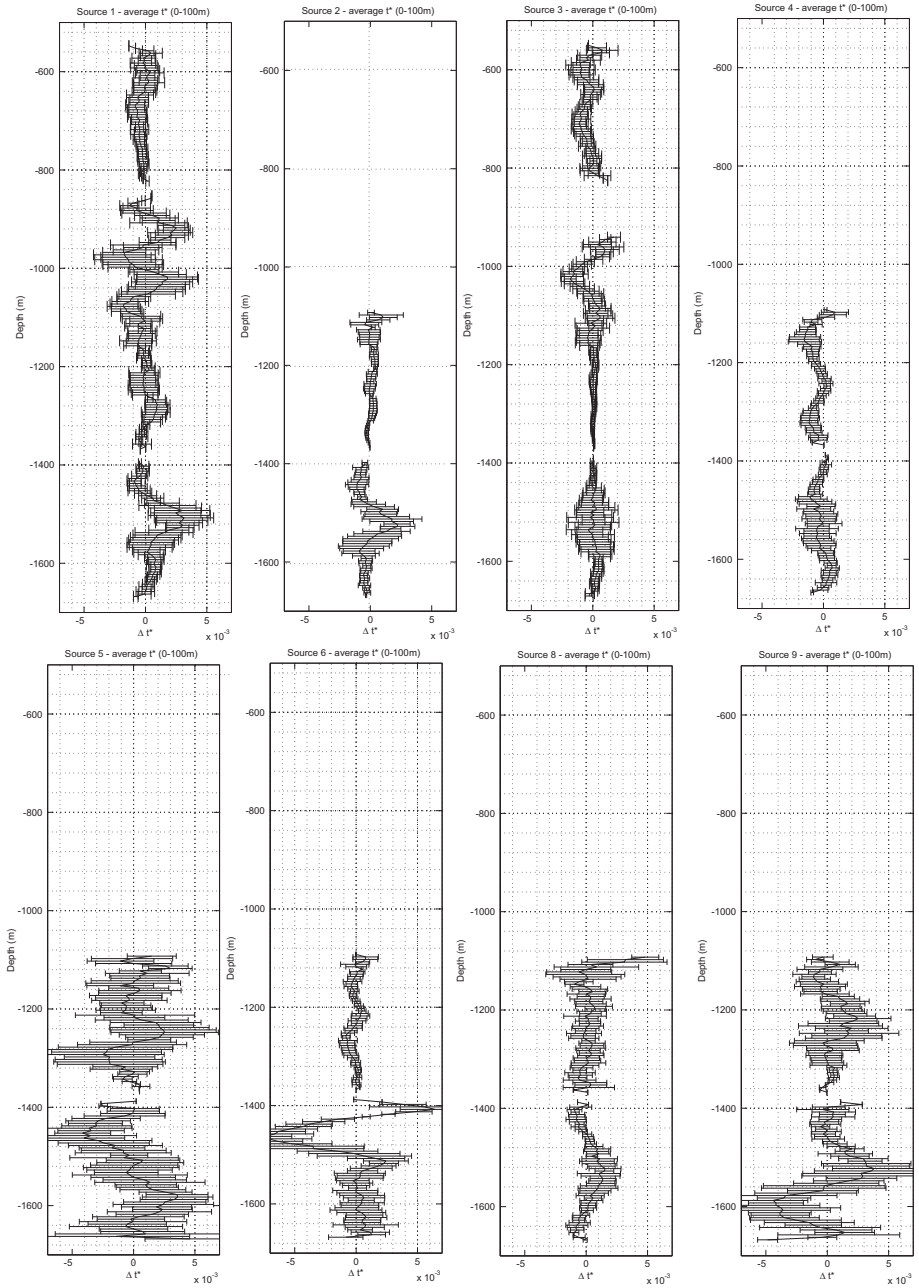

Figure 5.46: Average Δt^* results for centroid frequency (high) methodology for all sources.

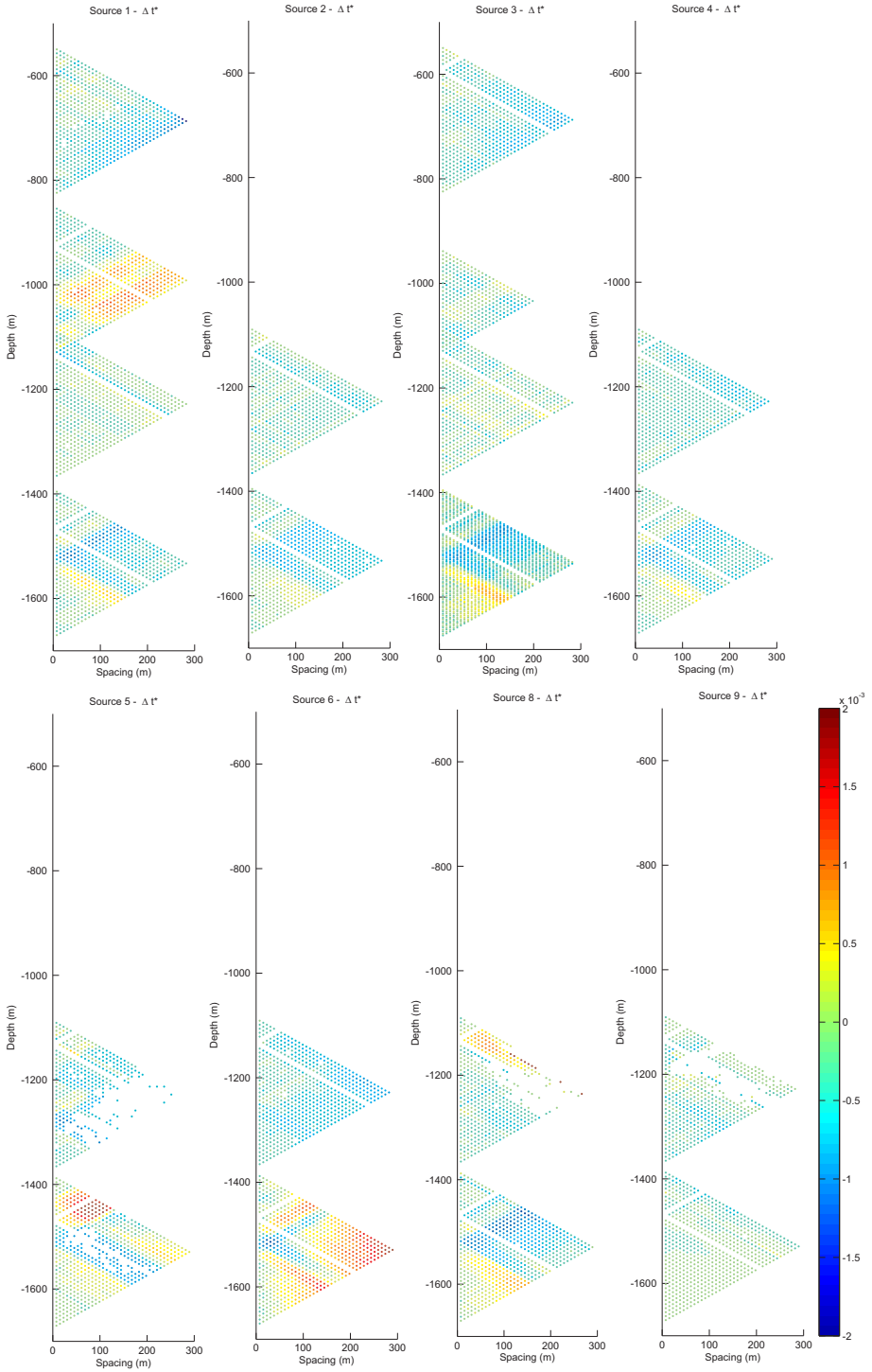

Figure 5.47: Δt^* results for Instantaneous frequency methodology for all sources.

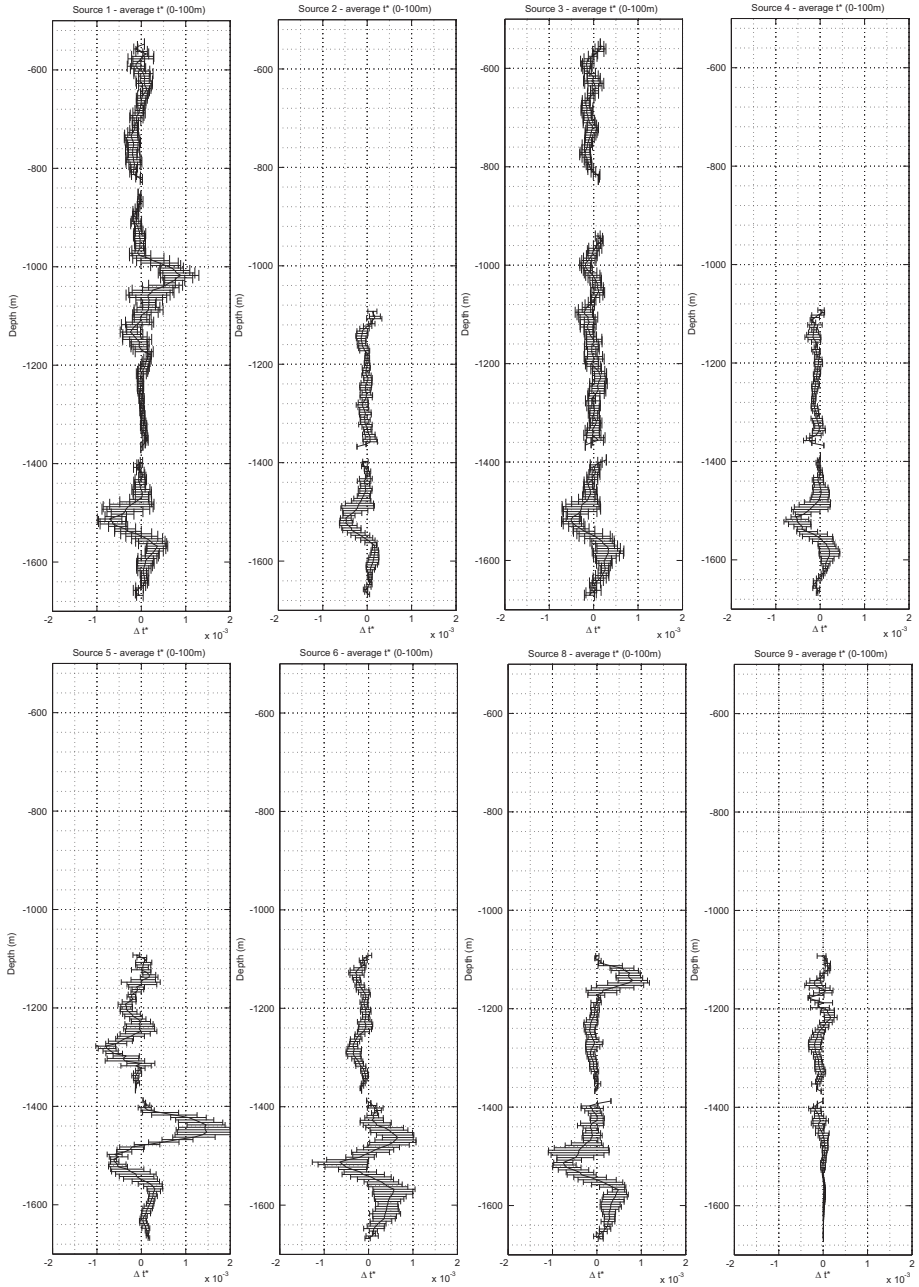

Figure 5.48: Average Δt^* results for Instantaneous frequency methodology for all sources.

5.3.5 Discussion and summary of observations

The lack of consistency between measurements of Δt^* may suggest that there are no significant changes in attenuation between vintages of data. There may be several reasons for this.

Firstly, changes in apparent attenuation may be larger than the changes in the intrinsic attenuation. With other changes in the thin-bed multiples, reflectivity and velocity it is possible that the changes in spectral contamination, scattering attenuation, travel time and frequency dependent reflectivity and transmission may dominate the measurement of intrinsic attenuation.

Secondly, the injection interval is very small and at best there is 10m thickness of injected CO_2. A 10m reservoir interval therefore may fall below the vertical resolution of the data-set. The velocity in the reservoir interval is around 2500m/s and at this velocity, a seismic wave would need to be of a frequency higher than 250Hz to travel a full wavelength for estimating Q. This is the worst case for a vertically propagating wave, however, most of the source locations are offset from the well so this minimum detectable frequency may be reduced. There has been some evidence for this behaviour in the real data examples. In Figure 5.40, where the lower centroid frequency showed no anomaly whilst the higher frequency centroid frequency produces a very strong increase in attenuation in the reservoir interval.

I showed in the parametrisation of the methodologies that the stable regression bandwidth was limited to around 100-150Hz (Figure 5.28), however, I also showed that the direct spectral ratio slopes (Figure 5.27) were stable up to 200-250Hz. In order to compare quantitatively how stable the direct spectral ratios are compared with the single vintage measurements, I compare the average spectral deviation for all spectral ratios 10 receivers apart from vintage 1 with the deviation of all of the spectral ratios from direct spectral ratios of all traces that have the same source and receiver acquisition. Figure 5.49 compares the standard deviation of the log spectral ratio for the first vintage of data (receiver separation of 10) with the standard deviation of direct log spectral ratios for 3 depth ranges. It can be seen that for the majority of depth ranges that the standard deviation of the direct log spectral ratios is considerably lower than the single vintage spectral ratios. This has the effect of having more stable spectral ratios at higher frequencies. It can also be seen in the figure that the deviation of the spectral ratio around the“notch” frequencies

has been significantly reduced. Although the source spectra may have changes between vintages, the improvement of using same ray-path spectral ratios between vintages shows that there is less deviation on the log spectral ratios. In Chapter 3 I proposed several direct methodologies for surface seismic data and assumed that source spectra must be the same between vintages of data. In the following section I outline a methodology in which the change in attenuation can be estimated directly between vintages of data, even if the source spectrum changes between strings and vintages of data, allowing the use of much higher frequencies in the analysis of the log spectral ratios.

5.4 Direct comparison

From the observations above it is clear that more stable log spectral ratios can be obtained through a direct comparison of spectra from each vintage. However, the impact of different sources must be considered. In the VSP data-set there are differences in the spectra from one vintage to the next and also between strings. By considering a single string of receivers that has the same geometry but different source spectra I will show that the absolute value of Δt^* is influenced by the change in source spectra but differences in the Δt^* for two receivers in the string represent the true change in Δt^* between them.

Consider a pair of traces from the same receiver pair for different vintages of seismic data (Figure 5.50),

$$A_1(f,t_1) = A_0(f)e^{-\pi f t_1/Q_1}, \tag{5.9}$$

$$A_2(f,t_2) = A_0(f)e^{-\pi f t_2/Q_2}, \tag{5.10}$$

$$A'_1(f,t'_1) = A'_0(f)e^{-\pi f t'_1/Q'_1}, \tag{5.11}$$

$$A'_2(f,t'_2) = A'_0(f)e^{-\pi f t'_2/Q'_2}, \tag{5.12}$$

where A_0, A_1 and A_2 represent the amplitude spectrum at the source, receiver 1 and receiver 2, Q_1 and Q_2 are the Quality factors down to receiver 1 and 2 and t_1 and t_2 are the travel times to receivers 1 and 2 ($'$ denotes the second vintage of data).

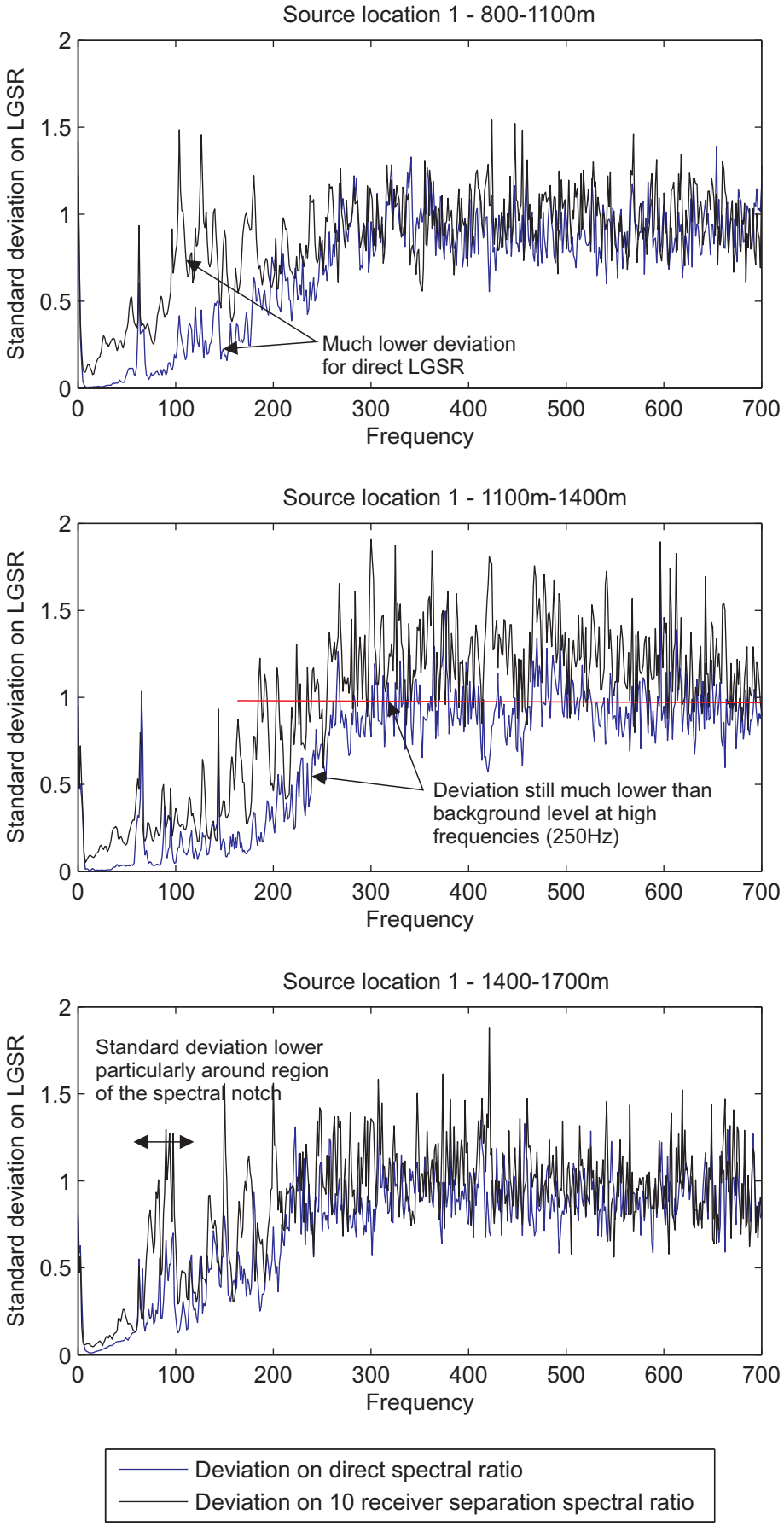

Figure 5.49: Comparison of the average standard deviation on the spectral ratio slopes between direct and single vintage spectral ratios. A receiver separation of 10 receivers was used to calculate the deviations from vintage 1.

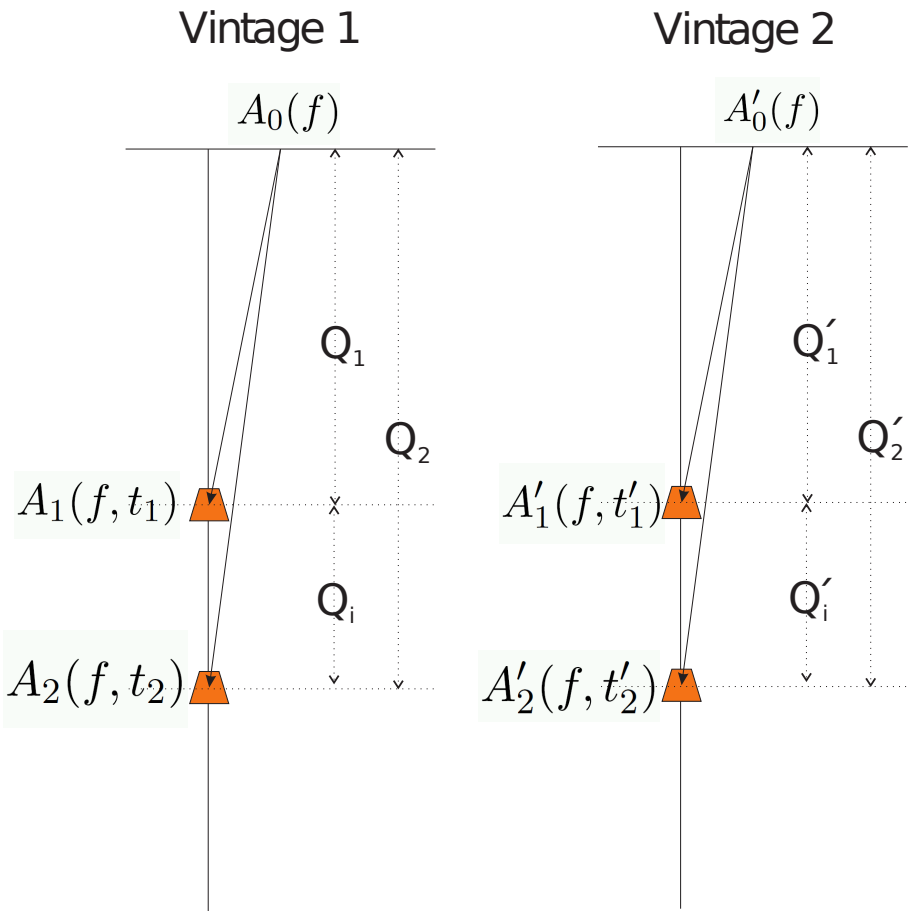

Figure 5.50: Schematic of the variables used to calculate the direct change in attenuation between vintages of data with different source spectra.

The direct spectral ratios of Equation 5.9 with 5.11 and Equation 5.10 with 5.12 yields the following equations (and assuming there is no change in travel-time)

$$\ln(\frac{A_1'(f,t_1)}{A_1(f,t_1)}) = \ln(\frac{A_0'(f)}{A_0(f)}) - \pi f t_1(1/Q_1' - 1/Q_1) \tag{5.13}$$

$$\ln(\frac{A_2'(f,t_2)}{A_2(f,t_2)}) = \ln(\frac{A_0'(f)}{A_0(f)}) - \pi f t_2(1/Q_2' - 1/Q_2) \tag{5.14}$$

By letting

$$g(f) = \frac{d}{df}\ln(\frac{A_0'(f)}{A_0(f)}), \tag{5.15}$$

$$p_1 = \pi t_1(1/Q_1' - 1/Q_1), \tag{5.16}$$

and

$$p_2 = \pi t_2(1/Q_2' - 1/Q_2) \tag{5.17}$$

the gradients of the spectral ratios as a function of frequency become:

$$g(f) - p_1 \tag{5.18}$$

and

$$g(f) - p_2 \tag{5.19}$$

The difference in the gradients can therefore be seen to equal

$$p_1 - p_2. \tag{5.20}$$

Using the equations for interval attenuation (Q_i) between the two receivers for each vintage

$$\frac{t_2 - t_1}{Q_i} = \frac{t_2}{Q_2} - \frac{t_1/Q_1}{,} \tag{5.21}$$

$$\frac{t_2 - t_1}{Q_i'} = \frac{t_2}{Q_2'} - \frac{t_1/Q_1'}{,} \tag{5.22}$$

the difference in the gradients yields

$$\frac{p_2 - p_1}{\pi} = (t_2 - t_1)(1/Q_i' - 1/Q_i) = \Delta(t_i^*), \tag{5.23}$$

where t_i^* is the interval change in t/Q.

For each string that has identical geometry for both vintages of data it is therefore possible to calculate directly the changes in attenuation, even if the source spectrum differs from one vintage to the next. In the case of the VSP analysis, several strings of data have been acquired with different spectral gradient shifts ($g(f)$) between vintages. The differences in $g(f)$ can be estimated for consecutive or overlapping strings by splining the individual direct spectral ratio slopes together.

5.4.1 Direct comparison - Synthetic results

Using the synthetic data created the direct log spectral ratios are calculated for each receiver and can be seen in Figure 5.51 (a). There are no changes in the spectra in the synthetic data, so the change in direct spectral ratio due to the change in attenuation can clearly be seen at depths below 1550m. Above 1550 some spectral contamination can be seen from the change in up-going energy. Spectral ratio slopes are calculated at each depth, giving an estimate of the total change in Δt^* to that depth. This profile of Δt^* vs depth can be seen in Figure 5.51 (b), along with the same profile but after a 3 point smoothing. The Δt^* can be seen to step at a depth of 1520m. To find the change in attenuation between each receiver (interval Δt^*), the differences between consecutive receiver pairs is calculated (Figure 5.51, (c)), yielding an increase in attenuation in the injection interval.

5.4.2 Direct comparison - Real Data

In order to look at the direct comparison of the real data I first of all look at the direct log spectral ratios of source location 1 for data acquired above and at the injection interval. I use a 1 second FFT in order to gain good frequency resolution. A Stockwell transform is not used in this analysis as the unwanted effect of spectral leakage will hinder attempts to estimate the spectral coherence accurately. Figure 5.52 displays an example of the direct spectral ratio slopes from source location 1. The differences in spectral ratios across the window relate to any change in attenuation. For the direct spectral ratios near the injection interval a change in the spectral content can be seen, particularly at higher frequencies, suggesting a change in t^* around the injection region.

The standard deviation of the spectral content shown in Figure 5.49 shows that in the

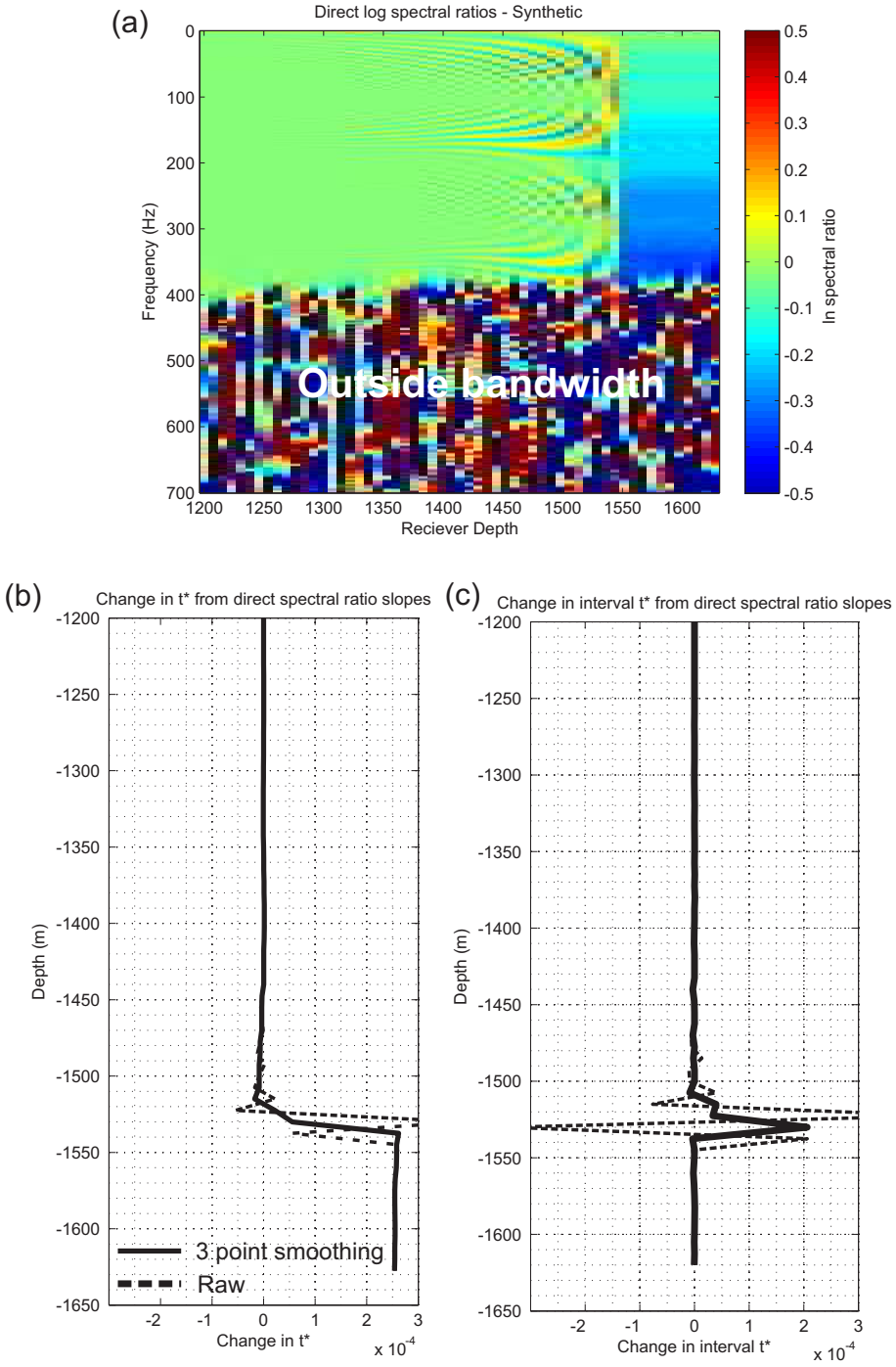

Figure 5.51: Results of the direct methodology for the synthetic example shown earlier in the chapter. (a) The direct spectral ratios of the raw data. (b) The cumulative change in t^* down that receiver (dotted) and smoothed change (solid). (c) Gradient of (b) giving the interval change in t^* between receivers. The expected overall change in t^* is 0.0025.

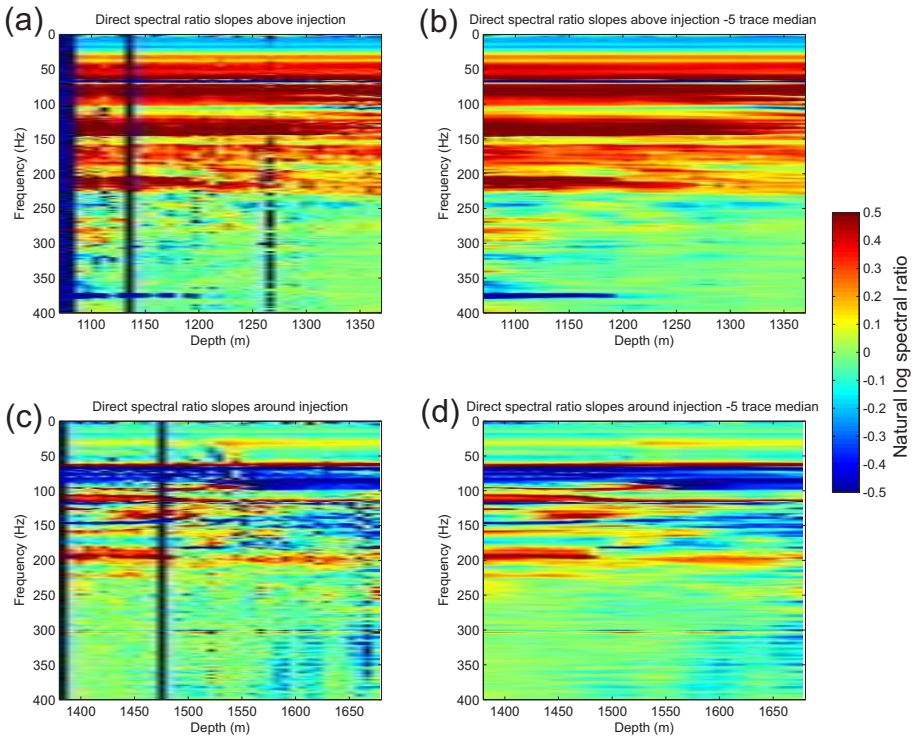

Figure 5.52: Direct spectral ratios for source location 1 for a string of geophones above the injection interval (a,b) and around the injection interval (c,d). The direct spectral ratios on the right (b and d) have been median filtered in the depth direction to reduce the number of unstable spectral ratios to highlight the decrease in higher frequency energy relative to lower frequency energy below the injection region (around 1500m).

direct methodology there are usable bandwidths potentially up to around 350Hz. For this reason I will calculate the direct change in t^* using a bandwidth of 10Hz-350Hz. To ensure that the most stable frequencies are used to calculate spectral ratio slopes a weighting function is included in the inversion. In this case each frequency will be weighted according to average standard deviation in the spectral ratio at that frequency for each string of 40 receivers.

Using source location 3 as an example, I calculate the change in t^* from shot-point to each receiver, for each pair of strings where the acquisition geometry is identical from one vintage to the next.

Each colour in Figure 5.53 corresponds to an identical matching pair of receivers. The absolute value of these t^* values still contain the contribution of the source spectral differences ($g(f)$, equation 5.19). These shifts are accounted for in two ways. If receiver locations overlap between different strings of data then the mean of these values can be subtracted to find the shift. When they do not overlap, but are located adjacent to one another, the upper 5 and lower 5 receivers are used to calculate the relative shift. The

corrected changes in Δt^* are also shown in Figure 5.53. The absolute values of these Δt^* still have no relevance, but the changes with depth indicate where there have been changes in attenuation.

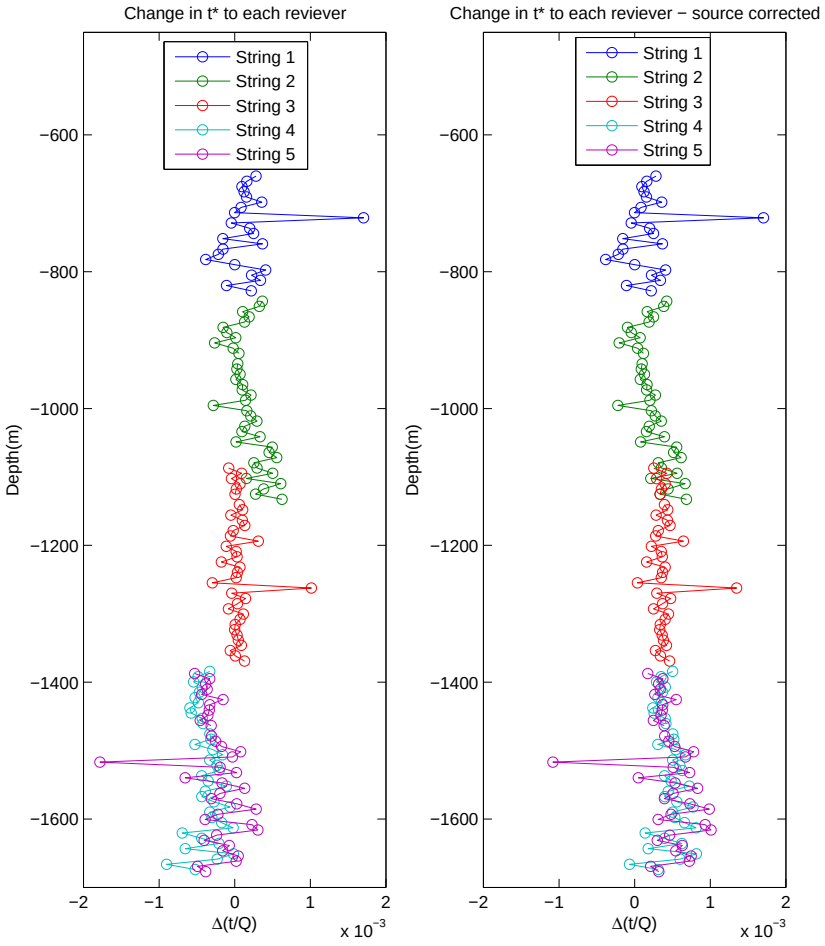

Figure 5.53: The calculated direct change in $\Delta(t/Q)$ for each geometrically identical string of geophones (left) and the same data plotted after correction for relative source terms $g(f)$ (right).

The corrected Δt^* are calculated for all of the source locations (Figure 5.54), with any two receivers that are within 0.5m of each other used to calculate direct spectral ratios. By doing this, the amount of data is maximised as acquisition between vintages only differs by 10's of centimetres. Results of all source locations can be seen in Figure 5.54 and there are strong correlations between values of Δt^*. For the majority of source locations a decrease in t^* can be seen between 1000m and 1400m followed by an increase in attenuation from as high as 1400m, peaking at around 1530-1600m depth - the depth of the injected CO_2.

All source locations apart from source location 5 show an increase in attenuation around

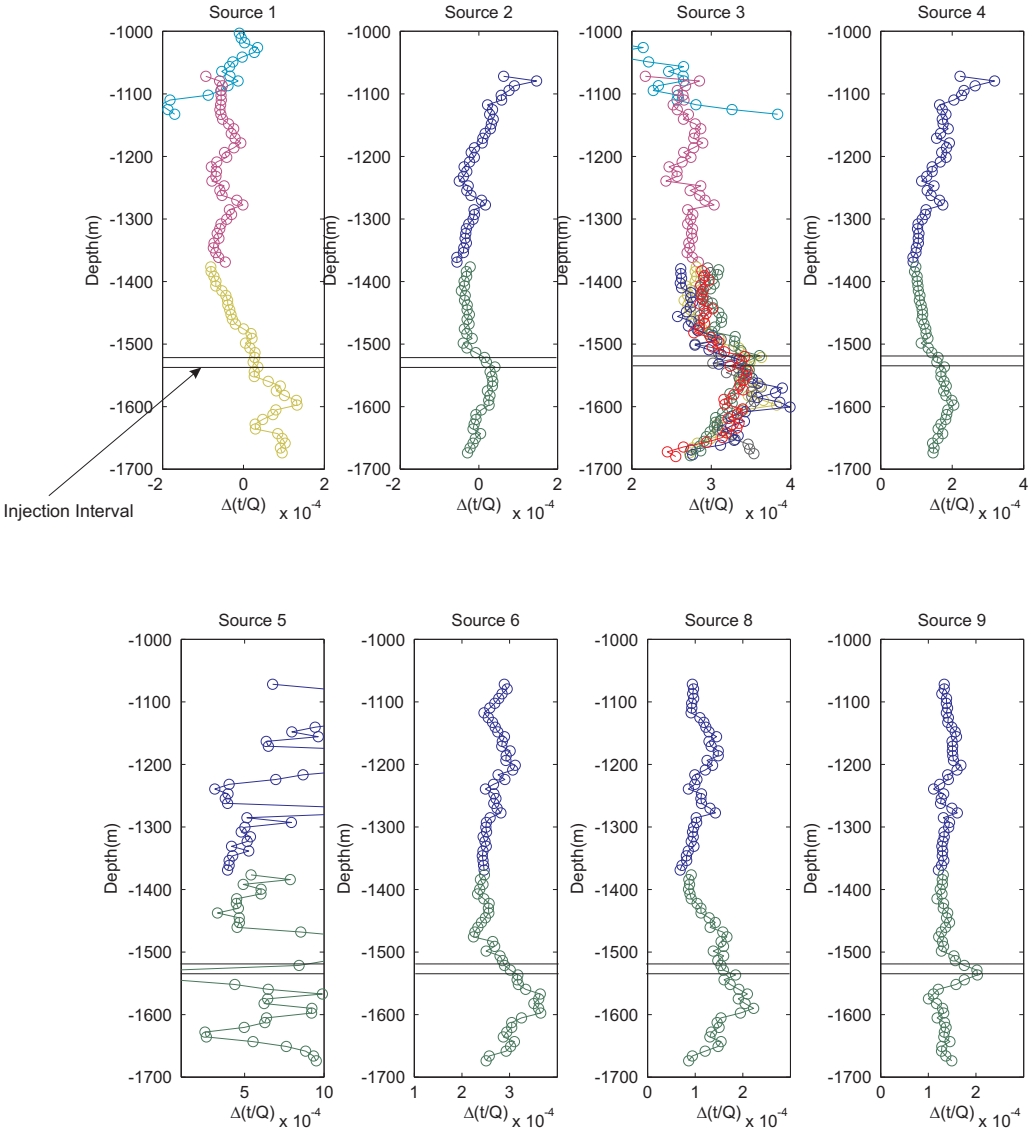

Figure 5.54: The change in Δt^* for all source locations after correction for relative source terms $g(f)$.

the injection interval. To compare these depth vs. Δt^* profiles for each source location, values are binned at common depth points in a rolling window of 20m every 10m. The interval t^* values are then calculated between consecutive depths. These are plotted in Figure 5.55 and are very noisy as it is effectively the numerical gradient being calculated. There is some indication of an increase in attenuation near to the reservoir interval. It may be possible to smooth the data further, however, this would mean losing the vertical resolution of the data and incorrect recovery of the magnitude of attenuation.

A more straight forward approach would be to calculate the change in t^* for an average value of Δt^* above and below the reservoir. In Figure 5.56 I take three of the small offset (and hence fewer assumptions about ray-paths) profiles and average them to get a profile of Δt^* along with uncertainties. This Figure clearly highlights that there is a significant anomaly occurring at the reservoir interval. It can be inferred from this that there is a maximum increase in Δt^* of around 0.6495×10^{-4}. This also indicates that there could be a decrease in attenuation above the reservoir at depths of around 1100m-1350m. Uncertainties on the estimate of Δt^* are $\pm 0.2000 \times 10^{-4}$. These results appear to be more coherent than those produced from the absolute methodologies, showing that extending the bandwidth through smaller errors in the log spectral ratios is beneficial in measuring time-lapse changes in attenuation.

5.5 Interpretation

I have shown in Figure 5.56 that an increase in Δt^* of 0.6495×10^{-4} has been observed across the reservoir interval for the near offset VSPs. This is compared with the average percentage change in velocity measured at the same source locations (Figure 5.60). There is good correlation between a peak decrease in velocity of around 5% and the maximum change in Δt^* as a function of depth.

Daley et al. (2008) showed using high resolution cross-well tomography that the thickness of injected CO_2 is around 5-7m (Figure 5.58). If we assume that the change in Δt^* of 0.6495×10^{-4} is purely due to an injection region 7m thick, then the change in attenuation $(1/Q)$ would be 0.0240 in the injection region, meaning that the quality factor (Q) in vintage 2 must be less than 41.6.

The assumption of no change in travel time is addressed by considering this a minimum value of Q generated from the results. In order to produce this magnitude change in t^*

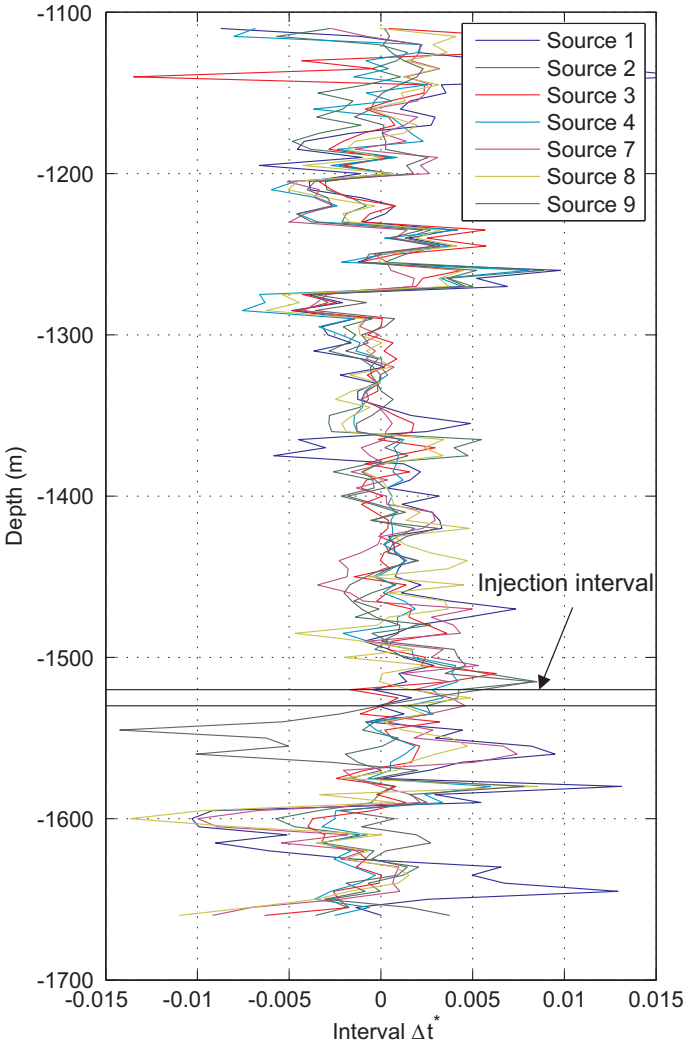

Figure 5.55: The change in $\Delta(t^*)$ for 10m intervals.

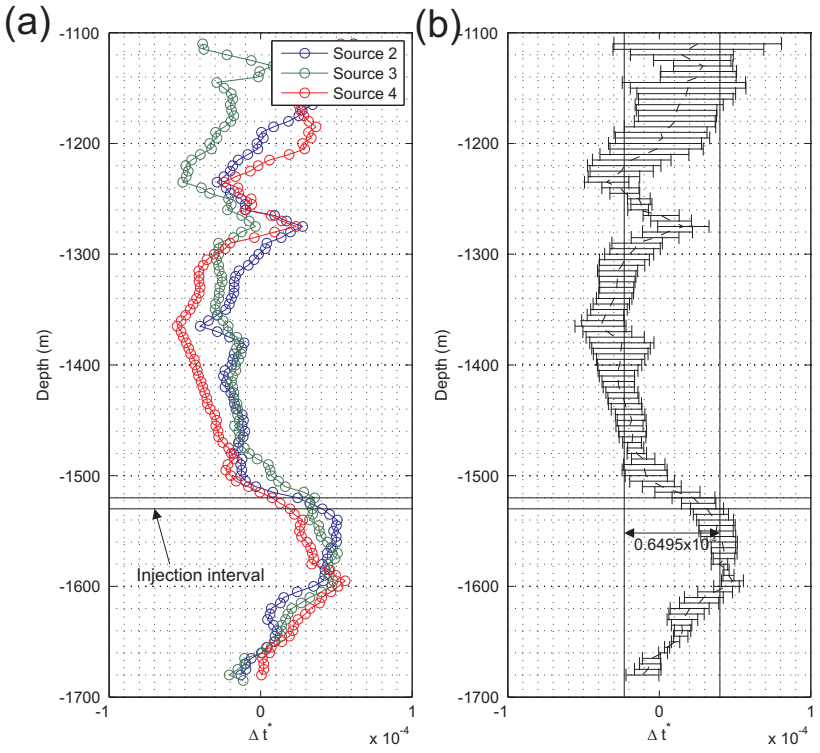

Figure 5.56: The change in $\Delta(t^*)$ to (a) each depth for the 3 similar small offset VSP locations and (b) the average Δt^* to each of the receiver locations.

purely due to the measured change in velocity, the quality factor would have to be much less than Q=20 (Figure 4.18, Chapter 4). The error on the change in attenuation with Q_2=40 would be 2×10^{-3} - a 10 percent error.

A full quantitative interpretation is not viable here as core data with information about the behaviour of the rock as a function of effective pressure is not available. Therefore the change in attenuation and velocity can only be interpreted as a function of CO_2 gas saturation. The 1D RPS model is used to calculate the properties of a typical high permeability, high porosity sand (Table 5.1). Velocity and attenuation as a function of the percentage saturation of gaseous, super-critical and liquid CO_2 for a correlation length of 1m can be seen in Figure 5.59. Attenuation and velocity as a function of correlation length and super-critical CO_2 saturation can be seen in Figure 5.60. Attenuation results would suggest an increase in CO_2 saturation of between 10 and 30% using correlation lengths of 0.1m-0.6m (as these are the only ones that predict the right magnitude of effect), whilst the velocity changes suggest an increase in CO_2 saturation of 5-10%, but with less dependence on correlation length. Discrepancies in these values are potentially due to the lack of information about the pressure dependence of the rock.

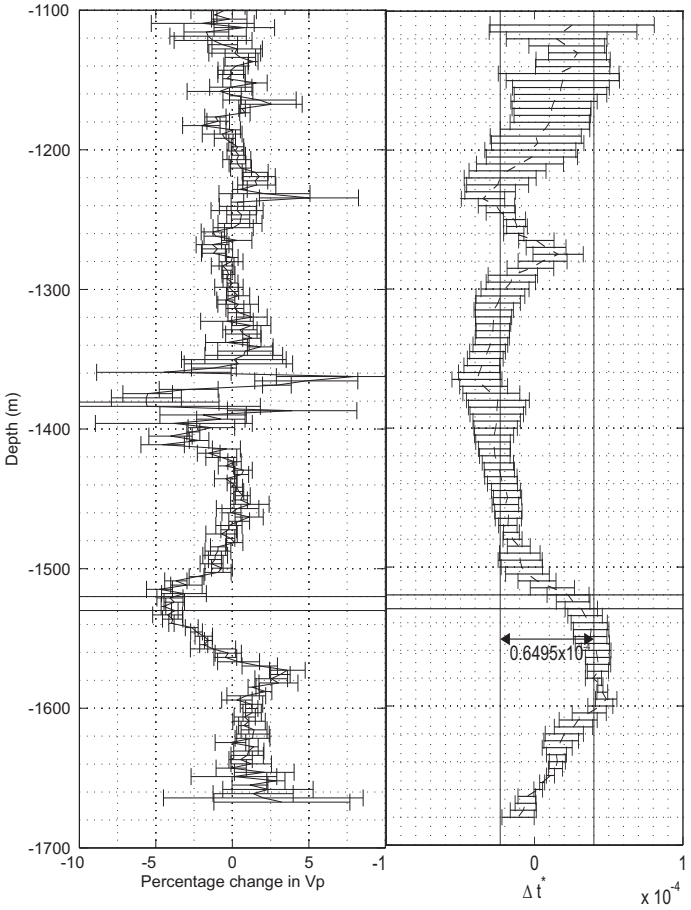

Figure 5.57: Comparison of percentage change in velocity and change in t^* with depth.

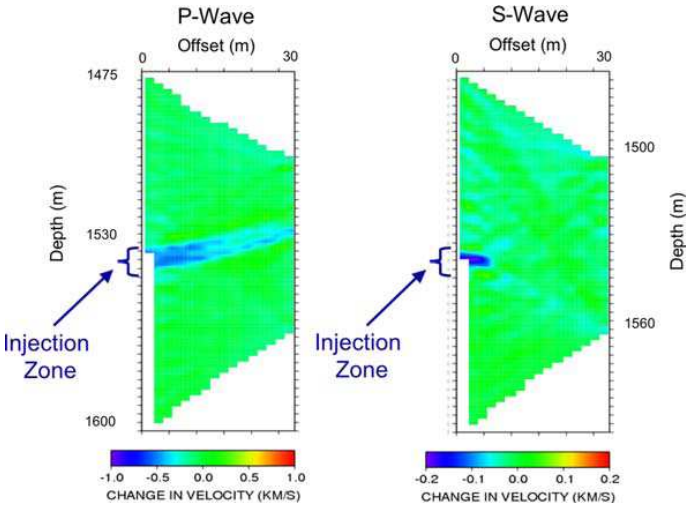

Figure 5.58: Results of the cross well P-wave velocity and S-wave velocity tomography (Daley et al., 2008).

Table 5.1: Rock properties used to generate RPS model, taken from Xu (2006)

Property	**Value**
Mineral	
Bulk modulus (K_0, [GPa])	38
Shear modulus (μ_0, [GPa])	28
Density (ρ_0,[kg/m^3])	2500
Rock	
Dry bulk modulus (K_{dry}, [GPa])	6
Dry shear modulus (μ_{dry}, [GPa])	6
Porosity (ϕ)	0.36
Permeability (κ)	2 Darcy, 2×10^{-12} m^2
CO_2 **(gas)**	
Bulk modulus [GPa]	0.025
Density [kg/m^3]	124
Viscosity [Pa.s]	1.70×10^{-5}
CO_2 **(liquid)**	
Bulk modulus [GPa]	0.066
Density [kg/m^3]	700
Viscosity [Pa.s]	8.50×10^{-5}
CO_2 **(super critical)**	
Bulk modulus [GPa]	0.046
Density [kg/m^3]	620
Viscosity [Pa·s]	7.00×10^{-5}
Water	
Bulk modulus [GPa]	2.25
Density [kg/m^3]	997
Viscosity [Pa·s]	$1\times10^{-3}/1\times10^{-3}/8\times10^{-4}$

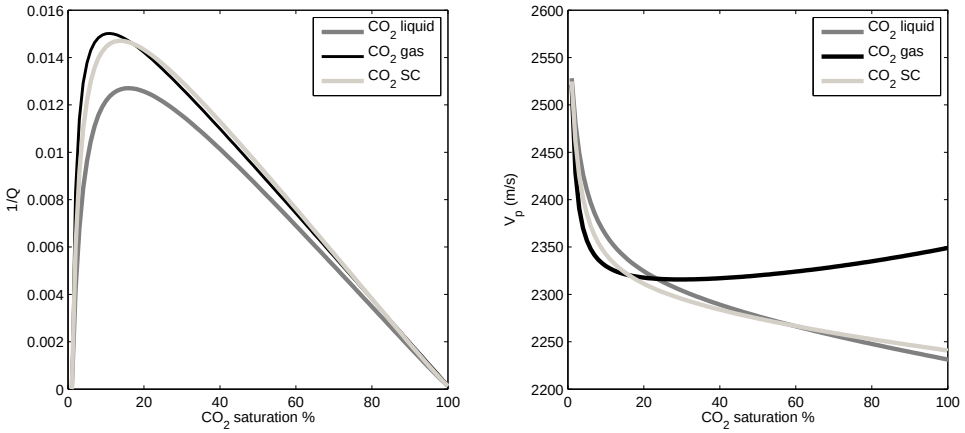

Figure 5.59: Example of velocity and attenuation relationships from RPS model using a correlation length of 1m. SC = Super-critical.

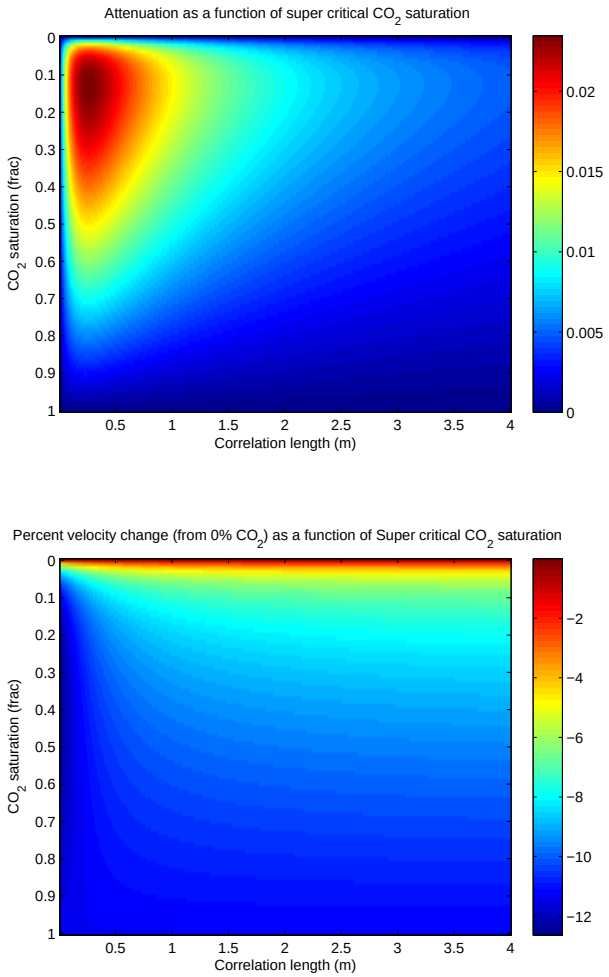

Figure 5.60: Velocity and attenuation changes as a function of CO_2 saturation and correlation length.

Without full core data it is not possible to calculate quantitatively the saturation of CO_2 as a full interpretation would be dependent on the behaviour of the rock as a function of effective pressure, however, it can be seen that model-consistent changes in attenuation and velocity have been recovered.

5.6 Discussion and conclusions

Through analysis of the synthetic and real data-sets we have seen that we are unlikely to be able to estimate the correct spatial distribution and magnitude of attenuation changes for such a small injection interval. However, synthetic data suggested that the attenuation change should still be detectable and we have seen evidence for this also in the real data.

By using a median filter to separate the up-going and down-going wavefields, high frequency noise was introduced into the spectra. This is a concern, especially when the spectral content is low compared with the magnitude of the noise introduced. There is, however a trade off between the increased high frequency noise and the reduction of spectral contamination from changes in the up-going reflected arrival, as demonstrated by the synthetic example.

Absolute values of attenuation were measured and contained a large component of apparent attenuation. Large negative values of attenuation were observed but were repeatable between vintages of data.

The differences in attenuation changes observed through the various methodologies suggest that changes in apparent attenuation may cause errors on the measurement of intrinsic attenuation changes. This was particularly true of the instantaneous frequency methodology, as it disagreed with both of the other methods. I have shown in Chapter 4 that a change in amplitude can cause errors in attenuation estimates through the instantaneous frequency matching which could be one of the possible reasons for discrepancies.

Through a new method that allows for the direct analysis of waveforms between vintages, even when source spectra are different, I have shown that there is a decrease in the deviation of spectral ratio slopes, allowing the inclusion of higher frequencies into the data. Results of this analysis showed much more coherent anomalies for all of the source locations.

There was good correlation between an increase in attenuation and a decrease in velocity,

which would be indicative of an increase in the CO_2 concentration predicted by an RPS model. With additional information from core and laboratory experiments it would be possible to perform a fully quantitative interpretation of the results with depth.

Differences in ray-paths between sources and receivers make it difficult to divide Δt^* values by the correct change in travel-time to estimate the change in $1/Q$. However, the direct changes in t^* measured would be an ideal input for the use of attenuation tomography. Although there are unlikely to be enough ray-paths generated from analysis of just the direct wave it may also be possible to calculate the direct changes in attenuation from reflected up-going and down-going waves.

From this Chapter I draw the following conclusions,

- Through the generation of complex synthetic data, I have shown that changes in attenuation may be feasibly detected but not quantified robustly from VSP data for a 10m thick injection of CO_2.
- I have presented a damped inversion strategy for calculating changes in attenuation as a function of depth from the "tartan triangles".
- Wave field separation through the use of median filters can have both negative impact due increase in high frequency noise content and a positive impact by decreasing spectral contamination caused by up-going energy.
- Single vintage attenuation measurements have been made and show that the effective attenuation contains a large component of apparent attenuation. These large components of apparent attenuation were shown to be repeatable between vintages.
- In this study, the direct spectral ratios have a lower deviation than the single vintage spectral ratios allowing higher frequencies to be used in a regression with less uncertainty.
- I introduce and apply a methodology to estimate directly attenuation from VSP data, where difference sources are used between vintages of data, resulting in more coherent estimates of attenuation across all source locations.
- Observed measurements of attenuation and velocity changes qualitatively agree with those predicted from a random patchy saturation model.

Chapter 6

Surface Seismic Data - Case Study

In this Chapter I look at the feasibility of using the methodologies outlined in Chapter 3 to measure changes in attenuation from a real surface seismic time-lapse data-set. I will begin by introducing the reservoir, production history and the data. I then investigate the feasibility of detecting changes in attenuation from this data set. This is primarily achieved via the generation of a synthetic CMP that resembles the real data-set. Four realisations of realistic changes in attenuation are considered and analysed using the methodologies described in Chapter 3, with the aim of determining what magnitude of attenuation changes are detectable and which methodology is more robust. This feasibility study also considers the quality of the real data. By comparing the average source repeatability and the average direct attenuation attributes along with standard repeatability metrics, an estimate of the limitations in detectability can be made.

I then go on to analyse a portion of the data-set where production, water injection and gas injection are all under-way. Each methodology presented requires careful parametrisation, which is shown in detail. Results from the various methodologies in Chapter 3 are then compared in an attempt to determine which methodology performs the best. This is achieved through the analysis of the errors produced in the inversions, the scatter in the final attenuation maps and comparison with other conventional, and presumed robust, attributes such as the TWT change, amplitude change and AVO (Amplitude vs. Offset) change.

6.1 Background

The Magnus reservoir is a mature reservoir, discovered in 1974 at a depth of 2.8km, it forms part of a easterly dipping rotated fault block underneath the northern North Sea (Figure 6.1). The reservoir itself is composed of several sand intervals, the thickest of which is the Magnus Sand Member (MSM) (Watts et al., 1996). Average pay-thickness of the reservoir is around 65m, however, the reservoir pinches out to North West as can be seen from the cross section in Figure 6.1. Oil produced is typically light with an API gravity of 39°. Production began in 1983 and has been enhanced through various stages of water injection and more recently, combined water and gas injection.

The two vintages of data used in this study were acquired in 2001 and 2007. The 2001 data were acquired prior to any gas injection into the reservoir interval whilst the 2007 data were acquired after several iterations of water-alternating-gas injection (WAG). The desirable outcomes of any 4D survey are to map the fluid movement and pressure changes within the reservoir, ideally quantitatively. The 2001 and 2007 data-sets have been processed simultaneously (by CGG-Veritas) to ensure that processes have the same impact on data from one vintage to the next. Data have been provided in the most basic form that BP had available, but have had various processing steps applied to it. A base map and examples of stacked in-line and cross-line profiles can be seen in Figure 6.2.

Time-lapse studies have been carried out on the Magnus reservoir previously in order to try and recover changes in reservoir pressure. Watts et al. (1996) compared acoustic impedance on two vintages (1983 and 1992) of time-lapse seismic data. They concluded that the interpretation of 4D seismic data must be done with great care and involve the integration of seismic and engineering data. For this reason, I have acquired several outputs of reservoir simulations run at BP including the predicted change in pore pressure and gas saturation. These models are plotted in Figure 6.3 along with the location of some of the WAG injectors, water injectors and producers located in this region. For the rest of this chapter, water and gas injectors are plotted as circles, water injectors as squares and producers as a diamonds. The reservoir models will provide useful information for the comparison of seismic attributes. We have seen in earlier chapters that attenuation has been shown to increase to a maximum value at around 20% gas saturation. The reservoir predictions of gas saturation in Figure 6.3 would suggest that large changes in attenuation should ocurr around the WAG injectors. The models also indicate that there

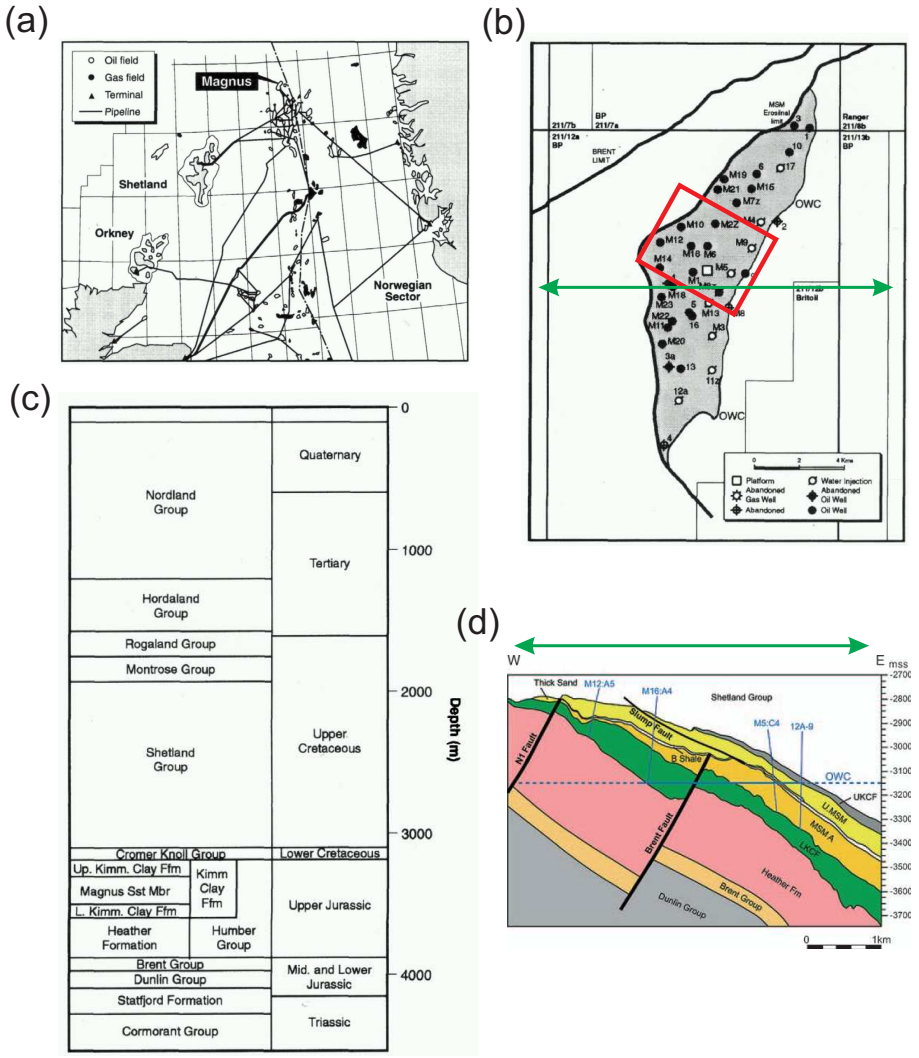

Figure 6.1: (a) Location of Magnus reservoir (Watts et al., 1996) , (b) Outline of Magnus reservoir (Watts et al., 1996) with location of data analysed in this chapter (red square), (c) Stratigraphy surrounding the Magnus reservoir (Watts et al., 1996) and (d) a cross section through the Magnus reservoir (MacGregor et al., 2005).

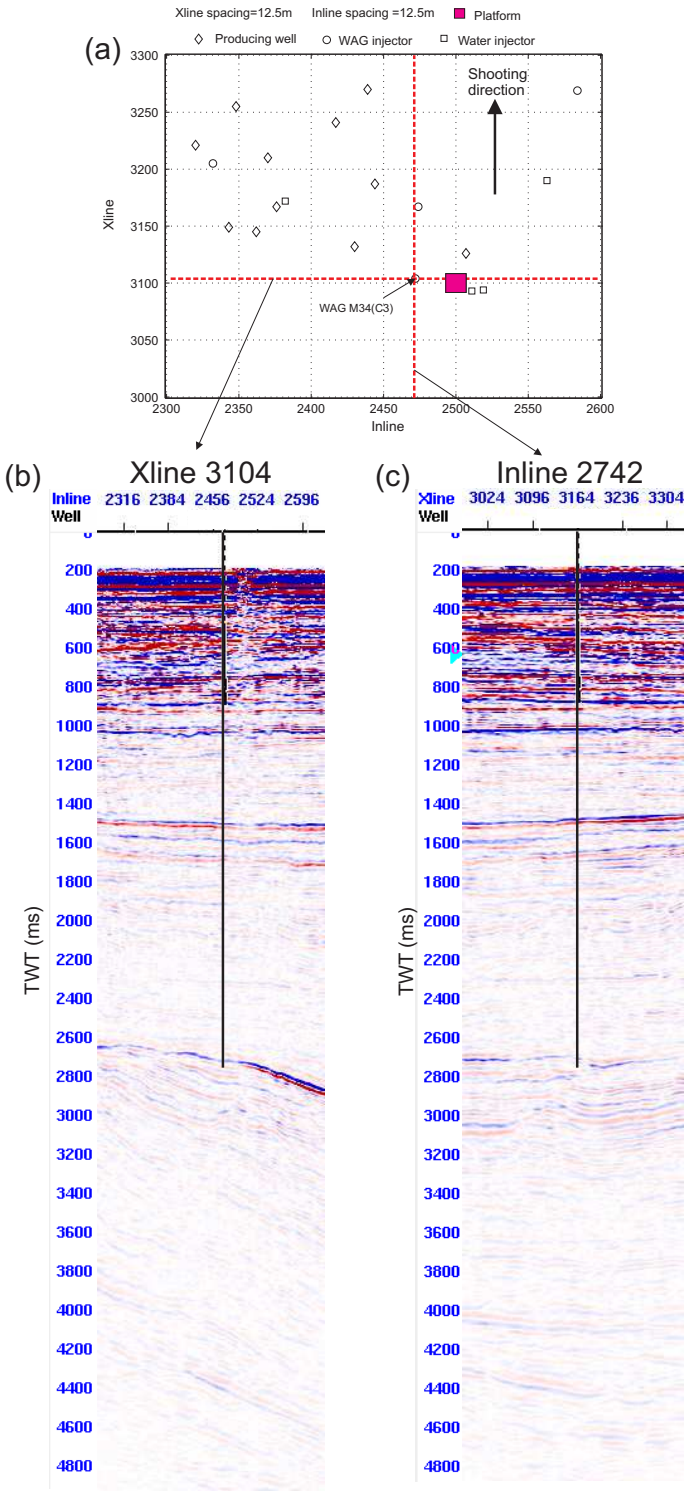

Figure 6.2: (a) Base map of the seismic data used in this study, (b) The stacked section of Xline 3104 (SEG normal polarity) and (c) inline 2742. Xline and inline spacing is 12.5m (12.5m×12.5m bin size).

are both large increases and decreases in reservoir pressure. Such changes may not only affect attenuation in the reservoir but may also affect the attenuation above the reservoir.

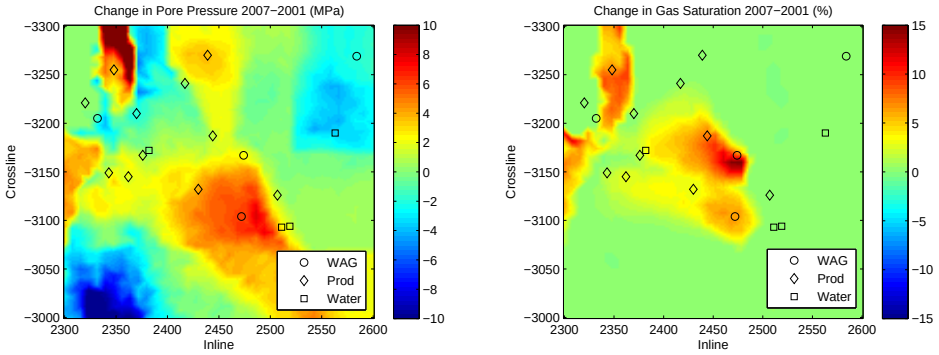

Figure 6.3: Reservoir model predictions of the average change in pore pressure in the reservoir interval (left) and average change in gas saturation (right) between 2001 and 2007. Data from E. Laws, BP, personal communication.

6.2 Synthetic study for feasibility

From the attenuation relationships in Chapter 2 I decided to use Q=100 for fully water or oil saturated rock and Q=30 for the post-injection case, assuming a 20% increase in gas saturation. Synthetic data are created to mimic the seismic data using sonic-log and seismic derived velocities using a constant Q of 100. Four realisations of changes in attenuation are then considered, varying only in thickness of the injected region (Q=30).

6.2.1 Creating the synthetic data and models

Before synthetic data are computed, V_p, V_s and density models must be created. This was achieved by combining the sparsely sampled interval velocities calculated from the stacking velocity (using Dix's equation) and the higher resolution information from the sonic logs (Figure 6.4). The density was estimated using Gardner's relationship for sandstones (Equation 6.1) and the shear wave velocity calculated using the empirical relationships of Han & Nur (1986) (Equation 6.2).

$$\rho[\mathrm{g/cc}] = 1.7411 V_p^{0.25}[\mathrm{km/s}] \tag{6.1}$$

$$V_s[\mathrm{km/s}] = 0.853 V_p[\mathrm{km/s}] - 1.137 \tag{6.2}$$

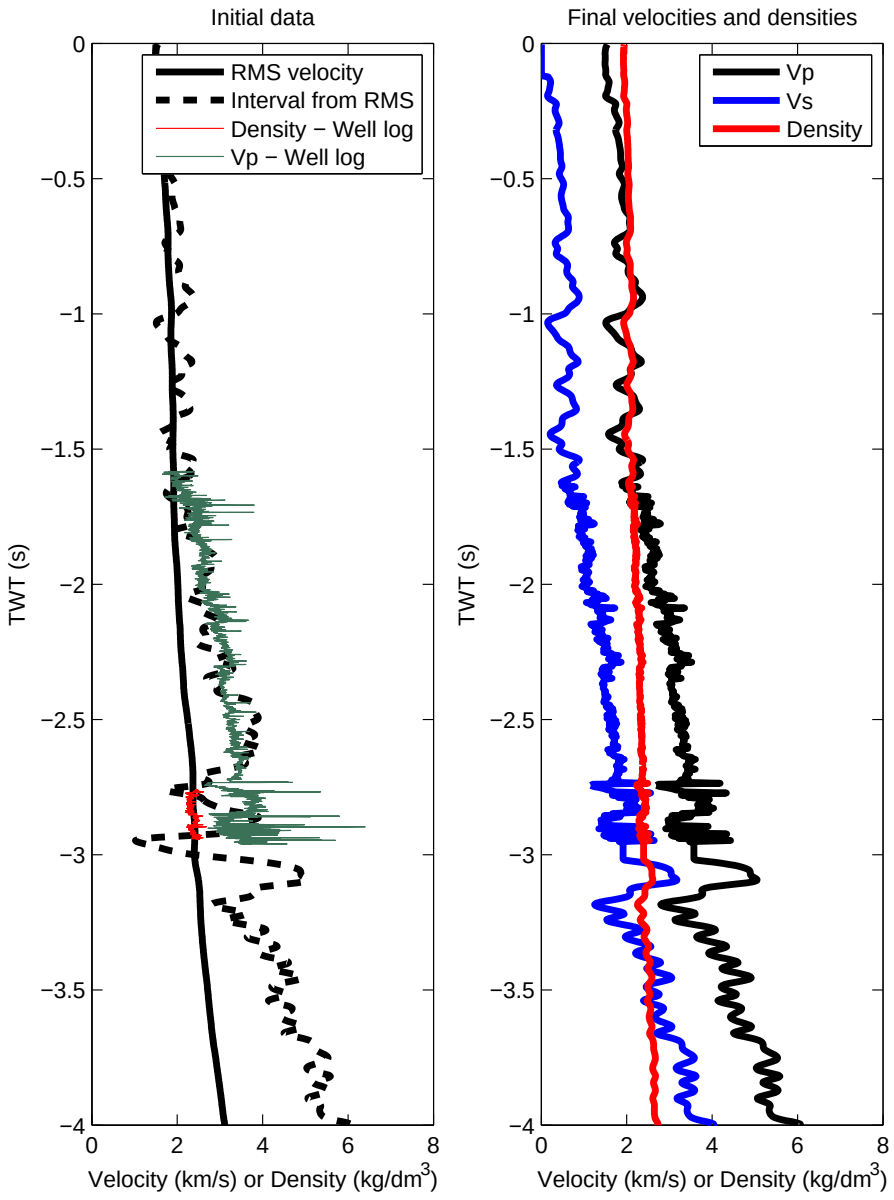

Figure 6.4: Left: Data used to create the model for the feasibility study including the RMS velocities, Interval velocities derived from the stacking velocities and the check shot corrected V_{p} and density from the well log. Right: The V_{p}, V_{s} and ρ models derived via empirical relationships.

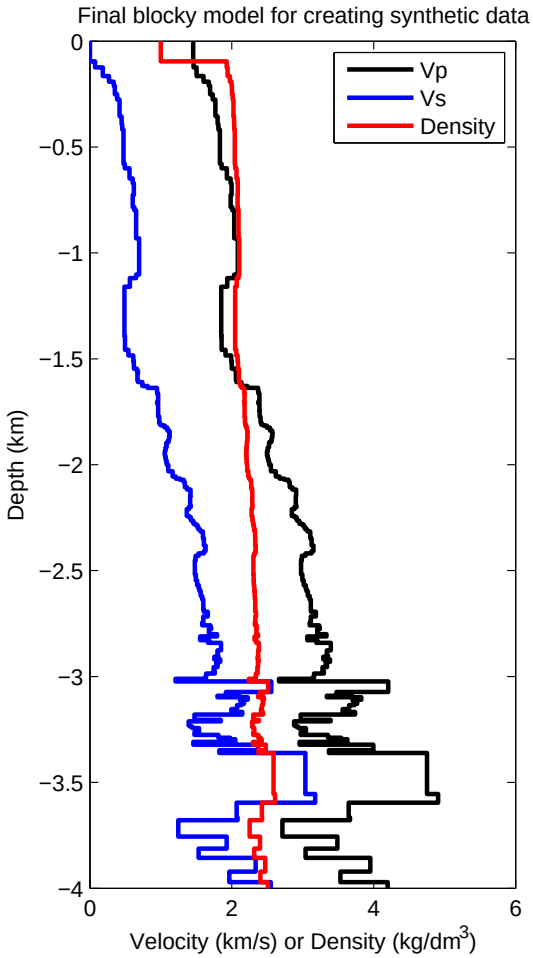

Figure 6.5: The final blocky models that were used to compute the synthetic seismogram.

The resulting models were then averaged between major changes in impedance to produce a blocky model for synthetic generation, with the section surrounding the reservoir having a more detailed reflectivity than elsewhere (Figure 6.5). Synthetic traces are calculated using a 1D reflectivity code (**skb**), producing a CMP sampled at 4ms with a fold of 60 and offsets ranging from 175m to 3125m every 50m using a 35Hz Ricker wavelet as the source. As with previous synthetic generation, a free surface is assumed but all inter-bed multiples are calculated. The pressure response is measured and used in all of the analysis. This synthetic CMP provides us with the same geometry as the CMPs from the prestack time migrated data. Figure 6.6 compares synthetic data to the real data (constant Q of 100). Although there are still large differences between the real and the synthetic data, the experiment is designed to look at the feasibility of calculating attenuation changes on a more complex synthetic example resembling the real data-set.

Four time-lapse scenarios will be tested where the constant $Q = 100$ will be used as the reference (or pre-injection) data-set. Four more synthetic CMPs are calculated, all of which assume a maximum change in attenuation to $Q = 30$ (post-gas injection). The Magnus sands can range from 10m up to 130m with an average pay-thickness of 65m so the four injection scenarios tested change only by the thickness of the region where attenuation changes occur. Four thicknesses (37.5m, 63m, 82m and 107m) are tested (the range of thicknesses located around the injectors of interest) and these models are displayed in Figure 6.7 and will be referred to as Thickness 1 (GAP1), Thickness 2 (GAP2), Thickness 3 (GAP3) and Thickness 4 (GAP4).

The synthetic CMPs produced from each of the four post-injection models are compared in Figures 6.8 and 6.9. Figure 6.9 shows the result of the subtraction of the constant Q=100 synthetic data (Figure 6.6) from the post-injection models and highlights greater magnitude changes being associated with the larger thickness of attenuation change.

Seven reflections were chosen at which to measure changes in attenuation; one above the reservoir where no changes would be expected (Horizon 1, Figure 6.10) one at the top reservoir (Horizon 2) and 5 more (Horizon 3-7) inside and below the region of attenuation change. Horizon 2 should in theory also show no change in attenuation, but we have seen from Chapter 4 that attenuation change in the layer beneath a reflection can contaminate the estimate of attenuation from that reflector.

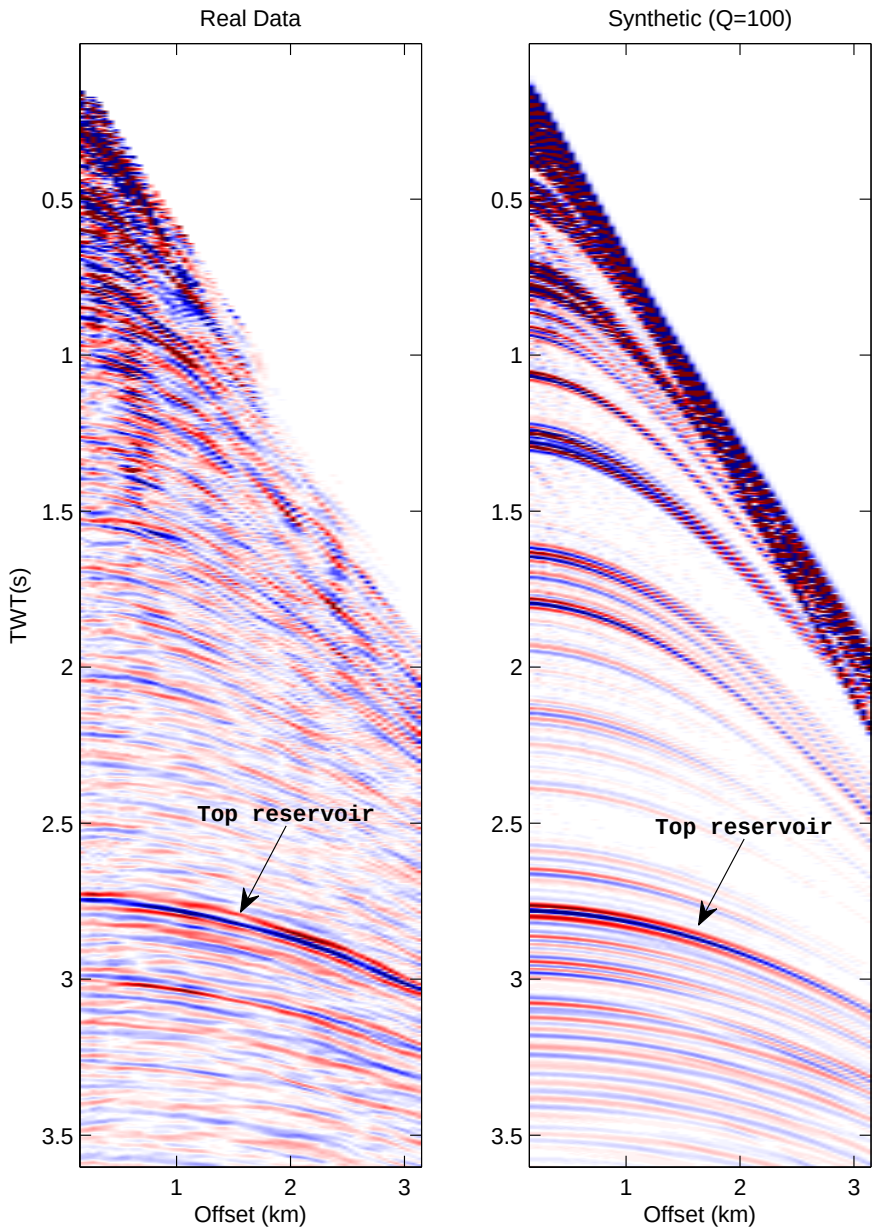

Figure 6.6: Synthetic data created in attempt to replicate real data from the Magnus field. Top reservoir is highlighted.

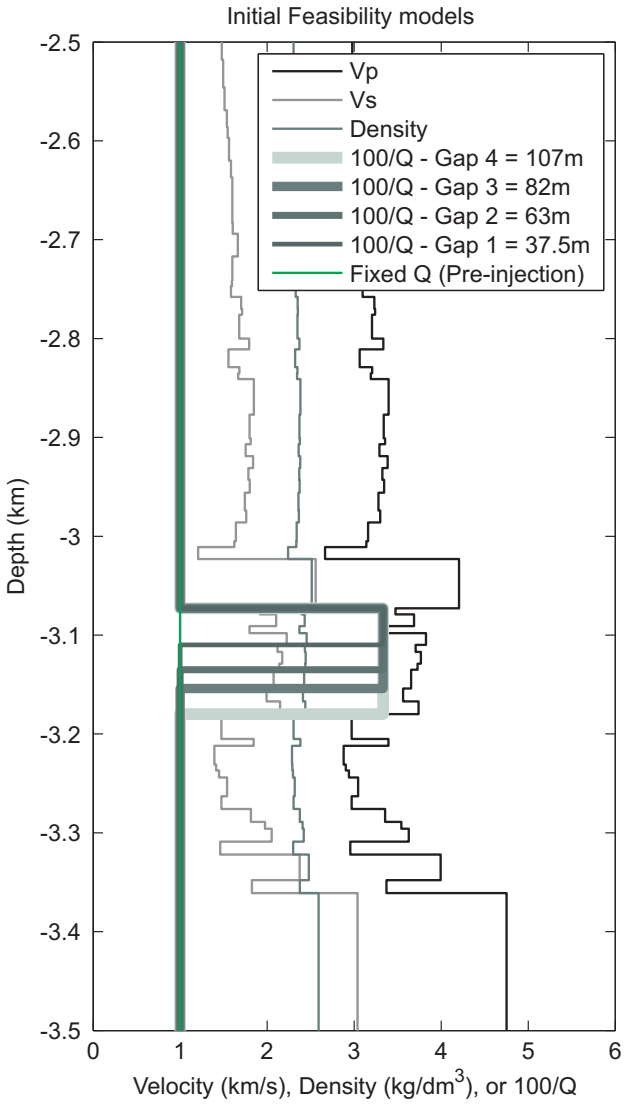

Figure 6.7: The models used in the feasibility study are shown in various shades of green. Velocity does not change between different models.

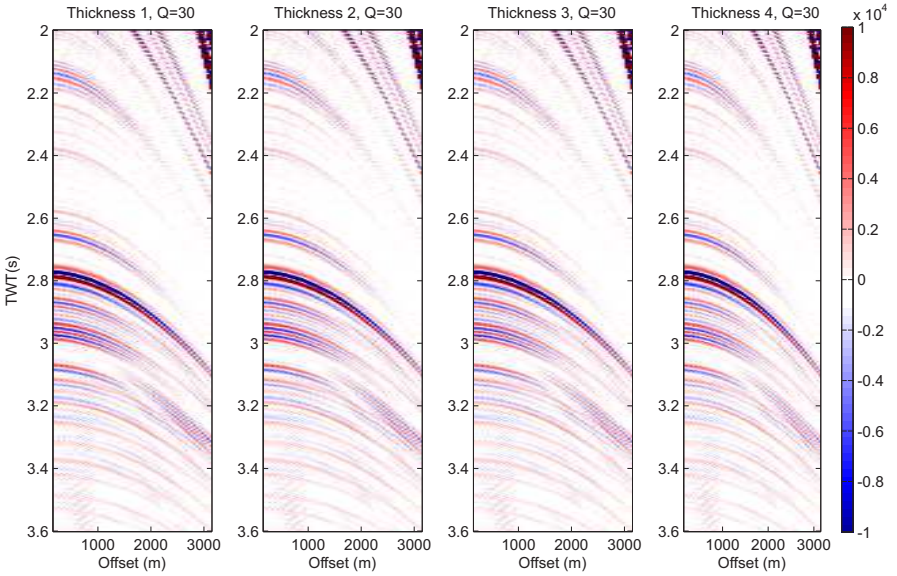

Figure 6.8: Synthetic data created for Thickness 1, 2, 3 and 4.

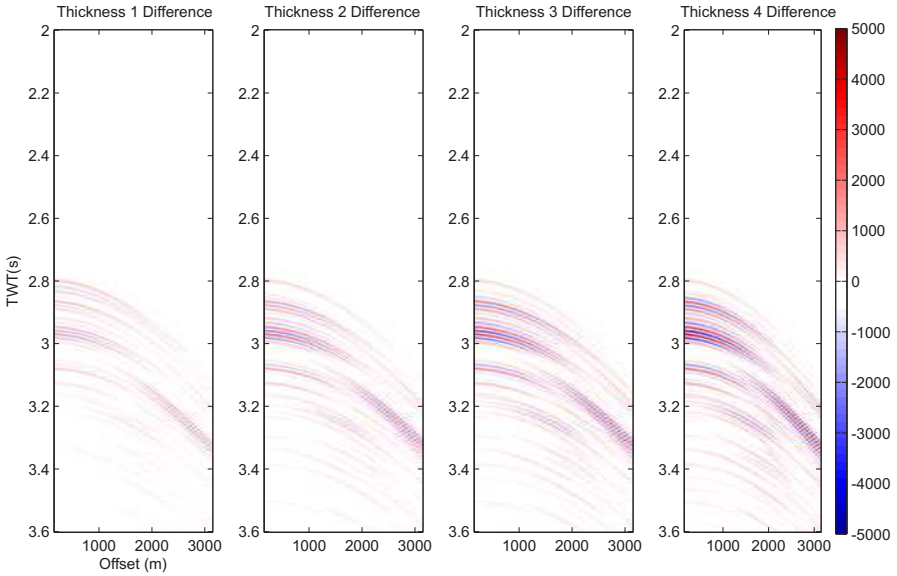

Figure 6.9: The differences between the Q=100 synthetic data and the synthetic data for Thickness 1, 2, 3 and 4.

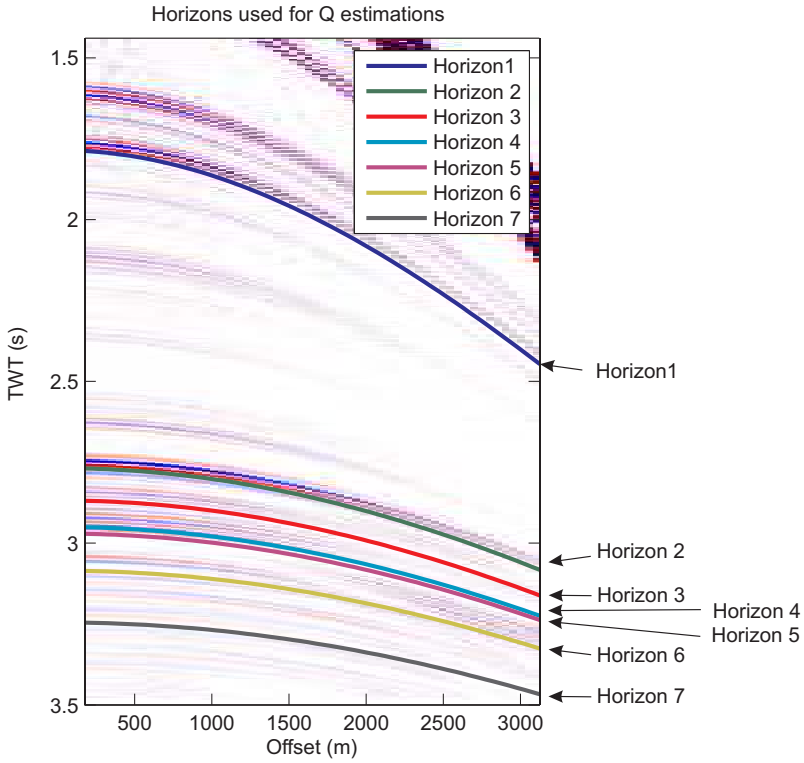

Figure 6.10: The horizons 1-7 used for analysis during the feasibility study.

It can be seen that the expected change in the interval attenuation should always be:

$$\Delta\frac{1}{Q} = \frac{1}{30} - \frac{1}{100} = 0.02333$$

As we know the thickness of the region of Q change and hence know the travel time of the interval in which attenuation has changed the change in t^* can be divided by the travel time through which attenuation changes, making interpretation of the result easier. In each of the methodologies, the expected change in attenuation will also be plotted along with the measured change. Therefore the expected change in attenuation for Horizon 1 and 2 is 0, and the expected change for Horizons 3-7 is +0.02333.

I will analyse the data using the Absolute PSQI methodology, the Direct PSQI methodology, Direct instantaneous frequency matching and the Direct centroid frequency methodology. This choice provides us with a comparison of each direct methodology and also a comparison between the absolute and direct methodologies.

6.2.2 Absolute PSQI

To begin with I look at the Absolute PSQI methodology as it is interesting to look at the absolute values of attenuation that are generated and gain insight into the level of

apparent attenuation present for single vintages of data. A bandwidth of 10-100 Hz is used to calculate the absolute values of attenuation using a near offset reflection from Horizon 1 as the reference event. Figure 6.11 compares the absolute values of interval attenuation derived from each vintage of data. Both positive and negative values of attenuation are measured, with much deviation around the expected Q=100 ($1/Q$=0.01) highlighting the sensitivity of single vintage measurements. Figure 6.12 shows that when the absolute values are subtracted much of the apparent attenuation cancels between vintages, with some of the true changes in attenuation recovered from the data. It is clear from Figure 6.12 that between lower Horizons (e.g 3-6), where no change in intrinsic attenuation is expected there are unexpected changes in the interval attenuation due to small changes in the apparent attenuation. It appears that interval changes are best determined from Horizon 2 and 3, and 2 and 4.

6.2.3 DPSQI-Direct prestack methodology

The direct PSQI (DPSQI) methodology was carried out with a regression bandwidth of 10 to 100Hz. The change in t^* to that reflector is then calculated and divided by the zero-offset travel time through the injection interval (Figure 6.13). Horizon 3 (just below the region of Q change) gives the best estimate of the change in attenuation. A perhaps surprising characteristic of these results is the diminishing magnitude of the attenuation predicted for horizons 3-7 and this behaviour will be discussed at the end of this section. Another interesting feature of the results is that analysis of the top-reservoir reflection (Horizon 2) also indicates an increase in attenuation. This could be due to the fact that spectral estimates require a window of data and hence include some energy from below the top reservoir but could also be an effect of change in the frequency dependent reflectivity.

6.2.4 DIFM - Direct Instantaneous frequency matching

In the Direct instantaneous frequency matching every trace pair from each vintage is analysed to calculate a value of attenuation. The result of the inversion gives a value of the change in t^*, which again can be divided by the TWT of the injection interval. For horizons 1 and 2, where there has been no travel time through the reservoir we divide by the two way time through the reservoir. Results are shown in Figure 6.14 along with the mean and standard deviation of estimates at all offsets. Unlike the previous two methodologies, there are significant differences between the accuracy of measurements

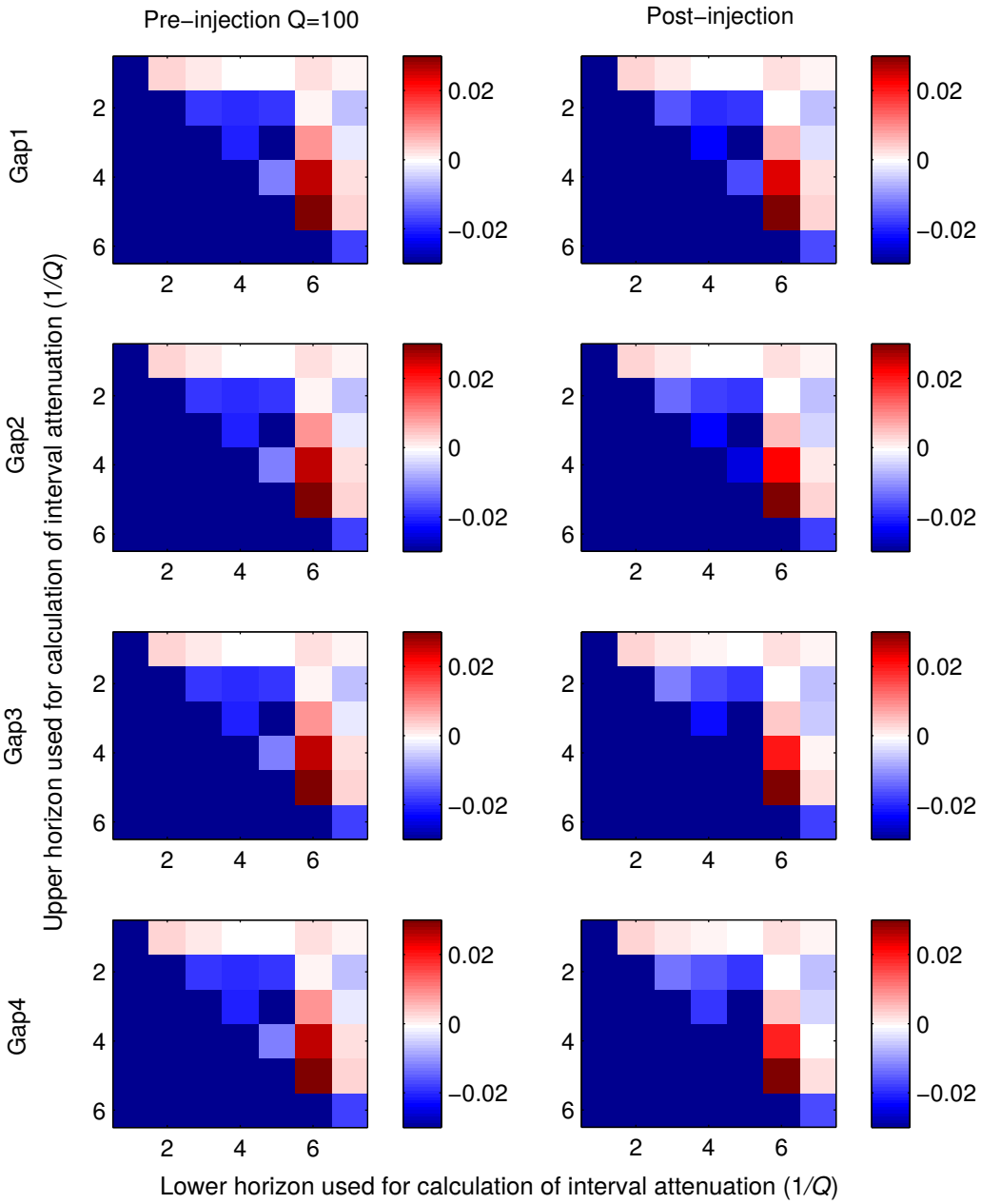

Figure 6.11: This plot shows the absolute values of attenuation ($1/Q$) calculated using the absolute PSQI method. The two columns represent the pre-injection and post-injection values. The rows represent the 4 different thicknesses of attenuation change. Each panel contains the attenuation value calculated between an upper horizon (y-axis) and a lower horizon (x-axis).

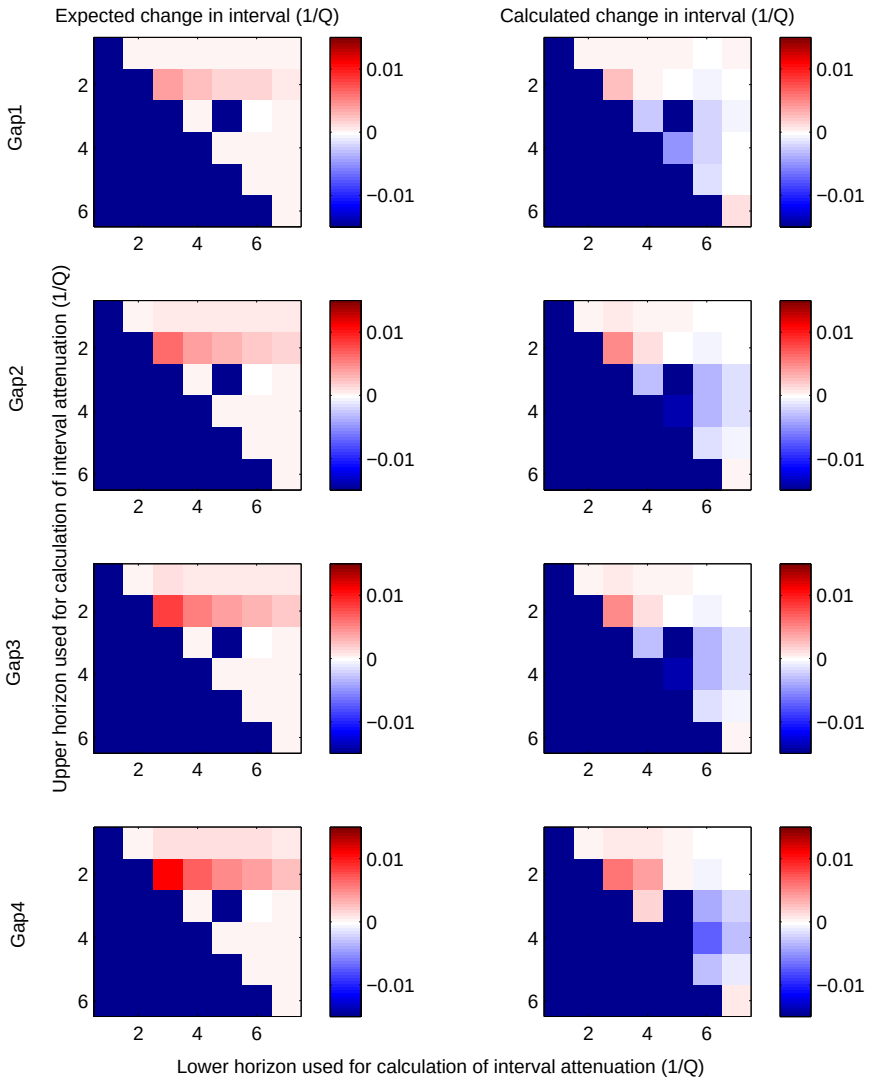

Figure 6.12: Figure comparing the expected change in attenuation for each scenario (Gap1-4) with the measured changes from the Direct PSQI methodology. The interval of injection lies between horizons 2 and 3 so the expected change in attenuation for intervals not enclosing this should be zero. Each panel contains the attenuation value calculated between an upper horizon (y-axis) and a lower horizon (x-axis).

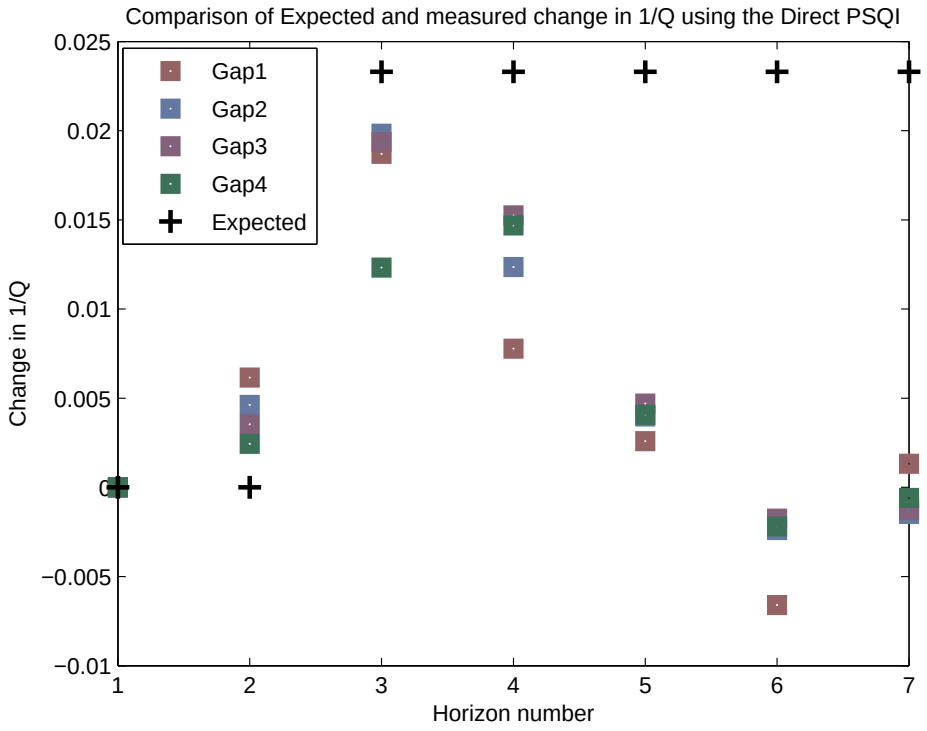

Figure 6.13: Comparison of expected (black crosses) with the measured change in $1/Q$ for Gap1, Gap2, Gap3 and Gap4 to each horizon for the Direct PSQI methodology.

for different thicknesses of injection. The correct polarity of attenuation is predicted for the majority of thicknesses and horizons with no evidence of the diminishing attenuation estimates seen in the Direct PSQI methodology. The top reservoir reflection also appears to be more heavily influenced by apparent attenuation effects.

6.2.5 Direct spectral ratio methodology (QVO)

Spectral ratios are calculated directly between the two vintages of synthetic data and a regression is performed against the product of time and frequency (by-passing the second regression). The slope of this equation yields the change in attenuation. This is calculated for each offset and horizon within the CMP and results can be seen in Figures 6.16 and 6.17 plotted with the standard deviation of results for each reflector. Results are similar to the Direct PSQI methodology, as one might expect, with the same effects on the top reservoir reflection and diminishing attenuation estimates for deeper reflectors.

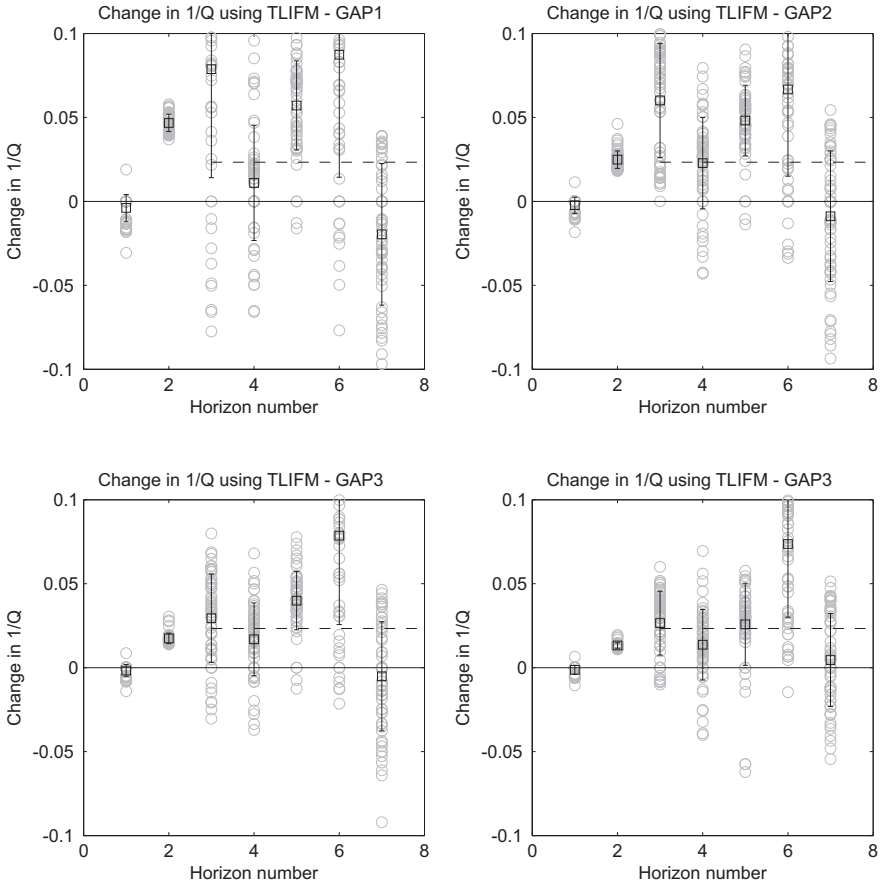

Figure 6.14: Four plots of the measured $1/Q$ for the Time-lapse instantaneous frequency matching method, one for each scenario showing the individual trace $1/Q$ estimates (grey) and the median value for each horizon. Error bars are calculated from the standard deviation of the results from the mean value.

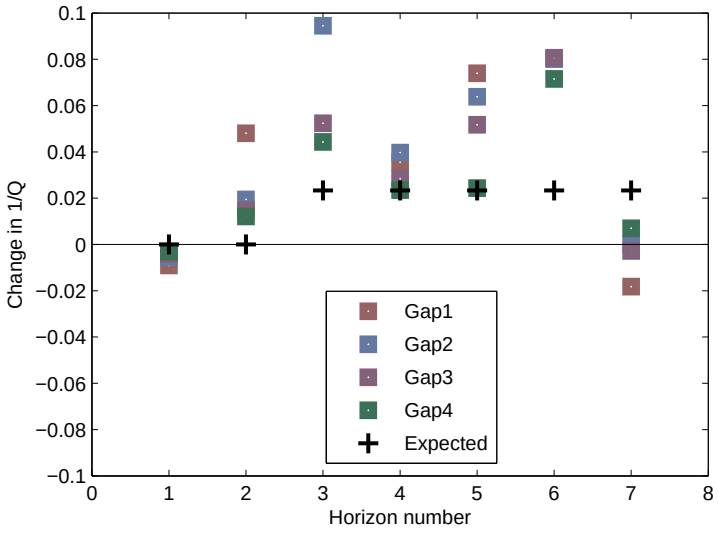

Figure 6.15: Comparison of expected (black crosses) with the measured change in $1/Q$ for Gap1, Gap2, Gap3 and Gap4 to each horizon for direct instantaneous frequency matching.

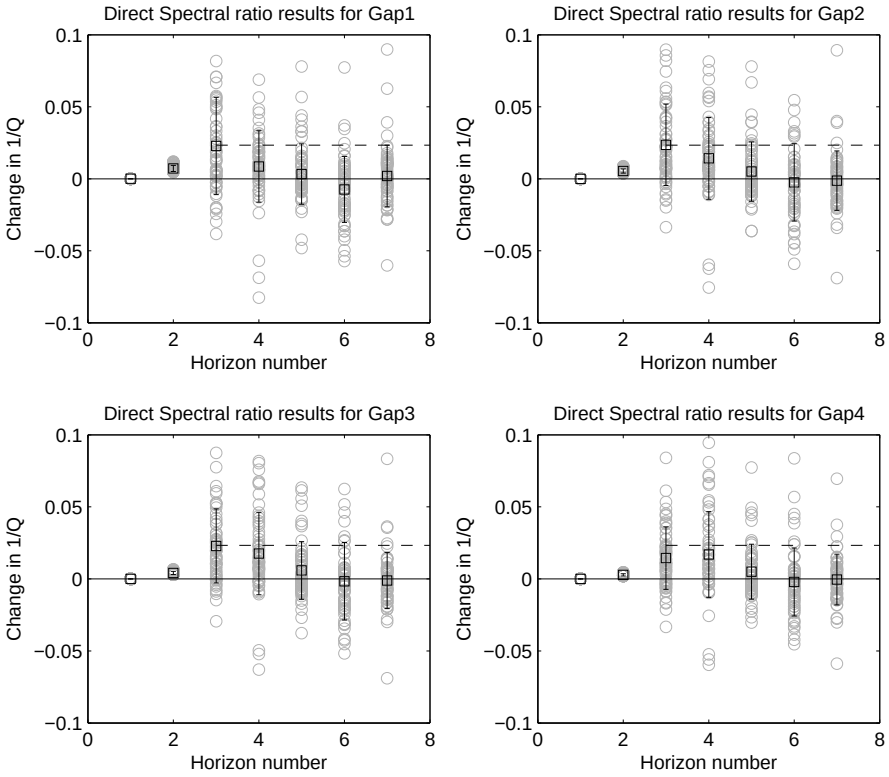

Figure 6.16: Results of the QVO second regression against offset squared. The values for each offset and horizon are plotted as grey circles with the mean (black squares) and standard deviation (error bars). The expected change is zero for horizons 1 and 2 and 0.0233 (black dotted line) for horizons 3 to 7.

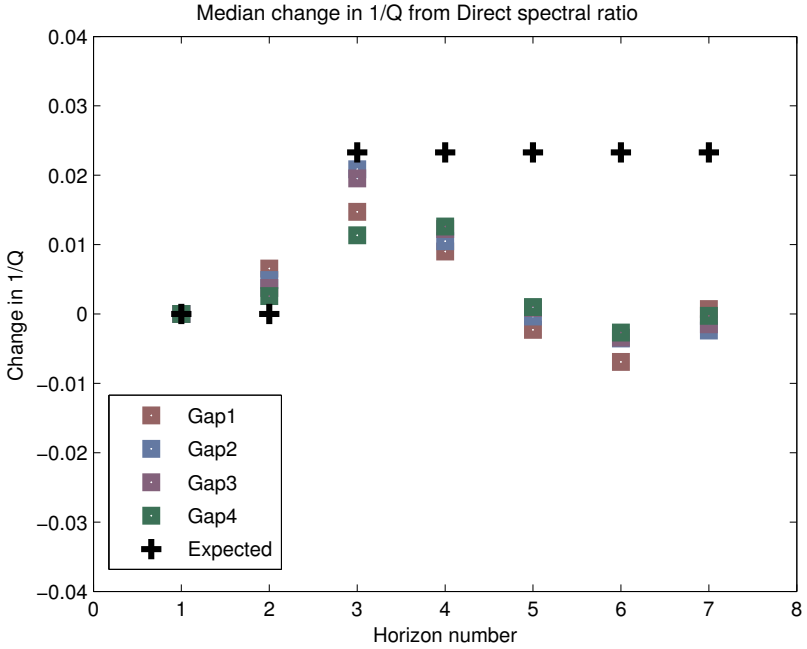

Figure 6.17: Median change in $1/Q$ from the Direct spectral ratio methodology (QVO) are plotted, comparing each of the scenarios and horizons. The regression bandwidth used was 10-100Hz.

6.2.6 Centroid frequency

A single value for the change in attenuation is derived for each trace and horizon in the CMP via the Centroid frequency methodology. Figure 6.18 shows that the centroid frequency appears to be stable when estimating the attenuation, and nearly always predicts the correct polarity change in attenuation. Similar diminishing attenuation values are seen in these results as with the spectral ratio methodologies but to a lesser extent, indicating that it is an effect that has greater sensitivity on spectral ratio slopes. Yet again, a small increase in attenuation has been measured for the top reservoir reflection, and is most likely caused by the same effects that produced this result in the spectral ratio methods.

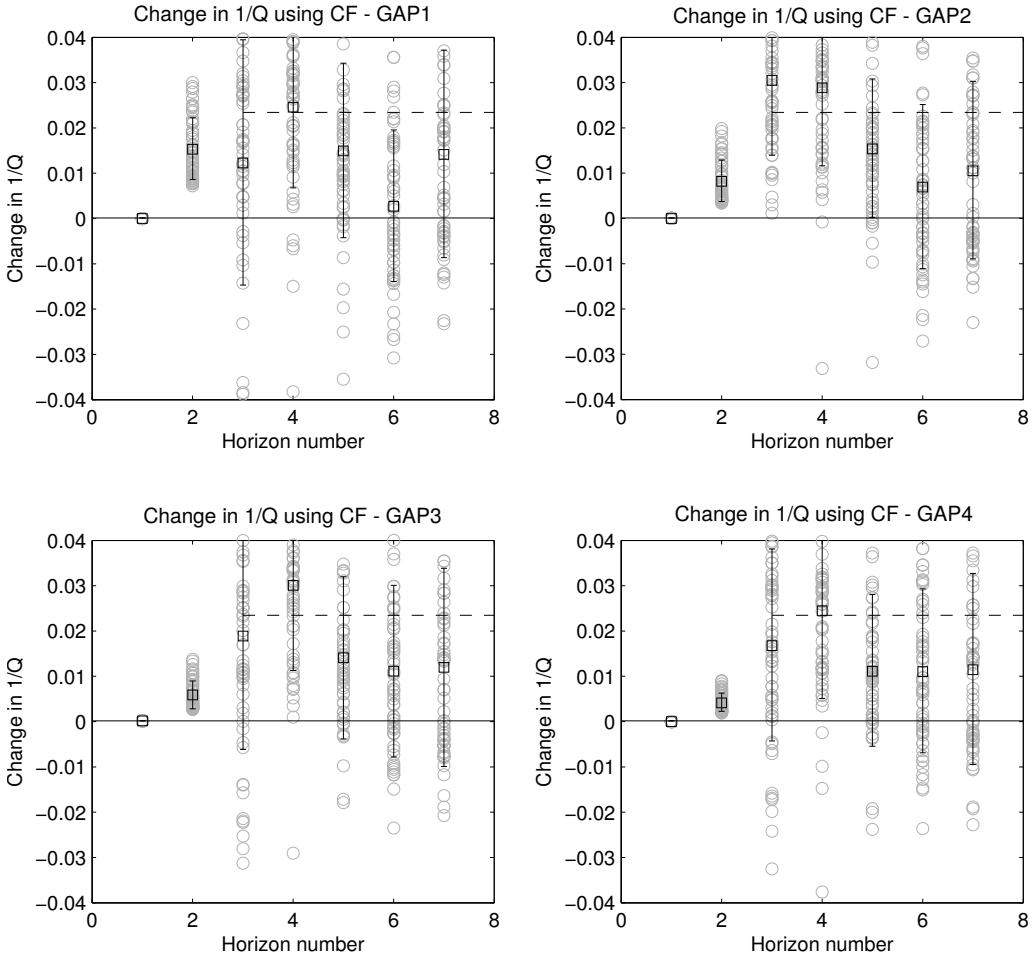

Figure 6.18: Figure showing attenuation changes derived from the centroid frequency shift methodology. Each plot shows a single scenario with the single trace estimates for each horizon and offset (grey circles), the mean (black squares) and standard deviation (error bars) for each horizon, along with the expected attenuation change (dashed line). Horizons 1 and 2 should show zero change in attenuation.

6.2.7 Comparison of methodologies

It is clear that all methodologies measure increases in attenuation for all of the input models, however there are limitations to the accuracy of the determination of the absolute change in attenuation. It can be seen in Figure 6.19 that the Instantaneous frequency matching has the largest error compared with other methodologies. All of the methodologies that rely on spectral estimates to compute attenuation show similar coherent behaviour, notably the measured increase in attenuation for the top reservoir reflection and the diminishing attenuation seen at the lower reflectors.

The result of the feasibility study suggests that attenuation changes are detectable in the Magnus reservoir using all methodologies, with larger error expected for the Instantaneous frequency and the most robust measurements made by the Centroid frequency methodology. Parametrisation of each methodology was not tested extensively on this synthetic example, so estimates could only improve through the addition of more rigorous testing, or the inclusion of weighting or damping schemes in the inversions.

Comparing the difference between the Direct PSQI and Absolute PSQI methodologies would suggest that there is very little difference between the two methodologies. However, this may change once applied to real data, with the true reflectivity and noise present.

The purpose of this experiment was to see if changes in attenuation could be detectable in a complex reflectivity sequence representative of that found at the Magnus field and to understand any coherent behaviour between the methodologies. Overall the synthetic data suggest that attenuation changes are detectable for the Magnus reservoir, assuming that the change in attenuation is as expected (Q=100 to Q=30). The increase in attenuation for the top reservoir reflection could be due to changes in dispersion and hence the frequency dependent reflectivity, which has shown to be a source of error in Chapter 4 and the coherent decrease in the estimates could be due to the increased presence of multiple energy.

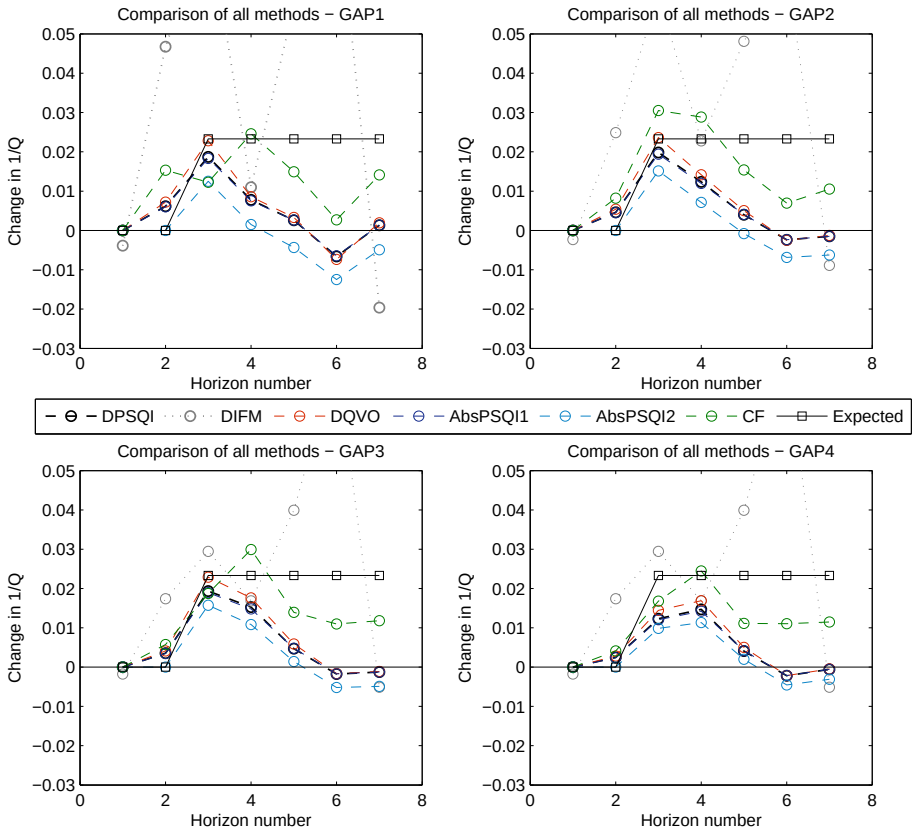

Figure 6.19: Comparison of methodologies used for the feasibility study for scenarios GAP1, GAP2, GAP3, GAP4. DPSQI=Direct prestack Q inversion, DIFM=Direct Instantaneous Frequency Matching, DQVO=Direct Spectral ratio, Abs-PSQI1=Absolute Prestack Q inversion using horizon 1 as the reference, Abs-PSQI2=Absolute Prestack Q inversion using horizon 2 as the reference, CF=Centroid frequency method, Expected= The expected change in attenuation.

6.3 Repeatability of the data

I aim to compute attenuation using all available methodologies, but in order to do so I must ensure that the assumptions imposed by some of the methodologies are justified for this data-set. One such example of this is the direct methodology where the assumption that source spectra are the same must be met for the methodology to be used. It is also essential to parametrise each of the methodologies to ensure that the most robust parameter choices are made by looking at the repeatability of the real data set as functions of frequency, time and offset. Commonly used repeatability metrics will be computed (PRED and NRMS) and the spectral repeatability analysed. In the 6 years between vintages of acquisition, the Magnus reservoir has continued producing oil and has undergone intensive water and gas injection, leading to many reservoir changes that may affect the repeatability of the seismic data.

6.3.1 Background trends in the spectral content

Here I look for background trends in the spectral content of the pre-stack data. Of particular importance is to look at the direct spectral differences between data-sets as this will determine whether the direct methodologies can be used. Here I take an in-line of data and sum the spectra in different ways across the in-line. This will enable us to look at the various background trends, and in particular the acquisition footprint caused by the platform (See Figure 6.2).

Figure 6.20 shows the NMO corrected, pre-stack, time-frequency data summed at constant times for all offsets and CMPs along the cross line of data along with the direct spectral ratios. It is clear to see from this that there are large differences in spectra in the near surface as may be expected and towards the lower half of the seismic data. In the lower half an increase in higher frequency between vintages of data can be seen. A variety of reasons could be responsible for this, including acquisition changes, processing effects, an average decrease in attenuation across the data set or an increase in noise at these frequencies.

To take a more quantitative look at frequency dependent changes in the data I look at some average attenuation attributes. Using the data in Figure 6.20 I compute both the change in centroid frequency and change in spectral ratio slope. Figure 6.21 shows that the direct attributes are noisy both near to top and the bottom of the seismic data. In the first second of the time series there are large spikes of noise. In the lower two seconds there

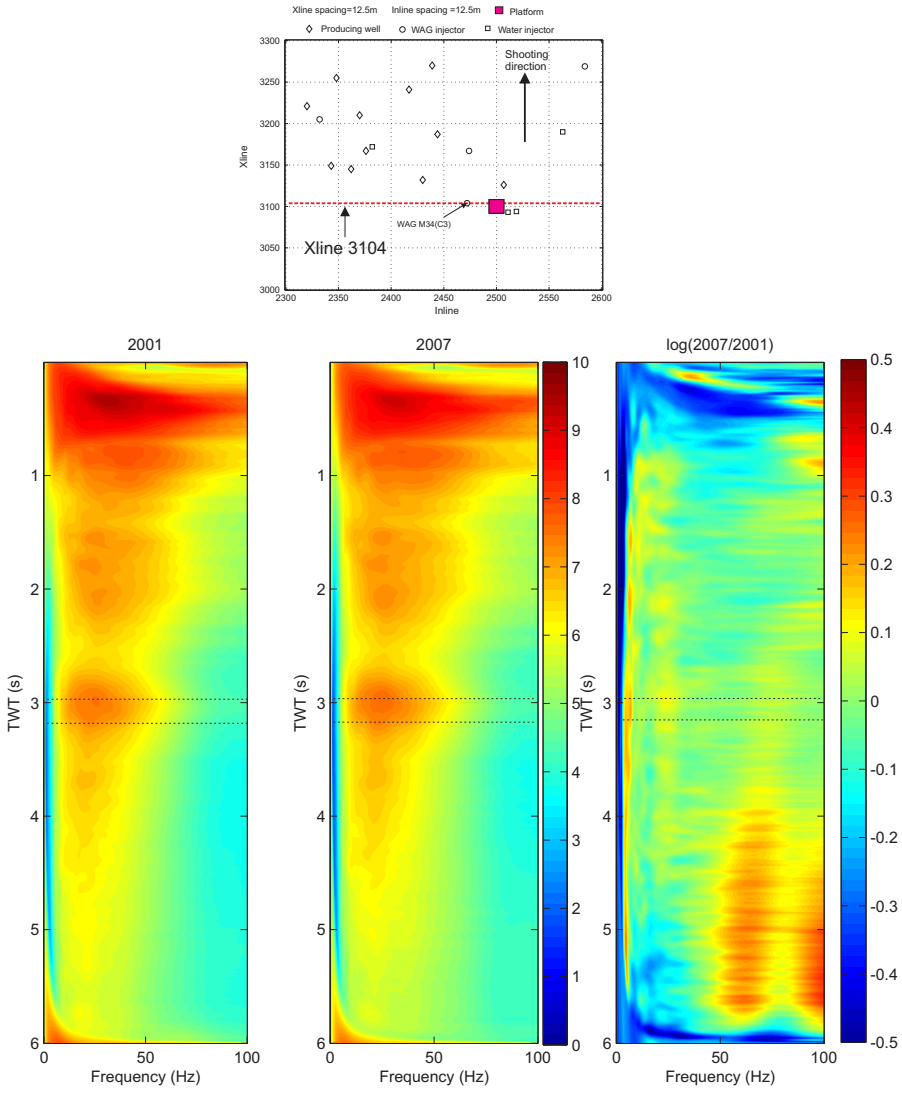

Figure 6.20: The average spectra for cross-line 3104 in 2001 (left), 2007 (middle) and the direct spectral ratio ln(2007/2001), (right). The dotted lines indicate the TWT interval containing the reservoir.

is a coherent increase in the spectral ratio slope and centroid frequency shift, correlating well with the observed increase in the higher frequencies in Figure 6.20.

I take this analysis a step further by summing the spectra at constant times for each offset. This will determine if the characteristics seen above occur at all offsets or within specific offset range. Figure 6.22 shows the result of fitting a spectral ratio slope and calculating a centroid frequency shift at each offset and time. Instead of plotting the change in attenuation, I plot the change in frequency divided by π times the variance of the spectra to yield the change in t^*. This makes both of the panels comparable and because of this suggests that the assumption of a Gaussian spectrum may be a valid choice for this data set. I now compare these values with the expected changes in t^*.

In order to estimate the relative magnitude of the noise between vintages of data, I estimate what changes in the direct attributes could be expected for a Q change of 100 to 30. In order to achieve this I take an approximate pay thickness of the reservoir to be 100m, and the average velocity at that depth to be 3.5km/s. I also estimate the likely maximum attenuation change to be from Q=100 (fully oil/water saturated) to Q=30 (15% gas saturation), giving a $\Delta\frac{1}{Q} = 0.0233$. I calculate the likely maximum change in spectral ratio slope to be $-\pi t\Delta(\frac{1}{Q}) = 0.0042$. Figures 6.23 and 6.24 both look at 3 scenarios for the detectability of a change in attenuation: the best case scenario of $-\pi t\Delta(\frac{1}{Q}) = 0.0042$, half of the best case $-\pi t\Delta(\frac{1}{Q}) = 0.0021$, and a quarter of the best case $-\pi t\Delta(\frac{1}{Q}) = 0.00105$. Dividing the best case scenario in half could be representitive of either the maximum change in attenuation occuring over half of the thickness, or half the maximum change in attenuation occuring over the same thickness. These results are shown by clipping the absolute value of the direct change in spectral ratio (Figure 6.23) and centroid frequency (Figure 6.24) at the value of $-\pi t\Delta(\frac{1}{Q})$. Any black areas therefore represent a region where one would expect not to be able to detect a change in attenuation of that magnitude. By comparing these results we can see that both attributes yield similar limits of detectability. The most significant difference between the two attributes is the nature of the background noise with the centroid frequency having a lower frequency noise than the spectral ratio. These figures suggest that attenuation changes are potentially detectable around the reservoir interval (3s TWT), however, these have been produced by stacking an inline of spectra together. One would expect the limitations of detectability to decrease as fewer traces are stacked together.

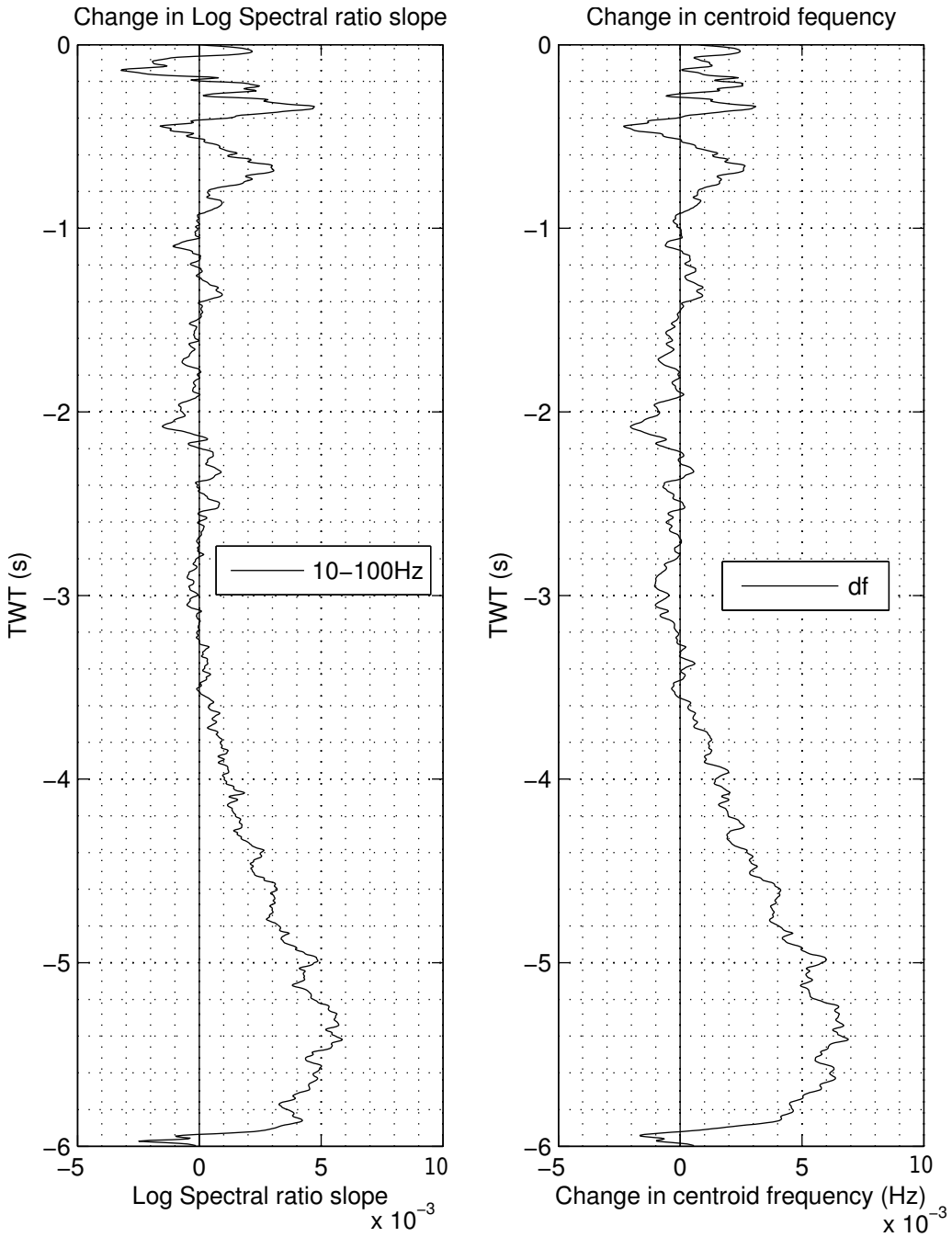

Figure 6.21: The direct log spectral ratio slope and the direct change in centroid frequency as a function of time.

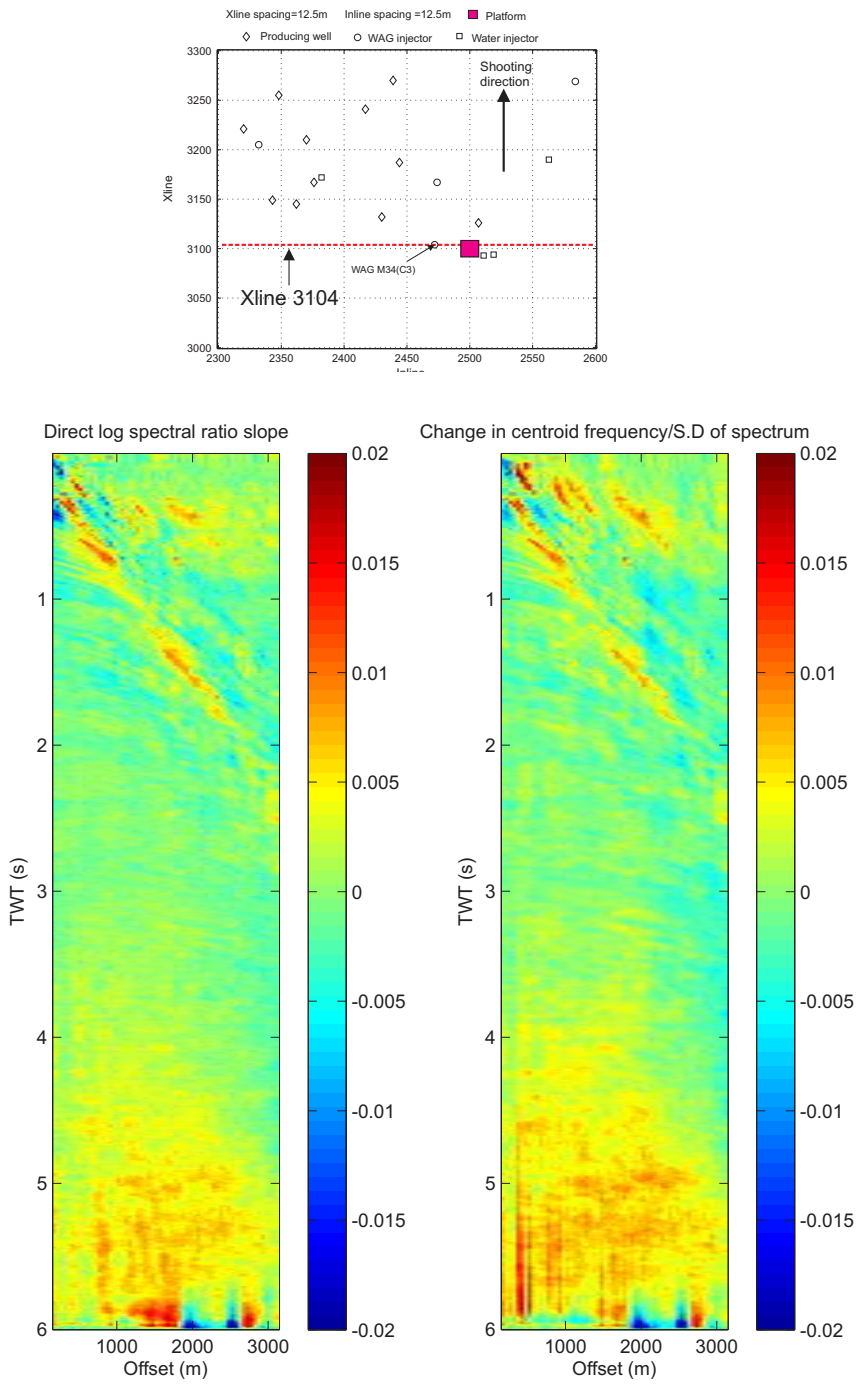

Figure 6.22: The direct log spectral ratio slope and the direct change in centroid frequency as a function of time and offset. Prestack traces (not NMO corrected) are summed in the time-frequency domain at each offset for Xline 3104.

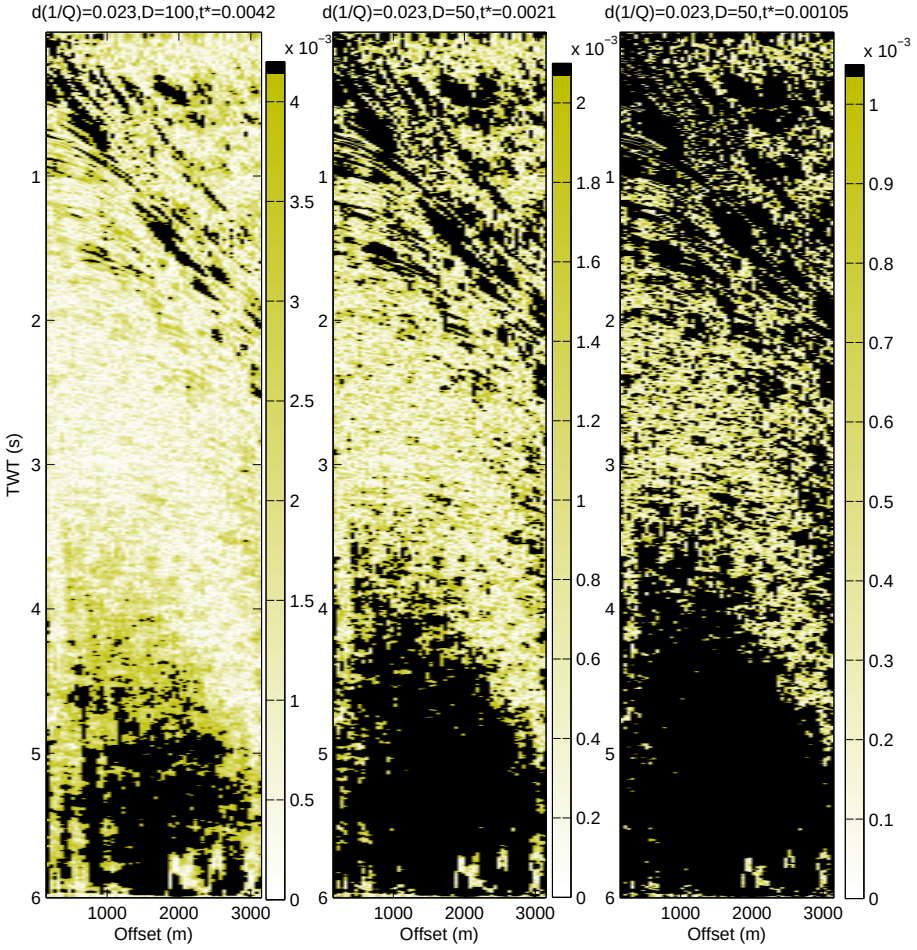

Figure 6.23: The magnitude of the change in the spectral ratio slope clipped at a) Best case change in spectral slope (0.0042) b) 1/2 best case change (0.0021) and c) 1/4 best case change (0.00105). Anywhere coloured in black lies outside the detectable range to measure a change in attenuation.

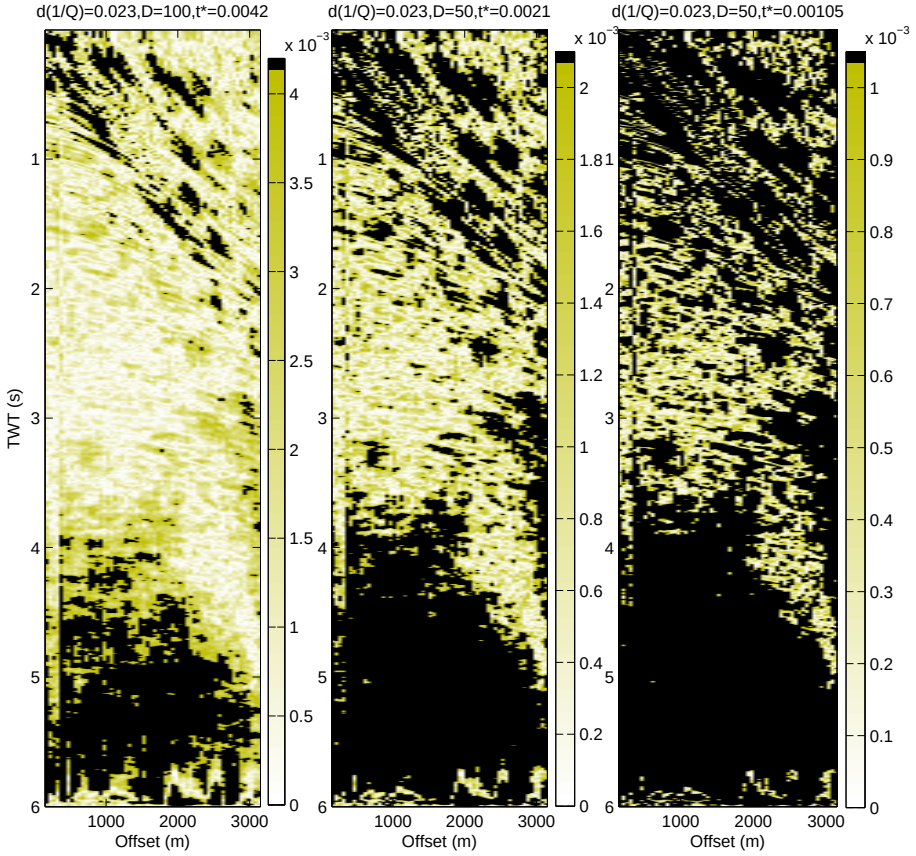

Figure 6.24: The magnitude of the CF attribute clipped at a) Best case change (0.0042) b) 1/2 best case (0.0021) and c) 1/4 best case (0.00105). Anywhere coloured black lies outside the detectable range to measure a change in attenuation.

6.3.2 Standard repeatability metrics

Here I look at the repeatability of the cross-line. I calculate the NRMS and Predictability (PRED) of the traces and then move on to look at the spectral repeatability. As I am investigating the repeatability of prestack data information is needed about the repeatability in various dimensions (time, frequency and offset).

However, to begin with I look at the repeatability of the stacked data, this will give the most basic distribution of repeatability. The repeatability is calculated for the entire trace and can be seen in Figure 6.25. A large decrease in repeatability can be seen at around CMP 175. This is located close to one of the injectors but is more likely to be predominantly due to the proximity of the platform (see base map, Figure 6.2). It must be noted that the repeatability of the full trace length will be dominated by the higher amplitude events in the upper portion of the data. What is of more interest is the repeatability near the reservoir depth. In Figures 6.26 and 6.27 I show the repeatability of a window above the reservoir and within the reservoir. The average repeatability for the window above the reservoir is larger than the average for the reservoir interval itself, however, it can be seen clearly that repeatability is a function of time and CMP. A sharp decrease in repeatability can be seen around the injector (CMP 175) and this could be due to actual changes in the reservoir interval as well as the impact of the platform upon acquisition. As the data-set is migrated we would expect that acquisition footprints will have been migrated along with true changes in the seismic signature. For random noise the noise to signal ratio can be estimated by

$$N2S = \frac{NRMS^2}{2} \tag{6.3}$$

(Kragh & Christie, 2002) and is also plotted in Figures 6.25 to 6.27. If this noise is truly random we may expect in the reservoir interval where $N2S$ is around 10-20% we would see a decrease in the magnitude of changes in attenuation predicted and an increase in uncertainty as seen in the band limited random noise tests in Chapter 4.

I now move on to look at repeatability as a function of offset, time and CMP.

Figures 6.28 and 6.29 show the prestack repeatability of the traces for three time windows (0-1.6s,1.6-3.2s,3.2-4.8s) for the NRMS and PRED metrics respectively. It is clear to see that there are offset ranges that are better than others. The nearer offsets are more

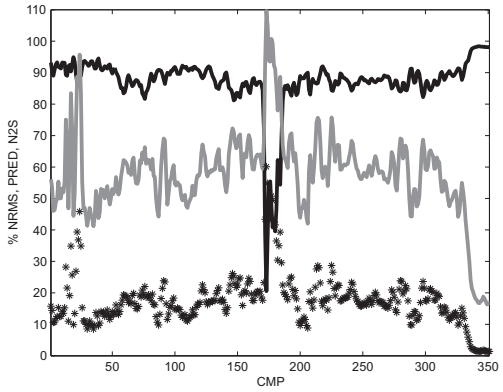

Figure 6.25: Repeatability metrics (black=PRED, grey=NRMS, *=N2S) for cross-line 3104, note the large repeatability issue around CMP 170.

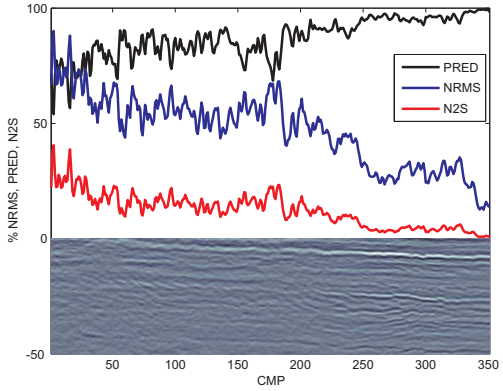

Figure 6.26: Repeatability metrics for a 0.2 second window above the reservoir interval along cross-line 3104.

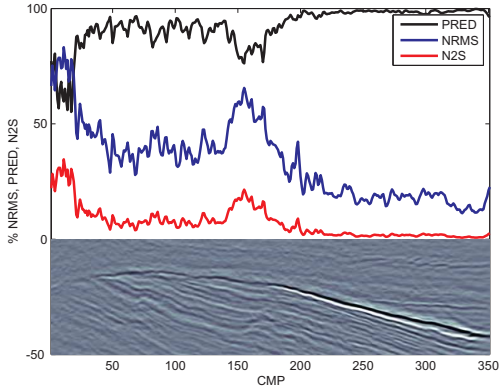

Figure 6.27: Repeatability metrics for a 0.2s window centred on the reservoir interval itself along cross-line 3104.

repeatable at nearly all depths and there is clearly a higher repeatability in the traces at higher CMP numbers. Some 2007 traces were replaced by 2001 data for missing traces at the furthest CMP numbers (hence the extremely good repeatability). Nearer offsets are generally more repeatable than others. These observations will be important in deciding which traces are to be used in the inversion for the prestack attributes with special interest in the 1.6s-3.2s interval. Obviously it will be important not to get rid of traces that contain changes to the seismic wave caused by intrinsic changes to reservoir rocks, but these repeatability measurements give a guideline to the offsets that should be used for the different methodologies.

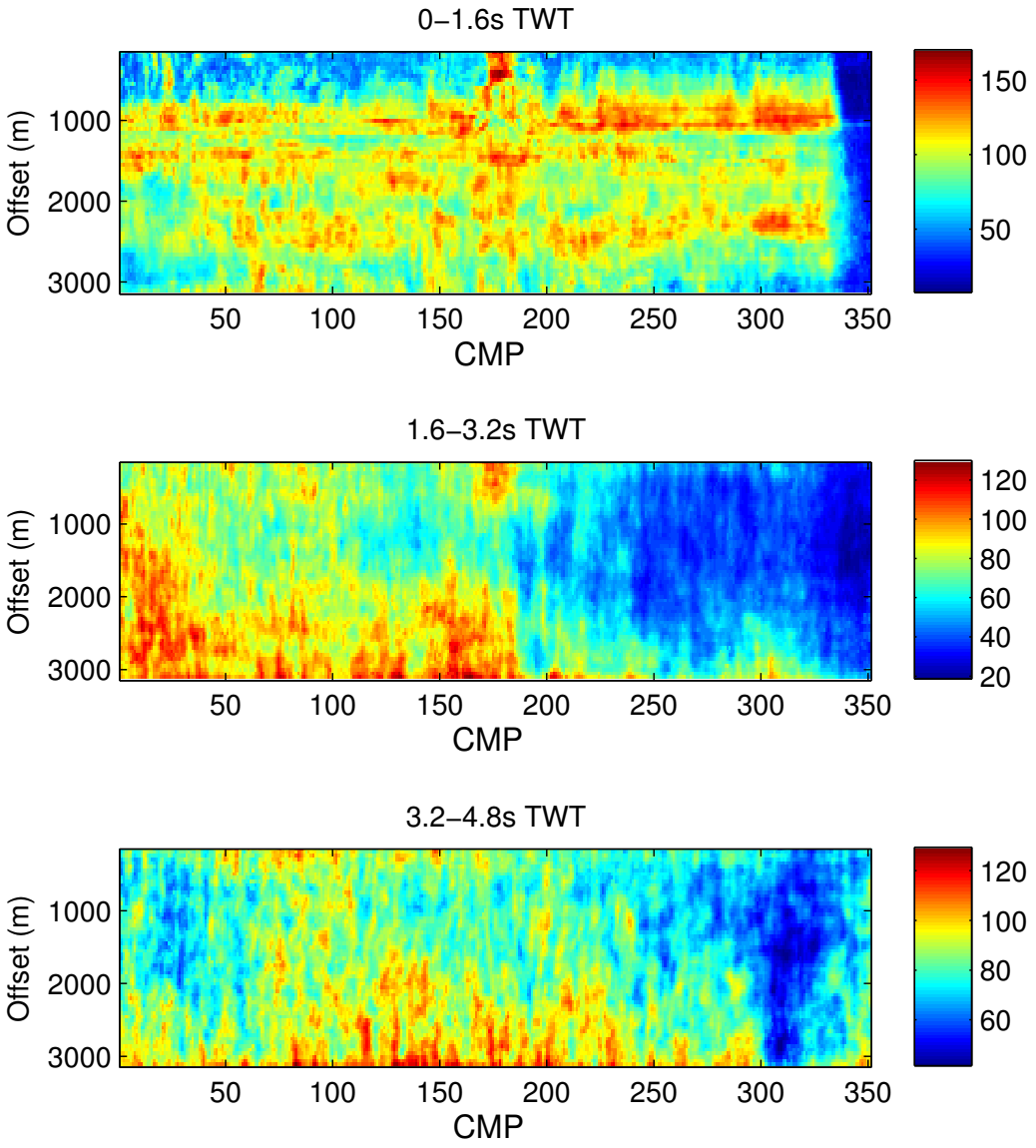

Figure 6.28: Repeatability NRMS for 3 time windows for all prestack traces in cross-line 3104.

One final test is to look at the frequency dependence of the repeatability. I achieve this

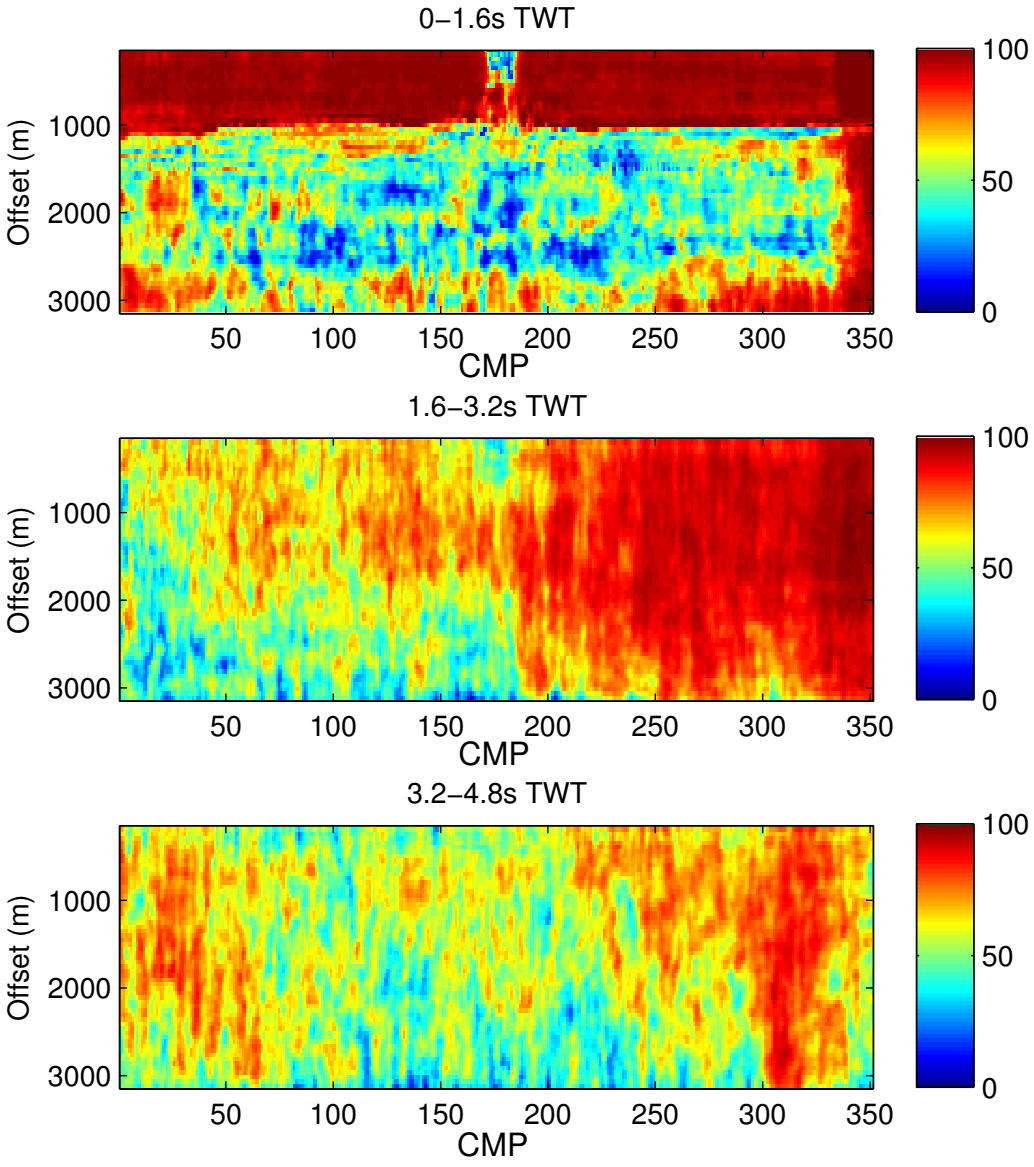

Figure 6.29: Repeatability PRED for 3 time windows for all prestack traces in cross-line 3104.

by bandpass filtering the data and looking at the NRMS and PRED parameters. Ten filers were chosen, each with a 10Hz bandwidth and 5Hz ramps on either side. Filter bandwidths were 0-10Hz, 10-20H, 20-30Hz through to 90-100Hz. The 0-10Hz filter was not band pass but low pass, cutting off at 10Hz and ramping down to 15Hz. Figures 6.30 and 6.31 show the frequency dependent nature of the repeatability (in the time interval 1.6-3.2s TWT) and the need for careful choice of regression bandwidths and offsets as it can be seen that repeatability is significantly reduced beyond 60-70Hz.

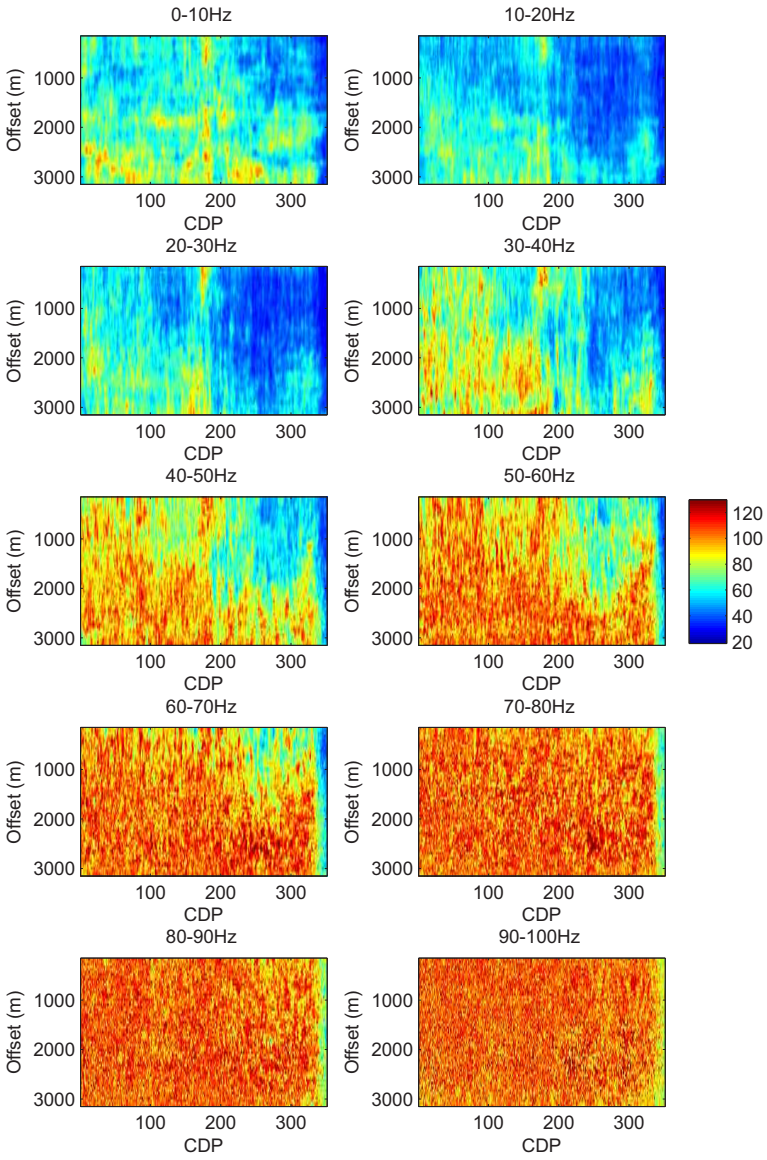

Figure 6.30: Frequency and offset dependence of NRMS in the prestack seismic data in the time window 1.6-3.2 seconds (flattened gathers).

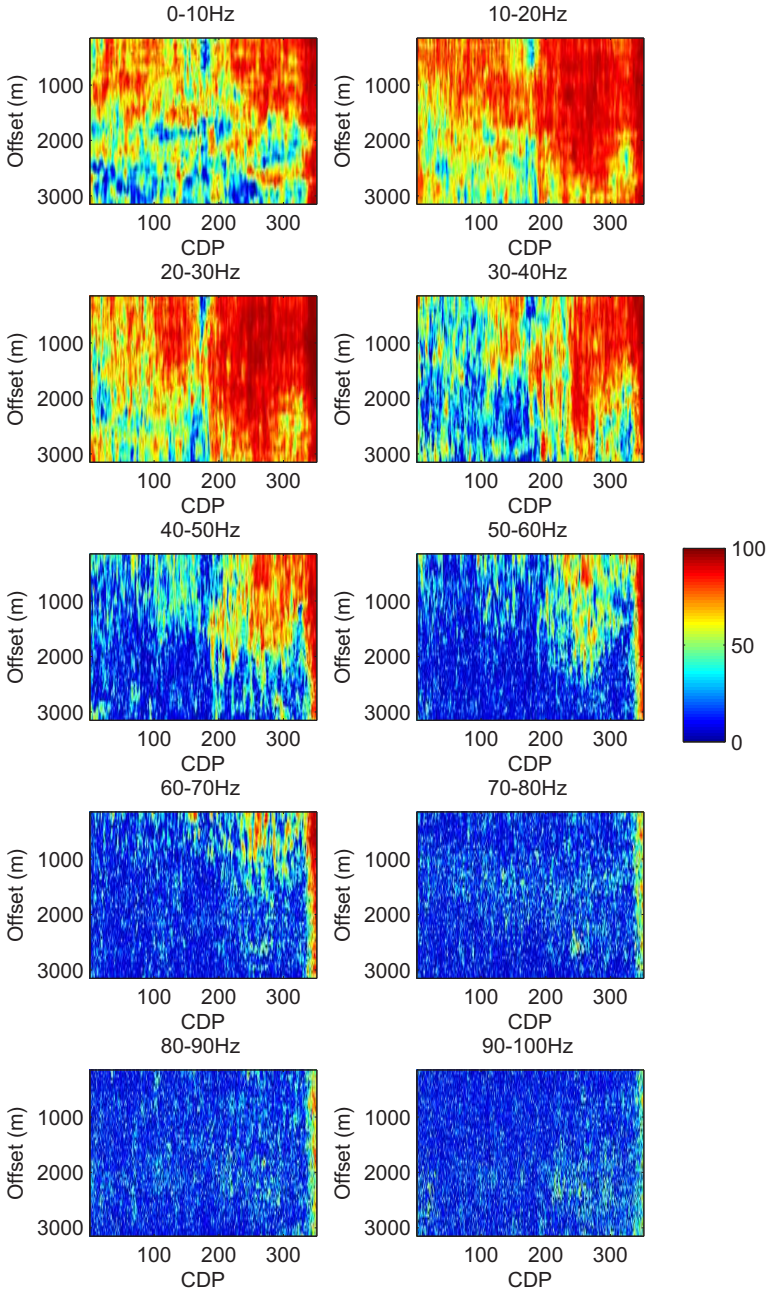

Figure 6.31: Frequency and offset dependence of PRED in the prestack seismic data in the time window 1.6-3.2 seconds (flattened gathers).

6.4 Standard attributes

Calculating other time-lapse attributes will allow for comparison with calculated attenuation changes. This comparison will not only allow us to look at where anomalies coincide, but also to compare the background noise level of the various attributes, identifying the locations of coherent noise and areas of incoherent noise. In this section I will look at 3 attributes that are commonly used for interpreting anomalies in prestack surface seismic data. I calculate the TWT shifts of the reservoir interval, the change in amplitude envelope of the top reservoir reflection and the 2 term and 3 term AVO attributes.

6.4.1 AVO

The AVO attributes are calculated using both the 2 and 3 term AVO anomalies and the details of the analysis carried out can be seen in Appendix B. The 2- and 3-term Shuey (Shuey, 1985) equations are given by

$$R(\theta) = A + B\sin^2(\theta) \tag{6.4}$$

and

$$R(\theta) = A + B\sin^2(\theta) + C(\tan^2(\theta) - \sin^2(\theta)). \tag{6.5}$$

The parameters A, B and C can be described in terms of the change in density and velocities

$$A = \gamma(\frac{1}{2}(\frac{\Delta V_\mathrm{p}}{V_\mathrm{p}} + \frac{\Delta\rho}{\rho})) \tag{6.6}$$

$$B = \gamma(\frac{1}{2}\frac{\Delta V_\mathrm{p}}{V_\mathrm{p}} - 2(\frac{V_\mathrm{s}}{V_\mathrm{p}})^2(2\frac{\Delta V_\mathrm{s}}{V_\mathrm{s}} + \frac{\Delta\rho}{\rho})) \tag{6.7}$$

$$C = \gamma(\frac{1}{2}\frac{\Delta V_\mathrm{p}}{V_\mathrm{p}}) \tag{6.8}$$

where γ is a scalar that relates the amplitude of the data to the reflection coefficient. A linear inversion can then be carried out to find A, B and C for the top reservoir horizon

(Horizon 2) for each CMP of data. In order to stabilise the inversions, damping can be added (again details given in Appendix B) in order to find the simplest model with the smallest data misfit. Trade-off curves were calculated for a cross-line of data and plotted, where a damping parameter of 10 was chosen.

Results for the 2 term regression are very consistent between vintages of data for both the intercept (A) and gradient (B) terms (Figure 6.32). The majority of intercepts are negative with some very large negative intercepts for large in-line and small cross-lines. When the difference between vintages are calculated, the change in the intercept (A) shows a large decrease around a couple of the injectors (Figure 6.33). The change in the gradient is more noisy than the change in intercept but does show some larger magnitude anomalies around the the WAG injectors.

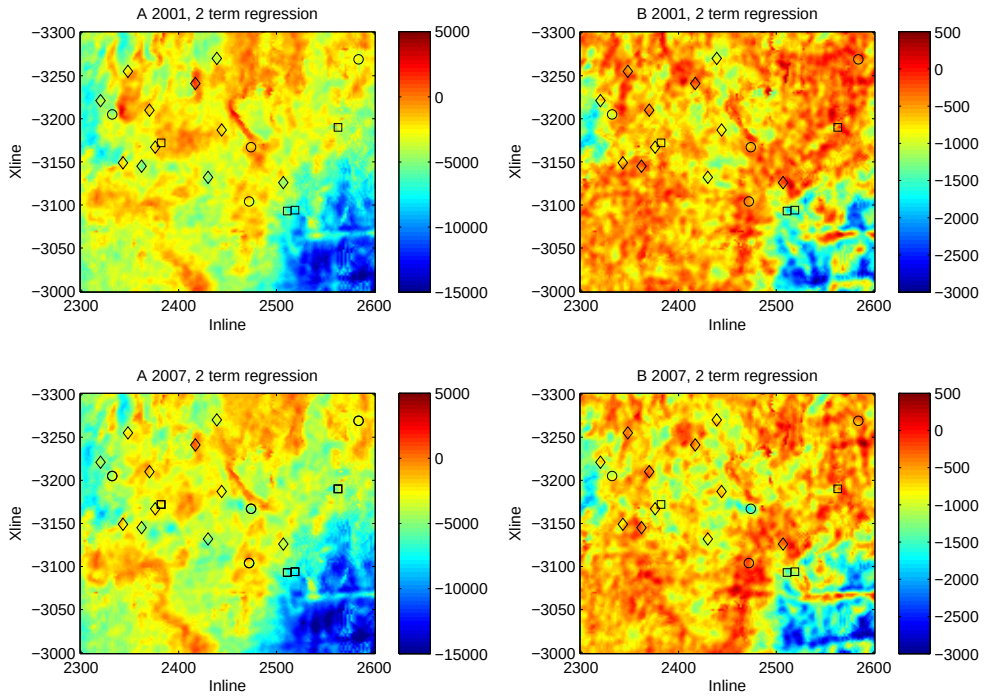

Figure 6.32: 2 term intercept (A) and gradient (B) terms calculated for 2001 and 2007.

For the 3 term regression (Equation B.2) it is also possible to introduce a secondary constraint by assuming that the change in density between the horizons is small. However, this assumption may be unreasonable as this reservoir is defined by an unconformity. Again, using a damping value of 10 in the inversion the results of the 3 term regression can be seen in Figure 6.34, with good correlation between both vintages of data. The differences between A terms again show good correlation with two of the WAG injectors

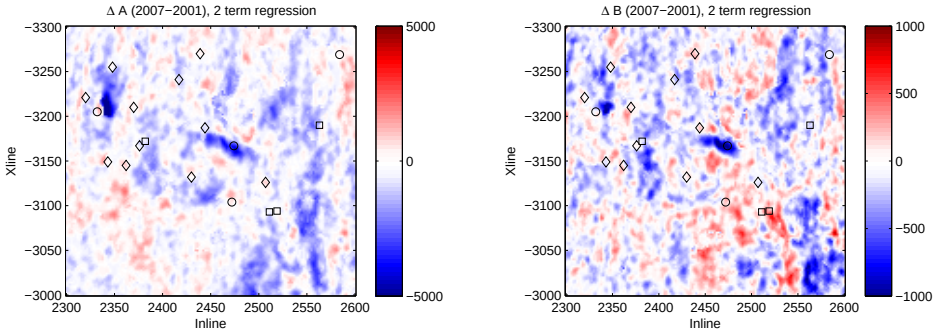

Figure 6.33: Change in 2 term intercept (A) and gradient (B) terms between 2001 and 2007.

(Figure 6.35). The change in B and C terms shows less coherency around the injectors, but there appears to be a large similarity between the change in B and C. This could be due to the limited number of events above a reflection angle of 35 degrees.

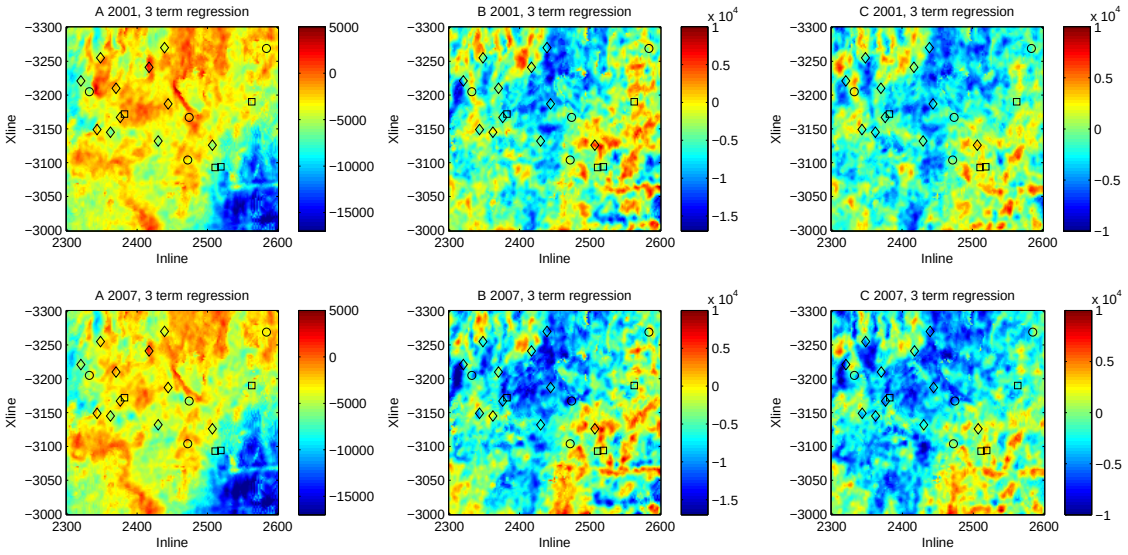

Figure 6.34: 3 term intercept (A) and gradient (B) and C terms for 2001 and 2007.

The difference between an undamped inversion, a damped inversion and the use of the secondary constraint (for details see Appendix B) on the change in A, B and C is shown in Figure 6.36. The effect between the damped and undamped inversion shows the largest differences, particularly in the reduction of noise in the intercept terms and the reduction in magnitude of the gradient terms (B and C).

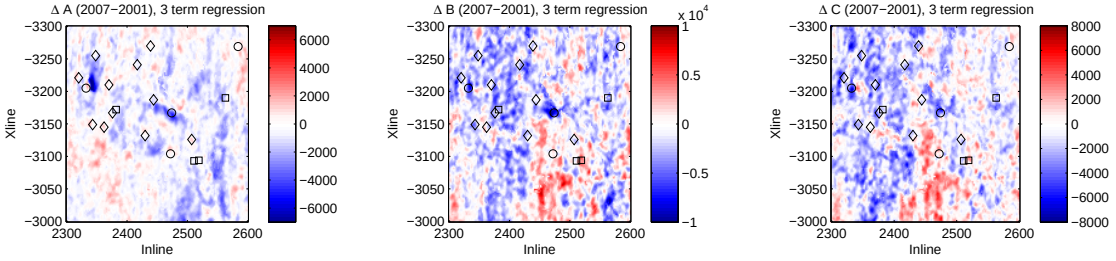

Figure 6.35: Changes in 3 term intercept (A) and gradient (B) and C terms for 2001 and 2007.

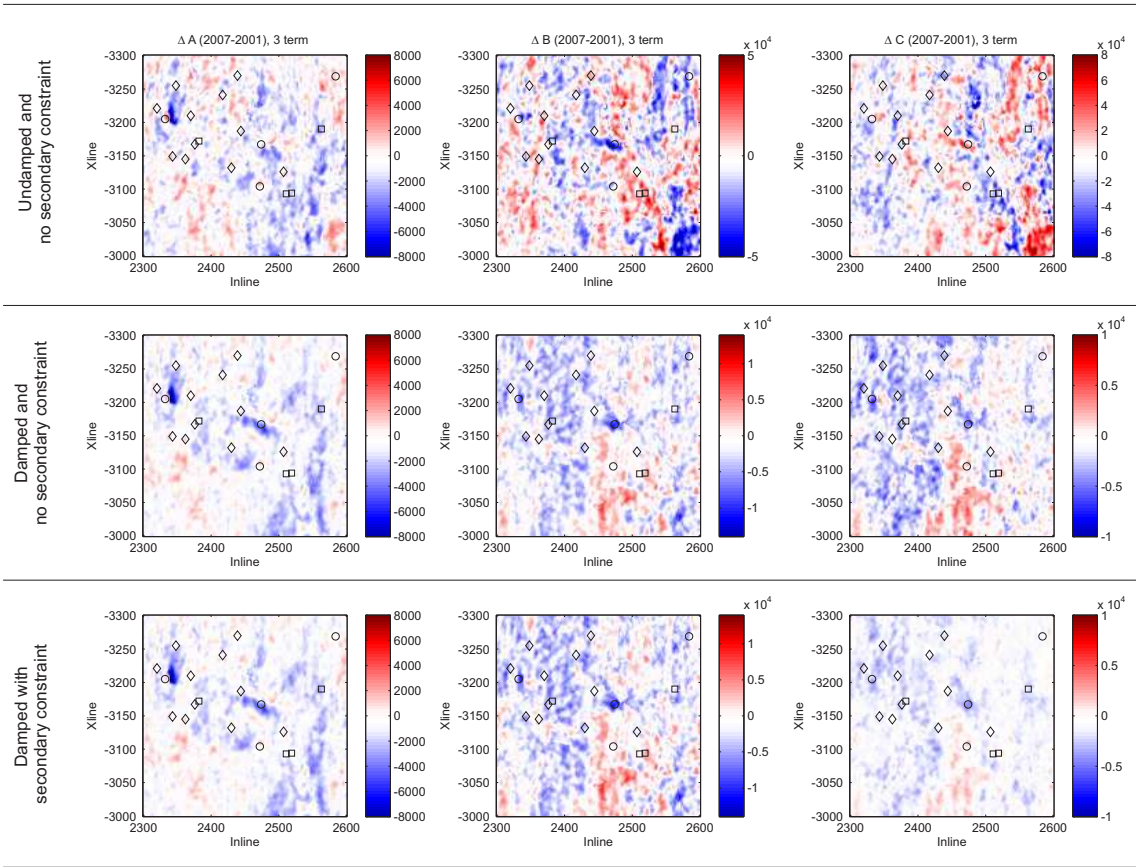

Figure 6.36: Changes in 3 term intercept (A, left)) and gradient (B, middle) and (C, right) terms for the undamped inversion (top), damped inversion (middle) and damped with secondary constraint (base). Note the linear patterns in the inline direction due to the acquisition footprint.

6.4.2 Amplitude envelope

The amplitude envelope can be used to look for changes in the magnitude of the reflectivity of the top reservoir reflection. In theory, results should resemble those of the changes in intercept from the AVO methodology shown above. Using the stacked data, the trace envelope is calculated for the 2001 and 2007 data-sets (Figure 6.37). The change in amplitude envelope has some strong anomalies located near to some of the WAG injectors, with other anomalies also present away from injectors or producers. Strong amplitudes are present in the bottom right of Figure 6.37 (a and b) and as 4D noise is partially a function of the strength of the reflectivity it may be better to express the change in amplitude as a percentage change rather than an absolute change (Figure 6.38). Large increases in amplitude are located around two of the injectors.

6.4.3 TWT

TWT changes can give us information primarily about changes in P-wave velocity but may also give information about compaction in some reservoirs (reservoirs with subsidence). In order to compute the TWT shifts as accurately as possible a prestack trace by trace cross-correlation was performed on the CMP gathers at each of the horizons shown in Figure 6.40 using a 400ms time window. Four of these time-shifts are plotted in Figure 6.39. As expected, Horizon 1 shows changes that are incoherent with the production wells and injectors but shows coherent changes along the in-lines caused by acquisition footprints. However, the top reservoir reflector (Horizon 2) shows large changes that are coherent with the locations of injectors and producers. These increases in travel-time, particularly those located in the centre of the analysis area, suggest a decrease in the velocity above the reservoir. These same time shifts appear to be coherent for the reflectors below the reservoir as well.

6.5 Methodology parametrisation

We have seen from the repeatability of the data set that parametrisation must be done carefully, and final choices must take into account the repeatability measurements made above. In this section I parametrise each methodology separately using a single CMP location, hoping to gain insight into the most suitable parameters to use for this data set. The CMP used is shown in Figure 6.40. It is located at a water and gas injector, so an

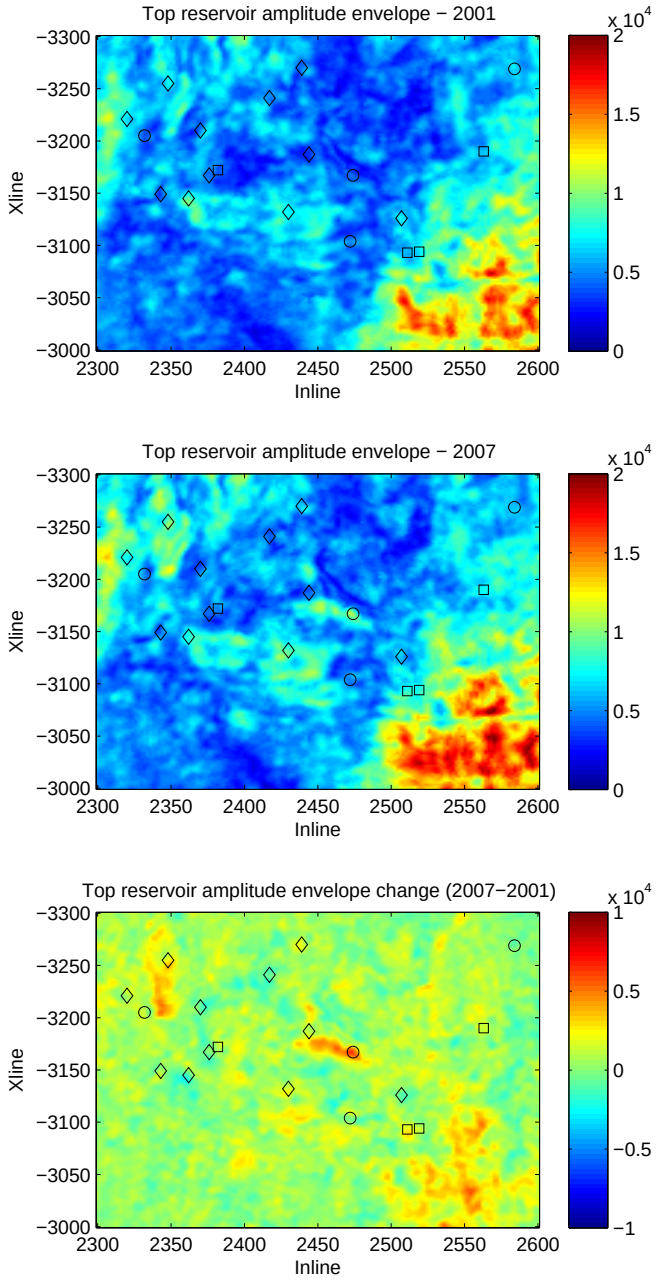

Figure 6.37: Changes in amplitude envelope for the top reservoir reflection.

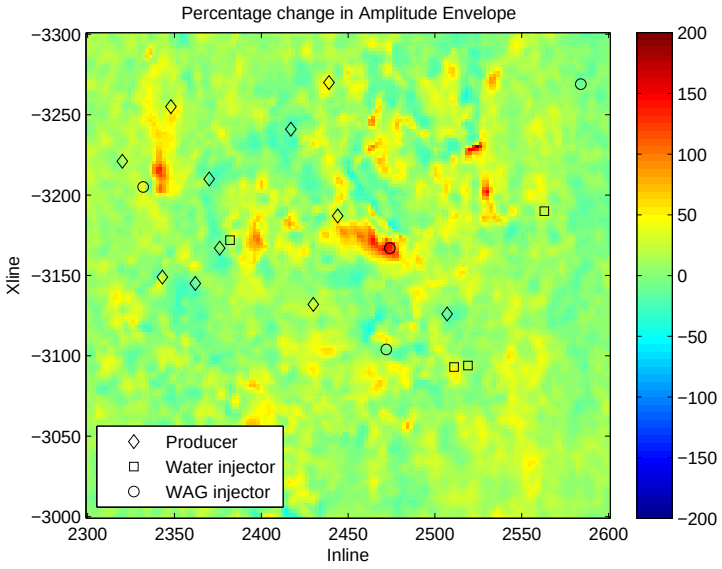

Figure 6.38: Percentage change in amplitude envelope from top reservoir.

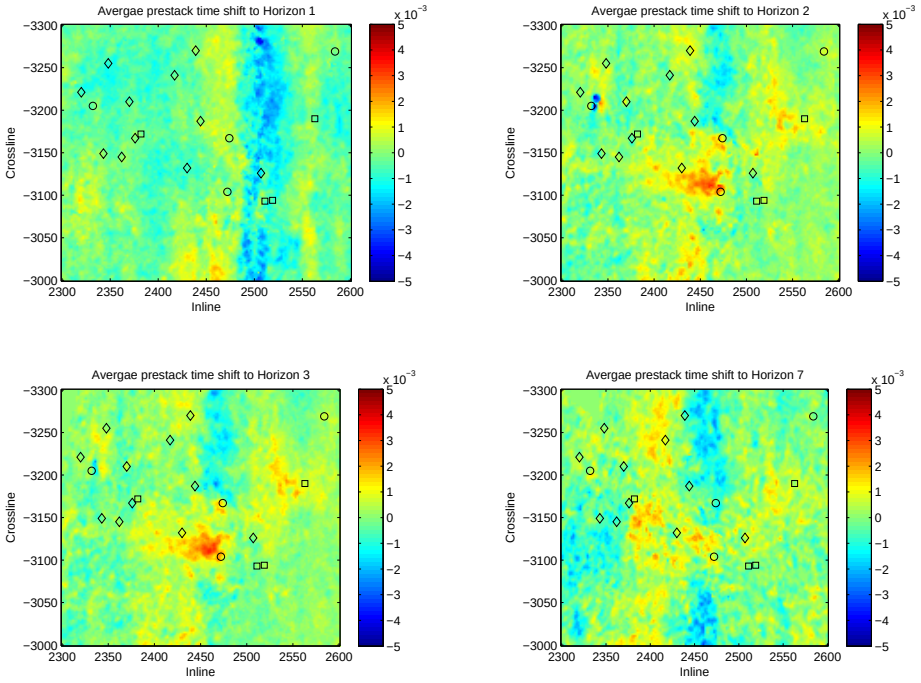

Figure 6.39: Change in travel time to 4 of the horizons of interest. Note that the top reservoir horizon (2) has a TWT shift similar to those of reflectors below the reservoir interval.

area of importance to the results of the data analysis.

6.5.1 Spectral ratio methodologies

Bandwidth and frequency resolution factor

I have shown in Chapter 4 that spectral ratio slopes are influenced by the bandwidth of measurement and the value assigned to the frequency resolution factor (k) when the s-transform is used. To find a stable spectral ratio regression bandwidth I will look at the effect of both bandwidth and resolution factor on the estimation of attenuation for both single vintage measurements of attenuation and direct measurements.

I test 4 resolution factors (1,2,5,10) and varying bandwidths between 2 and 100Hz. Stable values of attenuation are more likely to be observed for large travel times (hence large t^*) where the log spectral ratio gradient is likely to be large. For this reason I calculate effective attenuation estimates for each vintage between Horizon 1 and Horizon 2. The source spectrum is estimated by averaging the frequency spectra of near offset traces of Horizon 1. Therefore I would expect a positive attenuation estimate between Horizons 1 and 2 as there is a large travel-time difference, making attenuation estimates more stable.

In Figures 6.41 and 6.42 the effective attenuation has been calculated for the four resolution factors and various regression bandwidths for the 2001 and 2007 vintages respectively. For all resolution factors there appears to be noise generated at lower bandwidths and less noise at higher bandwidths. This effect is exaggerated for small values of k due to the large amounts of spectral averaging at higher frequencies. In all plots there appears to be a stable region of measurement for bandwidth between 10 and 60Hz for the lower frequency and 60 and 90Hz for the higher frequency. The effect of increased spectral averaging at small k can be seen by the increased smoothing of functions at higher bandwidths.

The direct change in attenuation for Horizon 2 (Figure 6.43) shows that there is noise present across all frequencies, and that spectral leakage is again apparent for low values of k. A large stable region (zero change in attenuation) can be seen for the higher resolution factors for bandwidths of 40-70Hz and wider. This figure also highlights the effect of spectral smoothing, enhancing the large negative spike in spectral ratio at around 40Hz. From these plots I choose to use a bandwidth of 10-80Hz and a resolution factor of 5.

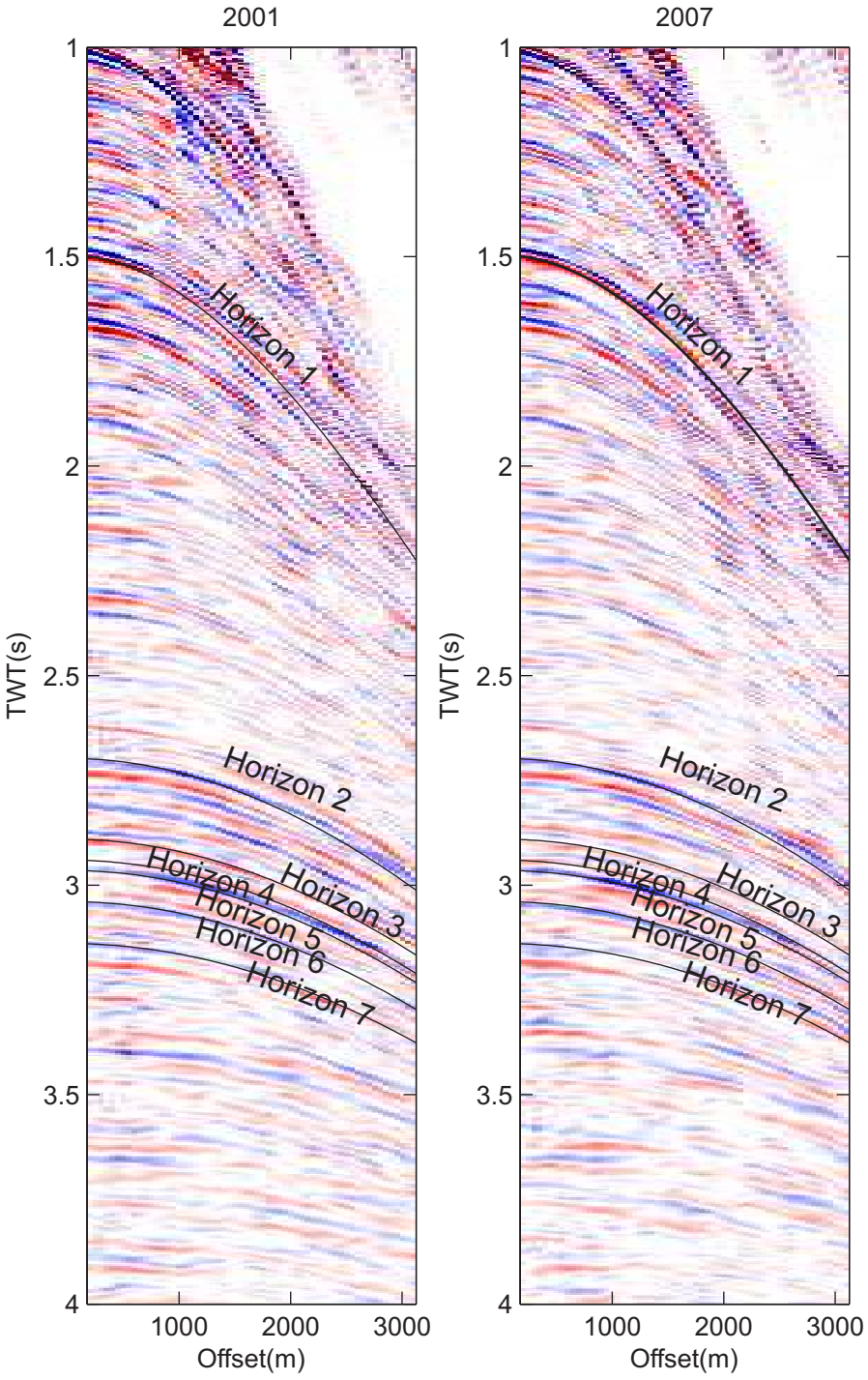

Figure 6.40: 2001 and 2007 data-sets used for the parameter test. Cross-line = 3104, In-line=2472. Located on WAG M34(C3). Horizons used for analysis are labelled Horizon 1 through 7. Horizon 2 is the top reservoir reflection. See Figure 6.2 for location.

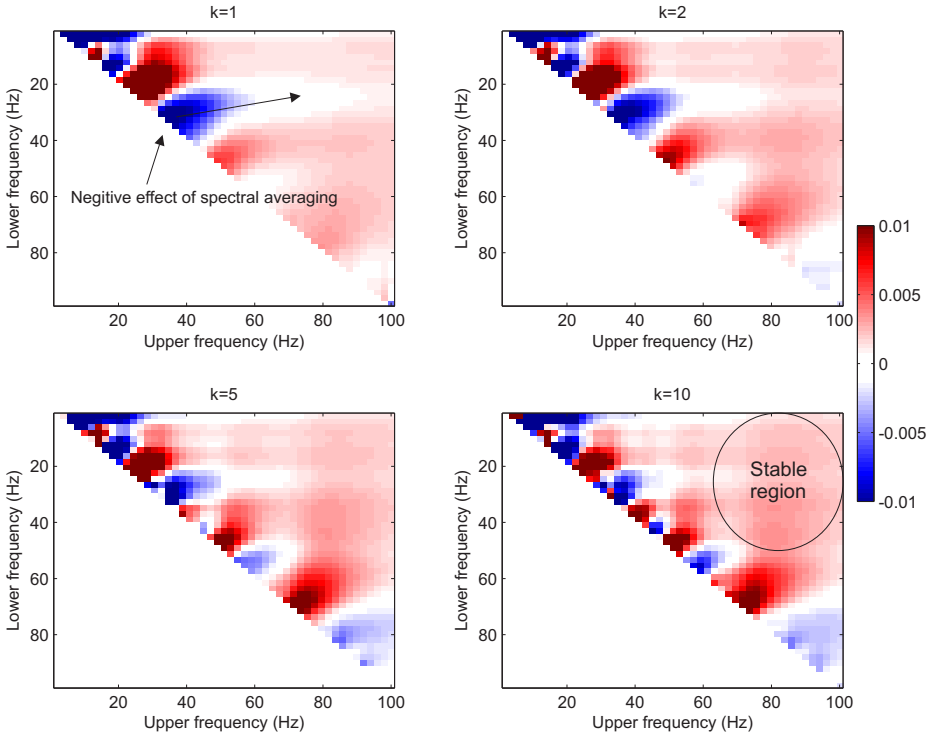

Figure 6.41: Effective attenuation of horizon 2 for the 2001 data-set using the PSQI methodology, using a source spectrum estimated from horizon 1. Each plot shows the calculation of a different resolution factor and the attenuation calculated is a function of Lower frequency and Upper frequency defining the bandwidth.

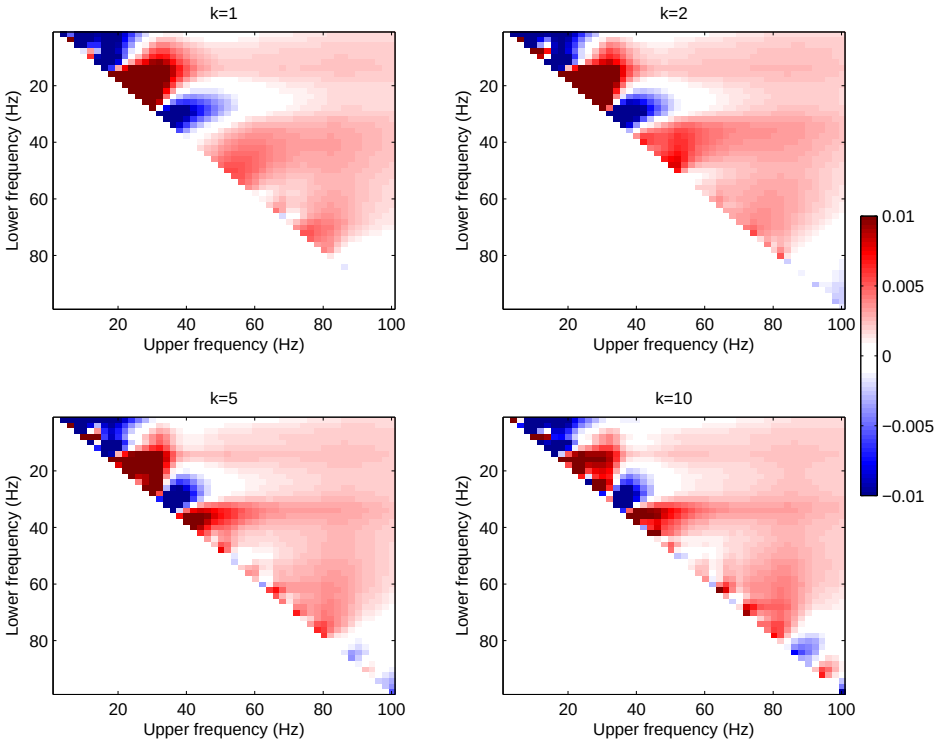

Figure 6.42: Effective attenuation of horizon 2 for the 2007 data set using the PSQI methodology, using a source spectrum estimated from horizon 1. Each plot shows the calculation of a different resolution factor and the attenuation calculated is a function of Lower frequency and Upper frequency defining the bandwidth.

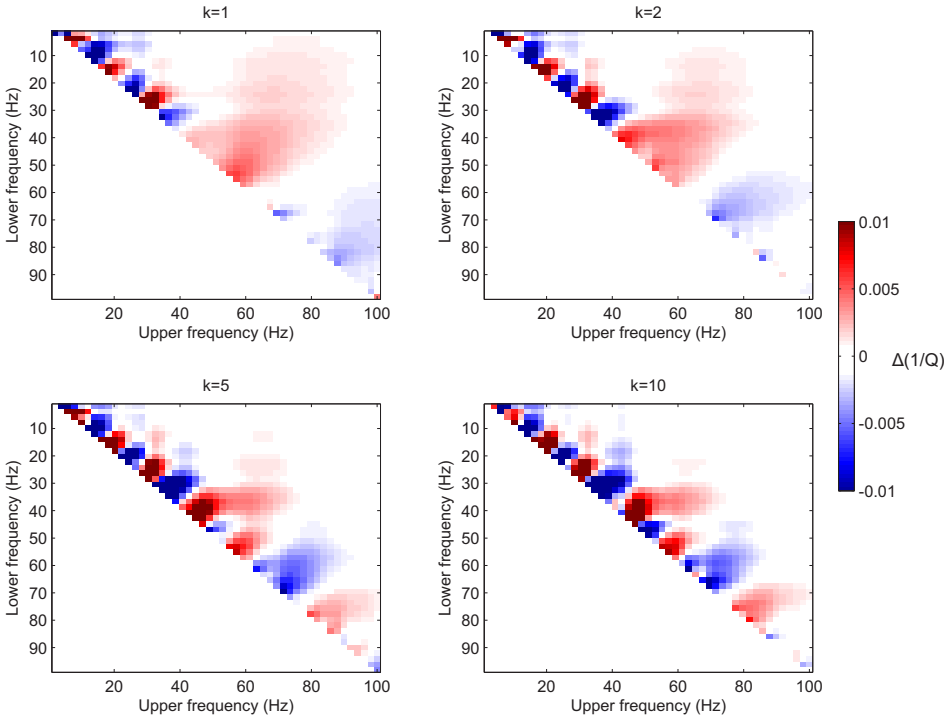

Figure 6.43: Direct attenuation of Horizon 2 between the 2001 and 2007 data-sets using the direct PSQI methodology. Each plot shows the calculation of a different resolution factor and the attenuation calculated is a function of Lower frequency and Upper frequency defining the bandwidth of the regression.

Offset range

A bandwidth of 10-80Hz and a resolution factor of 5 was used to calculate the attenuation to three horizons (2,3,and 7) for various offset bands. Tests show that there is no definite range of offsets that suits all horizons. It does however show that most positive attenuation estimates are gained from the near to mid offset ranges with very near and very far offsets showing instability in the attenuation measurement. A similar range of offsets had the best repeatability in Figures 6.28 and 6.29, giving further evidence to use this range of offsets. I therefore choose to limit the regression of the data set to offset ranges between 100 and 2500m. For Horizon 1 this will be reduced further (100-1000m) as there is large move-out and interference at far offsets (Figure 6.40).

6.5.2 Damping

We can add damping to the PSQI inversion to minimise the model size without compromising the misfit to data (Appendix A). Here I look at 3 CMPs from the data-set in order to find the correct damping parameter to use, if any. Normal damping is applied through a

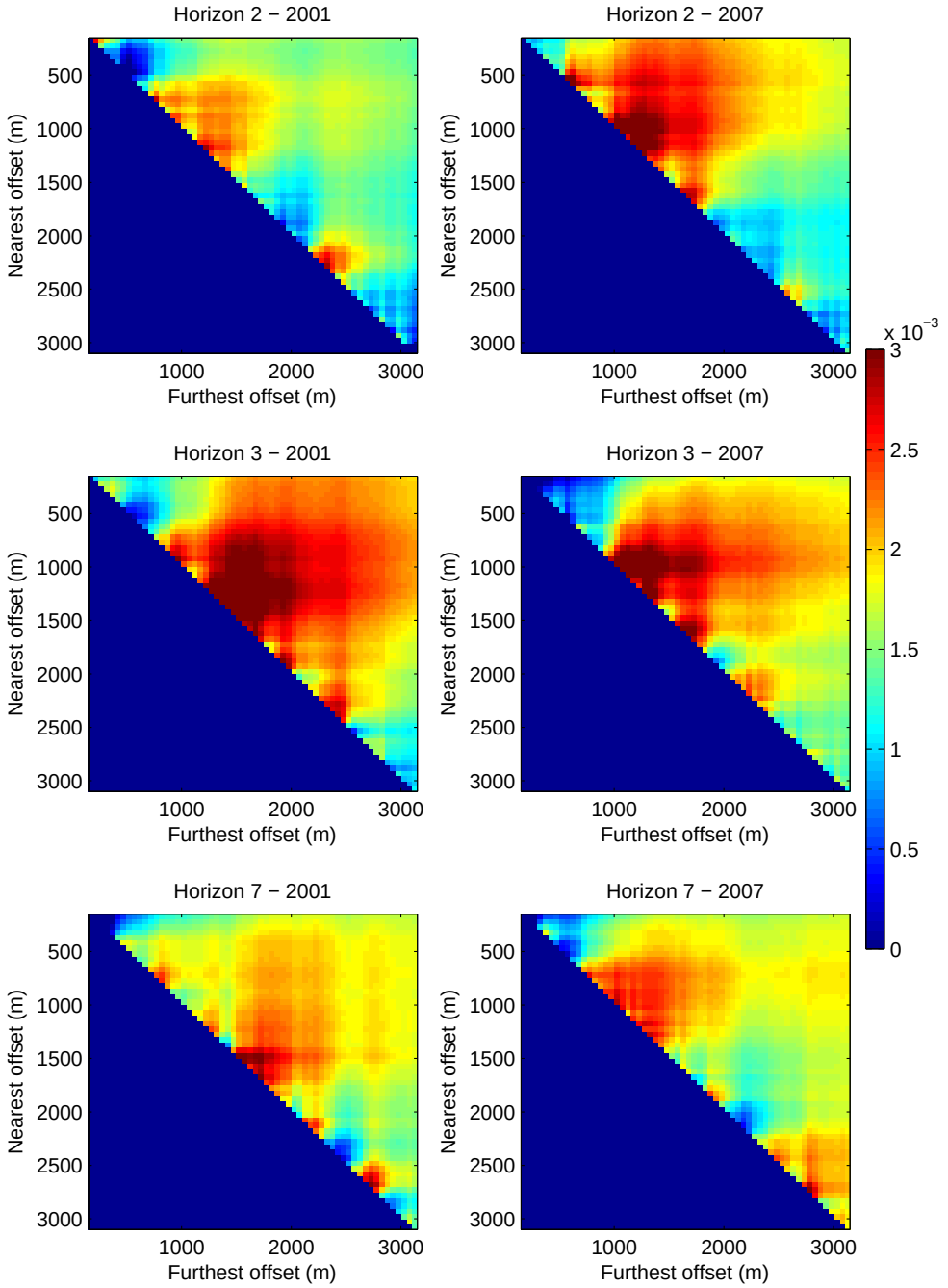

Figure 6.44: Comparison of effective attenuation estimates using a bandwidth of 10-80Hz for 3 horizons for each vintage of data.

damping term θ_1^2 in order to minimise the model size. The effect of the damping constant (θ_1^2) on the model size and data-misfit can be seen in Figure 6.45. The trade off curve shows that there is no significant benefit from reducing the size of the model as the data misfit increases sharply with a decreasing model size. I conclude from this that there is no beneficial trade-off made with model-size and misfit, hence for this data-set damping of the model size will not be included.

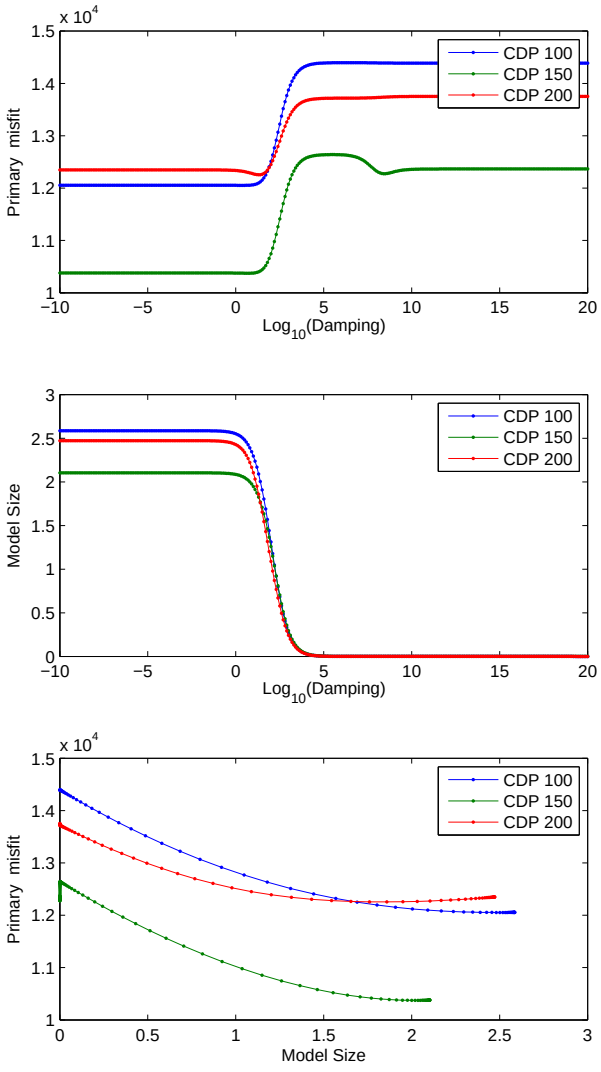

Figure 6.45: Effect of damping using the Direct PSQI methodology.

If we look at the more complex damping of the gradients of the intercepts (described in Appendix A) the trade off curve has a far more distinct "elbow" (Figure 6.46). This allows the misfit to the secondary constraint (model intercepts not varying greatly) to

be increased without significantly increasing the misfit to the data (Primary misfit). I therefore propose that a damping parameter to the secondary constraint should be chosen in the range of 10^2 to $10^{2.9}$.

6.5.3 Centroid frequency parametrisation

The centroid frequency methodology requires a similar parametrisation to that of the PSQI methodology. I therefore will use the same bandwidth and offset range as this will provide the most consistency in the results. I have already shown in Figure 6.20 that similar magnitudes of attenuation are predicted for the spectral ratio and centroid frequency methodologies, suggesting that the Gaussian assumption is valid.

6.5.4 IFM parametrisation

To parametrise the instantaneous frequency methodology, I utilize a single trace from the data-set at the reservoir interval. A typical trace (mid-offset) is chosen and can be seen in Figure 6.47. A 200 sample window is used to calculate the attenuation. Earlier tests in Chapter 3 showed that longer windows provide better estimates of attenuation.

Two of the parameters in the instantaneous frequency methodology control the stability of the calculation of the instantaneous frequency, these are the damping parameter (η^2) and the length of weighting. By leaving the weighting length at zero, several damping values are tested and the instantaneous frequency calculated. Figure 6.48 displays the instantaneous frequency calculated for the two vintages of seismic data for various damping values. The progression from under-damped to over-damped traces can be seen clearly in the data. The instantaneous frequency remains under-damped for damping values of 0 and 10^2, showing a large amount of noise, with no stable region of instantaneous frequency around the centre of the window. The instantaneous frequency is then over damped for values of 10^5 and 10^6 as the magnitude of the instantaneous frequency is far less than that observed in the undamped case. A good damping parameter to use is 10^4 as the noise on the instantaneous frequency is reduced but the magnitude of the instantaneous frequency is retained.

Now the damping values has been chosen the effect of weighting can be observed. We have seen previously that weighting can have a large impact on the data, but over-weighting the data can decrease the sensitivity of the inversion. With a constant damping parameter

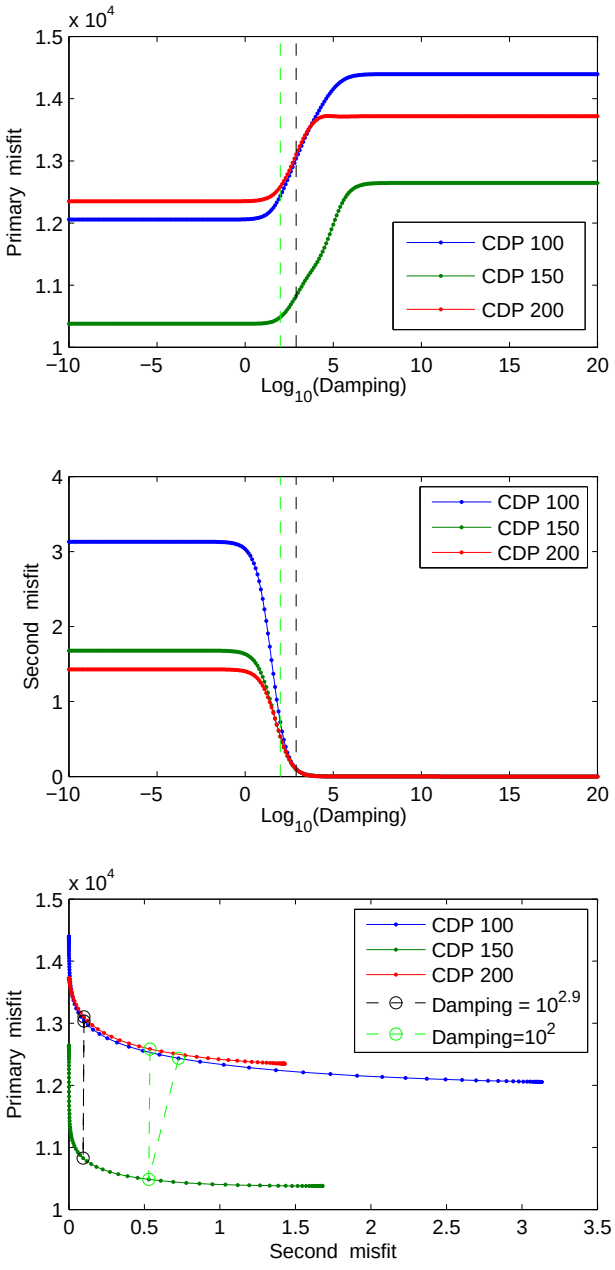

Figure 6.46: Effect of damping the Intercept gradients using the Direct PSQI methodology.

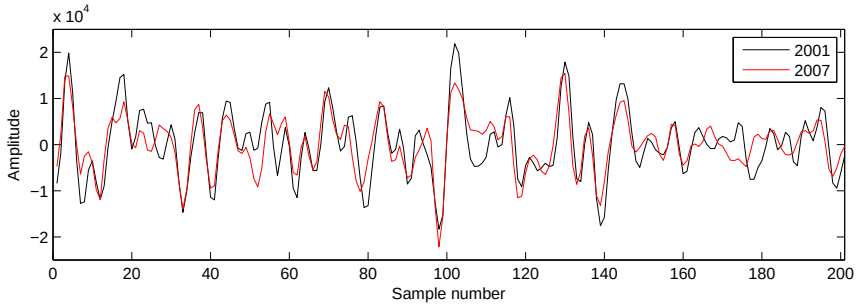

Figure 6.47: Two traces (from 2001 and 2007) use for parametrisation of the instantaneous frequency methodology.

of 10^4, 5 weighting lengths were tested. The gradual smoothing of the instantaneous frequency can be seen in Figure 6.49. For a weighting length of 1, the instantaneous frequency appears to be larger for the event in the centre of the window, however, too much averaging leads to this changing to an overall increase in instantaneous frequency across the window. I have chosen to use a weighting length of W=10 in the inversion.

Using the weighting length of 10 samples and a frequency damping of 10^4, I now test the regression length and inversion damping (θ^2). The inversion was tested on 7 reflectors for all offsets (60) and using regression lengths from 1 to 11 and inversion damping of 10^0 to 10^{10}. Two properties of these tests are shown in Figure 6.50. The average number of finite converged solutions solved for each reflector tells us where the inversion algorithm is able to resolve a solution efficiently. This shows that inversion damping over 10^6 would be unsuitable as very few solutions are found within 20 iterations. A slight decrease in the number of finite converged solutions can be seen as a function of increasing regression length. Also shown in Figure 6.50 is the standard deviation of results expressed as a percentage of the mean of the $\Delta(t^*)$ calculated. It can be seen that lower regression lengths have a smaller percentage error. I therefore choose to use an inversion damping of $\theta^2 = 10^4$ and a regression length of 5.

6.6 Attenuation Results

6.6.1 Direct Centroid frequency

Direct centroid frequencies are calculated for each of the 7 horizons for offsets up to 2500m using a bandwidth of 10-70Hz. The direct change in t^* for each reflector and offset are then calculated (Figure 6.51 for an example). As outlined in Chapter 3, a regression against offset squared is performed to find the zero offset intercept (zero offset Δt^*). The

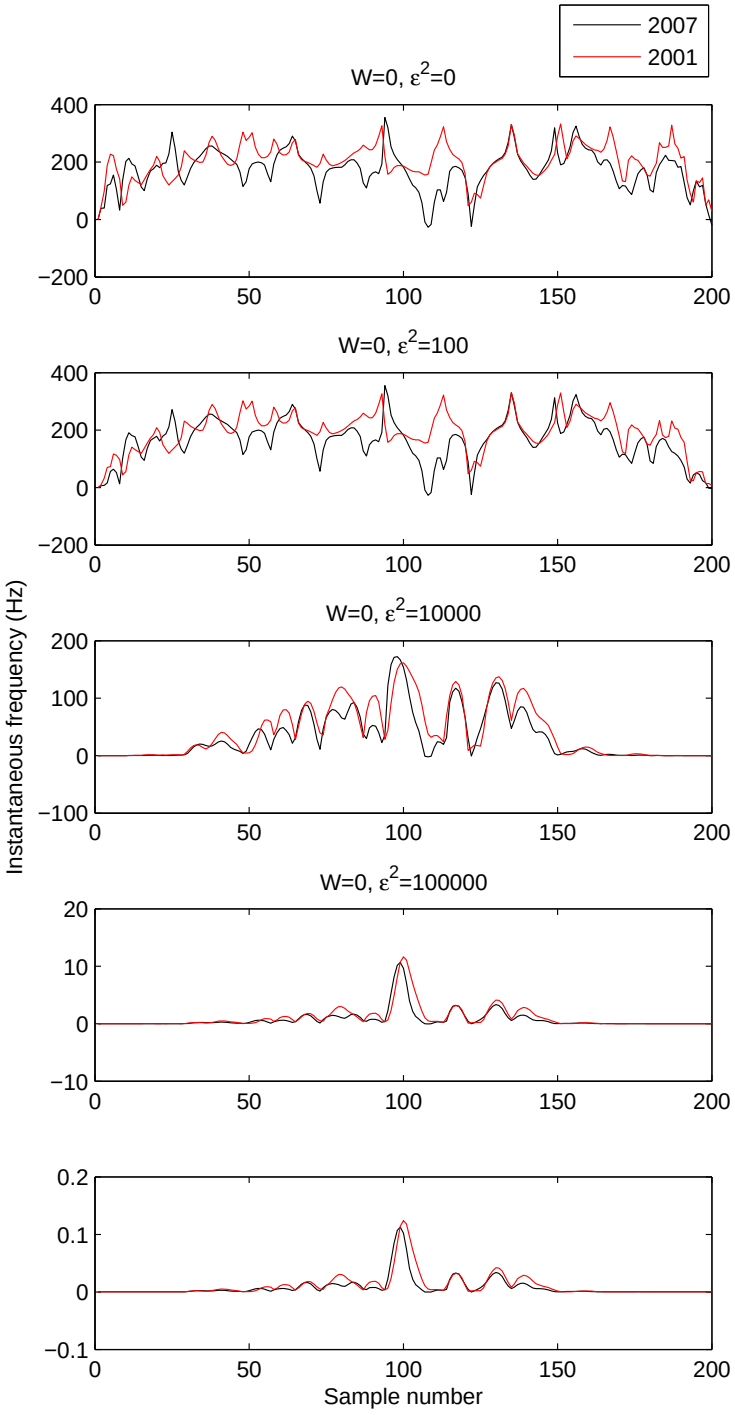

Figure 6.48: From top to bottom: Instantaneous frequency calculated for a single trace centred around Horizon 2 (top reservoir) for damping values of 0, 10^2, 10^4, 10^5 and 10^6. Instantaneous frequencies calculated using 0 and 10^2 are under-damped with the instantaneous frequency being very noisy, whilst the 10^5 and 10^6 damping parameters have over-damped the instantaneous frequency by reducing the magnitude of the instantaneous frequency measured. It can be seen that 10^4 provides the best estimation of instantaneous frequency as the correct magnitude compared to the under-damped instantaneous frequency has been preserved whilst reducing the noise.

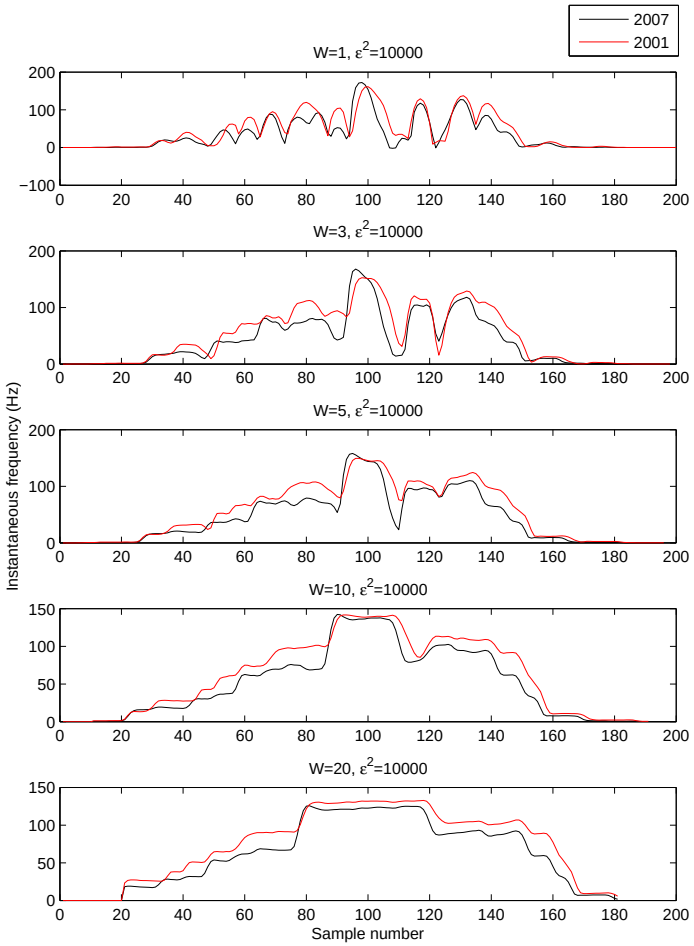

Figure 6.49: Instantaneous frequency for various weighting lengths.

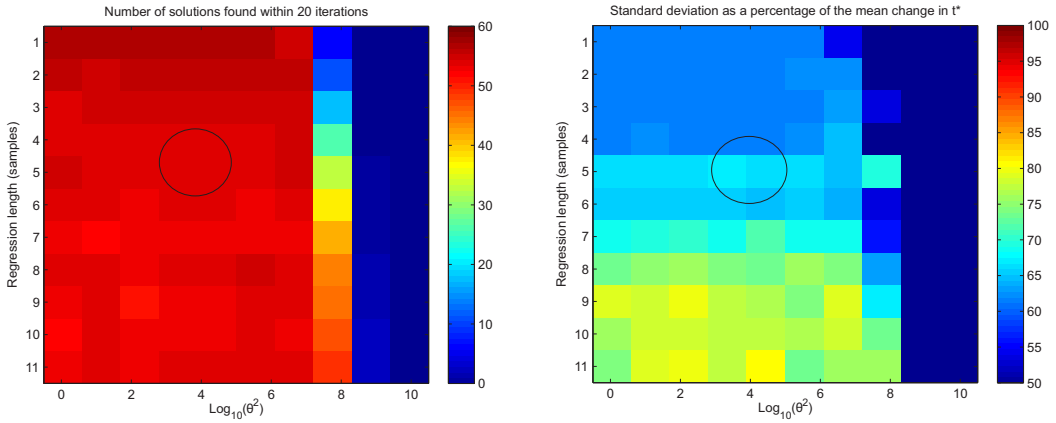

Figure 6.50: Left: The number of finite converged solutions (out of a maximum of 60 offsets) after 20 iterations of the inversion. Right: The standard deviation as a percentage of the measured change in t*.

uncertainty in the intercept is calculated through propagation of the standard deviation of the Δt^* estimated for all offsets. The model parameter covariance matrix can then be calculated by

$$C = (A^T C_e^{-1} A)^{-1} \tag{6.9}$$

where C_e is a diagonal matrix containing the errors on the measurements of Δt^* at each offset. This tells us how the errors propagate into the model parameters, and therefore the diagonal elements of the covariance matrix are the inverse of the variance squared on the model parameter (Gubbins, 2004). Results of Horizons 1, 2, 3 and 7 can be seen in Figure 6.52. The maximum and average uncertainties on Δt^* can be seen in Table 6.1. Average uncertainties are small relative to the largest changes in Δt^* (8.95x10^{-5}) compared with 0.01. The average uncertainty in the measurement increases with depth, which may be expected as signal to noise will likely decrease with depth.

In general the spatial distribution of t^* changes is fairly incoherent, however, there are some similar features, particularly for horizons below the reservoir.

	Centroid Frequency method	
	Max ($t^* \times 10^{-5}$s)	Mean ($t^* \times 10^{-5}$s)
Horizon 1	25.23	8.91
Horizon 2	24.74	8.51
Horizon 3	22.66	8.61
Horizon 4	22.39	8.55
Horizon 5	22.06	8.84
Horizon 6	22.21	9.27
Horizon 7	24.68	9.99
Mean	**23.42**	**8.95**

Table 6.1: Maximum and mean uncertainties in calculating the change in t^* via the Centroid frequency methodology.

6.6.2 PSQI

The PSQI calculations were performed in the bandwidth 10-70Hz using the s-transform with a resolution factor of 5. Offsets were restricted to 100-2500m and weighting was included by calculating the standard deviation of the spectral ratio surface at each frequency. Uncertainties are calculated by propagating these data uncertainties through to the model parameters using the covariance matrix (Equation 6.9). A secondary constraint (see Appendix A) of $\theta^2 = 2.9$ is also implemented in the inversion to reduce the varia-

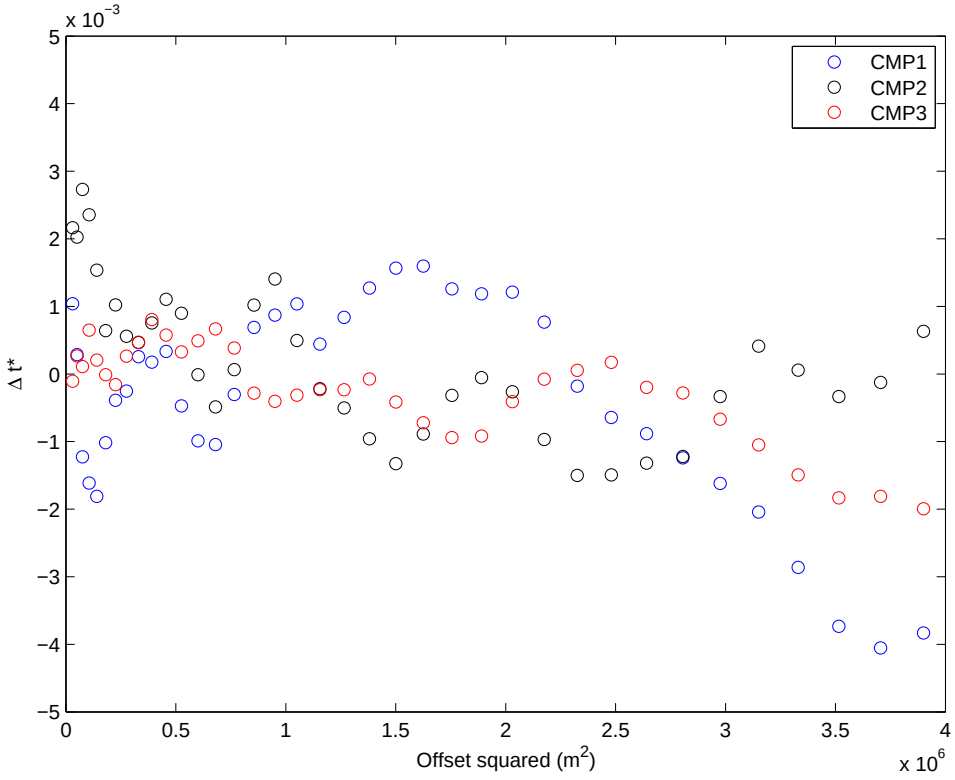

Figure 6.51: Direct Δt^* estimates made to each of the 7 reflectors using the Centroid frequency methodology.

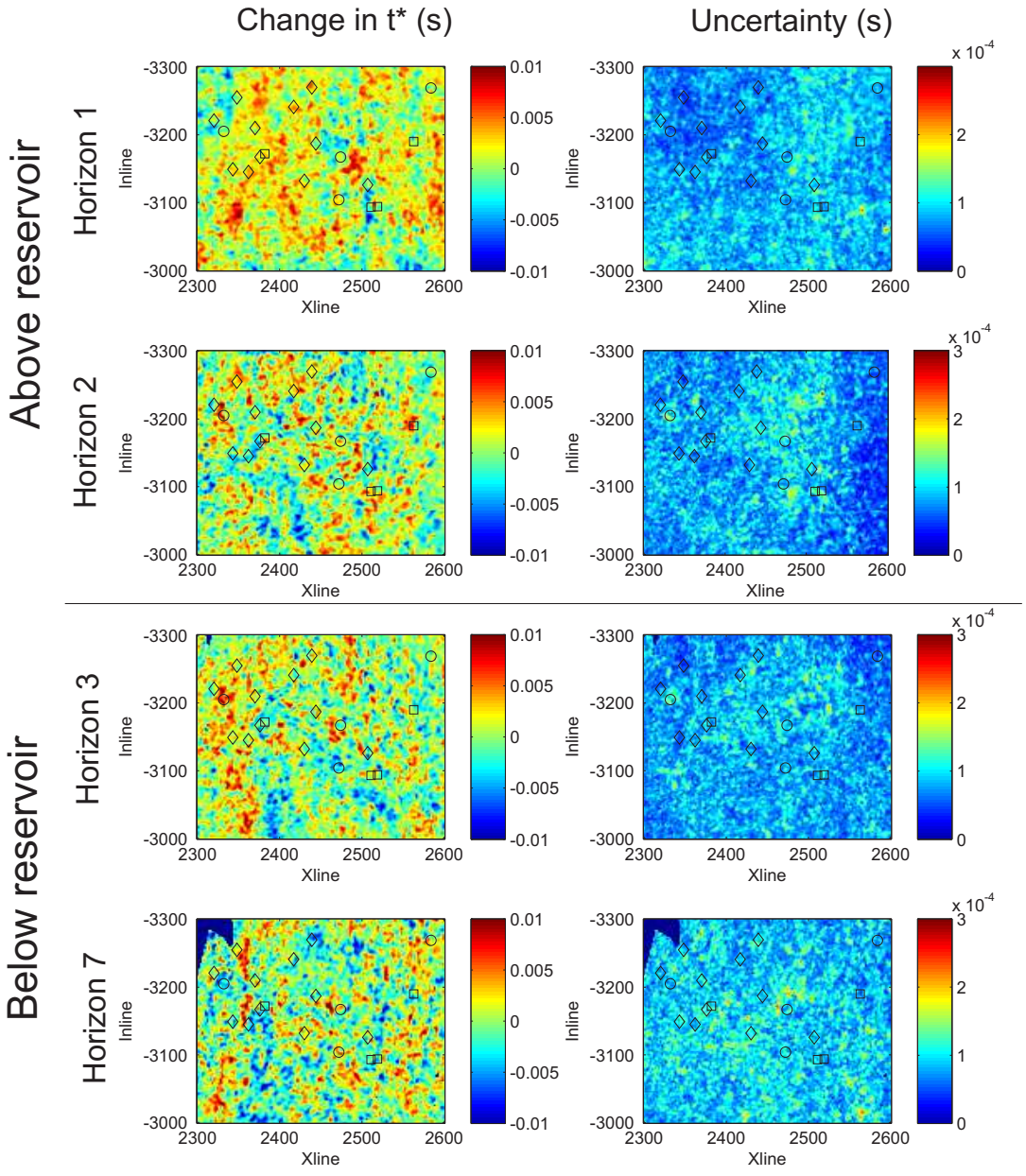

Figure 6.52: Direct Δt^* estimates made to Horizons 1,2,3 and 7 using the Centroid frequency methodology.

tion in the intercept terms with offset. The Direct methodology was carried out on all 7 horizons and results are displayed in Figure 6.53. Uncertainties are not plotted but are given in Table 6.2 with a maximum uncertainty of 9.96x10^{-5} and average uncertainty of 8.75x10^{-5}, much smaller than the observed changes in t^* (5x10^{-3}). Direct changes in t^* show some coherency but it is clear that there are some changes that correlate well with the acquisition direction (along in-line).

The absolute PSQI methodology is also performed with the same parameters as the Direct methodology. The reference wavelet is estimated from the average spectral properties of the near offset traces (<1000m) from Horizon 1 at each CMP location. The effective attenuation estimates for each vintage of data are displayed in Figures 6.54 and 6.55. The majority of effective t^* are positive with a slight increase in average uncertainty between vintages (6.75x10^{-5} to 6.78x10^{-5}, Table 6.2). The interval attenuation values between consecutive horizons is shown in Figure 6.56. The most coherent attenuation changes can be seen to occur in the interval above the reservoir. However, I have shown in the synthetic example that the change in attenuation may be detectable on the top reservoir reflection. I instead look at the change in effective t^* to each reflector between vintages of data (Figure 6.57) . The uncertainties of these changes can be found through the addition of the uncertainties of each vintage. Figure 6.57 shows large similarities of the changes in t^* for both the top reservoir reflection and the reflections below the reservoir interval. There are coherent anomalies seen in the data including an increase in attenuation near to the centre of the area and an increase in the top right of the survey area.

	Absolute 1 ($t^* \times 10^{-5}$**s**)		**Absolute 2** ($t^* \times 10^{-5}$**s**)		**Absolute diff** ($t^* \times 10^{-5}$**s**)		**Direct** ($t^* \times 10^{-5}$**s**)	
	Max	Mean	Max	Mean	Max	Mean	Max	Mean
Horizon 1	8.69	7.77	8.72	7.77	17.41	15.54	9.96	9.88
Horizon 2	7.42	6.48	7.63	6.52	15.04	13.00	8.55	8.51
Horizon 3	7.50	6.57	7.59	6.62	15.10	13.19	8.60	8.53
Horizon 4	7.34	6.57	7.55	6.61	14.88	13.17	8.61	8.55
Horizon 5	7.40	6.59	7.68	6.62	15.08	13.21	8.63	8.57
Horizon 6	7.35	6.57	7.49	6.60	14.84	13.17	8.66	8.58
Horizon 7	7.48	6.67	7.48	6.71	14.96	13.39	8.68	8.61
Mean	**7.60**	**6.75**	**7.73**	**6.78**	**15.33**	**13.53**	**8.81**	**8.75**

Table 6.2: The uncertainties in calculating t^* and the change in t^* via the Absolute and Direct PSQI methodologies. Columns "Absolute 1" and "Absolute 1" are the uncertainties in effective t^* to each horizon for 200 and 2007 respectively. Column "Absolute diff" is the uncertainty in $\Delta(t^*)$ to each reflector and Column "Direct" is the uncertainty in $\Delta(t^*)$ to each horizon using the direct PSQI methodology.

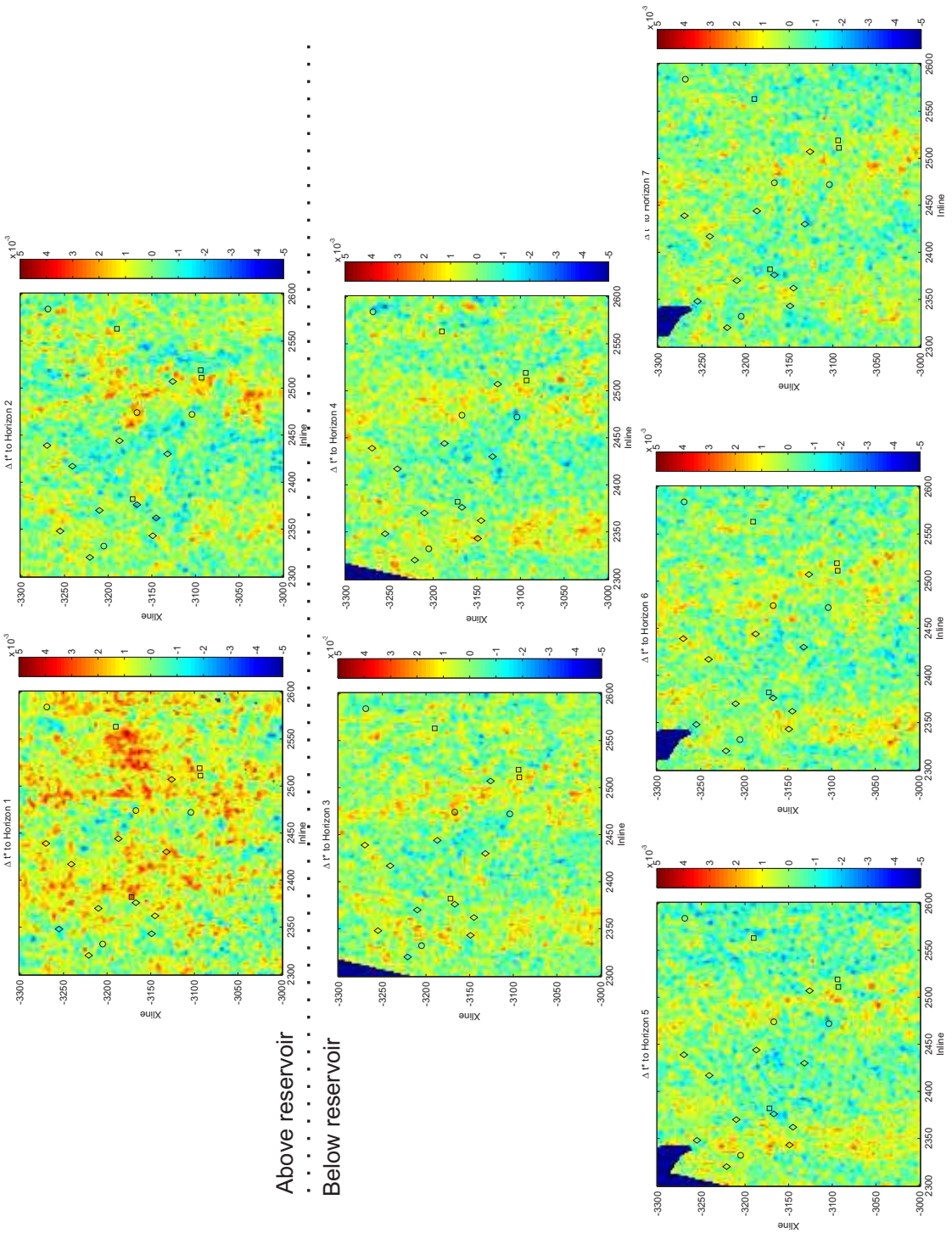

Figure 6.53: Direct Δt^* estimates made to each of the 7 reflectors using the Direct PSQI methodology.

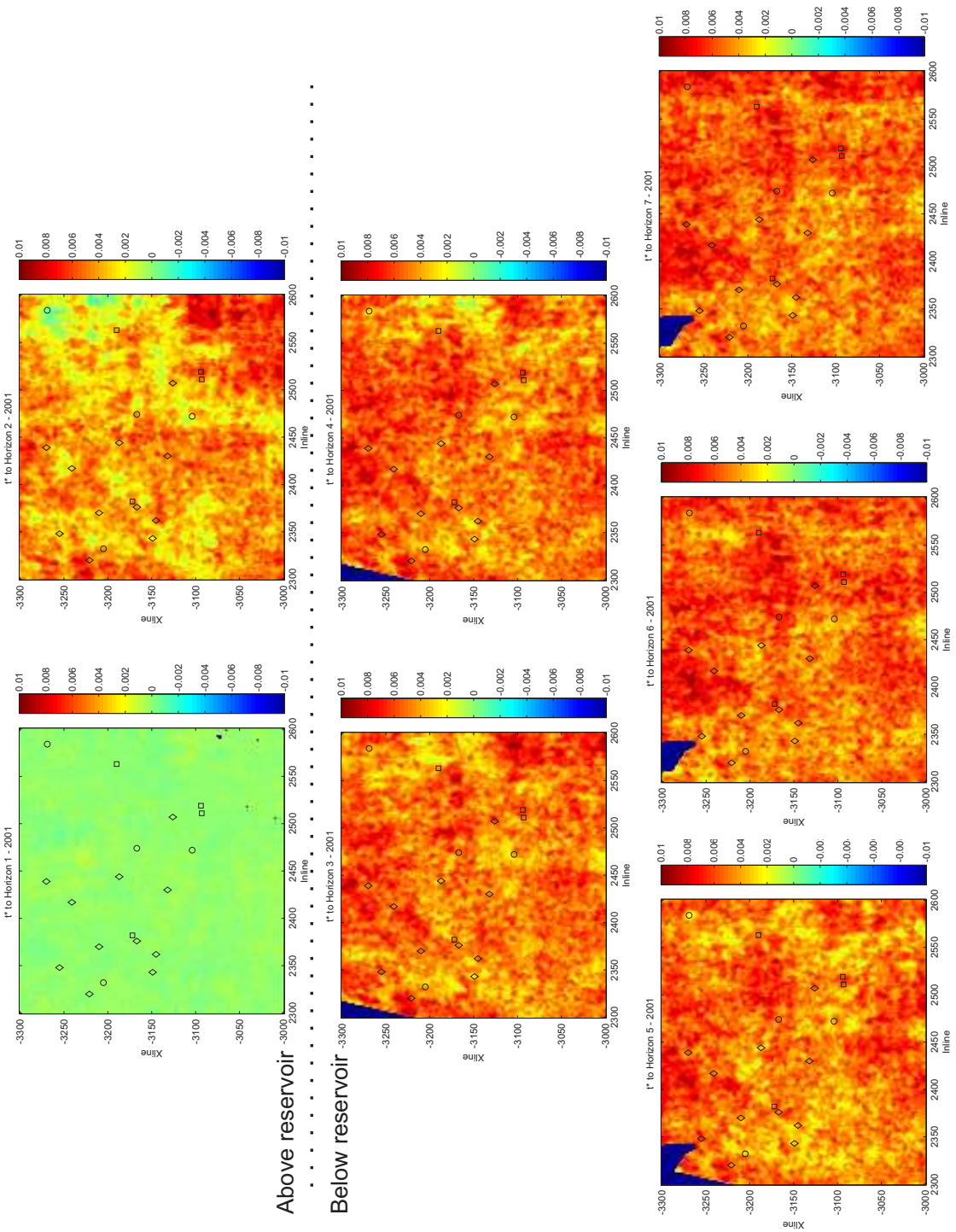

Figure 6.54: Effective Δt^* estimates for 2001 made to each of the 7 reflectors using the Absolute PSQI methodology.

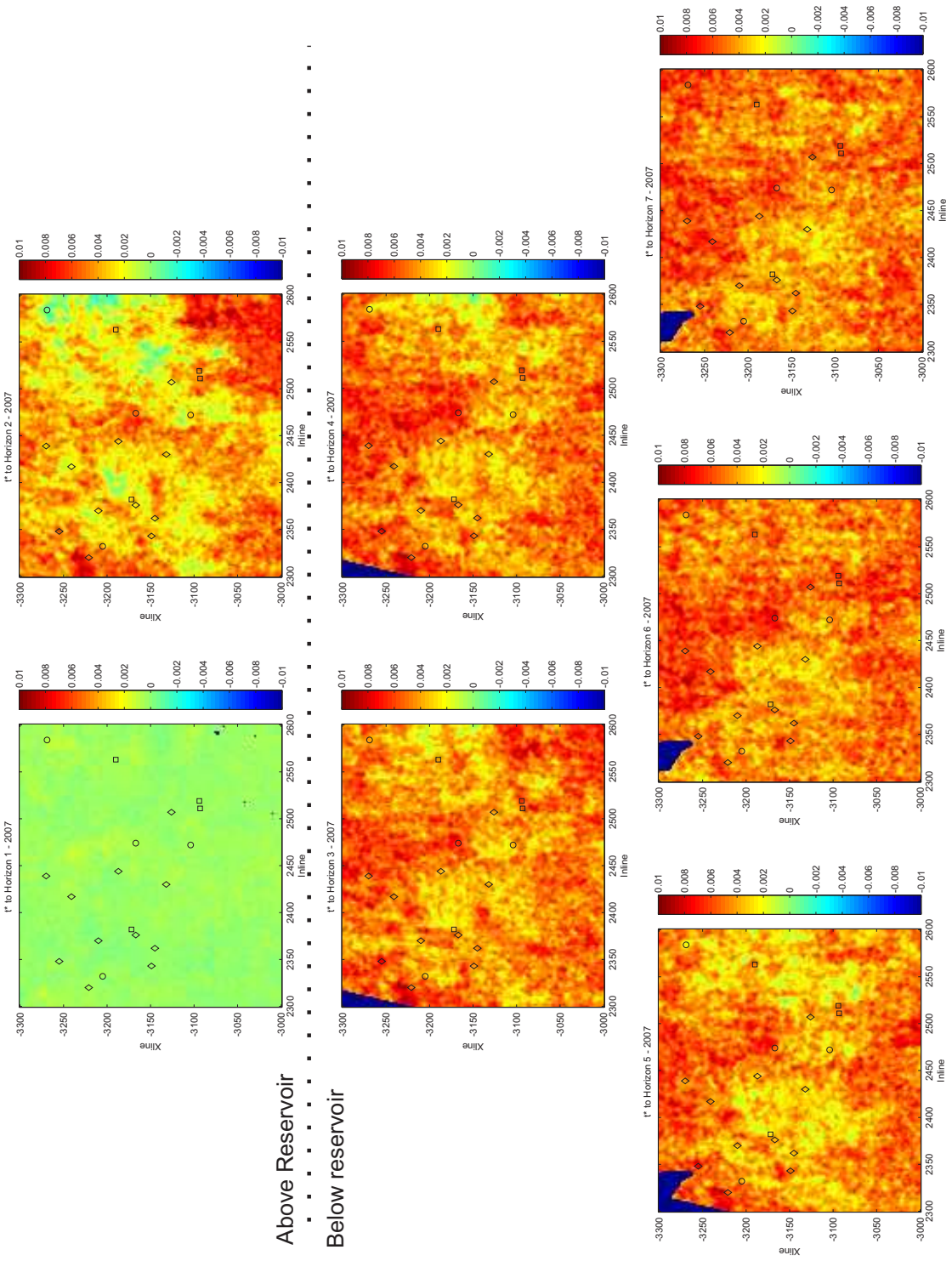

Figure 6.55: Effective Δt^* estimates for 2007 made to each of the 7 reflectors using the Absolute PSQI methodology.

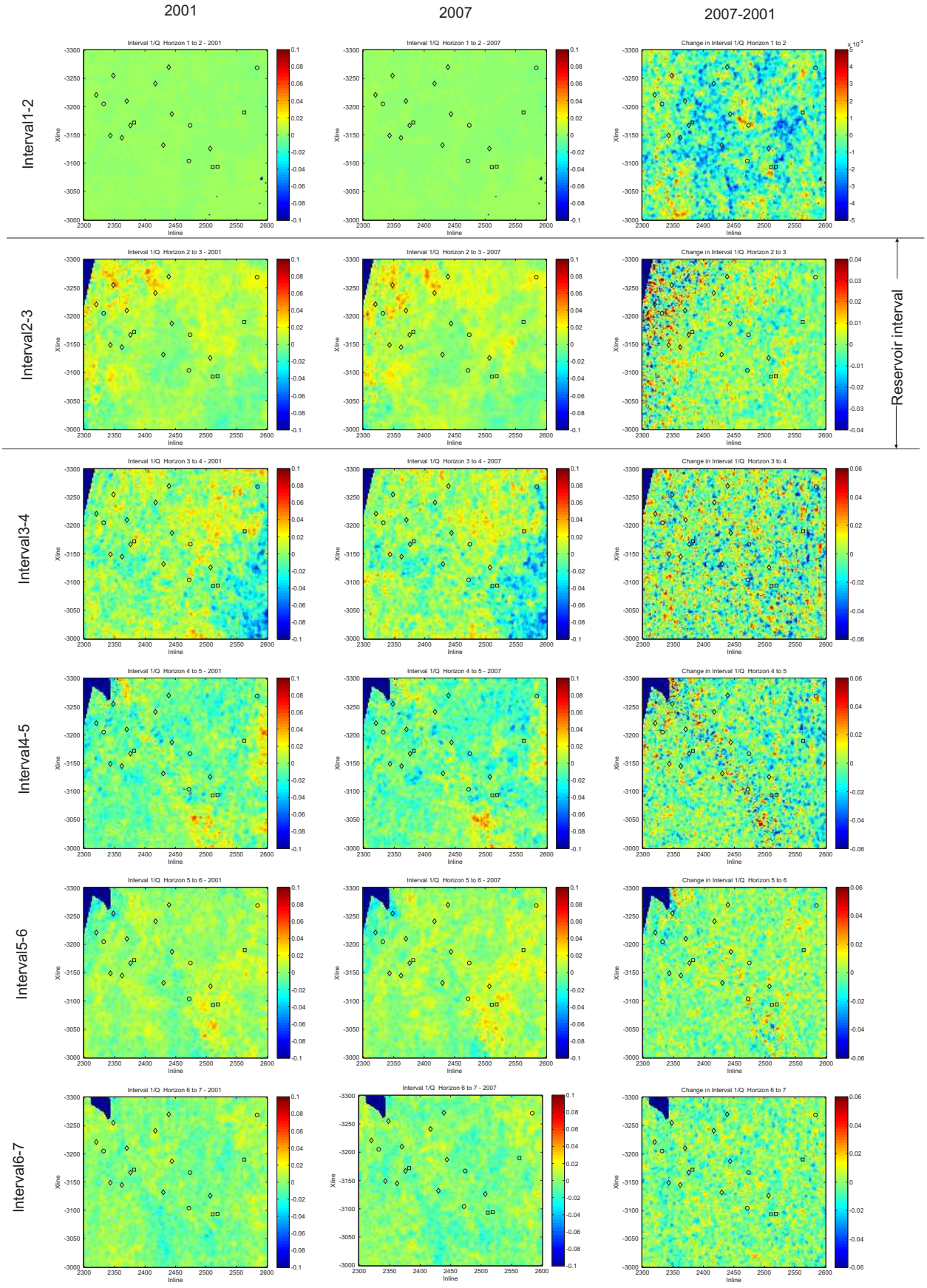

Figure 6.56: Interval $1/Q$ estimates for 2001 (left) and 2007 (centre) for each consecutive interval (6 intervals from top to bottom). Changes in interval (1/Q) are also plotted (right).

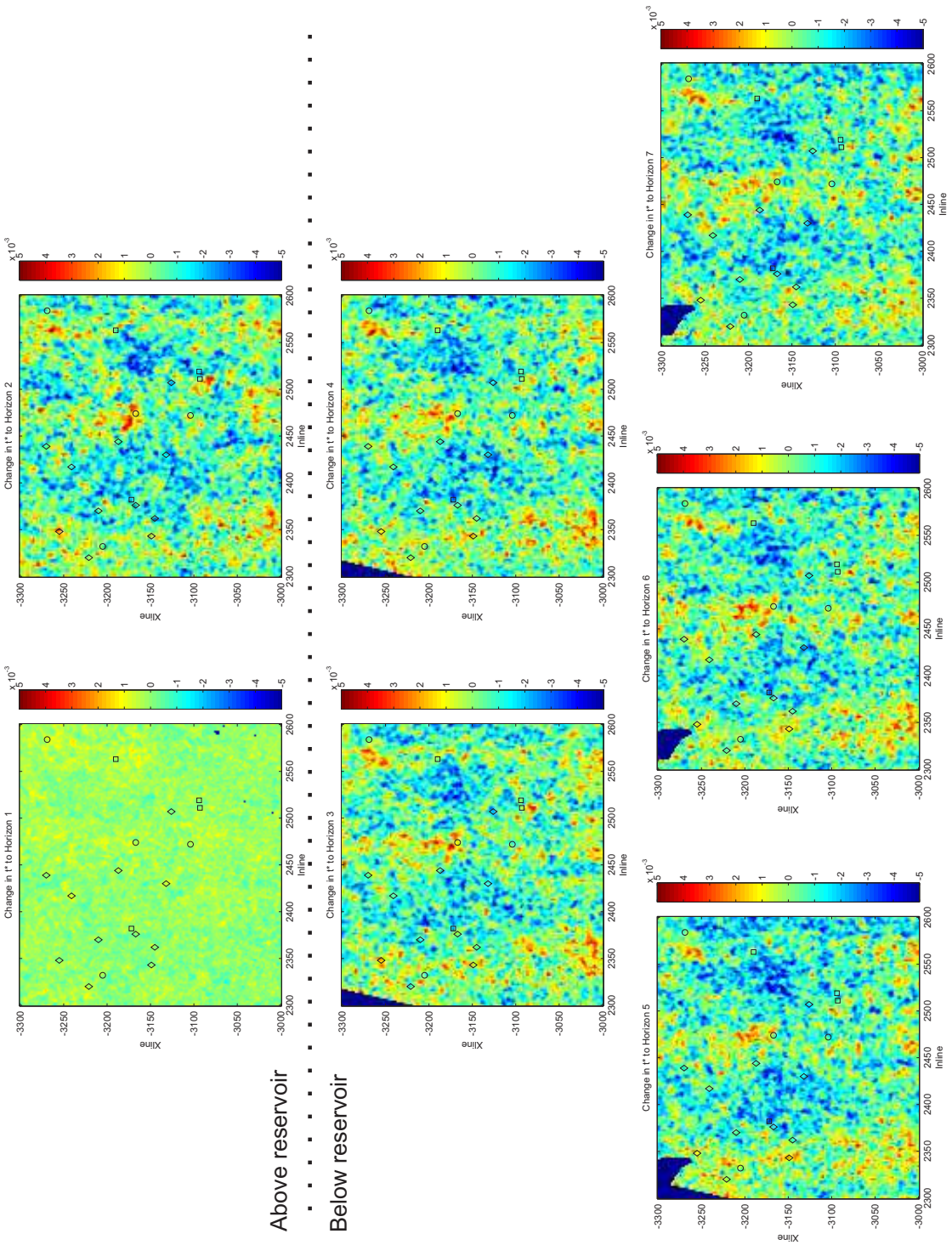

Figure 6.57: Change in t* to each of the 7 reflector analysed using the Absolute PSQI method. Horizons 2-7 are all very similar in the change in t*.

6.6.3 Instantaneous frequency matching

Direct time-lapse instantaneous frequency matching was used to calculate the change in t^* to three horizons (1-3) for offsets up to 2500m. A frequency weighting length of 10 samples, regression length of 5 samples, frequency damping of 10^4 and inversion damping of 10^4 were used to calculate the direct change in t^*. Initial results from these three horizons and the interval changes in t^* can be seen in Figure 6.58. The change in t^* in the reservoir interval shows very coherent anomalies, particularly around the WAG injectors (circles). It is clear that these anomalies are being produced from the direct comparison on the top reservoir reflection (Horizon 2). The correlation between these anomalies and the Amplitude and TWT anomalies can be seen in Figure 6.59. Good correlation can be seen between the amplitude and Δt^*. I have shown in Chapter 4 that the instantaneous frequency matching methodology is susceptible to changes in the amplitude between vintages of data and this suggests that it is causing artefacts in the analysis.

A solution to this problem is found by using a frequency damping that is proportional to the maximum envelope in the regression region. Results from this using a frequency damping of 20% of the maximum amplitude envelope in the regression region are calculated for 4 horizons (1,2,3 and 7) and results are displayed in Figure 6.60. It can be seen that these results no longer show the same coherent anomalies for the second horizon and therefore the dependence on the change in amplitude has been minimised. Results now correlate well with the results from the Centroid frequency methodology.

Uncertainties are estimated by propagating the standard deviation of measurements for all offsets. The uncertainty on the zero offset intercept in the regression against offset squared (error on t^*) is also plotted in Figure 6.60. Uncertainties for each of the Horizons are summarised in Table 6.3. Average uncertainties are small (3.49×10^{-5}) whilst there are some large uncertainties present (55.73×10^{-5}).

	Instantaneous Frequency method	
	Max ($t^* \times 10^{-5}$s)	Mean ($t^* \times 10^{-5}$s)
Horizon 1	55.73	3.25
Horizon 2	28.88	2.78
Horizon 3	33.60	3.41
Horizon 7	37.80	4.51
Mean	**39.00**	**3.49**

Table 6.3: The uncertainties in calculating the change in t* via the Instantaneous frequency methodology.

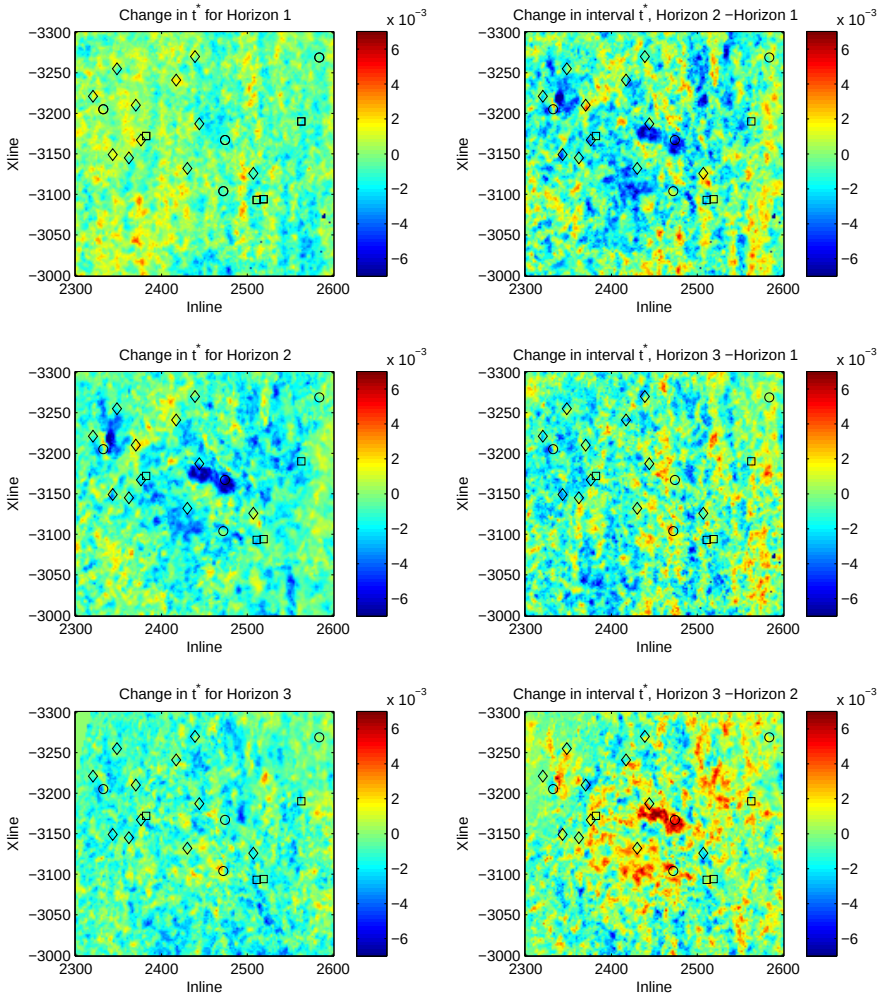

Figure 6.58: The direct change in t* calculated for Horizon 1, Horizon 2 and Horizon 3 (left hand side, from top to bottom respectively). Interval changes in t* are calculated between Horizon 1 and 2 (top right), Horizon 1 and 3 (middle right) and Horizon 2 and 3 (bottom right).

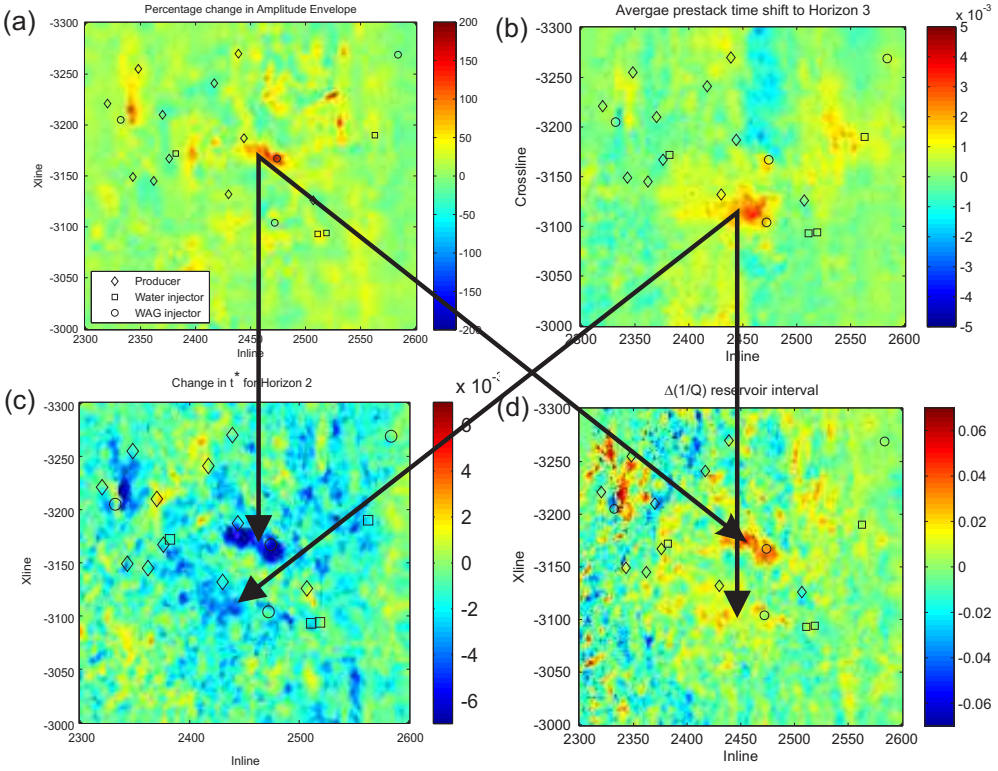

Figure 6.59: Comparison of percentage change in Amplitude Envelope from top reservoir (a), prestack two-way time shift to horizon 3 (b), direct change in t* calculated by TLIFM for horizon 2 (c) and the change in interval attenuation for the reservoir interval calculate from TLIFM (d). There are coherent anomalies across the different attributes, some of which are highlighted by arrows.

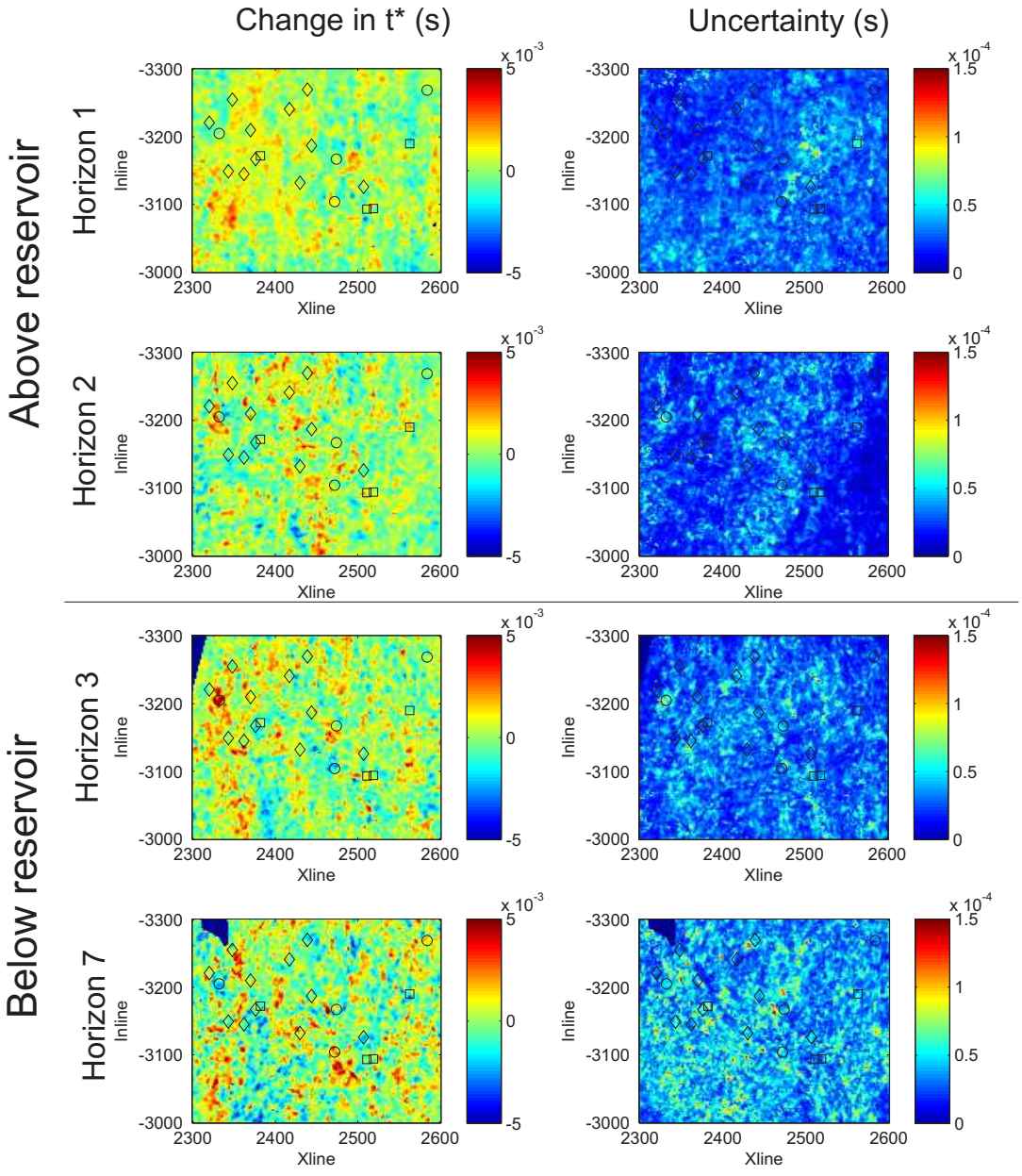

Figure 6.60: IF results with the percentage dependent damping and the uncertainty on each measurement.

6.6.4 Comparison of methodologies

The average maximum error and average mean error for all reflectors for the 4 methodologies (Tables 6.1 to 6.3) used are compared in Table 6.4. It can be seen that the methodology with the least average uncertainty is the Instantaneous frequency methodology and the method with the greatest mean uncertainty is the Absolute PSQI methodology. However, these statistics also show that the Instantaneous frequency has the largest maximum uncertainty. In the PSQI Direct and Absolute methodologies, maximum errors do not differ greatly from the mean uncertainties. By comparing the magnitude of Δt^* calculated in each of the methodologies it is clear that the Centroid frequency produces much larger values than the other methodologies (Compare Figures 6.52 with 6.60 and 6.53). This is because the magnitude of the centroid frequency change is controlled by the standard deviation of the spectrum. It may therefore be necessary to scale the centroid frequency accordingly with the other methodologies. Figure 6.61 compares the distribution of Δt^* measurements for all horizons. Standard deviations for all methodologies are around 0.001 apart from the Centroid frequency methodology, which has a standard deviation of 0.0028. This gives a method of reducing the magnitude of the centroid frequency estimates to match the magnitudes of the PSQI and Instantaneous frequency methodologies. We can therefore divide the centroid frequency attributes by $0.0028/0.001 = 2.8$. A standard deviation of $\approx$0.001 would suggest that this is the limit of significance of an anomaly in the attribute maps.

The interval change in t^* is calculated by averaging the Δt^* of reflectors below the reservoir and subtracting the change in t^* calculated for Horizon 1. Horizon 2 is not used as we have seen in Chapter 4 that reflectors that separate intervals in which attenuation changes may occur could cause problems due to frequency dispersion. Another problem with using Horizon 2 is that in the synthetic studies, an increase in attenuation was detected for the top reservoir horizon as well as below the reservoir. We have also seen evidence for this in the real data in Figure 6.57. Results for the 4 methodologies used here are displayed in Figure 6.62. Horizon 2 is omitted from these calculations as we have seen in the synthetic examples that changes in the reservoir interval can be detected on the top reservoir. Coherent anomalies can be seen from each of the methodologies, in particular next to the upper central WAG injector. Both the Direct PSQI and Absolute PSQI methodologies produce almost identical maps, as may be expected when interval changes are calculated.

	Maximum Uncertainty	**Mean uncertainty**
	$(t^* \times 10^{-5})$	$(t^* \times 10^{-5})$
PSQI absolute	15.33	13.53
PSQI direct	8.81	8.75
Centroid Frequency	23.42	8.95
Instantaneous frequency	39.00	3.49

Table 6.4: Comparison of uncertainties on the changes in attenuation for each methodology.

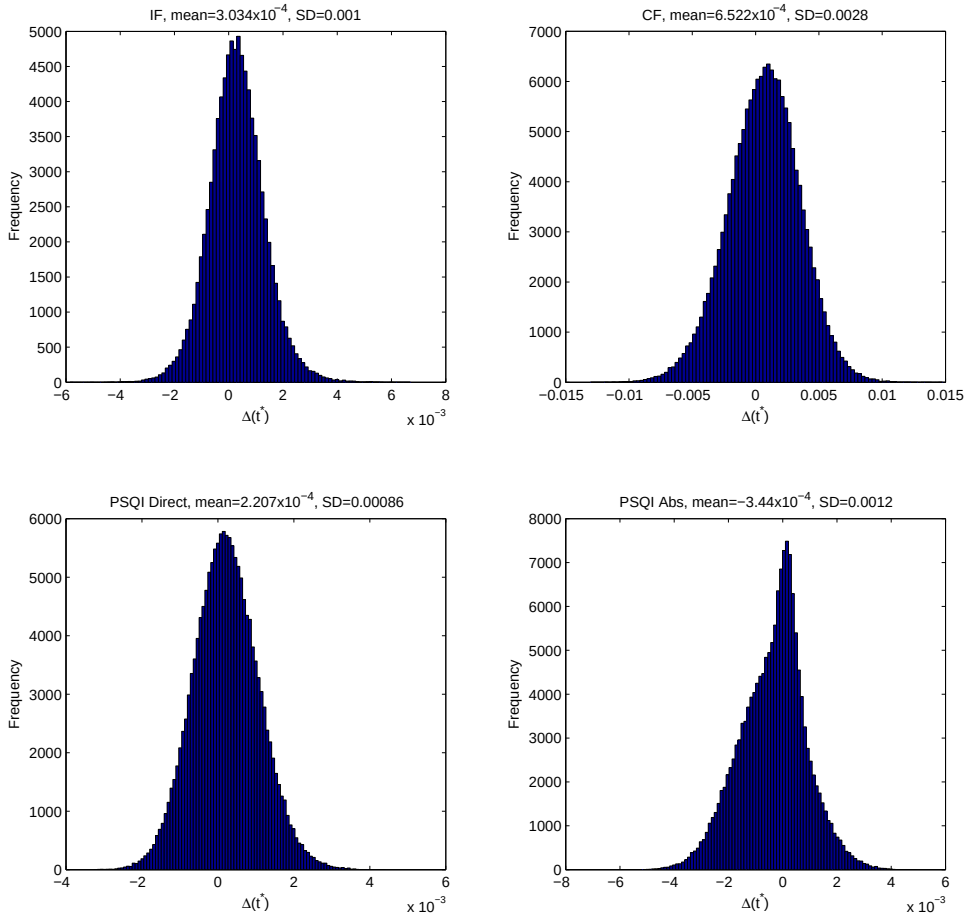

Figure 6.61: Histograms of all changes in Δt^* for all of the methodologies.

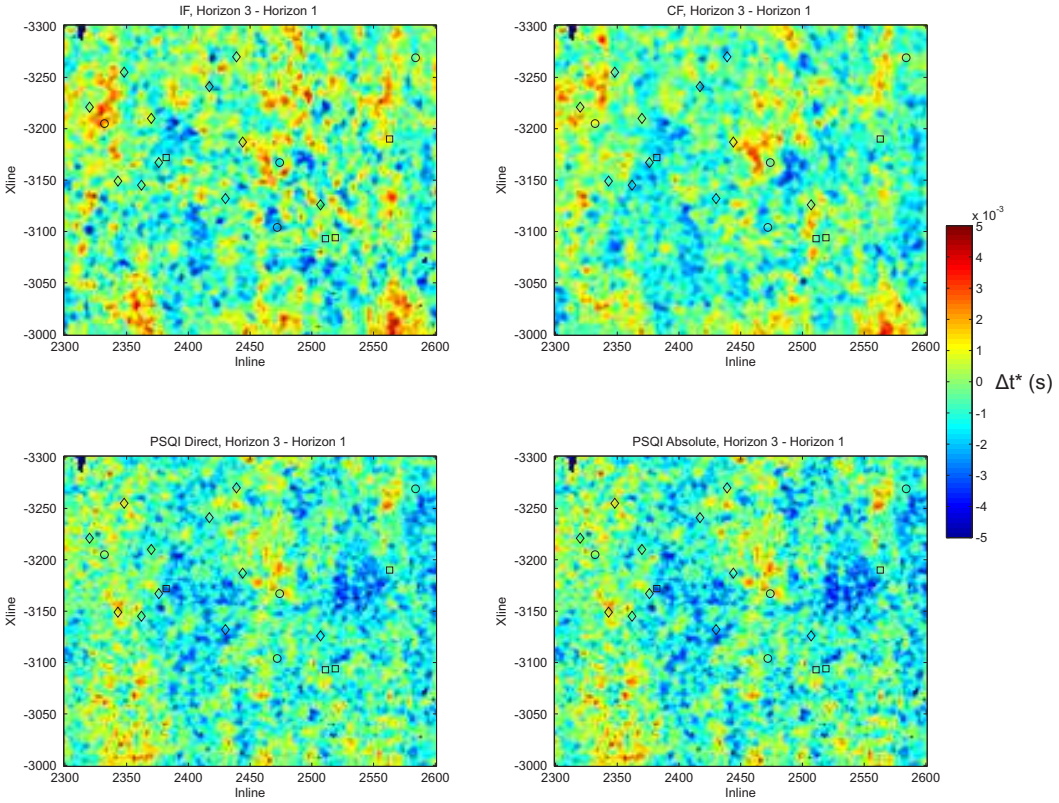

Figure 6.62: The interval change in t^* between Horizon 1 and the average of the horizons below the reservoir.

6.7 Comparison and Interpretation

In order to interpret attenuation it is necessary to have a forward model. In Chapter 2 I highlighted several models that could be used to model the behaviour of attenuation in the surface seismic frequency bandwidth. Here I will look at using the RPS model to interpret the results from the attenuation, velocity and AVO intercept. A RPS model is used as it is most likely to represent the random distribution of gas injected into the reservoir.

6.7.1 Reservoir properties of the Magnus field

The average properties of the Magnus reservoir can be seen in Table 6.5. These parameters will be used in the calculation of a general forward model for the Magnus Field.

Property	**Value**
Fluids	
Water salinity (ppm)	33000
Oil Gravity (API^o)	39
Gas Gravity	0.8
Gas Oil Ratio (L/L)	133.57
Reservoir Conditions	
Confining Pressure (MPa)	64
Typical Pore Pressure (MPa)	40
Temperature (^{o}C)	115
Mineral	
Bulk Modulus, K_0 (GPa)	22.8
Shear Modulus, μ_0 (GPa)	13.2
Density, ρ_0 (kg/m^3)	2680
Rock	
Bulk Modulus, K (GPa)	6.48-13.97, See Figure 6.63
Shear Modulus, μ (GPa)	6.10-10.5, See Figure 6.63
Permeability, κ (mD)	180
Porosity, ϕ	0.22

Table 6.5: Properties of the Magnus Reservoir, Fluids and Rocks. Personal communication, Ewan Laws.

In order to model the effect of pressure and saturation changes in the Magnus reservoir, fluid properties will need to be calculated as a function of pressure (and temperature). The empirical relationships of Batzle & Wang (1992) will be used to calculate the fluid properties. When the RPS model was presented in Chapter 2, the fluid changes were the

only changes taken into account when showing the behaviour of attenuation as a function of pore pressure. However, to be accurate, the change in the moduli of the rock as a function of effective pressure must also be calculated. Core data provided from BP (Ewan Laws, personal communication) show the behaviour of the bulk and shear modulus as a function of effective pressure (Figure 6.63). This gives two empirical relationships (Equations 6.10 and 6.11) where the bulk modulus (K) and the shear modulus (μ), are given in terms of the effective stress (or pressure, P_e) and the moduli (K_0 = 10.24GPa, μ_0 = 8.5GPa) at some reference effective pressure (P_0 = 17.44MPa). Rather than attenuation decreasing with increasing pore pressure, attenuation now increases with increasing pore pressure (decreasing effective pressure) matching the laboratory results of Prasad & Manghnani (1997) and the empirical relationships of Koesoemadinata & McMechan (2001). Velocity also now shows a much greater pressure dependence, as it is more sensitive to changes in the rock moduli than change in the moduli of the pore fluids.

$$\frac{K}{K_0} = 0.7313 \times \ln(\frac{P_e}{P_0}) + 0.9987 \tag{6.10}$$

$$\frac{\mu}{\mu_0} = 0.5621 \times \ln(\frac{P_e}{P_0}) + 0.9998 \tag{6.11}$$

A comparison of the behaviour of attenuation with and without taking into account these relationships is given in Figure 6.64. This figure highlights the importance of taking into account the effect of pore pressure on rock moduli as attenuation behaves very differently as a function of pore pressure.

The RPS model can now be used to calculate the change in attenuation, velocity and density as a function of gas saturation and pore pressure. The RPS model can only take into account a combination of two fluid phases, therefore I must either omit one fluid from the modelling strategy or replace one of the fluids with an effective combination of the other two fluids. To begin with I omit the oil from the reservoir simulation and study the effect of water and gas.

For each of these cases, the maximum and minimum changes in velocity and attenuation can be calculated for a defined range of expected changes in pressure (±10MPa) and saturation (+1.0 S_g, as there is no gas initially), and plotted against correlation length. These are shown in Figure 6.65. As the magnitude of the maximum changes in attenuation in the reservoir are around ±0.02, I choose to use a correlation length of 0.25m that

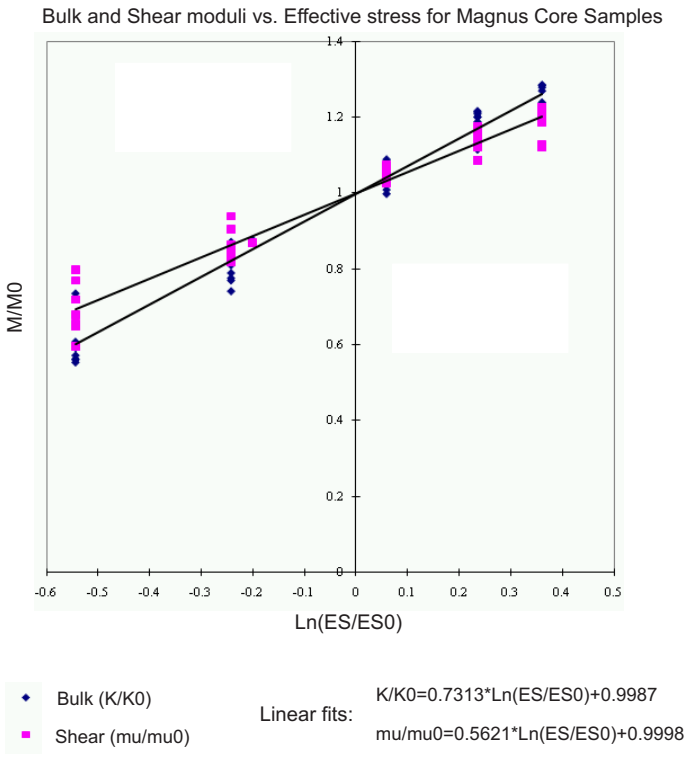

Figure 6.63: Empirical relationships relating bulk and shear moduli to the change in effective stress using all the Magnus Core data (for both sands and shales). Provided by BP.

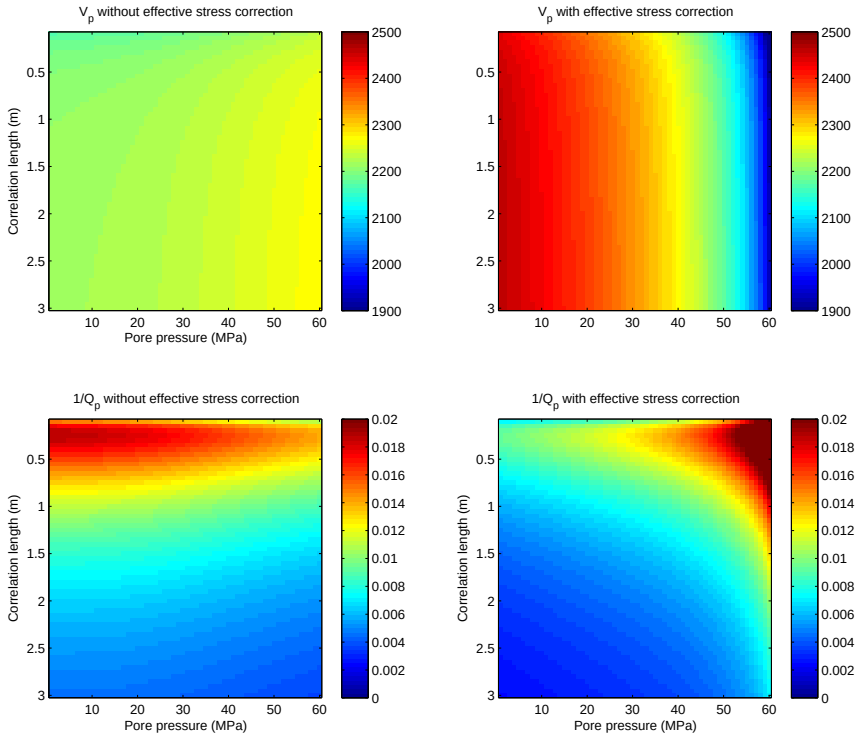

Figure 6.64: Predicted attenuation and velocities with and without compensating for the change in effective stress on the reservoir rock.

gives the maximum change in attenuation. The attenuation ($1/Q$), velocity and density produced by the RPS model for a correlation length of 0.25m can be seen in Figure 6.66. Attenuation peaks at around 20% gas saturation, and increases with increasing pore pressure. The velocity decreases sharply with a small increase in gas saturation, and steadily decreases with pore pressure. The effective density of the rock and fluid has little pressure dependence but decreases with increasing gas saturation.

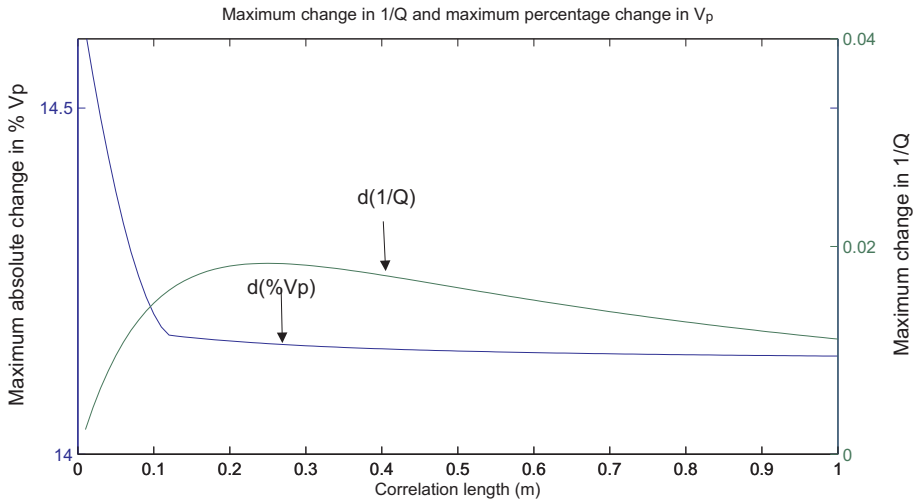

Figure 6.65: Maximum changes in attenuation and velocity for a gas water mixture for the expected range of changes in the Magnus reservoir.

The final attributes are qualitatively interpreted in Figure 6.67. Increases in attenuation coincide with decreases in the AVO intercept indicating possible increases in gas content near to the WAG injector. However, increases in attenuation are not seen adjacent to al of the injectors as may be expected. MacGregor et al. (2005) explains that after gas is injected, reservoir oil vaporises, and the gas becomes richer until the injected gas and reservoir oil have similar properties and effectively become a single phase. Once this single phase has formed, the magnitude of attenuation expected due to gas injection would be much smaller, and dominated by the water-oil mix. However in some instances, injected gas can rise to the attic areas of the field forming pockets to sweep oil that the water has bypassed.It is these pockets of gas that are more likely to produce larger magnitudes of attenuation. This could explain why some injectors show increases in attenuation whilst others do not. Although interpretations like this are useful, it would be more beneficial to be able to produce maps of the change in pressure and saturation. In the next section I introduce and utilise a possible algorithm that allows for the separation of pressure and saturation using the RPS model.

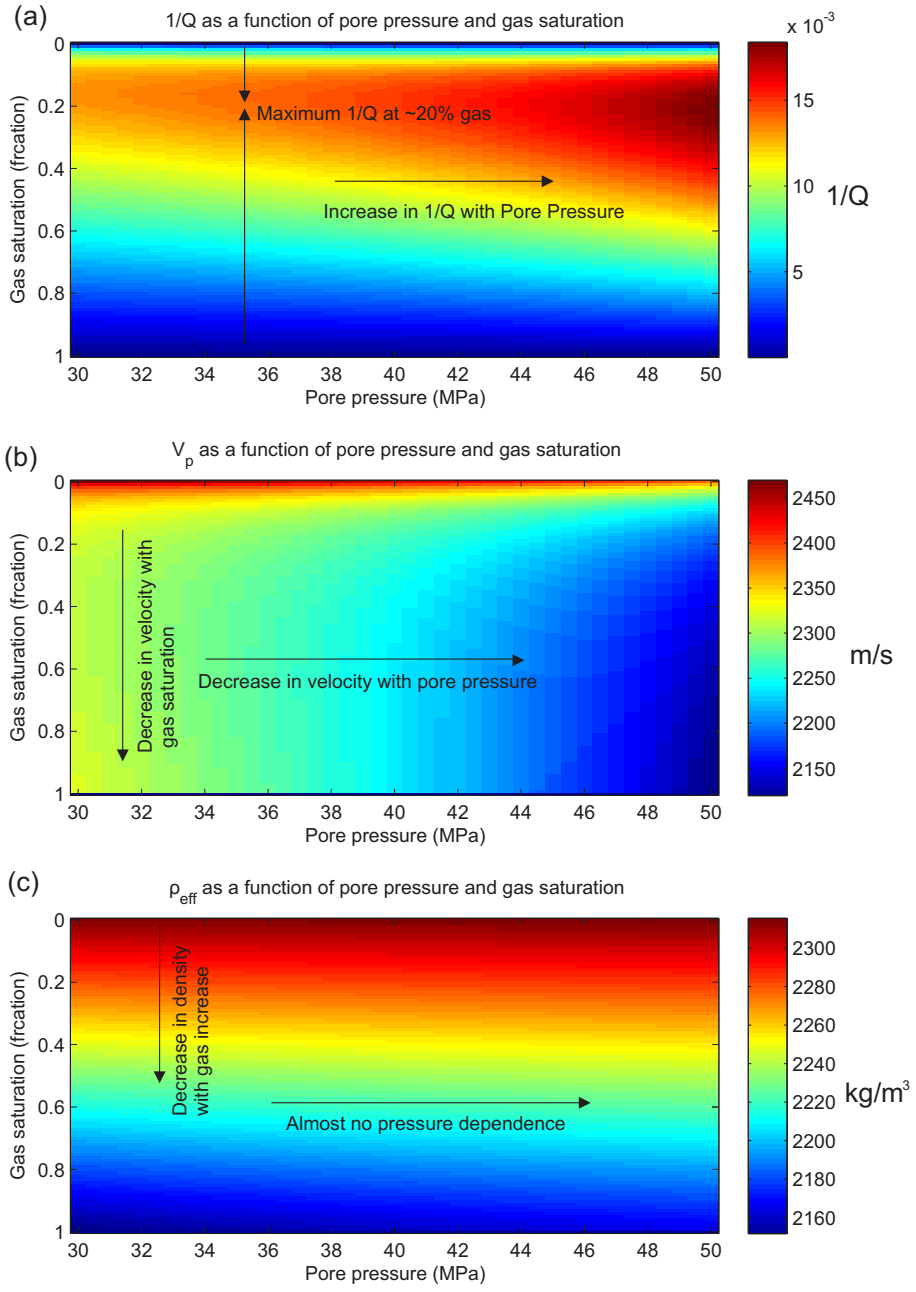

Figure 6.66: Changes in density, attenuation and velocity for patch size of 0.25m.

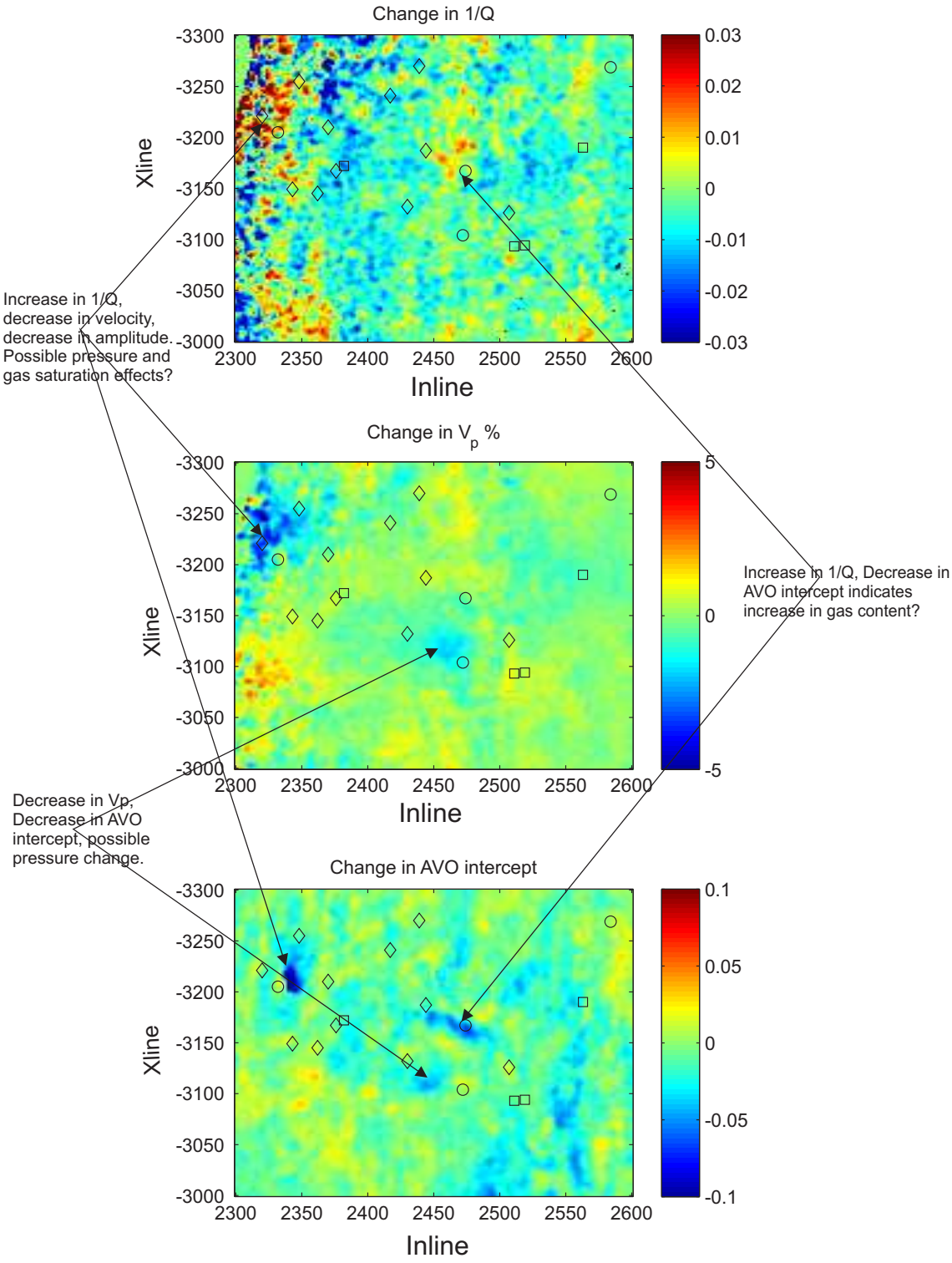

Figure 6.67: Final attributes for change in attenuation (top), change in velocity (middle) and change in AVO intercept for the top reservoir reflection (bottom).

6.7.2 Quantitative Inversion of Saturation and Pressure

In this inversion procedure, I aim to minimise the difference between the attribute maps seen in Figure 6.67 and a set of forward modelled attribute maps using the RPS model. If the error between the current amplitude maps was to be minimised then the largest of the attributes (in this case velocity) would dominate the other attributes, and therefore would not hold equal weighting in the inversion. I solve this problem by normalising each of the attributes by its standard deviation. The attributes, their distributions and their standard deviations can be seen in Figure 6.68.

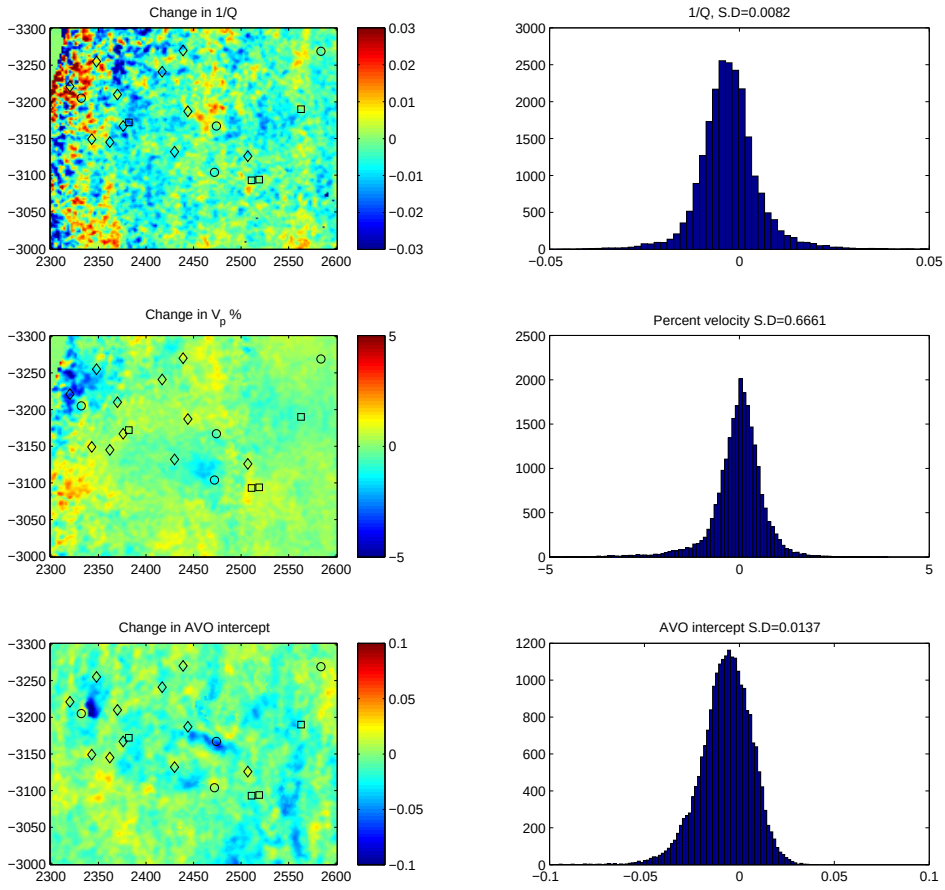

Figure 6.68: Final attributes for change in attenuation (top), change in velocity (middle) and change in AVO intercept (bottom).

Several assumptions must then be made about the initial conditions of the reservoir. In this case, I assume that the reservoir has remained above the bubble point and so the initial gas saturation is zero. The initial pore pressure must also be estimated and this

has been taken from the reservoir model of the Magnus field in 2001 (Figure 6.69). An initial guess of the change in pore pressure and change in saturation is also needed, and to begin with these will be zero. Fluid properties can then be calculated using the Batzle & Wang (1992) relationships and the RPS model used to model the attributes at an initial pressure and saturation, and the guessed pressure and saturation. The attribute changes can then be calculated, and minimised using a non-linear least square algorithm. This inversion procedure is shown below.

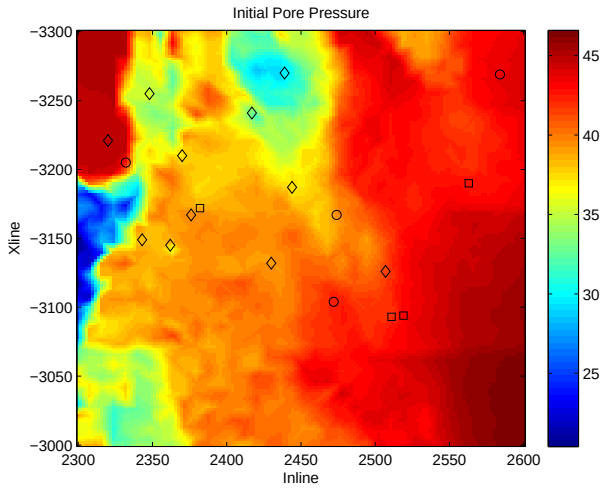

Figure 6.69: Initial pore pressure (MPa) used for inversion of pressure and saturation changes.

Inversion algorithm

Each step of this inversion is labelled in a schematic of the inversion algorithm in Figure 6.70. The quasi-linearisation follows the one outlined by Gubbins (2004).

Step 1: Normalise attribute maps Each of the attribute maps $D_i(x, y)$ should be normalised by the standard deviation of that attribute map, σ_i to get a normalised attribute map $d_i(x, y)$.

Step 2: Initial conditions Assume (or use a known/modelled) initial reservoir conditions of pore pressure (P_{p0}), gas saturation (S_{g0}), confining pressure (P_{c}), oil saturation (S_{o}) and temperature (T).

Step 3: Initial guess Make an initial guess of the change in pore pressure (δP_{p0}) and gas saturation (δS_{g0}). It is reasonable to assume the simplest model at this point where $\delta P_{\mathrm{p}} = 0$ and $\delta S_{\mathrm{g}} = 0$.

Step 4: Calculate fluid properties Using relationships of Batzle & Wang (1992) (BW), calculate the fluid properties (bulk modulus (K), density (ρ) and viscosity (ν)) of the water (w), gas (g) and oil (o) at original reservoir pressure (P_{p0}) and new reservoir pressure ($P_{\mathrm{p0}} + \delta P_{\mathrm{p}}$), at the reservoir temperature T.

$$(K_{\mathrm{w0}}, \rho_{\mathrm{w0}}, \nu_{\mathrm{w0}}, K_{\mathrm{g0}}, \rho_{\mathrm{g0}}, \nu_{\mathrm{g0}}, K_{\mathrm{o0}}, \rho_{\mathrm{o0}}, \nu_{\mathrm{o0}}) = BW(T, P_{\mathrm{p0}}) \tag{6.12}$$

$$(K_{\mathrm{w}}, \rho_{\mathrm{w}}, \nu_{\mathrm{w}}, K_{\mathrm{g}}, \rho_{\mathrm{g}}, \nu_{\mathrm{g}}, K_{\mathrm{o}}, \rho_{\mathrm{o}}, \nu_{\mathrm{o}}) = BW(T, P_{\mathrm{p0}} + \delta P_{\mathrm{p}}) \tag{6.13}$$

As only two fluids can be used in the RPS model, an effective fluid must be calculated from two of the fluids, in this case I calculate effective fluid properties of the combined water and oil to get K_{wo}, ρ_{wo} and ν_{wo} (weighted average by mass).

Step 5: Calculate rock properties From the empirical relationships using the core data (Figure 6.63), calculate the dry bulk modulus (K_{dry}) and dry shear bulk modulus (μ_{dry}) at initial effective pressure $P_{\mathrm{eff}} = P_c - P_{\mathrm{p0}}$ and new effective pressure $P_{\mathrm{eff}} = P_c - (P_{\mathrm{p0}} + \delta P_{\mathrm{p}})$.

Step 6: Calculate normalised seismic attributes Using the RPS model calculate the velocity (V_{p}), attenuation ($1/Q$) and density (ρ) for the initial conditions ($P_{\mathrm{p0}}, S_{\mathrm{g0}}$) and at the modelled conditions ($P_{\mathrm{p0}} + \delta P_{\mathrm{p0}}, S_{\mathrm{g0}} + \delta S_{\mathrm{g}}$).

Calculate the changes in the modelled seismic attributes ($D_i^*(x, y)$) from these properties and normalise with σ_i. We now have the normalised measured attributes ($d(x, y)$) and the normalised modelled attributes ($F(m)$), where F represents the combined function of calculating the normalised changes in attributes from our model parameters, $m = (P_{\mathrm{p0}} + \delta P_{\mathrm{p}}, S_{\mathrm{g0}} + \delta S_{\mathrm{g}})$

This now forms the basis of the inversion scheme where

$$\mathbf{d} = \mathbf{F}(\mathbf{m}) \tag{6.14}$$

Step 7: Quasi-linearisation and calculation of conditions matrix We now can iterate from some starting model m_0 and look to find a small improvement to the model through a linearised inversion of the residual $\delta d_0 = d - F(m_0)$, where

$$\delta\mathbf{d_0} = \mathbf{A_0}\delta\mathbf{m_0} + \mathbf{e} \tag{6.15}$$

A_0 is derived from calculation of the partial derivatives of the data with respect to the model.

$$(A_0)_{ij} = [\frac{\partial F_i}{\partial m_j}]_{m=m_0} \tag{6.16}$$

This gradient matrix can be found by calculating the numerical partial gradients of the forward model with respect to the model parameters. This involves repeating Steps 4, 5 and 6 for two cases where we find the change in the attributes for a small change in pressure (for fixed gas saturation) and a small change in gas saturation (at a fixed pressure).

Step 8: Calculate model update The new model can now be found using a damped least squares regression of the form

$$\mathbf{m_1} = \mathbf{m_0} + (\mathbf{A^T A} + \theta^\mathbf{2}\mathbf{I})^{-\mathbf{1}}(\mathbf{A^T}\delta\mathbf{d} - \theta^\mathbf{2}\mathbf{m_0}) \tag{6.17}$$

Step 9: Additional constraints It is plausible through this method that the model update may force one of the model parameters into a region of parameter space that cannot be modelled by the forward model. In the example used here, the gas saturation must never go below zero, or go above $1 - S_{\mathrm{ow}}$. In order to control this characteristic, if S_{g} falls below zero it is automatically reset to $S_{\mathrm{g}} = 0$, and if it goes past $1 - S_0$ it automatically set to $1 - S_{\mathrm{o}}$ for the next iteration. This allows the minimisation of pressure along either the $S_{\mathrm{g}} = 0$ or $1 - S_{\mathrm{o}}$ axis in parameter space.

Step 10: Iterate Numerous iterations can now be performed until it reaches convergence, this can either be defined by a minimum model update size or a minimum

improvement of the data misfit.

A schematic of the inversion can be seen in Figure 6.70 that contains less information, but shows the general flow of the inversion scheme.

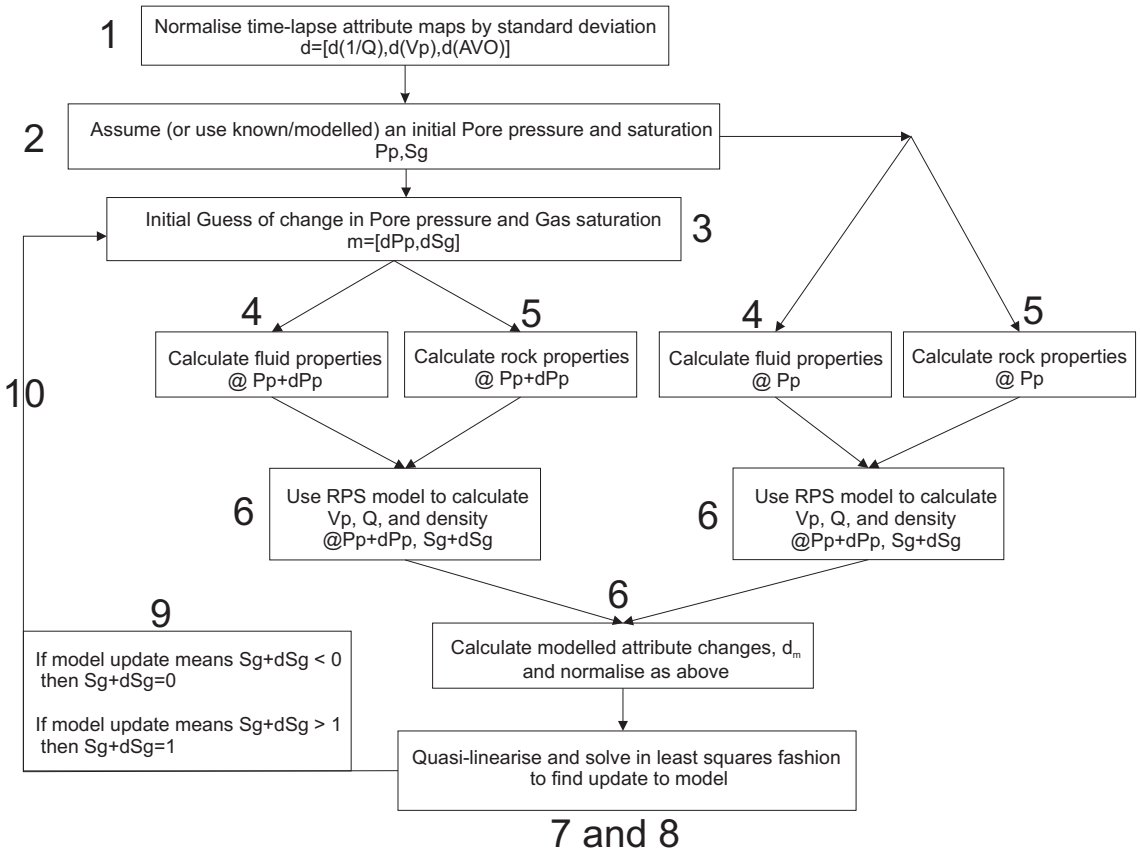

Figure 6.70: Flowchart showing the major steps (labelled 1-10) in the inversion procedure for saturation and pressure.

Inversion parametrisation

In order to stabilise the inversions, damping (θ^2) is used to minimise both the size of the model solved and the size of each model update. For a correlation length of 0.25m, an initial oil saturation of 0.5, initial pore pressure seen in Figure 6.69 and the reservoir properties in Table 6.5 the inversion is carried out over the whole data-set in patches approximately equal to the Fresnel zone of time-migrated data (100m^2), for 20 iterations, for damping parameters ranging between 10^{-5} and 10^3. Three plots of the mean (of the entire survey area) properties of the model and misfit are shown in Figure 6.71 that depict the behaviour of the inversion. It can be seen that for damping parameters less than 10^{-1}, the residual after 20 iterations is still large, this shows instability in the inversion. The difference between errors after each iteration can be seen also, and are still large for

damping parameters less than 10^{-1} indicating that the inversion is behaving erratically and not converging. At around $\theta^2 = 10^{-0.2}$ there is a minimum in the misfit, suggesting that this would be the best damping parameter to use for the entire data-set. This will be the damping parameter used to run the final inversion as there is an average reduction (although small) of the data misfit and all (at least the vast majority) of models converge.

Inversion results and interpretation

The inversion is run over the entire data-set and the results after 20 iterations can be seen in Figure 6.72. Results indicate gas saturation increases around three of the WAG injectors in the area. Changes in pore pressure show less coherence, and there could be several reasons for this. Firstly, the inversion procedure is fixed to a 2 fluid system, and changes in the oil saturation have been fixed, this in turn has not allowed for the potential effects that a patchy saturation of water-oil mix may have on the solution. Secondly, the pressure may be less well constrained relative to the saturation, meaning that the model parameter is allowed to fluctuate more than the change in gas saturation. Results can be compared with the reservoir prediction seen in Figure 6.3. Similarities in the magnitude and locations of the gas saturation increases are clearly evident, with changes in pressure less so.

The inversion is then performed a second time, this time omitting the attenuation measurement from the analysis. Results from this analysis are displayed in Figure 6.73. When attenuation is omitted there is no significant change in the saturation solved for, however, there are large changes to the pressure. This shows that attenuation contributes towards the pressure change, whilst has almost no impact on the change in gas saturation. Figure 6.66 may also provide insight into this behaviour, as it can be seen that both attenuation and velocity are more sensitive to changes in saturation than changes in pressure. At the initial saturation (S_g=0) neither velocity or attenuation change significantly with pressure, resulting in pressure being difficult to resolve.

6.8 Summary

In this chapter I started by testing the feasibility of estimating attenuation through the use of a complex synthetic example, and was able to confirm that changes in attenua-

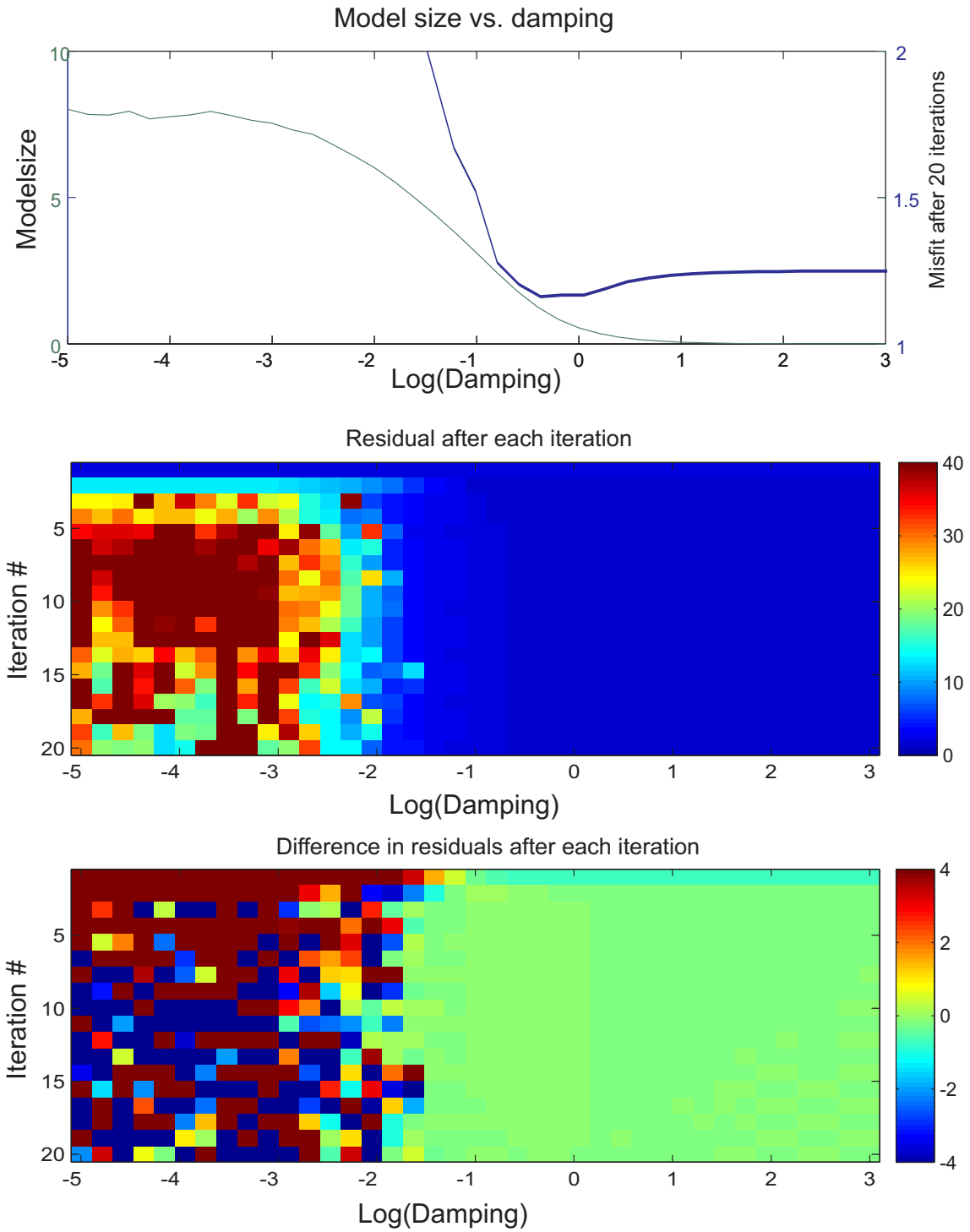

Figure 6.71: Testing the damping parameter. (a) the damping parameter and its effect on the model size, (b) the misfit after each iteration as a function of damping parameter and (c) the change in misfit after each iteration (to highlight the lack of convergence).

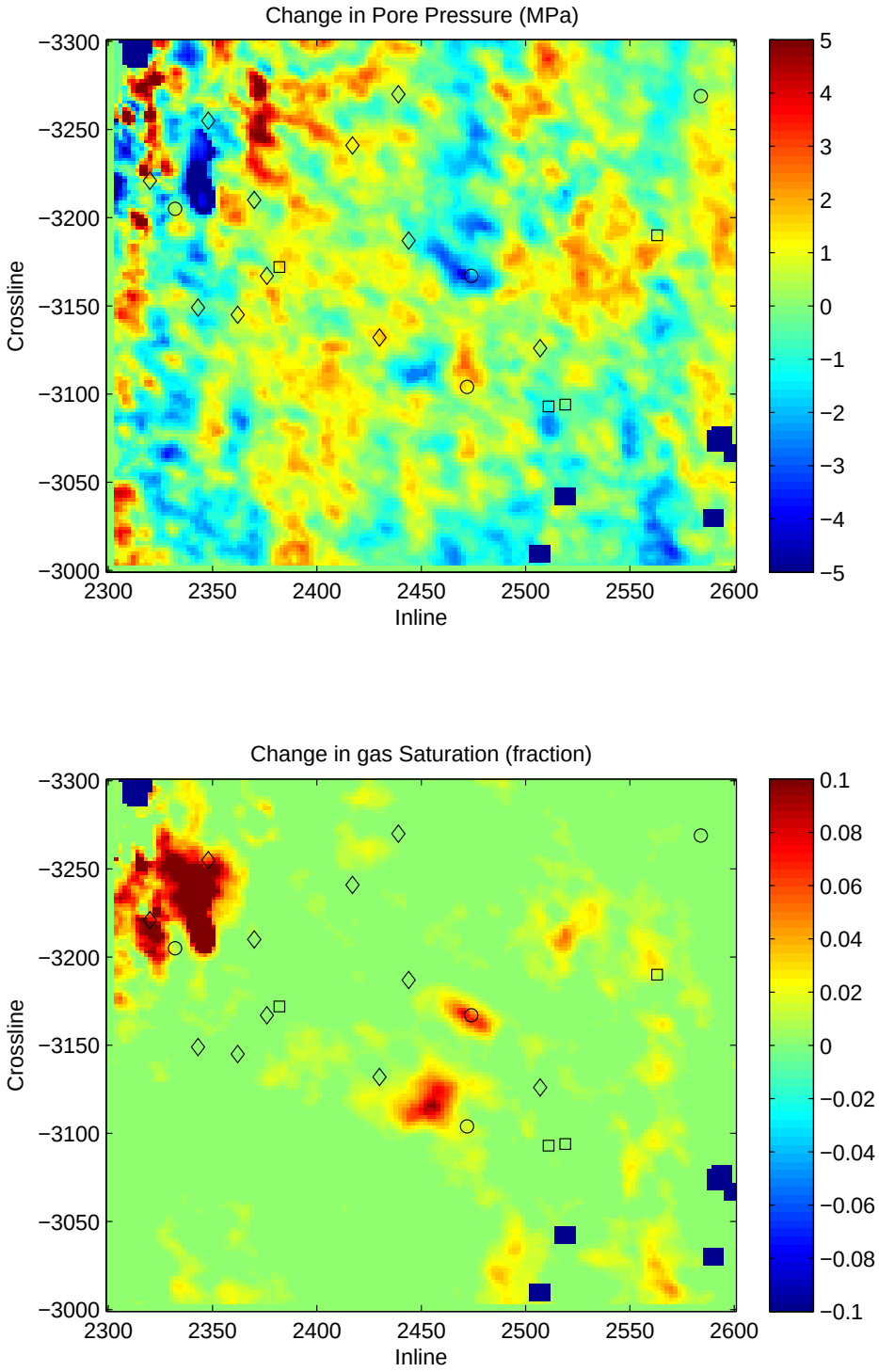

Figure 6.72: Change in pore pressure and gas saturation after 20 iterations.

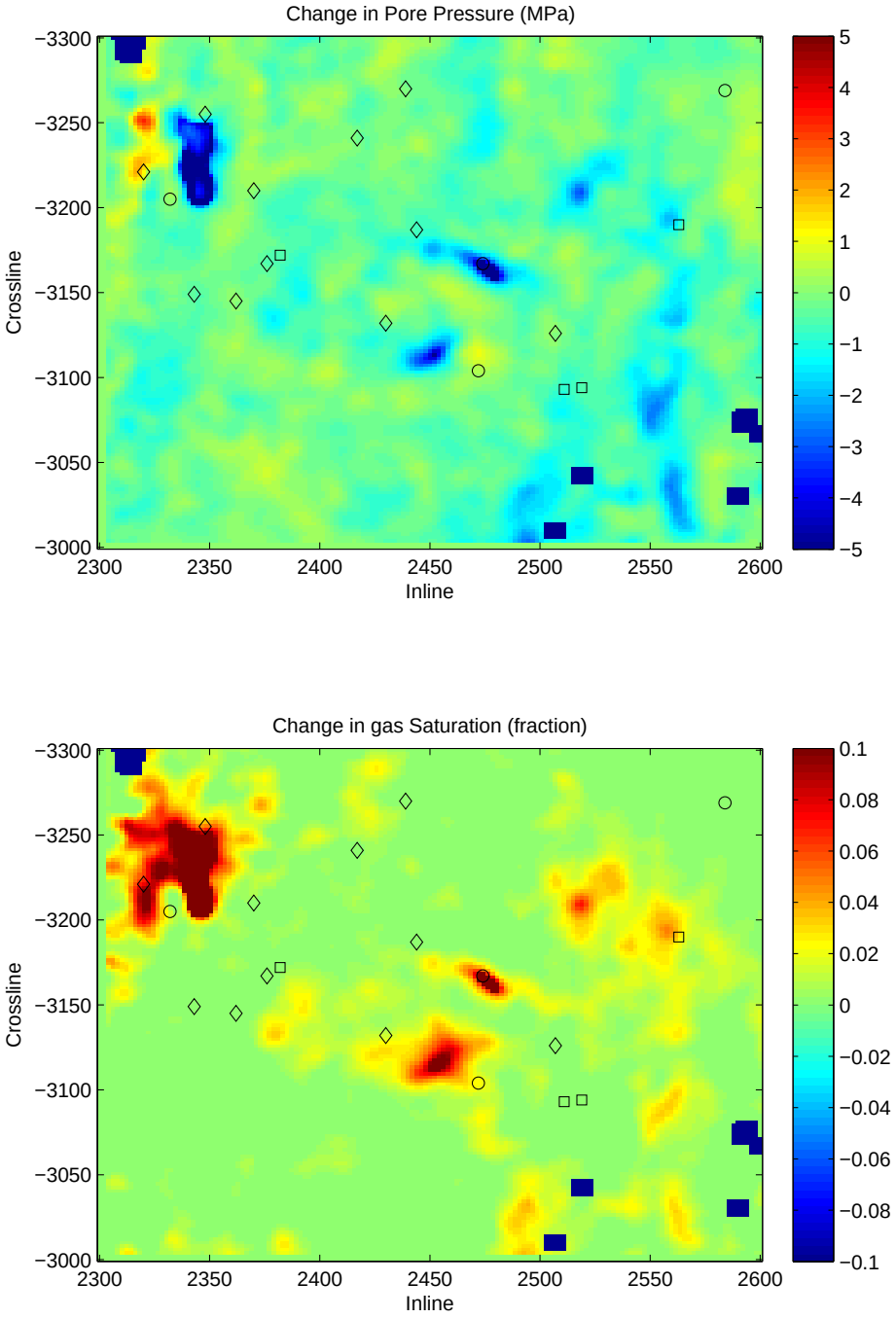

Figure 6.73: Change in pore pressure and gas saturation after 20 iterations, omitting change in attenuation from the inversion.

tion were potentially detectable from the data-set. I then proceeded to investigate the repeatability of the data between vintages defining the regions of the data (in frequency, offset and time) where repeatable data exist to perform the attenuation measurements. Four methodologies (Absolute PSQI, Direct PSQI, Direct Centroid frequency and Direct instantaneous frequency matching) were then used to estimate changes in attenuation from the data-set. All of the methodologies showed some agreement in the final attribute maps to encourage the development of a method to interpret these changes through the use of a rock physics model. A new quasi-linear inversion scheme has been developed to invert for changes in gas saturation and pressure using a rock physics model. In order to quantitatively interpret pressure and saturation, other seismic attributes must also be observed, a rock physics model and fluid prediction relationship must be chosen, and core data must be available that are able to account for changes in the rock properties as a function of effective pressure.

The main findings from this chapter are

- A complex synthetic test, mimicking the real data-set showed that attenuation changes were detectable using all of the methodologies.
- Through the use of standard repeatability metrics and comparison of the spectral content, repeatable data could be selected for the use for attenuation estimates.
- Estimates of changes in attenuation were shown to be statistically robust (small uncertainty relative to the size of attenuation change) and methodologies showed similarities, further increasing confidence in the measurement.
- A new inversion scheme has been developed and applied to the data-set that utilises a RPS rock physics model to invert for changes in pressure and saturation in the reservoir.
- From the inversion results, I have shown that pressure changes are poorly determined, whilst saturation changes can be confidently estimated. Attenuation provides an additional handle to constrain the pressure change, without significantly changing the saturation result.

Chapter 7

Discussion and conclusions

Measurements of attenuation can be noisy from single vintages of data due to a large component of apparent attenuation, however, the relative differences between attenuation calculated at different times provides an opportunity to look at changes in the intrinsic attenuation. The magnitude of these relative changes in attenuation not only provides another time-lapse attribute to identify change in petrophysical properties over time, but may enhance our understanding of the underlying physical mechanisms that are responsible for attenuation as a wave propagates. There are three aspects which must be understood in order for time-lapse attenuation to be useful:

1. To understand what mechanisms are likely to be responsible for attenuation and how to interpret measured attenuation changes.
2. To understand the sensitivity and vulnerabilities associated with making a quantitative measurement of attenuation changes.
3. To identify the methodologies that are most robust in estimating attenuation, or more specifically time-lapse attenuation from surface seismic and VSP data.

I now review in detail the findings of this thesis in relation to these three important aspects, followed by a summary of recommended future work and finishing with a summary of the major conclusions of the thesis.

7.1 Discussion

7.1.1 Interpretation of attenuation results

Interpretation of attenuation requires a forward model and hence an understanding of the underlying mechanisms responsible for the change in attenuation. In this thesis I chose to use predominantly a random patchy saturation model to interpret attenuation changes for three main reasons.

1. The work of Yin et al. (1992), Cadoret et al. (1995) and Cadoret et al. (1998) show that saturation history determines how fluids distribute themselves in the pore space. During gas injection, gas forms random pockets rather than the uniform distribution caused by de-pressurisation or imbibition. In each of the data-sets studied here, gas injection (whether it be CO_2 or hydrocarbon gas) is occurring in the reservoir and is the primary target for monitoring. It therefore seems reasonable to assume that a patchy saturation model would be a more realistic mechanism rather than global fluid flows or squirt flow mechanisms that require effective fluid properties (and hence a homogeneous mix of fluids) to be estimated.

2. The magnitudes of attenuation measured from the VSP and surface seismic data-sets adjacent to the injectors (assuming the change in attenuation occurs in the reservoir) were 0.024 and 0.02 respectively. These are relatively large magnitudes of attenuation in the seismic bandwidth, and using the true rock properties of the reservoir, it is possible to match these magnitudes of attenuation using patchy saturation models.

3. A random patchy saturation model was chosen (over the model of White (1975)) as it reduces the dependence on ideal geometries and broadens the bandwidth at which attenuation is significant (Figure 2.5). Other mechanisms are available to predict attenuation in the seismic bandwidth such as global fluid flow and squirt flow, however these have been shown to have much smaller magnitudes of attenuation in the seismic bandwidth than the values observed in the data.

There is a choice for the interpretation of attenuation results; to be quantitative or qualitative. In order to interpret attenuation quantitatively an understanding of the initial condition of the reservoir and the behaviour of fluids and rock with pressure must be known. In Chapter 5, core data were not available, so qualitative interpretation of the

attenuation and velocity changes were made with both attributes indicating an increase in CO_2 saturation in the injection interval. In Chapter 6 quantitative interpretation of attenuation was carried out via a new quasi-linear inversion scheme. By modelling fluid and rock properties of data and using a random patchy saturation model, changes in gas saturation and pore pressure were calculated from three observed time-lapse seismic attributes ($1/Q$, V_p and AVO intercept). A damping parameter was used to stabilise the inversion and to find a model solution that did not deviate greatly from the initial conditions. Although this inversion scheme was described in Chapter 6 for the specific example of the Magnus reservoir it is possible to generalise the inversion, so that changes in different reservoir properties could be solved for using a multitude of seismic attributes, using any set of forward models (for fluid, rock and seismic properties). Obviously, as with any inversion the number of model parameters should be less than the number of observations, so there are limitations as to what can be resolved, but if changes in V_s, Q_s and AVO gradients were measured, more model parameters could be introduced. In the case of Magnus this may allow for a three phase fluid distribution to be resolved rather than the two fluid approximation that was used in the analysis, assuming no principal trade-off between parameters. Results of the inversion in Chapter 6 found gas saturation of values up to 10% around the water and gas injector and pressure changes of ± 5 MPa across the reservoir, and showed similarities with the predictions of reservoir models.

The patchy saturation model of Müller & Gurevich (2004) provides a useful tool for modelling attenuation in a patchy saturated rock. There is only one parameter that needs to be chosen - the correlation length of the random distribution of patches. This could be solved for in the inversion for saturation and pressure itself or, as I have done in Chapter 6, chosen from matching the maximum observed changes in attenuation. Even if the correct correlation length cannot inferred from the data, I have also shown that some of the properties of the RPS model are independent of correlation length. One such observation of this is that the maximum attenuation remains at the same percentage saturation regardless of correlation length, allowing qualitative interpretation via the model. This model, however, is still not ideal for interpreting attenuation measurements and when interpreting results in Chapter 6 the following shortcomings were noted;

- Only a single mechanism is taken into account, so other more subtle effects that may produce attenuation in a single phase system (such as squirt flow) are not taken into account. For single phase saturations, zero attenuation is predicted and there is no

change in attenuation with pressure.

- The RPS model is limited to a two-phase fluid system, but ideally the interaction between water, oil and gas should be evaluated.

7.1.2 The sensitivity of time-lapse attenuation measurements

Single vintage measurements of attenuation have been shown to be sensitive to large levels of apparent attenuation. In Chapter 4 I showed an example of a tuned reflector causing apparent attenuation to be several times larger than intrinsic attenuation. However, these effects were shown to be repeatable between vintages of data leading to the correct relative measurement of the change in intrinsic attenuation. The assumption here is that the changes in intrinsic attenuation are greater than the changes in apparent attenuation. For both case studies, estimates of single vintage attenuation showed evidence for large values of apparent attenuation (as there were large negative attenuation estimates) but these were shown to be repeatable between vintages of data.

In Chapter 4 the introduction of band-limited noise was shown to reduce the magnitude of attenuation from that expected. This is because the relative differences in the spectra are reduced by the addition of other energy into the signal. In this case, the noise that was added was relatively "flat" in the frequency domain or matched the spectrum of the desired signal. It may be noted that additional energy in a small range of frequencies (i.e. not flat) may impose more significant effects on the estimation of Q. For example, additional noise at high frequencies for the second vintage of data would cause an apparent increase in attenuation. An example of where this may be a problem in real seismic data would be when 4D tuning effects occur, and horizons with such effect should be avoided as they would produce a large magnitude of apparent attenuation. Another effect that could cause this is through stratigraphic filtering, however, lithological boundaries do not change between vintages of data so it may be expected that changes in the stratigraphic filtering would be small.

When attenuation changes occur, frequency dependent travel-time changes also occur. In Chapter 4 these were investigated by considering the impact of dispersion in two ways; through frequency dependent travel-times; and through frequency dependent reflectivity. These were investigated through the use of analytical relationships and numerical examples. The percentage error due to frequency dependent travel-times was found to be proportional to the magnitude of attenuation in each vintage of data. If Q is less than

20 in each vintage of data the maximum error on the measurement is around 15%. Frequency dependent reflectivity is more difficult to quantify as the magnitude of the error is independent of the traveltime through the region of subsurface where attenuation is measured. Error on log spectral ratios were found to be much larger for low frequencies than at high frequencies, and effects exaggerated where reflection coefficients change sign with angle. To avoid these effects it may be beneficial to avoid the use of horizons where the attenuation is expected to change within the bounding intervals either side. This was one of the reasons why the top reservoir reflection was not used in the final analysis of the change in attenuation for the surface seismic data example in Chapter 6, as attenuation changes would be expected in the lower interval controlling the reflection, and AVO curves for the top reflector were small, sometimes changing polarity with offset. As mentioned above, although potentially being a source of noise, frequency dependent reflectivity has also been used to try and estimate attenuation (Wilson et al., 2009), and hence could also be used to estimate changes in time-lapse attenuation.

Finally, if attenuation changes occur in the reservoir one may also expect changes in velocity and amplitude of the data. Although velocity changes do not affect the absolute methodologies, the direct methodologies assume that there is no change in travel-time along the ray-path between vintages of data. Through analytic relationships, this effect was found to be equal to the fractional change in velocity divided by the quality factor of the second vintage of data (Equation 4.17). Errors are therefore large when Q is small and the change in velocity large, but for typical velocity changes (<10%) and Quality factors the maximum error on $\Delta(1/Q)$ was found to be 6×10^{-3} and independent of the magnitude of the change in attenuation between vintages. Frequency independent amplitude changes cannot affect the spectral ratio and centroid frequency methods directly, however, the instantaneous frequency is sensitive to these changes as was seen in a numerical example in Chapter 4 and observed in real data in Chapter 6. This effect can be negated if a frequency damping parameter (ϵ^2) is used that is proportional to the amplitude of the wavelet where the regression is being performed.

7.1.3 Methodologies for estimating changes in attenuation

In Chapter 3 I introduced four methodologies that could be used to estimate attenuation from seismic data. By performing a second regression against offset squared (analogous to that seen in the original QVO methodology (Dasgupta & Clark, 1998)) the centroid

frequency and instantaneous frequency matching can now be used to estimate attenuation from the specific geometries of prestack surface seismic data. I also extended each of the methodologies to enable the measurement of attenuation directly between waveforms that have travelled the same ray-path in each vintage of data.

The direct analysis of attenuation between same ray-path event between vintages of data potentially provides a beneficial measurement of attenuation for several reasons. Firstly the need to isolate events in the $\tau - p$ domain is not needed as the event have travelled the same ray-path and hence will have the same horizontal slowness - avoiding any of the artefacts produced in the transform. Secondly, a change in t^* can be directly estimated and interpreted reducing the need for a reference spectrum or an interval calculation - immediately reducing the statistical uncertainty of the measurement. In Chapter 4 I showed that with the addition of band-limited random noise, direct measurement of attenuation estimated the correct change in attenuation, whilst the absolute methodologies were biased through incorrect determination of attenuation to the top reflector (Figure 4.1). In the surface seismic case study in Chapter 6 no significant differences could be identified in the interval estimate of Δt^* between vintages of data for the absolute and direct methodologies (Figure 6.62). In the VSP study (Chapter 5) a new methodology for calculating direct changes in t^* was introduced that did not need the otherwise necessary assumption of identical source spectrum for each vintage of data. A significant improvement in both the variance in spectral ratio slopes (Figure 5.49) and an increase in the coherency of anomalies across all source locations (Figure 5.54) suggests that the direct methodology provides a more robust estimate of attenuation changes. Interpretation of the CO_2 was made difficult because of ray-path differences between each source location.

Another benefit of direct Δt^* estimates is that they lend themselves to be potentially used as the input for time-lapse attenuation tomography. Attenuation tomography has already been used on surface seismic data and crosswell tomography to better resolve the spatial distribution of attenuation (Quan & Harris, 1997; Rossi et al., 2007). The change in t^* along a ray-path would therefore be a summation of Δt^* along that ray-path

$$\Delta t_i^* = \sum_j t_{i,j} (\Delta 1/Q)_{i,j} \tag{7.1}$$

where i is a ray-path, and j represents a cell of the medium through which the ray-path has travelled. By ray tracing to find $t_{i,j}$ for each ray-path the $\Delta 1/Q_{i,j}$ at each cell can be

found (assuming no changes in travel time). In the VSP case study, just analysis of the direct arrival would give a null space due to many parallel ray-paths. A solution to this would be to calculate arrivals from both the up-going and down-going arrivals. For surface seismic data, Δt^* estimates from a large number of reflectors for each prestack trace, could provide an abundance of data for the input into attenuation tomography. Another benefit of this type of analysis would be the smearing of "apparent attenuation", which would be spatially incoherent. Tomography would allow for better vertical and lateral resolution of attenuation changes.

In Chapter 6, 4 methodologies are used to compute change in interval attenuation and there is coherency in the final attribute maps from each of the methods. Conversely, in the VSP case study, the various methodologies produced quite different results. This indicates that each of the attributes that the methodologies utilise (spectral ratios, centroid frequencies and instantaneous frequencies) have different sensitivities to different types of noise. It may therefore be beneficial to introduce an inversion scheme that uses all three attributes to estimate a single value of attenuation.

The robustness of the methodologies with respect to band-limited noise is investigated in Chapter 4. Through basic parametrisation, the PSQI methodology was found to be the most robust at estimating the changes in attenuation for a simple synthetic example. However by using a band-limited estimate of the centroid frequency and an instantaneous frequency damping proportional to the noise level in the data, all methodologies appeared to perform with the similar levels of uncertainty. This does suggest however, that some methodologies require careful parametrisation, and in particular for the instantaneous frequency, if noise levels vary across a data-set, a single parametrisation may be inappropriate. Such detailed parametrisation of a data-set is time consuming and intensive, which suggests that the methodologies with the least parametrisation (spectral ratios, centroid frequency) may be more favourable over others (instantaneous frequency).

In the surface seismic data-set in Chapter 6 uncertainties on the estimate of Δt^* were calculated. The instantaneous frequency method had the smallest mean uncertainty (3.49×10^{-5}) followed by the direct PSQI method (8.75×10^{-5}), centroid frequency method (8.95×10^{-5}) and the Absolute PSQI (13.53×10^{-5}). However, maximum uncertainties of 39.0×10^{-5} (Instantaneous frequency), 8.81×10^{-5} (Direct PSQI), 23.42×10^{-5} (Centroid frequency) and 15.33×10^{-5} (Absolute PSQI) highlight the fact that some methodologies have the potential to produce a wider range of uncertainties. This again, may be caused

by the use of a single parametrisation for the entire data-set as some methodologies are more sensitive to the sets of parameters, and in particular this applies to the instantaneous frequency. To parametrise robustly the instantaneous frequency is time consuming and therefore would be the least favourable of the methodologies to apply to a large prestack dataset.

In Chapter 6 large AVO and amplitude anomalies were seen for the top reservoir reflection. In the PSQI inversion offset dependent intercept terms are also solved for along a single attenuation estimate Equation 3.16. These intercept terms are related to the reflectivity of the data, or in the Direct method relate to log of the ratio of the change in reflectivity

$$\ln(\frac{R'}{R}) \tag{7.2}$$

where R and R' are the reflectivity to a given reflector for the first and second vintage of data respectively. In Figure 7.1 I compare the exponential of the average intercept term (R'/R) with the ratios of the amplitudes of the top reservoir horizon (A'/A) and the ratios of the absolute values of the AVO intercept (R'_0/R_0). Clear similarities lie between the three different measures of amplitude change indicating that the inversion for both attenuation (frequency dependent amplitude) and reflectivity (frequency independent amplitude) is robust. I have also introduced a secondary constraint into the PSQI inversion in order to stabilise the intercept terms (Appendix A) as they should not vary massively as a function of offset. It may however be possible to constrain the intercepts further based on our understanding of amplitude versus offset. If time-lapse AVO estimates are made prior to $\Delta(1/Q)$ calculation it may be possible to constrain further the relationships between individual offsets. Also, the AVO analysis in this thesis and in many published examples does not consider the impact that attenuation can have on reflectivity (Adriansyah & McMechan, 1998). In Chapter 4 I investigated the impact that changes in frequency dependent dispersion have on the estimate of attenuation, but dispersion will also introduce a bias in AVO attributes. Some authors have already tried to estimate dispersion and attenuation through analysis of frequency dependent AVO (Wilson et al., 2009), there therefore lies a possibility of detecting time-lapse attenuation through a similar analysis. It may therefore be possible to set up an inversion scheme that not only solves for attenuation changes, but also inverts for AVO at the same time, taking into account the effect of attenuation.

As the analysis of attenuation from surface seismic data becomes more complex it may be plausible that full waveform inversion may become the simplest method of estimating

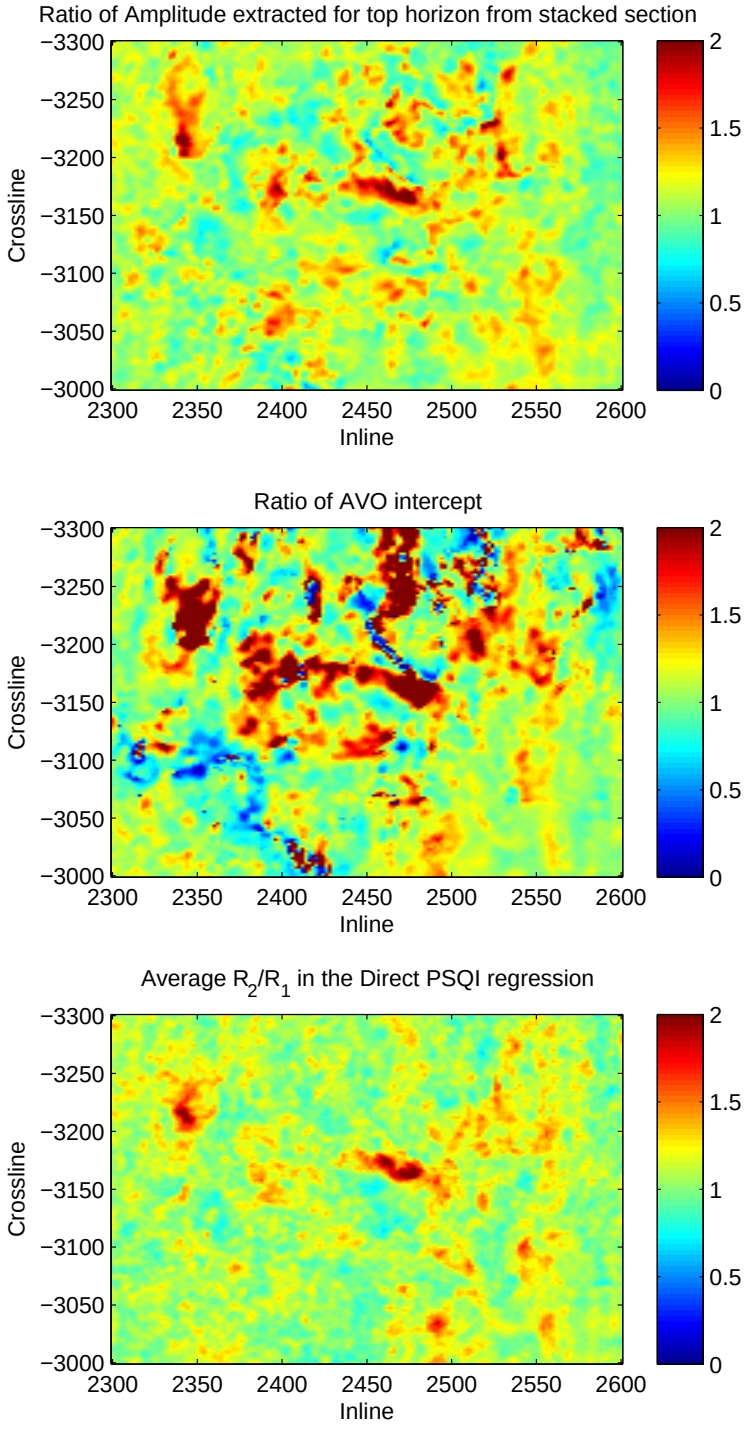

Figure 7.1: Comparison of top: ratio of Amplitude changes. Middle: ratio of absolute values of AVO intercept and Bottom: the exponential of the average intercept from the direct PSQI methodology (R'/R) fro the top reservoir reflector.

attenuation, or attenuation changes from surface seismic data. In some circumstances, full waveform inversion is not used to invert for attenuation changes but instead to perform independent inversions for single values of Q (Pratt, 1999), but has occasionally been used to estimate the distribution of attenuation in the subsurface (Hicks & Pratt, 2001).

Out of the methodologies used in this thesis, the centroid frequency and spectral ratio methodologies have shown similar levels of robustness. With just the offset range and bandwidth to choose, these methodologies are also simple to parametrise, with the parametrisation being stable over a large data-set. Furthermore, the spectral ratio methodology requires no assumptions about the shape of amplitude spectra making it more favourable. The instantaneous frequency on the other hand was found to be accurate in determining attenuation once the correct set of parameters was found, however, the number of parameters available makes this a difficult and data dependent task. It is also more computationally intensive due to its non-linear nature. When future time-lapse measurements of attenuation are made I would recommend using the spectral ratio methodologies to ensure the robustness of the estimate, avoid unnecessary assumptions and save time in parametrisation and computation.

7.2 Summary of Future work

Throughout this work I have developed a framework for making and interpreting time-lapse seismic attenuation and quantified, where possible, our understanding of the sensitivities of such a measurement. As with most research, there are always additional avenues of investigation that may improve the methodology, make interpretation more robust or understand the sensitivities better. Here I outline what I think are the main steps to improvement:

- Firstly, and most importantly, to gain a true understanding of the reliability and robustness of time-lapse attenuation measurements, the application to many more time-lapse data-sets would be beneficial. In an ideal scenario, these measurements would be made on several vintages of data where other more widely used attributes have been measured accurately and quantitatively. More knowledge of the frequency dependence of attenuation mechanisms could also be gained from the use of several seismic acquisition types such as low frequency surface seismic data, vertical seismic profile, cross-well-tomography, full waveform sonic logs and laboratory analysis of

core data. Examples of this kind of experiment have been carried out by Sams et al. (1997) where attenuation is calculated at a range of different seismic frequencies and compared to attenuation predicted from a squirt flow model. The same experiment could be applied close to a gas injection well, to determine if a patchy saturation model can be used to predict the magnitude of the change in attenuation in each frequency range.

- Methodological improvements could be made by combining the observation of changes in spectral ratios, centroid frequencies and instantaneous frequencies and inverting directly for a single change in attenuation between vintages. A suggested algorithm for this would follow closely the non-linear instantaneous frequency matching methodology, where a reference waveform FFT is updated by an attenuation operator, and the misfit between the modelled parameters and parameters measured from another waveform are minimised. The number of attributes sensitive to changes in attenuation are not limited to those used in this thesis (Tonn, 1991), and other properties such as the phase and rise-time of a wavelet could also be modelled and minimised with respect to an attenuation operator. This would inevitably create a more robust measurement of attenuation, as each attribute will have different sensitivities to different types of noise and changes in apparent attenuation.

- A drawback of the current methodologies is that the spatial and vertical distribution is poorly defined, so to gain the correct magnitude of attenuation, some assumptions must be made about the thickness or interval over which changes in attenuation are likely to occur. The spatial resolution could be improved through the use of direct measurements of Δt^* along same-ray-path events and a tomographic inversion.

- To my knowledge, no rock physics model exists to date that is able to predict attenuation and velocity, taking into account a variety of mechanisms for any number of pore fluids. Such a model may never exist due to the obvious complexities of such a task, but it may be realistic to foresee a patchy saturation model developed that can accommodate more than 2 fluids. This is particularly important in reservoirs where there is a gas-water-oil mixture, like the one used in Chapter 6.

- There is also room for improvement in the inversion scheme for saturation and pressure outlined in Chapter 6. Constraints may be included in the inversion such that pressure changes inverted for must match the pressure changes observed at production and injection wells. If more attributes are included in the inversion (V_s, AVO

gradients) more parameters can potentially be solved for such as changes in additional fluid saturation, porosity, permeability and temperature. The inversion allows for any forward model to be used and therefore, where data are available, it may be more accurate to use relationships derived from core samples of the reservoir.

7.3 Summary of Conclusions

I have shown that relative changes in attenuation may be a useful additional attribute to measure from time-lapse seismic data as it is sensitive to changes in pore pressure and partial saturation. I conclude that:

- Large values of apparent attenuation, that often cause unreliable measurements of attenuation in single vintages of data, are repeatable between vintages, allowing changes in intrinsic attenuation to be detectable.
- Time-lapse attenuation measurements are sensitive to different types of noise, but through analytical relationships and synthetic studies they may be quantified.
- Measurement of changes in attenuation through the direct analysis of waveforms between vintages can decrease the variation of spectral ratio slopes and improve estimates of the changes in t^* along a ray-path.
- Methodologies that measure attenuation changes made through analysis of spectral ratios (PSQI), centroid frequencies (CF) and instantaneous frequencies (IF) are all robust once parametrised correctly with similar uncertainties and sensitivity to band-limited noise. However, the instantaneous frequency methodology is time consuming to parametrise and more sensitive to changes in parameters, hence it is less desirable than the other methods.
- Magnitudes of attenuation observed in regions where hydrocarbon gas and CO_2 are being injected ($\Delta(1/Q) \approx 0.02$) can be described using a random patchy saturation model.
- Attenuation, measured together with other time-lapse attributes can be used to invert for changes in pressure and saturation in a hydrocarbon reservoir, yielding valuable information for the future planning and monitoring of the field. In the example shown here, attenuation helped constrain the pore pressure change, without impacting the change in gas saturation estimated from velocity and amplitude information.

References

Adam, L., Batzle, M., & van Wijk, K., 2010. Feasibility of estimating time-lapse q: a modelling example, *SEG Technical Program Expanded Abstracts*, **29**(1), 4215–4220.

Adriansyah & McMechan, G., 1998. Effects of attenuation and scattering on AVO measurements, *Geophysics*, **63**(6), 2025–2034.

Ahrens, T, 1995. *Rock physics and phase relations: a handbook of physical constants*, American Geophysical Union.

Aki, K. & Richards, P. G., 2002. *Quantitative Seismology* , University Science Books.

Arts, A., Eiken, O., Chadwick, A., Zweigel, P., Van der Mer, L., & Zinszner, B., 2004. Monitoring of CO2 injected at Sleipner using time-lapse seismic data, *Energy*, **29**, 1383–1392.

Avseth, P., Mukerji, T., & Mavko, G., 2005. Quantitative Seismic Interpretation - Applying Rock Physics Tools to Reduce Interpretation Risk.

Barkved, O. I., Kristiansen, T., & Fjaer, E., 2005. The 4D seismic response of a compacting reservoir—examples from the Valhall field, norway, *SEG Technical Program Expanded Abstracts*, **24**(1), 2508–2511.

Batzle, M. & Wang, Z., 1992. Seismic properties of pore fluids, *Geophysics*, **57**(11), 1396–1408.

Batzle, M. L., Han, D., & Hofmann, R., 2006. Fluid mobility and frequency dependent seismic velocity - Direct measurements, *Geophysics*, **71**(1), N1–N9.

Berryman, J., 1992. Exact effective-stress rules in rock mechanics, *Physical review A*, **46**, 3307–3311.

Best, A., McCann, C., & Sothcott, J., 1994. The relationships between the velocities, attenuation and petrophysical properties of reservoir sedimentary rocks, *Geophys. Prosp.*, **42**, 151–178.

Best, A. I. & McCann, C., 1995. Seismic attenuation and pore-fluid viscosity in clay-rich reservoir sandstones, *Geophysics*, **60**(5), 1386–1397.

Biot, M. A., 1956. Theory of propogation of elastic waves in a fluid-saturated porous solid - I. Low-frequency range, *The Journal of the acoustical soc. of America*, **28**(2), 168–179.

Bouchon, M., 1981. A simple method to calculate green's functions for elastic layered media, *BULLETIN OF THE SEISMOLOGICAL SOCIETY OF AMERICA*, **71**(4), 959–971.

Cadoret, T., Marion, D., & Zinszner, B., 1995. Influence of frequency and fluid distribution on elastic wave velocities in partially saturated limestones, *J. Geophys. Res.*, **100**(B6), 9789–9803.

Cadoret, T., Mavko, G., & Zinszner, B., 1998. Fluid distribution effect on sonic attenuation in partially saturated limestones, *Geophysics*, **63**(1), 154–160.

Calvert, R. C., 2005. Insights and methods for 4D reservoir monitoring and characterization, *2005 distinguished lecturer shortcourse*, **8**.

Carcione, J., Kosloff, D., & R.Kosloff, 1998. Wave propagation simulation in a linear viscoelastic medium, *Geophysical Journal*, **95**, 597–611.

Carter, A. J., 2003. Seismic wave attenuation from surface seismic reflection surveys-an exploration tool?, *University of Leeds PHD thesis*.

Chapman, M. & Liu, E., 2006. Seismic attenuation in rocks saturated with multi-phase fluids, *SEG Expanded Abstracts*, **25**(1988).

Clark, R. A., Carter, A., Neville, P., & and, P. B., 2001. Attenuation measurements from surface seismic data: azimuthal variation and time-lapse case studies., *EAGE Expanded Abstracts*, **63rd EAGE Conference and Technical Exhibition**(L028).

Clark, V. A., Tittmann, B. R., & Spencer, T. W., 1980. Effect of volatiles on attenuation (q^1) and velocities in sedimentary rocks, *J. Geophys. Res.*, **85**(B10), 5190–5198.

Daley, T., Myer, L., Peterson, J., Majer, E., & Hoversten, G., 2008. Time-lapse crosswell seismic and VSP monitoring of injected CO_2 in a brine aquifer, *Environmental Geology*, **54**, 1657–1665, 10.1007/s00254-007-0943-z.

Dasgupta, R. & Clark, R. A., 1998. Estimation of Q from surface seismic reflection data, *Geophysics*, **63**(6), 2120–2128.

Dutta, N. C. & Ode, H., 1979. Attenuation and dispersion of compressional waves in fluid-filled porous rocks with partial gas saturation (white model)—part i: Biot theory, *Geophysics*, **44**(11), 1777–1788.

Dvorkin, J., Mavko, G., & Nur, A., 1995. Squirt flow in fully saturated rocks, *Geophysics*, **60**, 97–107.

Frisillo, A. L. & Stewart, T. J., 1980. Effect of Partial Gas/Brine Saturation on Ultrasonic Absorption in Sandstone, *J. Geophys. Res.*, **85**, 5209–5211.

Gardner, G. H. F., Gardner, L. W., & Gregory, A. R., 1974. Formation velocity and density—the diagnostic basics for stratigraphic traps, *Geophysics*, **39**(6), 770–780.

Gassmann, F., 1951. Uber die elastizitat poroser medien, *Vier. Natur. Gesellschaft Zurich*, **96**, 1–23.

Gubbins, D., 2004. *Time series analysis and invserse theory for geophysicists*, Cambridge University Press.

Gurevich, B. & Lopatnikov, S. L., 1995. Velocity and attenuation of elastic waves in finely layered porous rocks, *Geophysical Journal International*, **121**(3), 933–947.

Han, D. & Nur, A., 1986. The effects of porosity and clay content on wave velocities in sandstones, *SEG Technical Program Expanded Abstracts*, **5**(1), 1–3.

Hashin, Z. & Shtrikman, S., 1963. A variational approach to the theory of the elastic behaviour of multiphase materials, *Journal of the Mechanics and Physics of Solids*, **11**(2), 127 – 140.

Hedlin, K., Mewhort, L., & Margrave, G., 2001. Delineation of steam flood using seismic attenuation, *SEG Expanded abstracts*, **71st Annual International Meeting**(20), 1572–1575.

Hicks, G. J. & Pratt, R. G., 2001. Reflection waveform inversion using local descent methods: Estimating attenuation and velocity over a gas-sand deposit, *Geophysics*, **66**(2), 598–612.

Hovorka, S. D., Benson, S. M., Doughty, C., Freifeld, B. M., Sakurai, S., Daley, T. M., Kharaka, Y. K., Holtz, M. H., Trautz, R. C., Nance, H. S., Myer, L. R., & Knauss, K. G., 2006. Measuring permanence of CO_2 storage in saline formations: the Frio experiment, *Environmental Geosciences*, **13**(2), 105–121.

Hustedt, B. & Clark, R. A., 1999. Source/receiver array directivity effects on marine seismic attenuation measurements, *Geophysical Prospecting*, **47**(6), 1105–1119.

Johnston, D. H., Toksoz, M. N., & Timur, A., 1979. Attenuation of seismic waves in dry and saturated rocks: II. mechanisms, *Geophysics*, **44**(4), 691–711.

Kanasewich, E., 1981. *Time sequence analysis in Geophysics*, The University of Alberta Press.

Kennett, B. L. N. & Kerry, N. J., 1979. Seismic waves in a stratified half space, *Geophysical Journal of the Royal Astronomical Society*, **57**(3), 557–583.

Klimentos, T. & McCann, C., 1990. Relationships among compressional wave attenuation, porosity, clay content, and permeability in sandstones, *Geophysics*, **55**(8), 998–1014.

Koesoemadinata, A. P. & McMechan, G. A., 2001. Empirical estimation of viscoelastic seismic parameters from petrophysical properties of sandstone, *Geophysics*, **66**(5), 1457–1470.

Kolsky, H., 1956. The propagation of stress pulses in viscoelastic solids, *Philosophical Magazine*, **1**(8), 693–710.

Kragh, E. & Christie, P., 2002. Seismic repeatability, normalized RMS, and predictability, *The Leading Edge*, **21**(7), 640–647.

Lackner, K., 2003. A guide to CO_2 sequestration, *Science*, **300**(5626), 1677–1678.

Landrø, M., 2001. Discrimination between pressure and fluid saturation changes from time-lapse seismic data, *Geophysics*, **66**(3), 836–844.

Landrø, M., Solheim, O., Hilde, E., Ekren, B., & Strønen, L., 1999. The Gullfaks 4D seismic study, *Petroleum Geoscience*, **5**(3), 213–226.

Liu, H.-P., Anderson, D. L., & Kanamori, H., 1976. Velocity dispersion due to anelasticity; implications for seismology and mantle composition, *Geophysical Journal of the Royal Astronomical Society*, **47**(1), 41–58.

MacBeth, C., Floricich, M., & Soldo, J., 2006. Going quantitative with 4D seismic analysis, *Geophysical Prospecting*, **54**(3), 303–317.

MacGregor, A., Trussel, P., & Lauver, S., 2005. The Magnus field: extending field life through good reservoir management and enhanced oil recovery, *Petroleum Geology Conference series*, **6**(1), 469–475.

Matheney, M. P. & Nowack, R. L., 1995. Seismic attenuation values obtained from instantaneous-frequency matching and spectral ratios, *Geophysical Journal International*, **123**(1), 1–15.

Mavko, G. & Jizba, D., 1991. Estimating grain scale fluid effects on velocity dispersion in rocks, *Geophysics*, **56**, 1940–1949.

Mavko, G., Mukerji, T., & Dvorkin, J., 2003. The rock physics handbook - tools for seismic analysis in porous media.

Müller, M. & Gurevich, B., 2004. One-dimensional random patchy saturation model for velocity and attenuation in porous rocks, *Geophysics*, **69**(5), 1166–1172.

Müller, M., Gurevich, B., & Lebvedev, M., 2010. Seismic wave attenuation and dispersion resulting from wave induced flow in porous rocks, *Geophysics*, **75**(5), 75A147–75A164.

Murphy, W. F., 1982. Effects of partial water saturation in Massilon sandstone and Vycor porous glass, *J. Acoust. Soc. Am.*, **71**(6), 1458–1468.

Murphy, W. F., Roberts, N., Yale, D., & Winkler, K. W., 1984. Centimeter scale heteogeneities and microstratification in sedimentary rocks, *Geophys. Res Lett*, **11**(8), 697–700.

O'Brien, J., Kilbride, F., & Lim, F., 2004. Time-lapse VSP reservoir monitoring, *The Leading Edge*, **23**(11), 1178–1184.

O'Connell, R. & Budiansky, B., 1978. Measures of dissipation in viscoelastic media, *Geophys. Res. Lett.*, **5**(1), 5–8.

O'Doherty, R. F. & Anstey, N. A., 1971. Reflections on amplitudes, *Geophysical Prospecting*, **19**(3), 430–458.

Prasad, M. & Manghnani, M., 1997. Effects of pore and differential pressure on compressional wave velocity and quality factor in Berea and Michigan sandstones, *Geophysics*, **62**(4), 1163–1176.

Pratt, G., 1999. Seismic waveform inversion in the frequency domain, part 1: Theory and verification in a physical scale model, *Geophysics*, **64**(3), 888–901.

Quan, Y. & Harris, J. M., 1997. Seismic attenuation tomography using the frequency shift method, *Geophysics*, **62**(3), 895–905.

Raikes, S. A. & White, R. E., 1984. Measurements of earth attenuation from downhole and surface seismic recordings, *Geophysical Prospecting*, **32**(5), 892–919.

Reine, C., 2009. A robust prestack Q-inversion in the t-p domain using variable-window spectral estimates, *University of Leeds, PhD Thesis*.

Reine, C., Clark, R., & van der Baan, M., 2011. Robust prestack Q-determination using surface seismic data: I - method and synthetic examples, *Geophysics*, **submitted 18-Feb-2011**.

Reine, C., Clark, R., & van der Baan, M., 2011. Robust prestack Q-determination using surface seismic data: II - 3d case study, *Geophysics*, **submitted 18-Feb-2011**.

Rickett, J., 2006. Integrated estimation of interval-attenuation profiles, *Geophysics*, **71**(4), A19–A23.

Rickett, J., 2007. Estimating attenuation and the relative information content of amplitude and phase spectra, *Geophysics*, **72**(1), R19–R27.

Rossi, G., Gei, D., Böhm, G., Madrussani, G., & Carcione, J. M., 2007. Attenuation tomography: An application to gas-hydrate and free-gas detection, *Geophysical Prospecting*, **55**(5), 655–669.

Sams, M. S., Neep, J. P., Worthington, M. H., & King, M. S., 1997. The measurement of velocity dispersion and frequency-dependent intrinsic attenuation in sedimentary rocks, *Geophysics*, **62**(5), 1456–1464.

Shuey, R. T., 1985. A simplification of the Zoeppritz equations, *Geophysics*, **50**(4), 609–614.

Spencer, T. W., Edwards, C. M., & Sonnad, J. R., 1977. Seismic wave attenuation in nonresolvable cyclic stratification, *Geophysics*, **42**(5), 939–949.

Spencer, T. W., Sonnad, J. R., & Butler, T. M., 1982. Seismic Q—stratigraphy or dissipation, *Geophysics*, **47**(1), 16–24.

Stewart, R. R., 1984. VSP interval velocities from traveltime inversion, *Geophysical Prospecting*, **32**(4), 608–628.

Stockwell, R., Mansinha, L., & Lowe, R., 1996. Localization of the complex spectrum: the s transform, *Signal Processing, IEEE Transactions on*, **44**(4), 998–1001.

Tao, G., King, M., & Nabi-Bidhendi, M., 1995. Ultrasonic wave propagation in dry and brine-saturated sandstones as a function of effective stress: laboratory measurements and modelling, *Geophysical Prospecting*, **43**(3), 299–327.

Toksöz, M. N., Johnston, D. H., & Timur, A., 1979. Attenuation of seismic waves in dry and saturated rocks: I. laboratory measurements, *Geophysics*, **44**(4), 681–690.

Tonn, R., 1991. The determination of the seismic quality factor Q from VSP data: A comparison of different computational methods, *Geophys. Prosp.*, **39**, 1–27.

Torp, T. A. & Gale, J., 2004. Demonstrating storage of CO_2 in geological reservoirs: The Sleipner and SACS projects, *Energy*, **29**(9-10), 1361 – 1369, 6th International Conference on Greenhouse Gas Control Technologies.

Ursin, B. & Toverud, T., 2002. Comparison of seismic dispersion and attenuation models, *Studia Geophysica et Geodaetica*, **46**, 293–320, 10.1023/A:1019810305074.

Van der Baan, M., 2001. Acoustic wave propagation in one-dimensional random media: thewave localization approach, *Geophysical Journal International*, **145**(3), 631–646.

Van der Baan, M., 2002. Constant Q and a fractal, stratified earth, *Pure and Applied Geophysics*, **159**, 1707–1718, 10.1007/s00024-002-8704-0.

Wang, Y., 2008. *Seismic inverse Q filtering*, Blackwell Publishing.

Watts, G., Jizba, D., Gawith, D. E., & Gutteridge, P., 1996. Reservoir monitoring of the Magnus field through 4D time-lapse seismic analysis, *Petroleum Geoscience*, **2**(4), 361–372.

White, B., Sheng, P., & Nair, B., 1990. Localization and backscattering spectrum of seismic waves in stratified lithology, *Geophysics*, **55**(9), 1158–1165.

White, J. E., 1975. Computed seismic speeds and attenuation in rocks with partial gas saturation, *Geophysics*, **40**(2), 224–232.

Williams, T., 2001. Time-lapse seismic wave attenuation for reservoir monitoring, *Leeds MSc dissertation*.

Wilson, A., Chapman, M., & Li, X., 2009. Use of frequency dependent AVO inversion to estimate P-wave dispersion properties from reflection data, *71st EAGE Conference and Exhibition*, **Amsterdam**(6).

Winkler, K. & Nur, A., 1979. Pore fluids and seismic attenuation in rocks, *Geophys. Res. Lett.*, **6**(1), 1–4.

Winkler, K. W., 1986. Estimates of velocity dispersion between seismic and ultrasonic frequencies, *Geophysics*, **51**(1), 183–189.

Xu, H., 2006. Calculation co2 acoustic properties using Batzle-Wang equations, *Geophysics*, **71**(2), F21–F23.

Yilmaz, O., 2001. Seismic data analysis: Processing and interpretation of seismic data, Volumes 1 and 2.

Yin, C., Batzle, M., & Smith, B., 1992. Effects of partial liquid/gas saturation on extensional wave attenuation in Berea Sandstone, *Geophysical Research letters*, **19**(13), 1399–1402.

Zoeppritz, K., 1919. Erdbebenwellen VIIIB, On the reflection and propagation of seismic waves, *Göttinger Nachr*, **1**, 66–84.

Appendix A

PSQI - Damping and Secondary constraint

Here I outline how both damping and a secondary constraint can be included in the PSQI inversion outlined in Chapter 3.

A.1 Model size damping

In Chapter 3 I outlined the PSQI methodology (Reine, 2009) for estimating attenuation from a CMP of data, where the following system of equations was solved to gain a single value of attenuation.

$$\begin{pmatrix} d_{1,1} \\ d_{2,1} \\ \vdots \\ d_{N,1} \\ d_{1,2} \\ \vdots \\ d_{N,2} \\ \vdots \\ d_{1,M} \\ \vdots \\ d_{N,M} \end{pmatrix} = \begin{pmatrix} t_1 f_1 & 1 & 0 & \cdots & 0 \\ t_1 f_2 & 1 & 0 & \cdots & 0 \\ \vdots & \vdots & \vdots & \ddots & \vdots \\ t_1 f_N & 1 & 0 & \cdots & 0 \\ t_2 f_1 & 0 & 1 & \cdots & 0 \\ \vdots & \vdots & \vdots & \ddots & \vdots \\ t_2 f_N & 0 & 1 & \cdots & 0 \\ \vdots & \vdots & \vdots & \ddots & \vdots \\ t_M f_1 & 0 & 0 & \cdots & 1 \\ \vdots & \vdots & \vdots & \ddots & \vdots \\ t_M f_N & 0 & 0 & \cdots & 1 \end{pmatrix} \begin{pmatrix} A \\ B_1 \\ B_2 \\ \vdots \\ B_M \end{pmatrix} \tag{A.1}$$

This can be written in vector an matrix notation as

$$d = Gm. \tag{A.2}$$

where d contains the spectral ratio values at frequencies n and times m ($d_{m,n}$), G is the conditions matrix and m contains the model parameters (gradients and intercepts of the fitted surface). This is then solved in a least squares fashion and including a weighting matrix (W) the model can be found by

$$\mathbf{m} = (\mathbf{G'WG})^{-1}\mathbf{G'Wd} \tag{A.3}$$

By including normal damping, we can try to minimize the size of the model $\sum m^2$ found. If θ_1^2 is the damping parameter - a positive scalar, Equation A.4 becomes.

$$\mathbf{m} = (\mathbf{G'WG} - \boldsymbol{\theta}_\mathbf{1}^\mathbf{2}\mathbf{I})^{-\mathbf{1}}\mathbf{G'Wd} \tag{A.4}$$

where I is the identity matrix. This has the effect of adding a constant to each element of the normal equations matrix ($G'WG$), therefore decreasing the contribution to the solution of noisy model parameters (Gubbins, 2004). The effect and use of this damping parameter should be tested on a dataset by dataset basis.

A.2 Secondary constraint - minimizing the gradient of the intercept terms

In the regression outlined above, no relationship is assumed between the terms that hold information about the reflectivity within the data. However, this term contains information about the reflectivity of the form:

$$B_n = log(R_n G_n) \tag{A.5}$$

It may be possible to constrain some relationship between the values of B_n as they contain information about the reflectivity as a function of offset. In the direct PSQI methodology, this information will primarily contain information about the change in AVO between vintages.

Here, I do not propose introducing an AVO style regression simultaneously with the Q inversion. Instead I propose a secondary constraint whereby the adjacent intercept terms B_n and B_{n-1} should not vary greatly. AVO curves tend to vary smoothly particularly in the near offset range where they are a function of $sin^2\theta$ (Aki & Richards, 2002; Avseth et al., 2005).

Allowing these terms to vary greatly, when they should in theory vary smoothly may impact the regression for the spectral ratio slope. This can be achieved by minimizing the secondary constraint:

$$B_n - B_{n-1} = 0 \tag{A.6}$$

$$\begin{pmatrix} 0 \\ 0 \\ 0 \\ \vdots \\ 0 \\ 0 \end{pmatrix} = \begin{pmatrix} 0 & 1 & -1 & 0 & \cdots & 0 & 0 \\ 0 & 0 & 1 & -1 & \cdots & 0 & 0 \\ 0 & 0 & 0 & 1 & \cdots & 0 & 0 \\ \vdots & \vdots & \vdots & \vdots & \ddots & \vdots & \vdots \\ 0 & 0 & 0 & 0 & \cdots & -1 & 0 \\ 0 & 0 & 0 & 0 & \cdots & 1 & -1 \end{pmatrix} \begin{pmatrix} A \\ B_1 \\ B_2 \\ B_3 \\ \vdots \\ B_{M-1} \\ B_M \end{pmatrix} \tag{A.7}$$

Or written in vector notation;

$$\mathbf{Hm} = \mathbf{b} \tag{A.8}$$

This can then be solved via a least squares method by

$$\mathbf{m} = (\mathbf{G^T WG} + \boldsymbol{\theta}_\mathbf{2}^\mathbf{2}\mathbf{H^T H})^{-\mathbf{1}}(\mathbf{G^T Wd} + \mathbf{H^T b}) \tag{A.9}$$

θ_2^2 therefore determines how errors on the secondary constraint should be minimized. Again, the value of θ_2^2 should be determined from the real data.

It can then be seen that the overall inversion scheme, including weighting (W), modelsize damping (θ_1^2) and the secondary constraint (θ_2^2) can be written as

$$\mathbf{m} = (\mathbf{G^T W G} + \theta.\mathbf{_2^2 H^T H} + \mathbf{\theta_1^2 I})^{-1}(\mathbf{G^T W d} + \mathbf{H^T b}). \tag{A.10}$$

Appendix B

AVO - Magnus Data

Classical AVO analysis can tell us information about variations in density, P-wave velocity and S-wave velocity contrasts. AVO interpretations can be difficult for reservoirs like Magnus where top reservoir is defined by an unconformity. This means there is spatially varying lithological properties of the rock and hence AVO signatures are not the same across the reservoir. Here we look at the 2 and 3 term Shuey equations and fit them to amplitudes extracted at the top reservoir horizon. Amplitudes are extracted from the flattened CMP gathers at times picked for the top reservoir reflection. The raw amplitudes of an example crossline 3104 can be seen in Figure B.1 and show the variation in class of AVO along a dipline across the reservoir. Angles are then calculated for each offset and CMP using velocities obtained from the stacking velocity and a 1D ray tracing algorithm. These angles are then smoothed and can be seen in figure B.2. The variation in angle along the crossline is due to the changing depth of the top reservoir reflection.

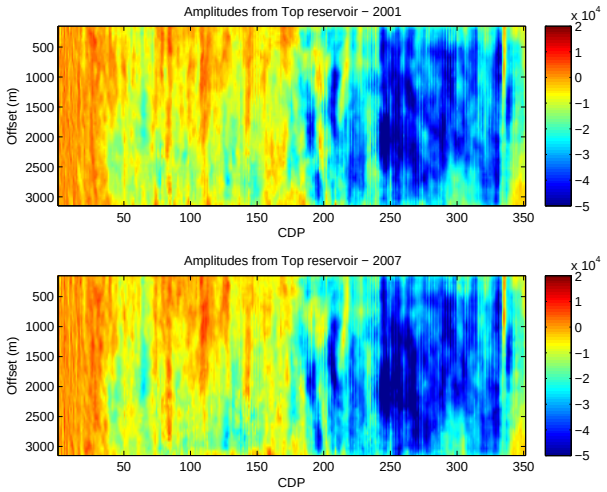

Figure B.1: Extracted amplitudes for top reservoir for AVO analysis.

The two-term Shuey approximation is then inverted for using angles less than 30 degrees (Equation B.1). By plotting these intercept and gradient terms (Figure B.3) we can classify the AVO signal that we have in the dipline. The AVO anomalies mostly lie within classes II and III with some lying outside this in class IV and class IIp Avseth et al. (2005). AVO gradients are slightly more scattered for the 3 term Shuey approximation (Equation B.2) using all angles of incidence.

$$R(\theta) = A + B\sin^2(\theta) \tag{B.1}$$

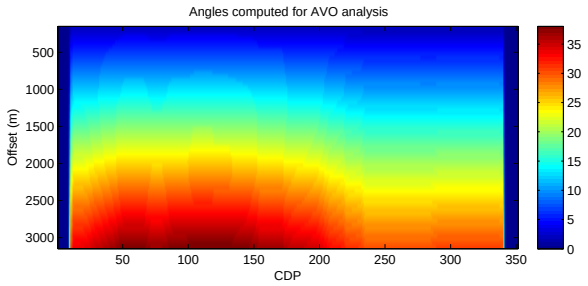

Figure B.2: Angles calculated using a 1D ray-tracing code.

$$R(\theta) = A + B\sin^2(\theta) + C(\tan^2(\theta) - \sin^2(\theta)) \tag{B.2}$$

The parameters inverted for above (A, B and C) can be described in terms of the change in density and velocities for vintage 1:

$$A = \gamma(\frac{1}{2}(\frac{\Delta V_p}{V_p} + \frac{\Delta\rho}{\rho})) \tag{B.3}$$

$$B = \gamma(\frac{1}{2}\frac{\Delta V_p}{V_p} - 2(\frac{V_s}{V_p})^2(2\frac{\Delta V_s}{V_s} + \frac{\Delta\rho}{\rho})) \tag{B.4}$$

$$C = \gamma(\frac{1}{2}\frac{\Delta V_p}{V_p}) \tag{B.5}$$

where V_p,V_s and ρ are the averages of intervals either side of the reflector, ΔV_p,ΔV_s and $\Delta\rho$ are the changes in properties across the interface and γ represents a scaling factor that scales the amplitudes we measure ($Z(\theta)$) to the true reflection coefficient ($Z(\theta)\gamma = R(\theta)$).

$$m = (A^T A)^{-1} A^T d \tag{B.6}$$

where $m = [ABC]^T$, $A = [1 sin^2(\theta_1)\tan^2(\theta_1) - \sin^2(\theta_1); .....; 1 sin^2(\theta_n)\tan^2(\theta_n) - \sin^2(\theta_n)]$ and $d = [Z(\theta_1).....Z(\theta_n)$ where $Z(\theta_n)$ is the amplitude measured for that particular angle of incidence. There is no data covariance matrix included initially as all measurements are assumed to be linearly independent of one another and measurement error the same for each measurement.

Difference plots of the AVO constants A, B and C from the three term Shuey equation can be seen in Figure B.4. There appear to be no significant differences in any of the attributes between vintages of data. However, what is clear to see is the magnitude of the differences between the A, B and C term. There is approximatly a two order of magnutide difference between the A and C term. This means that we need to introduce damping into the AVO inversion to reduce the size of the model vector.

B.1 Damping of AVO

We can add model damping to the inversion scheme by adding to the diagonal of multiplication of the conditions matrix. This will increase the stability in finding the inverse of the matrix. We can then solve

$$m = (A^T A + \lambda I)^{-1} A^T d \tag{B.7}$$

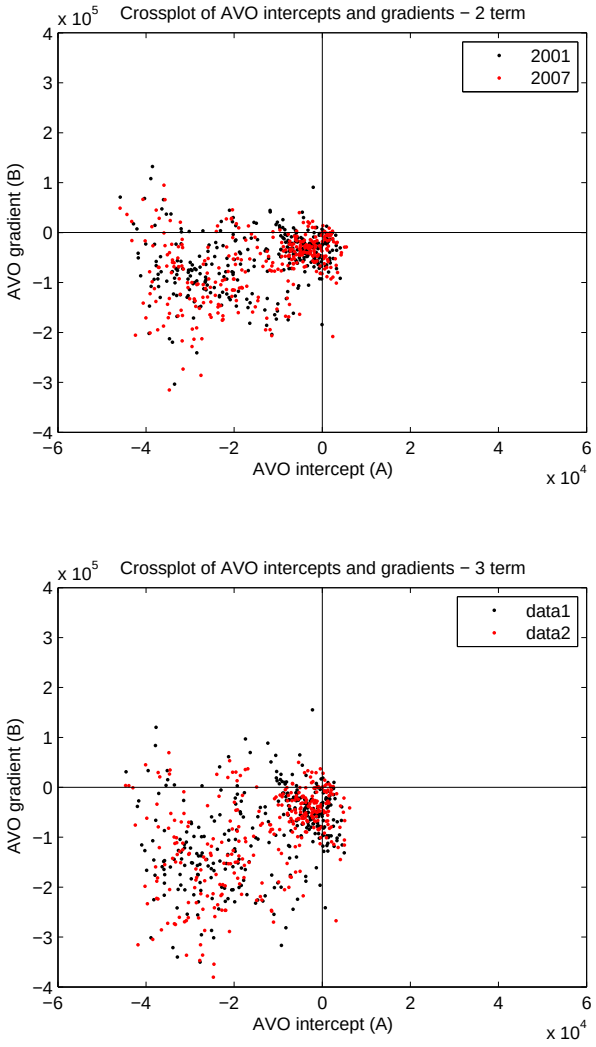

Figure B.3: Cross plot comparing Intercept and Gradient terms from the 2 term and 3 term Shuey equations.

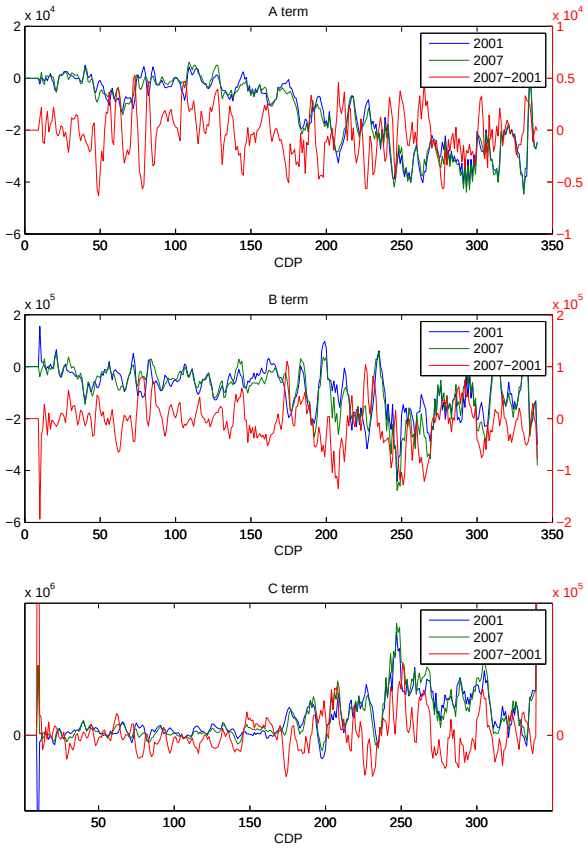

Figure B.4: Comparison of A,B and C from Shuey's 3 term equation.

A suitable damping parameter λ must then be found where λ must be positive with $\lambda = 0$ yielding the non-damped solution seen in Equation B.6. The inversion is then calculated using a number of damping values. 201 damping values are tested ranging from $10^{-10} to 10^{10}$. Initially these were tested on a single CMP and plotted in 3 ways: λ vs. Misfit (E^2), λ vs Model Norm (N), and the Model Norm vs. Misfit, where the Model Norm (N) is given by $\sqrt{A^2 + B^2 + C^2}$ and Misfit (E^2) given by $(d - Am)^2$. We calculate these misfits for the whole inline and average the model size and misfit for all CMP's. Figure B.5 shows these averaged parameters and a clear region exists centred upon 10^0 where we have significantly reduced the model size without significantly increasing the data misfit. This region is represented as the 'knee' in the bottom graph of Figure B.5. As the stable region is centred around the 10^0, this would be a suitable damping parameter to use for the whole dataset.

We can see the effect of damping on the size of individual model parameters in Figure B.6.

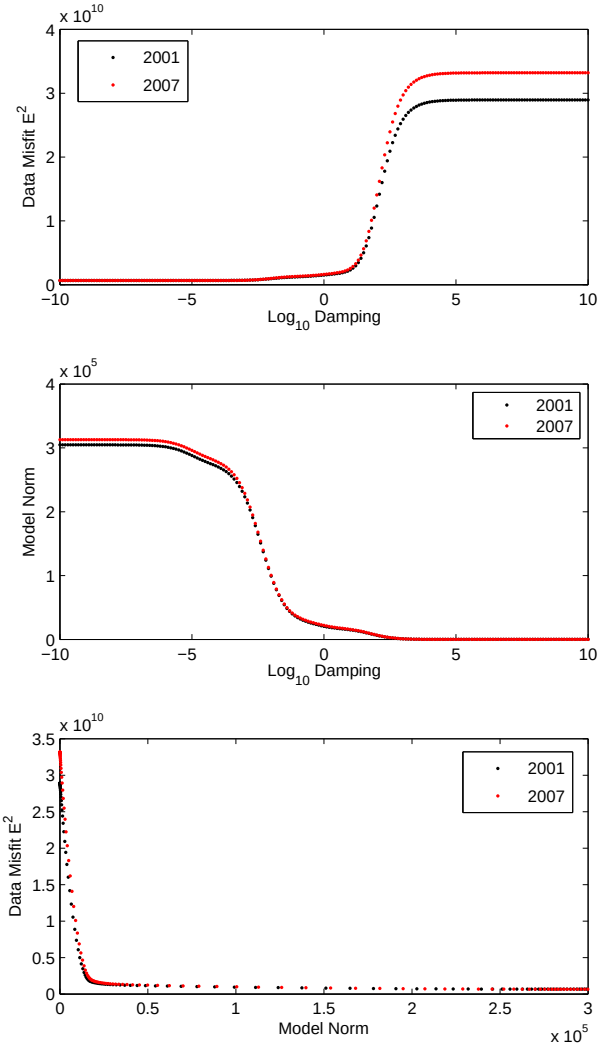

Figure B.5: Top: Average Data misfit vs Damping constant. Middle: Average Model Norm vs. Damping constant. Bottom: Average Data Misfit vs. model Norm.

Ideally we need all 3 parameters to be of approximately the same magnitude. We can see the effect of damping on the size of individual model parameters in Figure B.6. At

around $10^{-1.2}$ all model parameters are approximately the same size and this is as we would desire from the output of the inversion. What we can see is the variation of the position of intersection for varying averages of data. For example the average parameters from the entire dataset intersect between -1 and -0.5, the average parameters from the region with good angle coverage (CDP 50 to 200 (solid line)) intersect between -0.5 and 0.25 and the parameters for CDP 100 (dashed line) intersect between 0.5 and 1. This may suggest that it may be more appropriate to have a changing damping parameter across the dipline.

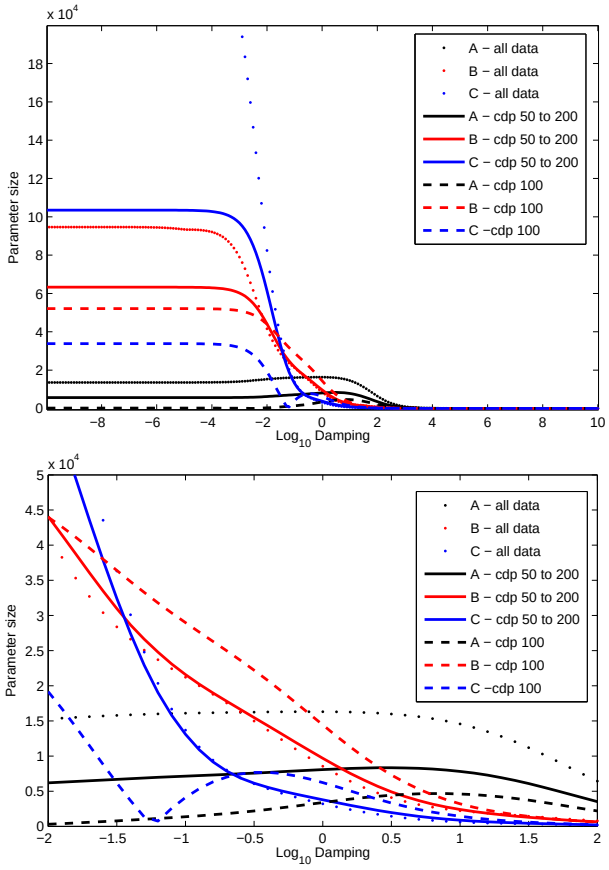

Figure B.6: Average Size of the individual model parameters as a function of damping.

However to begin with a damping parameter of 10^0 will be used in the inversion.

B.2 Secondary constraint

We can also introduce a secondary constraint. It is plausible in some circumstances to assume initially that the density contrast across the boundary is small compared with the velocity change and hence A should be very similar to C. We can therefore introduce a secondary constraint of

$$\mathbf{b} = \mathbf{Hm} \tag{B.8}$$

where

$$b = A - C = \gamma(\frac{1}{2}\frac{\Delta\rho}{\rho}) = 0 \tag{B.9}$$

$$\mathbf{m} = [\mathbf{ABC}]^{\mathbf{T}} \tag{B.10}$$

$$\mathbf{H} = [\mathbf{1}, \mathbf{0}, -\mathbf{1}] \tag{B.11}$$

we can therefore add this to the function to be minimized to get

$$E = |\mathbf{d} - \mathbf{Am}|^{\mathbf{2}} + \beta|\mathbf{b} - \mathbf{Hm}|^{\mathbf{2}} \tag{B.12}$$

and differentiate this w.r.t $\mathbf{m}$, and re-arrange for $dE/dm = 0$ to get

$$\mathbf{m} = (\mathbf{A^T A} + \beta\mathbf{H^T H})^{-\mathbf{1}}(\mathbf{A^T d} + \mathbf{H^T b}) \tag{B.13}$$

Initially b=0 and we can solve

$$\mathbf{m} = (\mathbf{A^T A} + \beta\mathbf{H^T H})^{-\mathbf{1}}\mathbf{A^T d} \tag{B.14}$$

NB, This is not included in the final inversion as it is difficult to parametrize and assumptions are too large for the Magnus field.

B.3 AVO - Dipline Results

Final results from the AVO using a damping parameter can be seen in Figure B.7. A decrease in the intercept (A) can be seen along the dipline which matches the increasing negative amplitude seen in the seismic stacked section. There is also a strong correlation between both the gradient terms (B and C) as may be expected. We can also look at the uncertainty in the measurements by calculating the model covariance matrix.

$$C_m = (A^T A + \lambda I)^{-1} \tag{B.15}$$

The diagonals of this matrix represent the variance of each parameter of data. And the off-diagonal elements correspond to the co-variances of each combination of model parameters. Variances for each model parameter for each CMP are plotted in Figure B.8. It is clear that the intercept (A) is much better determined than the gradient terms. What is more important however is the sharp increase in uncertainty in C at around CDP=200. This is due to the sharp drop in the availability of far-angles in the regression at these CDP's (Figure B.2).

B.3.1 Well Control

In order to get quantitative estimation from the AVO data it is important to calculate the value γ. This will effectively allow the amplitudes measured to be scaled to the magnitude of true reflection coefficients and hence allow the estimation of true changes in velocity and density. Here I shall look at using the A and C values calculated above and velocity changes and density changes measured from well data.

Well information that is available exists on crossline 2950, and inline 2500. Seismic data quality is poor in this region due to the proximity of the platform so the well will be shifted along strike (to avoid crossing lithological boundaries) until reaching the crossline processed above. This now places the well at CDP 175 in our profile. Only velocity information is available either side of the top reservoir horizon. We can then estimate the velocity above (V_{p_1}) and below (V_{p_2}) the top reservoir horizon.

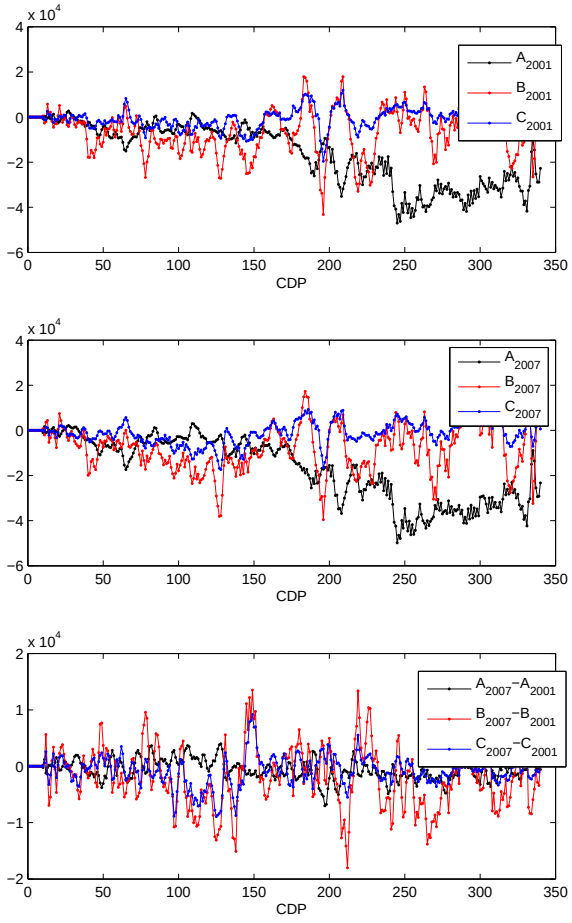

Figure B.7: A,B and C calculated for 2001 (top) and 2007 (middle). Differences for A, B and C from 2001 to 2007 (bottom).

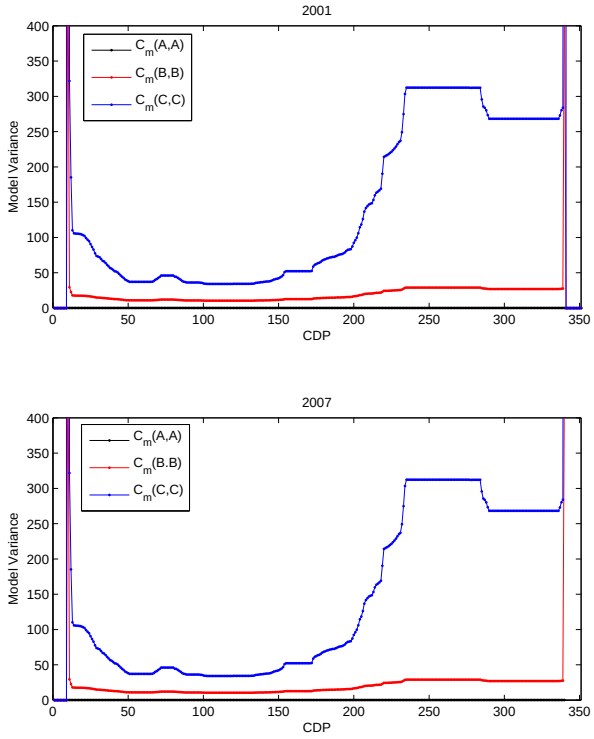

Figure B.8: Diagonals of Model covariance matrix, corresponding to uncertainty on A, B and C for 2001 (top) and 2007 data (bottom).

$$V_{p_1} = 3.23km.s^{-1}$$
$$V_{p_2} = 2.73km.s^{-1}$$

As densities are not available directly from the well information we can estimate using the equation of Gardner et al. (1974) (Equation B.16) with $d = 1.75, 1.66$ and $f = 0.265, 0.261$ for a shale (above reservoir) and sandstone (below reservoir) respectively.

$$\rho = dV_p^f \tag{B.16}$$

This then gives us empirical estimates for the density above and below the reservoir.

$$\rho_1 = 2.39g.cm^{-3}$$
$$\rho_1 = 2.16g.cm^{-3}$$

We can then calculate the true value for A in the Shuey equation.

$$A* = \frac{1}{2}(\frac{\Delta V_p}{V_p} + \frac{\Delta \rho}{\rho}) \tag{B.17}$$

where

$$\Delta V_p = V_{p_2} - V_{p_1}$$
$$V_p = 0.5(V_{p_2} + V_{p_1})$$
$$\Delta \rho = \rho_2 - \rho_1$$
$$\rho = 0.5(\rho_2 + \rho_1)$$

so when calculated,

$$A* = -0.135$$

We can now take the average A value from CMP's 170 to 180,

$$A = -9590$$

and take the ratio to get γ

$$\gamma = \frac{A}{A*} = 71,034$$

We can now scale the results of A, B and C generated above to get a plot of A*, B* and C* (top and middle Figure B.9). We can then look at the change in C* and A*-C* to get an estimate of the change in P-wave velocity and density respectively (bottom Figure B.9).

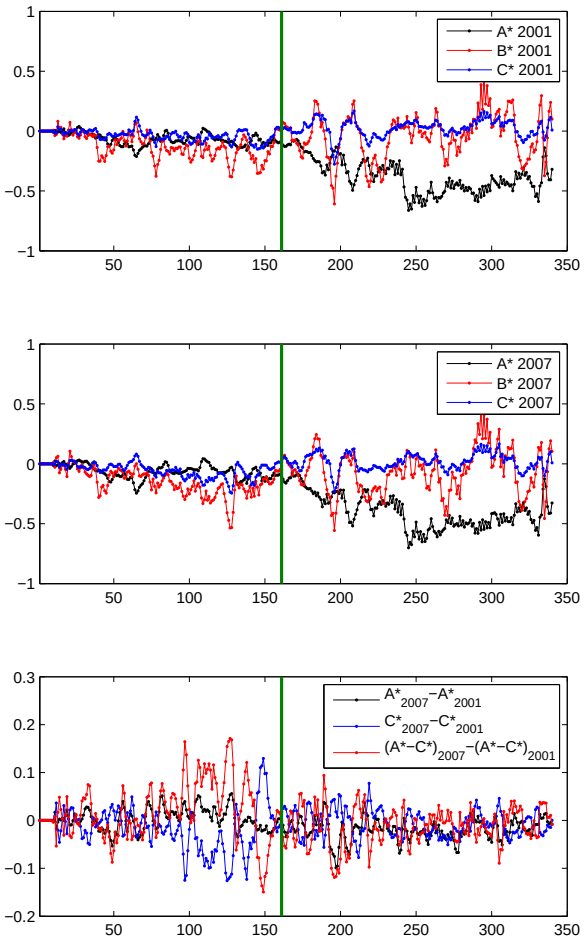

Figure B.9: A*,B* and C* calculated for 2001 (top) and 2007 (middle) using $\gamma = 71,034$. Differences in C* and A*-C* from 2001 to 2007 (bottom).